

*Periodicals of*  
**Engineering and Natural Sciences**

VOL. 5 NO. 3  
(2017)

**Periodicals of Engineering and Natural Sciences (PEN)**

Periodicals of Engineering and Natural Sciences (ISSN: 2303-4521) is an international open access single-blind review journal published online.

Publication frequency: Semiyearly (1. January - June; 2. July - December).

Publication Fees: No fee required (no article submission charges or processing charges).

Digital Object Identifier DOI: [10.21533/pen](https://doi.org/10.21533/pen)

**Editorial Office**

**Mailing Address**

Hrasnicka cesta 15  
71000 Sarajevo  
Bosnia

**Principal Contact**

Benjamin Durakovic  
Managing Editor  
International University of Sarajevo  
Hrasnicka cesta 15  
71000 Sarajevo  
Bosnia  
Phone: +387 33 957 229  
Email: [pen@ius.edu.ba](mailto:pen@ius.edu.ba)

Available online at:

<http://pen.ius.edu.ba>

## Editorial Team

### Editor in Chief

Dr. Fuat GÜRCAN, Erciyes University, Turkey

### Managing Editor

Benjamin Durakovic, International University of Sarajevo, Bosnia and Herzegovina

### Editorial Board

Dr. Seong Jin Park, Pohang University of Science and Technology, Korea, Republic of  
Dr. Mehmet Sabih Aksoy, Computer Science, King Saud University, Saudi Arabia  
Dr. Fehim Findik, Material Science, Sakarya University, Turkey  
Dr. Muzaffar A. Shaikh, Industrial Engineering, Florida Institute of Technology, United States  
Dr. Youssef Hammi, Mechanical Engineering, Mississippi State University, United States  
Dr. Nezhir Mrad, Mechanical Engineering, National Research Council, Canada  
Dr. Izudin Dzafic, Electrical and Electronics, Bosnia and Herzegovina  
Dr. John Dee, Achitecture, IUS, Australia  
Dr. Vanessa Ratten, La Trobe University, Australia  
Dr. Veland Ramadani, South East European University, Macedonia, FYR  
Dr. Ramo Palalic, Dhofar University, Oman  
Dr. Mustafa Akay, Mechanical Engineering, Ulster University, United Kingdom  
Dr. İbrahim Özsert, Mechanical Engineering, Sakarya University, Turkey  
Dr. Muzaffer H Saračević, University of Novi Pazar, Serbia  
Dr. Hazim Basic, Faculty of Mechanical Engineering Sarajevo, Bosnia and Herzegovina  
Dr. Raşit Köker, Electrical & Electronics, Turkey  
Dr. Adem Demir, Material Science, Sakarya University, Turkey  
Dr. Muhamed Hadziabdic, Mechanical Engineering, IUS, Bosnia and Herzegovina  
Dr. Orhan Torkul, Industrial Engineering, Sakarya University, Turkey  
Dr. Semra Boran, Industrial Engineering, Sakarya University, Turkey  
Dr. Benjamin Durakovic, Industrial Engineering

## Publication Frequency

Expected frequency of publication is twice per year:

1. January - June;
2. July - December.

Journal items can be published collectively, as part of an issue with its own Table of Contents. Alternatively, individual items can be published as soon as they are ready, by adding them to the "current" volume's Table of Contents.

## Open Access Policy

This journal provides immediate open access to its content on the principle that making research freely available to the public supports a greater global exchange of knowledge.

## Journal Ethics and Malpractice Statement

PEN Journal is committed to ensure and uphold standards of ethical behavior at all stages of the publication process, whereby such values also rely on editors, reviewers, contributors and authors who are expected to behave ethically. The standards are based on Committee on Publication Ethics' (COPE) code of conduct, and provide guidelines for best practices in order to meet these requirements. The following ethical guidelines are only intended to give a summary of our key expectations of editors, peer-reviewers, and authors but if you have any questions or concerns please also feel free to contact the Editor of the Journal.

### 1. Ethical Expectations

#### Editors' responsibilities

- To carry out their duties in a fair, objective and consistent manner, without discrimination on grounds of gender, sexual orientation, religious or political beliefs, ethnic or geographical origin of the authors.
- To take care that each article undergoes the proper peer-review process.
- To promote consistent ethical policies of PEN journal, and to ensure the confidentiality of the reviewing process.
- To uphold integrity in their work as editors of the journal, doing away with any personal interest, so that articles are considered and accepted solely on their academic merit and without commercial influence.
- To work with authors, reviewers, and the Editorial Board members to ensure the implementation of journals' ethics and publishing policies.
- To adopt and follow reasonable procedures in the event of complaints of an ethical or conflict nature, in accordance with the policies and procedures. To handle process of complaints and giving authors an opportunity to respond any complaints. All complaints should be investigated and the documentation associated with any such complaints should be retained.

#### Reviewers' responsibilities

- To act objectively, fairly and in a timely manner in reviewing submitted manuscript with the aim of improving its quality such as pointing out relevant published work, which is not cited, etc.
- To alert PEN in case of any competing interest that could affect the impartiality of their reviewing, or any potential conflict of interest that includes any relationship between reviewer and author, or any content that is substantially similar to that under review.
- To conduct themselves fairly and impartially.
- To keep the confidentiality of the review process and to not retain or copy the manuscript.

**Authors' responsibilities**

- To ensure that their work submitted to the journal is original and authored by them and has not been previously published nor under consideration or accepted for publication elsewhere.
- To ensure that original ideas, data, findings and materials taken from other sources (including their own published writing) are properly documented and cited. Any content reproduced from other sources author should have permission.
- To ensure that their data is their own, true and not manipulated. Thus, authors are responsible to maintain accurate records and to provide access to their data associated with their manuscript.
- To ensure their work does not violate any rights of others, including privacy rights and intellectual property rights. In addition, authors should ensure that any studies involving human or animal subject are in accordance with local laws and requirements.
- To declare any real or apparent conflicting or competing interest at any stage during the publication process that could be considered or viewed as exerting an undue influence on his/her duties.
- To alert PEN in case if a significant error in their publication is identified and correct any errors prior or subsequent to publication of their work.
- To adhere to all research ethics guidelines of their discipline, and to ensure that authorship and/or co-authorship of the paper was accurately represented.

**PEN responsibilities**

- The journal and the publisher shall ensure that good practice is maintained to the standards outlined above.
- To deal with research misconduct allegations appropriately when it is occurred. The journal and the publisher shall undertake reasonable actions to identify and prevent the publication of papers where research misconduct has occurred.
- To maintain the editorial independence of journal editors.
- To support journal editors in ethical and academic matters.
- To ensure critical and objective assessment of all articles by reviewers and referees. To keep an accurate and transparent record, including publishing corrections and retractions when necessary.
- The following commonly recognized procedure for dealing with unethical behavior is adopted.

**2. Procedures for Dealing With Unethical Behavior****Identification of unethical behavior**

- Misconduct and unethical behavior may be identified and brought to the attention of the editor and publisher at any time, by anyone.
- Misconduct and unethical behavior may include, but need not be limited to, examples as outlined above.
- For an investigation sufficient information and evidence should be provided. All allegations should be taken seriously and treated in the same way, until a successful decision or conclusion is reached.

**Investigation**

- An initial decision should be taken by the editor, who should consult with or seek advice from the publisher, if appropriate.
- Evidence should be gathered, while avoiding spreading any allegations beyond those who need to know.

**Minor breaches**

- Minor misconduct might be dealt with without the need to consult more widely. In any event, the author should be given the opportunity to respond to any allegations.

**Serious breaches**

- Serious misconduct might require that the employers of the accused be notified. The editor, in consultation with the publisher should make the decision whether or not to involve the employers, either by examining the available evidence themselves or by further consultation with a limited number of experts.

**Outcomes** (in increasing order of severity; may be applied separately or in conjunction)

- Informing or educating the author or reviewer where there appears to be a misunderstanding or misapplication of acceptable standards.
- A more strongly worded letter to the author or reviewer covering the misconduct and as a warning to future behavior.
- Publication of a formal notice detailing the misconduct.
- Publication of an editorial detailing the misconduct.
- A formal letter to the head of the author's or reviewer's department or funding agency.
- Formal retraction or withdrawal of a publication from the journal, in conjunction with informing the head of the author or reviewer's department, Abstracting & Indexing services and the readership of the publication.
- Imposition of a formal embargo on contributions from an individual for a defined period.
- Reporting the case and outcome to a professional organization or higher authority for further investigation and action.

**Originality and Plagiarism Policy**

Authors by submitting their manuscript to PEN declare that their work is original and authored by them, their work submitted to PEN has not been previously published, original ideas, data, findings and materials taken from other sources (including their own published writing) are properly documented and cited, their work does not violate any rights of others, including privacy rights and intellectual property rights, their data is their own, true and not manipulated. Plagiarism in whole or in part without proper citation is not tolerated by the Journal. Manuscripts submitted to the journal will be checked for originality using anti-plagiarism software.



# Effects of Cooling Rate on Strength and Microstructure of Powder Metallurgy Superalloys

Gokhan Yıldız<sup>1</sup>, Ali Gursel<sup>2</sup>, Enes Akca<sup>1</sup>

<sup>1</sup>Department of Mechanical Engineering, Faculty of Engineering and Natural Sciences, International University of Sarajevo

<sup>2</sup>Department of Mechanical Engineering, Faculty of Engineering, Duzce University

## Article Info

### Article history:

Received Jan 19<sup>th</sup>, 2017

Revised Aug 19<sup>th</sup>, 2017

Accepted Oct 18<sup>th</sup>, 2017

### Keyword:

Powder Metallurgy

Cooling Rate

Superalloys

## ABSTRACT

The excellent mechanical properties of powder metallurgy superalloys strongly depend on the microstructure, grain size, morphology, and size distribution of the  $\gamma'$  precipitates. In this study, the effects of cooling rate on strength and microstructure of powder metallurgy superalloys were investigated. Articles were reviewed about this topic and they all were evaluated. Different types of powder metallurgy superalloys such as FGH4096, U720LI, UDIMET 500, MAR-M247, K465, IN738LC, Rene88DT, CM247LC and K5 were selected for this study. These materials were tested in different parameters (temperature and time) and different cooling rates were applied. Test results showed that cooling rate has considerable effects on strength and microstructure of powder metallurgy superalloys. It was observed that the strength increased by the increment of cooling rate. Also, almost homogeneous microstructure was obtained at high cooling rate.

## Corresponding Author:

Gokhan Yıldız,

Departement of Mechanical Engineering,

International University of Sarajevo,

Hrasnickacesta 15, 71210, Sarajevo, Bosnia and Herzegovina.

Email: [gokhan.yildiz1987@hotmail.com](mailto:gokhan.yildiz1987@hotmail.com)

## 1. Introduction

The excellent high temperature performance of a nickel-based powder metallurgy alloy depends most often on strengthening  $\gamma'$  precipitates. To increase the strength and flexibility of the alloy by heat treatment it is necessary to control the amount, size, morphology and distribution of the  $\gamma'$  phase [1]. In general, the volume percentage of the  $\gamma'$  phase is about 35% to 60% in the high-alloy superalloy. The ratio  $\gamma_c'$  of the cooling  $\gamma'$  precipitates formed during the cooling process exceeds 60%, and therefore examination of  $\gamma_c'$  precipitation behaviors at various cooling conditions is one of the important baseline investigations to increase the temperature ability. [2]. The grain boundaries are weak bonds in the superalloys and easily become rupture at high operating temperatures due to defects in the microstructure. Some carbides and  $\gamma'$  particles as boundary precipitants have significant effects on the high temperature creep resistance and plasticity of nickel-based superalloys. For this reason, examining the morphology and component of the micro-phase near the grain boundaries is a very important issue to strengthen the grain boundaries [2].

## 2. Discussion

Tian and et al. examined the effect of cooling rate on cooling  $\gamma'$  precipitation behavior in nickel-based powder metallurgy superalloy (FGH4096). Chemical composition of the alloy is given in Table 1. The samples were dissolved at 1150 °C for 5 minutes and then cooled to room temperature at different controlled cooling rates.

Experimental conditions are shown in Table 2. The cooling rate plays a crucial role in controlling the amount, size, morphology and distribution of cooling  $\gamma'$  precipitates. The mean sizes of the secondary and tertiary  $\gamma'$  precipitates were inversely correlated with the cooling rate. The shape of the secondary  $\gamma'$  precipitates within grain changes from butterfly like to spherical with cooling rate. However, regardless of the cooling rate, all the tertiary  $\gamma'$  precipitates formed are spherical. The cooling rate has a significant effect on the precipitation behavior of the  $\gamma'$  phase at the grain boundaries and the apparent extent of the grain boundaries; the higher the cooling rate, the narrower the visibility of the grain boundaries [2].

Mao et al. investigated cooling precipitation and strengthening in powder metallurgy superalloy. The excellent mechanical properties of powder metallurgy superalloys depend on the microstructure such as grain size, morphology and size distribution. The microstructure is determined in turn by heat treatment quenching and then aging. Experimental conditions are shown in Table 2. To investigate the effect of quenching, two types of quenching methods (continuous cooling and interrupted cooling) were used to produce different cooled microstructures in the UDIMET 720Li (U720LI) alloy. Chemical composition of the alloy is given in Table 1. In continuous cooling tests, the tensile strength increased linearly with the cooling rate. Interrupted cooling tests have shown that  $\gamma'$  growth is a linear function of decreasing temperature for a given cooling rate. A non-monotonic decay of the tensile strength against the interrupt temperature has been discovered [1]. Tian et al. applied two cooling schemes (continuous cooling and interrupted cooling tests) to investigate the cooling  $\gamma'$  precipitation behavior in the powder metallurgy superalloy FGH4096. Chemical composition of the alloy is given in Table 1. The maximum tensile strength of the samples was tested under various cooling conditions. Experimental conditions are shown in Table 2. The average sizes of the secondary and tertiary  $\gamma'$ -precipitates were obtained between the strength and the cooling rate. The results show that there is an opposite correlated between the average sizes. Interrupted cooling tests show that the mean size of secondary  $\gamma'$  precipitates increases as a linear function of the cutting temperature for a constant cooling rate of 24 °C/min. The ultimate tensile strength of the alloy increases with increasing cooling rate, but it first decreases and increases with decreasing temperature caused by the third  $\gamma'$  precipitate [3].

Table 1: Chemical composition of alloys (wt %)

	<b>FGH409 6</b>	<b>U720L I</b>	<b>UDIME T 500</b>	<b>MAR- M247</b>	<b>K465</b>	<b>IN738L C</b>	<b>Rene88D T</b>	<b>CM247L C</b>	<b>K5</b>
<b>Ni</b>	Balance	Balance	Balance	Balanc e	Balanc e	Balance	55.63	Balance	Balanc e
<b>Cr</b>	16.04	16.35	17.9	4.43	8.30	16.49	18.02	8.09	10.3
<b>Co</b>	12.70	14.75	17.2	9.08	9.45	8.72	13.00	9.35	10.2
<b>W</b>	3.98	1.3	-	7.62	9.85	3.36	1.21	9.41	5.1
<b>M o</b>	3.84	3.02	4.00	2.02	1.78	1.90	2.48	0.52	3.96
<b>Nb</b>	0.72	-	-	1.00	0.90	0.88	0.46	-	-
<b>Al</b>	2.18	2.46	-	5.72	5.56	3.26	4.45	5.51	5.54
<b>Ti</b>	3.71	4.99	3.00	-	2.38	3.23	4.74	0.82	2.62
<b>C</b>	0.028	0.025	0.11	0.012	0.14	0.06	-	0.075	0.137
<b>Zr</b>	0.04	0.035	-	-	-	0.04	-	-	-
<b>B</b>	0.0095	-	-	-	-	0.08	-	-	-
<b>N</b>	0.0022	-	-	-	-	-	-	-	-
<b>S</b>	-	0.005	-	-	-	-	-	-	-
<b>Fe</b>	-	0.06	2.1	-	-	-	-	-	-
<b>Re</b>	-	-	-	2.02	-	-	-	-	-
<b>Ta</b>	-	-	-	6.74	-	1.63	-	3.24	-
<b>Hf</b>	-	-	-	0.10	-	-	-	1.53	-

Table 2: Experimental conditions of superalloys

Alloys	Temperature (°C)	Time (min)	Cooling Rates (°C/min)					
<b>FGH4096</b>	1150	5	24	84	258	648		
<b>U720LI</b>	1175	5	11	27	55	110	167	800
<b>UDIMET500</b>	1080	240	3.85	35.4	49.8	90.35	129.5	186
<b>IN738LC</b>	1120	120	36	48	66	-	-	-
<b>Rene88DT</b>	1124	240	24	280	300		-	-
<b>IN738LC</b>	1120	120	11	72	98	247	368	-
<b>CM247LC</b>	1230	120	81	125	168	-	-	-

Sajjadi et al. investigated the effect of cooling rate on microstructure and mechanical properties. For this purpose, after making a partial solution for 4 hours at 1080 °C on the samples of UDIMET 500. Experimental conditions are shown in Table 2. Chemical composition of the alloy is given in Table 1. The microstructures of the samples were examined using optical and electron microscopy. As a result, it was determined that the volume of  $\gamma'$  precipitates decreased with increasing cooling rate. Thus, as the cooling rate increases, homogeneity is observed in the microstructure. It is observed that the increased cooling rate increases the strength but decreases the ductility [4]. Zhang et al. investigated the development of solidification cooling rate microstructures in Ni-based superalloy using conventional casting, injection casting and melt bending methods. MAR-M247 nickel-based superalloy was selected as material. Chemical composition of the alloy is given in Table 1. The sample was dissolved at a temperature of 1273 K for 5 min. Experimental conditions are shown in Table 3. As a result, irregular structures decreased as the cooling rate increased. It has been found that the interspaces of  $\gamma'$  precipitates in the cell structure reduced [5].

Table 3: Experimental Conditions of superalloys

Alloys	Temperature (K)	Time (min)	Cooling Rates (K/min)					
<b>MAR-M247</b>	1273	5	0.72	2.1	9	39	75	870
<b>K465</b>	1483	240	12	120	612	-	-	-
<b>MAR-M247</b>	1633	5	15	60	300	600	-	-

Pei et al. investigated the effect of cooling rate on the microstructure and mechanical properties of K465 superalloy. The chemical composition of K465 is given in Table 1. For this purpose, samples were dissolved at 1483 K for 4 hours. Experimental conditions are shown in Table 3. As a result, as the cooling rate increased, the size of the  $\gamma'$  precipitates decreased and the mechanical properties of the samples increased. It has also been found that the coarse  $\gamma'$  particles are greatly influenced by the cooling rate of the shape and volume fraction [6].

Kavoosi and colleagues investigated the effect of cooling rate on the microstructure and mechanical properties of the IN738LC superalloy. Chemical composition of the alloy is given in Table 1. For this purpose, it was dissolved for 2 hours at 1120 °C. Experimental conditions are shown in Table 2. As a result, as the cooling rate increased, the size of the  $\gamma'$  precipitates decreased and the mechanical properties of the samples increased. It has also been found that the shape and volume fraction of the unified  $\gamma'$  particles are greatly reduced by the effect of the cooling rate [7].

Singh et al. investigated the effect of cooling rate on the development of multiple generation  $\gamma'$  precipitates of Rene88DT superalloy. The chemical composition of Rene88DT is given in Table 1. For this purpose, it was dissolved for 4 hours at 1124 °C. Experimental conditions are shown in Table 2. Continuous cooling at a very high rate after dissolving in the single gamma phase results in a high degree of nucleation and a monomodal size distribution with non-equilibrium compositions. A relatively slow cooling rate (24 °C/min) Resulting in a multimodal size distribution; the larger first generation primary precipitates exhibit near-equilibrium composition, while the smaller-scale secondary  $\gamma'$  precipitates exhibit non-equilibrium composition [8].

Milenkovic et al. examined the effect of cooling rate on the microstructure of MAR-M247 superalloy. The chemical composition of MAR-M247 is given in Table 1. The samples were dissolved at about 1633 K for 5

min. Experimental conditions are shown in Table 3. MAR-M247 showed cellular (15 K/min) and dendritic (60, 300 and 600 K/min) microstructures. It has been determined that the microstructures also change with the cooling rate.  $\gamma/\gamma'$  matrix with carbides and  $\gamma/\gamma'$  eutectic at 15 K/s,  $\gamma/\gamma'$  matrix with carbides at 60 K/min, and  $\gamma/\gamma'$  matrix with carbides and  $\gamma/\text{MC}$  eutectic at 300 and 600 K/min. Furthermore, it has been observed that the range of secondary dendritic arms decreases and the hardness increases as the cooling rate increases [9].

Behrouzghaemi and Mitchell examined the effect of cooling rate on the microstructure of IN738LC superalloy. The chemical composition of IN738LC is given in Table 1. The samples were dissolved at about 1120 °C for 2h. Experimental conditions are shown in Table 2. As the cooling rate decreases, the  $\gamma'$  solid state shows morphological instability and the  $\gamma'$  size shrinks as the cooling rate decreases. The shape changes observed in this study revealed the effect of the cooling rate on the disturbances between  $\gamma$  and  $\gamma'$  [10].

Mehta et al. examined the effect of cooling rate on the microstructure of CM247LC superalloy. The chemical composition of CM247LC is given in Table 1. The samples were dissolved at about 1230 °C for 2 h. Experimental conditions are shown in Table 2. As a result, as the cooling rate increased, the size of the  $\gamma'$  precipitates decreased and the mechanical properties of the samples increased [11].

### 3. Conclusion

The cooling rate plays a very important role in controlling the amount, size, morphology and distribution of cooling  $\gamma'$  precipitates. The average sizes of the secondary or tertiary  $\gamma'$  precipitates are inversely correlated with the cooling rate. The shape of the secondary  $\gamma'$  precipitates in the grain varies from butterfly like to spherical with the cooling rate. However, all the tertiary  $\gamma'$  precipitates formed, irrespective of the cooling rate, are spherical.

Cooling rate has an important effect on the precipitation behaviors of  $\gamma'$  phase at grain boundaries and the apparent width of grain boundaries; the higher the cooling rate, the narrower is the apparent width of grain boundaries. As the cooling rate increased, the size of the  $\gamma'$  precipitates decreased and the mechanical properties of the samples increased. It is observed that the increased cooling rate increases the strength.

### References

- [1] J. Mao, K.-M. Chang, W. Yang, K. Ray, S. P. Vaze and D. U. Furrer, "Cooling Precipitation and Strengthening Study in Powder Metallurgy Superalloy U720LI," *Metallurgical and Materials Transactions*, vol. 32, no. 10, pp. 2441-2452, 2001.
- [2] G. Tian, C. Jia, Y. Wen and B. Hu, "Effect of solution cooling rate on the  $\gamma'$  precipitation behaviors of a Ni-base P/M superalloy," *Journal of University of Science and Technology Beijing*, vol. 15, no. 6, pp. 729-734, 2008.
- [3] G. Tian, C. Jia, Y. Wen, G. Liu and B. Hu, "Cooling  $\gamma'$  precipitation behavior and strengthening in powder metallurgy superalloy FGH4096," *Rare Metals*, vol. 27, no. 4, pp. 410-417, 2008.
- [4] S. Sajjadi, H. R. Elahifard and H. Farhangi, "Effects of cooling rate on the microstructure and mechanical properties of the Ni-base superalloy UDIMET 500," *Journal of Alloys and Compounds*, vol. 455, p. 215–220, 2008.
- [5] Y. Zhang, Y. Huang, L. Yang and J. Li, "Evolution of microstructures at a wide range of solidification cooling rate in a Ni-based superalloy," *Journal of Alloys and Compounds*, vol. 570, p. 70–75, 2013.
- [6] Z.-y. Pei, W. Han, G. Zhao, X.-f. Chen, J.-t. Li and Y.-w. Tian, "Effect of Cooling Rate on Microstructure and Mechanical Properties of K465 Superalloy," *Journal of Iron and Steel Research*, vol. 16, no. 6, pp. 70-74, 2009.
- [7] V. Kavooosi, S. M. Abbasi, S. G. Mirsaed and M. Mostafaei, "Influence of cooling rate on the solidification behavior and microstructure of IN738LC superalloy," *Journal of Alloys and Compounds*, vol. 680, p. 291–300, 2016.
- [8] A. Singh, S. Nag, J. Hwang, G. Viswanathan, J. Tiley, R. Srinivasan, H. Fraser and R. Banerjee, "Influence of cooling rate on the development of multiple generations of  $\gamma'$  precipitates in a commercial nickel base superalloy," *Materials Characterization*, vol. 62, pp. 878-886, 2011.
- [9] S. Milenkovic, I. Sabirov and J. LLorca, "Effect of the cooling rate on microstructure and hardness of MAR-M247 Ni-based superalloy," *Materials Letters*, vol. 73, pp. 216-219, 2012.
- [10] S. Behrouzghaemi and R. J. Mitchell, *Materials Science and Engineering A*, vol. 498, pp. 266-271,

2008.

- [11] K. K. Mehta, R. Mitra and S. Chawla, "Effect of post-solutionizing cooling rate on microstructure and low cycle fatigue behavior of a cast nickel based superalloy," *Materials Science & Engineering A*, vol. 611, pp. 280-289, 2014.
- [12] E. Akca and A. Gursel, "A Review on Superalloys and IN718 Nickel-Based INCONEL Superalloy," *Periodicals of Engineering and Natural Sciences*, vol. 3, pp. 15-27, 2015.

# Controlling the Building Model Using High Order Sliding Mode Control Optimized by Multi Objective Genetic Algorithm

Hasan Omur Ozer<sup>1</sup>, YukselHacioglu<sup>2</sup>, NurkanYagiz<sup>2</sup>

<sup>1</sup>Programme of Air Conditioning and Refrigeration Technology, Vocational School of Technical Science, Istanbul University

<sup>2</sup>Department of Mechanical Engineering, Faculty of Engineering, Istanbul University

---

## Article Info

### Article history:

Received May 15<sup>th</sup>, 2017

Revised Aug 18<sup>th</sup>, 2017

Accepted Oct 18<sup>th</sup>, 2017

### Keyword:

High Order Sliding Mode  
Controller

Multi-Objective Genetic  
Algorithm

Building Model

Active Tuned Mass Damper

Simulation

---

## ABSTRACT

High Order Sliding mode control (HOSMC) has been used in many mechanical systems and structural system due to its accuracy, chattering attenuation and high control performance. However, choosing controller parameters for systems is still an important research area. This study, presents a numerical analysis to decrease the effect of earthquake vibrations on building model having Active Tuned Mass Damper (ATMD). The system is excited by an earthquake and a linear motor is used as the control device. ATMD is installed on top floor of building model. Tuning of High Order Sliding Mode Controller (HOSMC) using Super Twisting Algorithm with Multi Objective Genetic Algorithm (MOGA) is designed for a three storey building model with ATMD. HOSMC parameters have been chosen by MOGA with multiple objective functions. Then, simulation results of uncontrolled and controlled model are compared. The results show that building model with HOSMC tuned by MOGA is effective to decrease the effects of vibrations.

---

## Corresponding Author:

Hasan Omur Ozer,

Programme of Air Conditioning and Refrigeration Technology, Vocational School of Technical Science,  
Istanbul University

34320 Avcilar/ Istanbul, TURKEY.

Email: omurozer@istanbul.edu.tr

---

## 1. Introduction

External loads such as earthquakes have the potential to cause dangerous vibrations on buildings. Therefore, the need for studies on decreasing the effects of vibrations on buildings has increased during last decades and it is an important research area. Firstly, buildings have been protected by using the tuned mass damper (TMD) from hazardous effects of vibrations. The TMD, designed in 1909, is a passive control system consisting of mass, springs and viscous dampers. The optimum parameters of TMD for different systems are proposed by several researchers [1]-[2]-[3], a new approach for TMD is suggested by Villaverde [4-6], Sadek [7] improved study of Villaverde. In order to control vibrations more effectively, numerous active control algorithms have been suggested. Pourzeynali et al. [8] have recommended that combining the GAs and fuzzy logic controller to obtain optimum values of ATMD is highly effective in decreasing seismically excited building vibrations. As a variable structure controller [9], Sliding mode control (SMC) is known to be a robust control method. In SMC, by changing control law according to certain predefined rules, the states are switched between stable and unstable trajectories until they reach the sliding surface [10]. When the system is on the sliding surface the closed-loop control system is insensitive to external disturbances and parameter variations. On the other hand, chattering may occur, that is high frequency oscillations may arise in control signal and states of the system. Therefore, high order sliding mode controller (HOSMC) method has been proposed in literature to prevent chattering [11, 12]. In particular, The Super-Twisting Algorithm (STA) which is a well-known second order

sliding mode (SOSM) algorithm is developed by Levant [12]. This control methodology has been properly used for different control problems [13-15]. This study presents a numerical analysis to decrease the effect of earthquake vibrations on building model having Active Tuned Mass Damper (ATMD). To select suitable switching gain and sliding surface parameter is significant for system performance. The search for these parameters has been done by two different fitness functions with Multi Objective Genetic Algorithm (MOGA). High Order Sliding Mode Controller (HOSMC) tuned with MOGA is designed for a three storey building model with ATMD. The simulation results of uncontrolled and controlled model are compared.

## 2. Building Model with ATMD

The building model has three degree of freedom (Figure 1). ATMD has been placed on top floor of the building model.  $m_i$ ,  $k_i$  and  $b_i$  ( $i = 1,2,3$ ) denote the mass, stiffness and damping values related to each storey of the building model and  $m_4$ ,  $k_4$  and  $b_4$  stand for the mass, stiffness and damping values of the ATMD respectively.  $u$  is the control signal generated by the HOSMC.

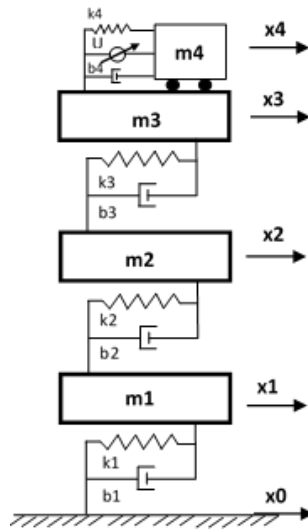


Figure 1. The physical model of building model.

The mathematical model of the three-storey building model with ATMD has been obtained using Lagrange's equations and presented Eq. (1). The system has been excited by using recorded acceleration data of El-Centro earthquake.

$$[M] \ddot{x}(t) + [B] \dot{x}(t) + [K] x(t) = P(t) \tag{1}$$

$$x(t) = [x_1 \quad x_2 \quad x_3 \quad x_4]^T \tag{2}$$

Mass, stiffness and damping matrix is shown in Eqs. (3-5).

$$[M] = \text{diag} [m_1 \quad m_2 \quad m_3 \quad m_4] \tag{3}$$

$$[B] = \begin{bmatrix} b_1 + b_2 & -b_2 & 0 & 0 \\ -b_2 & b_2 + b_3 & -b_3 & 0 \\ 0 & -b_3 & b_3 + b_4 & -b_4 \\ 0 & 0 & -b_4 & b_4 \end{bmatrix} \tag{4}$$

$$[K] = \begin{bmatrix} k_1 + k_2 & -k_2 & 0 & 0 \\ -k_2 & k_2 + k_3 & -k_3 & 0 \\ 0 & -k_3 & k_3 + k_4 & -k_4 \\ 0 & 0 & -k_4 & k_4 \end{bmatrix} \tag{5}$$

A linear motor is used as the control device. Linear motor force  $F_u$ , has been calculated using Eqs. (6) and (7) as shown in Eq. (8).

$$Ri + K_e(\dot{x}_4 - \dot{x}_3) = u \tag{6}$$

$$F_u = K_f i \tag{7}$$

$$F_u = (K_f / R)u - (K_e K_f / R)(\dot{x}_4 - \dot{x}_3) \tag{8}$$

$$E_{ATMD} = F_u(t)\Delta x_4 \tag{9}$$

External loads have consisted of earthquake force and control force shown in Eq. (10).

$$[P] = [-m_1\ddot{x}_0 \quad -m_2\ddot{x}_0 \quad -m_3\ddot{x}_0 - F_u \quad -m_4\ddot{x}_0 + F_u]^T \tag{10}$$

The mass and stiffness parameters of the building model have been taken from study of Sadek [7]. The damping parameters have been derived from  $C = (0.0129)K$  [16] and the parameter of the ATMD has been shown Table 1-2.

Table 1. Ratios for building model (adapted from Sadek [7]).

Number of Floors	Mass ratio	Tuning Ratio (f)	TMD damping ratio ( $\xi$ )	$M_1 = \Phi_1^T [M] \Phi_1$ ( $10^3$ kg)	$\omega_{01}$ (Hz)
3	0.100	0.8701	0.3694	271	1.41

Table 2. Parameters of building model with ATMD (adapted from Sadek [7]).

Floor	Mass ( $10^3$ kg)	Stiffness (kN/m)	Damping Coefficient (kNs/m)
1	100	41000	528.9
2	100	38000	490.2
3	100	36000	464.4
ATMD	27.1	1610.73	154.35

### 3. Control Strategy

#### 3.1. High Order Sliding Mode Controller Design with Super Twisting Algorithm

Suppose that the system is defined as:

$$\dot{x}_1 = x_2 \tag{11}$$

$$\dot{x}_2 = f(x_1, x_2) + g(x_1, x_2)\bar{u} + \bar{d} \tag{12}$$

Here sliding surface is chosen as

$$\sigma(x, t) = \alpha(x_{1r} - x_1) + (\dot{x}_{1r} - \dot{x}_1) \tag{13}$$

Then by defining

$$\phi(x) = \alpha(x_{2r} - x_2) + \dot{x}_{2r} - f(x_1, x_2) \tag{14}$$

$$u = -g(x_1, x_2)\bar{u} \tag{15}$$

$$d = -\bar{d} \tag{16}$$

$$\dot{\sigma} = \phi(x_1, x_2) + u + d \tag{17}$$

$$|(\phi(x_1, x_2) + d) / g(x_1, x_2)| < U_M \tag{18}$$

If the control law is chosen to be [12]:

$$u = -k_1 |\sigma|^{1/2} \text{sign}(\sigma) + v \tag{19}$$

$$\dot{v} = \begin{cases} -u & |u| > U_M \\ -k_2 \text{sign}(\sigma) & |u| \leq U_M \end{cases} \tag{20}$$

Suppose that  $U_M$  is sufficiently large then the Lyapunov function can be selected as in [17]:

$$\xi^T = [|\sigma|^{1/2} \text{sign}(\sigma) \quad v] \tag{21}$$

$$P = \frac{1}{2} \begin{bmatrix} 4k_2 + k_1^2 & -k_1 \\ -k_1 & 2 \end{bmatrix} \tag{22}$$

$$V = \xi^T P \xi \tag{23}$$

$$V = 2k_2 |\sigma| + \frac{1}{2} v^2 + \frac{1}{2} (k_1 |\sigma|^{1/2} \text{sign}(\sigma) - v)^2 \tag{24}$$

It is assumed that the derivative of Lyapunov function with the bounded perturbation term is as in [17]:

$$\dot{V} = -\frac{k_1}{2|\sigma|^{1/2}} \xi^T \tilde{Q} \xi \tag{25}$$

$$\tilde{Q} = \begin{bmatrix} 2k_2 + k_1^2 - \left(\frac{4k_2}{k_1} + k_1\right)\Delta & -k_1 + \frac{\Delta}{2} \\ -k_1 + \frac{\Delta}{2} & 1 \end{bmatrix} \tag{26}$$

It can be shown that by choosing  $k_1 > 2\Delta$  and  $k_2 > \Delta^2 k_1 / [8(k_1 - 2\Delta)]$  then  $\dot{V} < 0$  then reaching to the sliding surface is guaranteed.

### 3.2. Searching Optimum Controller Parameters using Multi-Objective Genetic Algorithm

The proposed method can efficiently choose the appropriate gain parameters for high order sliding mode controller based on two proposed fitness functions. First fitness function is devised to obtain maximum reduction in the third floor response. The aim of the second fitness function is minimizing the control force and also minimizing third floor's response quantity. MOGA is implemented for tuning of the parameters of high order sliding mode controller. The obtain parameters of the controller have been shown Table 3.

$$FF_1 = \sum_{i=1}^n |x_{3ri} - x_{3i}| \tag{27}$$

$$FF_2 = \sum_{i=1}^n |u_i| \tag{28}$$

Table 3. Optimum Controller Parameters with MOGA.

Controller	Parameter	Value
HOSMC	$\alpha$	4.75
	$k_1$	7.01
	$k_2$	0.66

### 3.3. Simulation Results

Time responses are presented in Fig. 2-3. The building model has been excited by the recorded acceleration data of El-Centro earthquake that occurred in 1940. It is also seen that the displacement of the ATMD is also in reasonable ranges. From Fig. 2, it is observed that the best improvement in time response on floor 3 is obtained with designed HOSMCGA, since magnitudes for displacements in Fig. 2 are much more reduced if compared with the case without controller.

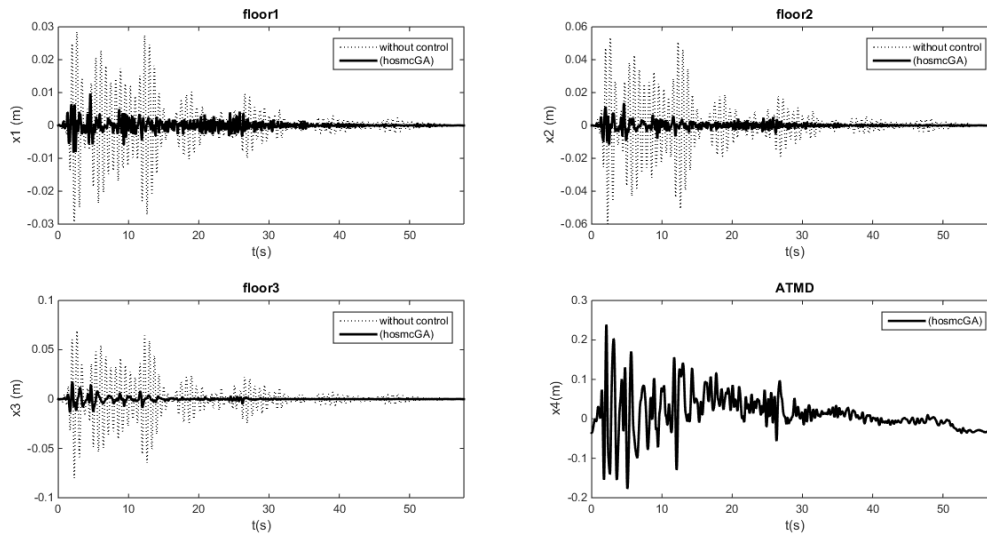


Figure 2. Displacements of floors and ATMD.

If Fig.3 is investigated, it is seen that magnitude of accelerations are also reduced while the best reduction is obtained for floor 3.

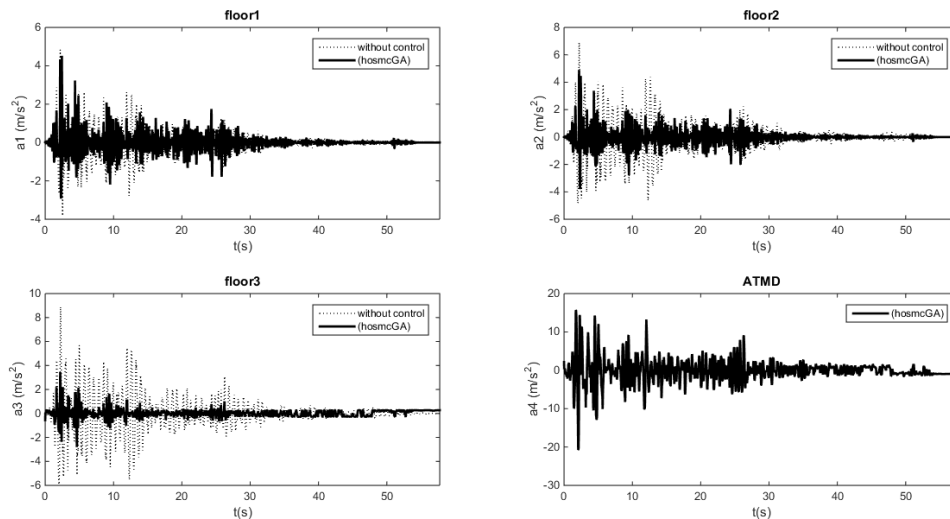


Figure 3. Accelerations of floors and ATMD.

The Root Mean Square (RMS) values for the displacements and accelerations of the building floors and ATMD are also calculated and presented in Table 4. It is deduced from those results that the designed HOSMCGA has decreased the RMS values substantially.

Table 4. RMS values of all floors and ATMD.

Floor	RMS Values					
	Displacement(m)			Acceleration(m/s <sup>2</sup> )		
	Without Controller	HOSMCGA	%	Without Controller	HOSMCGA	%
1	0.00654	0.00139	-78.7	0.6320	0.4700	-25.6
2	0.01230	0.00196	-84.1	1.1100	0.5430	-51.1
3	0.01580	0.00232	-85.3	1.4100	0.3400	-75.9
ATMD	-	0.04960	-	-	2.9900	-

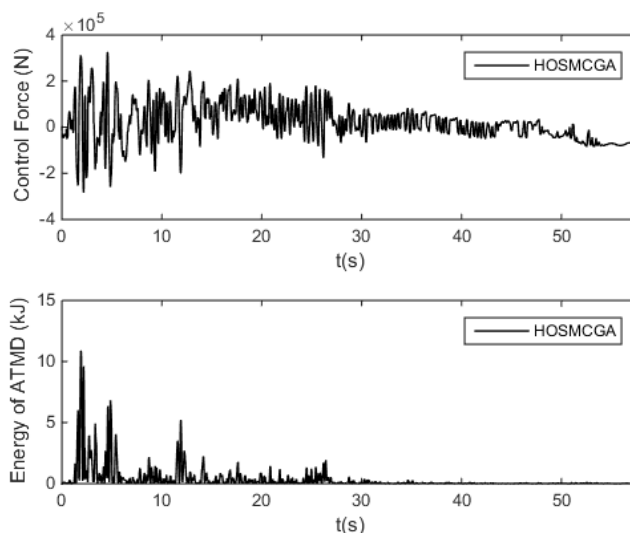


Figure 4. The time variation for the actuator force and energy consumption.

#### 4. Conclusions

In this study, Active Tuned Mass Damper (ATMD) with high order sliding mode controller (HOSMC) tuned by Multi Objective Genetic Algorithm (MOGA) has been designed to reduce the vibrations of the three storey building model. The optimum values of HOSMC parameters ( $\alpha, k_1, k_2$ ) are obtained by MOGA. The RMS displacement value of third floor has been decreased by 85.3 % if uncontrolled and controlled systems are compared. Similarly, the RMS acceleration value of third floor has been decreased by 75.9 % if uncontrolled and controlled systems are compared. Finally, it can be concluded that the designed optimized HOSMCGA may perform well for the reduction of building vibrations.

#### References

- [1] G.B. Warburton and E.O. Ayorinde, "Optimum Absorber Parameters for Simple Systems," *Earthquake Engineering & Structural Dynamics*, Vol. 3, pp. 197-217, 1980.
- [2] G.B. Warburton, "Optimum Absorber Parameters for Various Combinations of Response and Excitation Parameters," *Earthquake Engineering & Structural Dynamics*, Vol. 3, pp. 381-401, 1982.
- [3] A.G. Thompson, "Optimum Tuning and Damping of a Dynamic Vibration Absorber Applied to a Force Excited and Damped Primary System," *Journal of Sound and Vibration*, Vol. 3, pp. 403-415, 1981.
- [4] R. Villaverde, "Reduction in Seismic Response with Heavily-Damped Vibration Absorbers," *Earthquake Engineering & Structural Dynamics*, Vol. 1, pp. 33-42, 1985.
- [5] R. Villaverde and L.A. Koyama, "Damped Resonant Appendages to Increase Inherent Damping in Buildings," *Earthquake Engineering & Structural Dynamics*, Vol. 6, pp. 491-507, 1993.
- [6] R. Villaverde and S.C. Martin, "Passive Seismic Control of Cable-Stayed Bridges with Damped Resonant Appendages," *Earthquake Engineering & Structural Dynamics*, Vol. 2, pp. 233-246, 1995.

- [7] F. Sadek, et al., "A method of estimating the parameters of tuned mass dampers for seismic applications," *Earthquake Engineering & Structural Dynamics*, Vol. 6, pp. 617-635, 1997.
- [8] S. Pourzeynali, H.H. Lavasani, and A.H. Modarayi, "Active control of high rise building structures using fuzzy logic and genetic algorithms," *Engineering Structures*, Vol. 3, pp. 346-357, 2007.
- [9] V.I. Utkin, "Variable structure systems with sliding modes," *IEEE Transactions on Automatic control*, Vol. 2, pp. 212-222, 1977.
- [10] C. Edwards and S. Spurgeon, *Sliding Mode Control: Theory and Applications*. Taylor & Francis Ltd. 1998.
- [11] G. Bartolini, A. Ferrara, and E. Usai, "Chattering avoidance by second-order sliding mode control," *IEEE Transactions on Automatic Control*, Vol. 2, pp. 241-246, 1998.
- [12] A. Levant, "Sliding Order and Sliding Accuracy in Sliding Mode Control," *International Journal of Control*, Vol. 6, pp. 1247-1263, 1993.
- [13] A. Levant, "Homogeneity approach to high-order sliding mode design," *Automatica*, Vol. 5, pp. 823-830, 2005.
- [14] A. Levant, "Principles of 2-sliding mode design," *Automatica*, Vol. 4, pp. 576-586, 2007.
- [15] H.O. Ozer, Y. Hacioglu, and N. Yagiz, "High order sliding mode control with estimation for vehicle active suspensions," *Transactions of the Institute of Measurement and Control*, Doi: 10.1177/0142331216685394.
- [16] R.W. Clough and J. Penzien, *Dynamics of structures*. McGraw-Hill. 1975.
- [17] J.A. Moreno and M. Osorio, "A Lyapunov approach to second-order sliding mode controllers and observers," *47th IEEE Conference on Decision and Control, 2008 (CDC 2008)*, Vol., pp. 2856-2861, 2008.

## A Structured Selection Process for Small and Medium Enterprises in Construction Industry: Case of International Projects

Serdar Ulubeyli<sup>1</sup>, Aynur Kazaz<sup>2</sup>, Volkan Arslan<sup>1</sup>

<sup>1</sup>Department of Civil Engineering, Bulent Ecevit University

<sup>2</sup>Department of Civil Engineering, Akdeniz University

---

### Article Info

#### Article history:

Received May 16<sup>th</sup>, 2017

Revised Aug 18<sup>th</sup>, 2017

Accepted Oct 18<sup>th</sup>, 2017

---

#### Keyword:

Construction projects

International projects

Selection criteria

Small and medium enterprise

Subcontractor

Sustainability

---

### ABSTRACT

Construction industry in most countries relies heavily on small and medium enterprises (i.e., subcontractors). Therefore, in today's highly competitive construction business, it is inevitable to select suitable subcontractors which physically execute almost all of production activities in construction projects. In this context, through a proper selection process, their competences should be guaranteed as much as possible. In fact, this becomes a more significant issue if the project undertaken is performed abroad. In this regard, it should be noted that Turkish construction companies have been significantly active in the international arena for decades. Based on these arguments, subcontractor characteristics to be considered in international projects should be revealed clearly. Accordingly, this paper proposes a structured process for subcontractor selection in international construction projects. Toward this aim, a questionnaire survey was applied to 96 construction companies, all of which are members of Turkish Contractors Association, and the corresponding numerical results were evaluated via descriptive statistics and 95% confidence interval. Thus, a three-step selection procedure together with their specific criteria was suggested from the conceptual point of view. These steps include (i) shortlisting with ten criteria, (ii) negotiation with seven criteria, and lastly (iii) final selection with seven criteria. Hence, this study can provoke potential researchers to find similarities or differences of such criteria between their countries and Turkey. Also, it can help both main contractors to execute the whole construction process in a financially sustainable environment and subcontractors to increase business opportunities in the international market.

---

### Corresponding Author:

Volkan Arslan,

Department of Civil Engineering,

Bulent Ecevit University,

Incivez Mahallesi, Farabi Kampusu, 67100, Zonguldak, Turkey

Email: [volkanarslan@beun.edu.tr](mailto:volkanarslan@beun.edu.tr)

---

## 1. Introduction

Subcontracting is a recognized function of the construction industry. It refers to sub-letting some portions or complete units of the work in the total project to subcontractors. Since the physical capital investment and technology requirements are quite low for most subcontracting trades and an access to productive factors is an easy task, the entry barrier to the subcontracting business is minimum in the industry. In other words, the cost of entering the market is not high relative to other sectors. Many of these subcontracting companies do not have any necessary expertise to undertake a work satisfactorily and, as a consequence, are unable to give their clients a service they require.

Subcontracting has also a significant aspect in executing construction activities in international projects which are generally performed in uncommon regions and conditions. In fact, this may lead to some unexpected risks. Thus, a main contractor's ability to select suitable subcontractors in international projects is a key competitive advantage [1]. However, in the literature, improvements in subcontractor selection criteria have not received the attention that one would expect from a significant contribution to the construction industry. Therefore, the present study aims to introduce subcontractor selection criteria in international construction investments.

## 2. Materials and Methods

The data presented in this study were obtained by a two-stage questionnaire survey that was given to members of Turkish Contractors Association [2]. First, a pilot survey was carried out with 30 members selected by random sampling to remove practical concerns on questions. After the pilot study, modifications were incorporated into the final version of the questionnaire. This sample group was selected because it is an accepted list of firms within the Turkish construction industry. Member firms of this Association perform approximately 70% of total investments made in Turkey, and have also undertaken 90% of the work done abroad in the field of construction. There are 139 members in total, of which 96 firms (69.06%) positively responded to the survey request. The number of companies interviewed is statistically adequate ( $n \geq 30$ ) to represent the whole. Furthermore, Babbie [3] suggested that any return rate over 50% can be reported, that over 60% is good, and that over 70% is excellent. Respondents were contractors' professional managers who choose subcontractors. Interviews were conducted face-to-face at interviewees' offices and ranged from 1 to 2 hours, with each interview being tape-recorded. They were carried out in an open and semi-structured manner, allowing respondents to introduce whatever information was felt to be relevant. In order to make the interviewing more effective and to save the time of interviewees, respondents were briefed about overall objectives and the methodology of the survey before interviews through either (i) an e-mail or (ii) a telephone conversation. The fact that each company's business philosophy could guide the interviewee's personal opinion was also stressed.

The survey was statistically evaluated by the 95% confidence interval of results [4]. To this aim, respondents were asked to assign a value between 0 (extremely unimportant) and 100 (extremely important) to each stage of selection. For the analysis of this method, mean values and standard deviation were initially obtained. Upper and lower limits were then calculated. In order to apply these equations, SPSS (Statistical Package for Social Sciences) was used.

Demographic features of surveyed firms, including both respondents' characteristics and structures of construction companies, were revealed by survey results. Tender Managers made up 81.25% of participants and 18.75% were Chairmen of the Board of Directors. The statistical data indicated that participants had adequate business experience in the construction industry to answer the questionnaire satisfactorily. The mean work experience of respondents was 17.69 years, the standard deviation was 10.05 years, and the median was 13.5 years. Minimum and maximum values of the work experience were 7 and 36 years, respectively. A diversified group of decision makers who currently perform subcontractor qualifications participated in the study. Each participant had taken part in the selection process of at least one subcontractor, 25% had taken part in more than 50 selection processes, 18.75% had participated in fewer than 5 selections, 18.75% had been involved in 6-10 selections, 25% had been involved in 11-20 selections, and 12.5% had taken part in 21-50 selections.

Besides individual characteristics of respondents, features of surveyed firms are also very important. Considering their average annual revenues, a vast majority of companies (81.25%) can be considered as being in the large scale (> \$20 million) category while 6.25% of main contractors were middle scale firms (\$10-20 million) and 12.5% were small scale firms (< \$10 million). The fact that large scale firms are likely to have high standards in terms of the internal organization and project characteristics both indicates the reliability of the survey and has led to further research projections for the future. Surveyed companies had undertaken foreign construction projects in more than one field of construction to date. According to types of international projects, 81.25% of main contractors had performed engineering projects (highways, bridges, harbors, tunnels, dams, and infrastructure). The fact that international projects are composed of engineering investments in general is an expected finding. In addition, 62.5% of companies had executed industrial investments (power plants, refineries, and pipelines) and 62.5% had completed building projects (residential, commercial, schools, hotels, and hospitals). This indicates that main contracting firms have not specialized in only one specific project type and that subcontracting has become an inevitable tool of trade contracting for main contractors in

the international construction industry. Considering the firms' business experience, 18.75% of them had been in the global construction market for 1-5 years, 25% for 6-10 years, 6.25% for 11-20 years, and 50% for more than 20 years. A significant portion of main contractors (56.25%) have been undertaking international projects for more than 10 years. This points out that they have adequate experience in foreign markets. Another indicator of the surveyed firms' international experience is the number of projects undertaken abroad. Of firms, 18.75% had served as a main contractor in 1-5 projects, 15.62% in 6-15 projects, 15.62% in 16-25 projects, and 12.5% in 26-50 projects. The fact that 37.5% of main contractors had successfully completed more than 50 foreign projects is an important finding, which shows their widespread experience. Similarly, it was found out that main contractors had successfully concluded many large scale foreign projects. Considering the maximum size of the labor force, 12.5% of main contractors had employed fewer than 100 workers in a project, 18.75% had employed 100-500 workers, 25% had employed 501-1000 workers, 31.25% had employed 1001-5000 workers, and 12.5% had employed more than 5000 workers. Firms had concurrently undertaken construction projects in three different continents. Former Soviet Countries (75%), Middle East (62.5%), and North Africa (43.75) are especially vital and strategic markets for Turkish construction companies.

### 3. Subcontractor Selection Criteria

The literature review was instrumental in the identification and the design of factors affecting the selection decision of main contractors about subcontractors in international projects. Respondents were also encouraged to add to the list any other criteria they considered to be important. Since subcontractors are a kind of contractor, factors used for the main contractor selection are also utilized. More criteria could have been taken into account in the model, and the complexity of the selection procedure could have been increased using additional evaluation techniques. However, criteria ignored by respondents in the pilot survey were not factored into the model to avoid negligible details. In fact, infinite numbers of criteria can be suggested without considering their importance weights in any decision problem. Conversely, restricting the number of evaluation variables to, for example, three or five is simply too few to run a robust, thorough, and reliable qualification. Another aspect for improvements of the model is the number of criteria. The number and importance of criteria used for contractors to select a good subcontractor during the tender evaluation may vary from one to another. For this reason, the present research concentrated on a set of 'standard' criteria. This may raise problems of 'inadequacy' and 'irrelevance' of criteria when implemented to different types of project. Nevertheless, an attempt has been made to select and find the most 'suitable' set of criteria via a survey.

In most instances, the sole deciding factor is the tender amount, and subcontractors that do not meet price requirements are excluded from further consideration. Because of the considerable weight which most contractors attach to price, the influence of other factors is 'hidden' in reality. However, if price alone dominates the specialist selection, then it is unlikely that requirements of a small subcontracting firm and a main contractor will be satisfied because this behavior (that is, single criterion decision making) is not conducive to harmonization and good relationships between two parties, which is in turn resulted in a poor project performance. As such, relying singularly on tender price alone can be fatal as the capability of the tenderer may not be adequately assessed. A single criterion cannot give a full expression of goals pursued by various contractors. In other words, taking solely cost figures into account raises quality problems during and upon the completion of the project. However, the lowest tender price tends to attract a contractor's interest as superior to other criteria, and thereby, some contractors simply award contracts to lowest tenderers for the sake of cost savings. Subcontractors are forced to make a profit by providing the 'cheapest' possible construction, and 'low bid' based selections have been common. In practice, generally subcontractors who submit lowest tender prices obtain subcontracts. However, the lowest tender may not necessarily deliver prompt and good quality works. Awarding contracts to low bidders usually results in a poor performance in terms of quality and excessive delays. This means that a price that is too low likely inhibits the attainment of contractor's other objectives of quality and speed. Most of such cases end up in litigation. As a result, selecting the lowest bidder in a sealed tender auction can sometimes result in serious performance problems after the contract is awarded. Moreover, stiff competition causes subcontractors to cut their margins to get jobs and subcontractors trying to win a contract often lower the bid price. In fact, lower profit margins bring higher risks and lower levels of quality. Outcries against substandard construction (for example, in Turkey) or escalating construction claims have been often traced to the selection of lowest priced tenders. Another

disadvantage of using the lowest bid as a principal discriminating criterion is that some subcontractors (e.g., those facing a shortage of work) may enter unrealistically low bid prices. Namely, low bids as the sole criterion for selection encourage unqualified subcontractors to submit bids. Of course, competitions are expected to drive costs down, but a low price cannot ensure quality standards expected by a contractor, because a subcontractor can reduce costs at the expense of the product's quality or can desperately quote low prices by reducing their quality of work. It means that low price awards motivate subcontractors to provide minimally acceptable construction products and that a low bidder can become a very expensive proposition. The practice of awarding tenders on a basis of the low tender price eventually will lead to ultimate quality problems. Therefore, a best value procurement should focus on selecting a suitable subcontractor with an offer that is most advantageous to a contractor when price and other important factors are appropriately combined. In terms of public investments, however, public clients have to aim to demonstrate the accountability for public funds and even-handedness to suppliers and contractors.

Characteristics of subcontractors and guidelines in the selection procedure examined in this study are largely based on subjective rather than objective criteria, as explained in detail as follows. Since the model developed as illustrated in Figure 1 suggests three different stages as shortlisting, negotiation, and final selection, all criteria were classified according to these groups. Such a three-tier tendering structure prevents subcontractors bidding for subcontracts outside their capabilities.

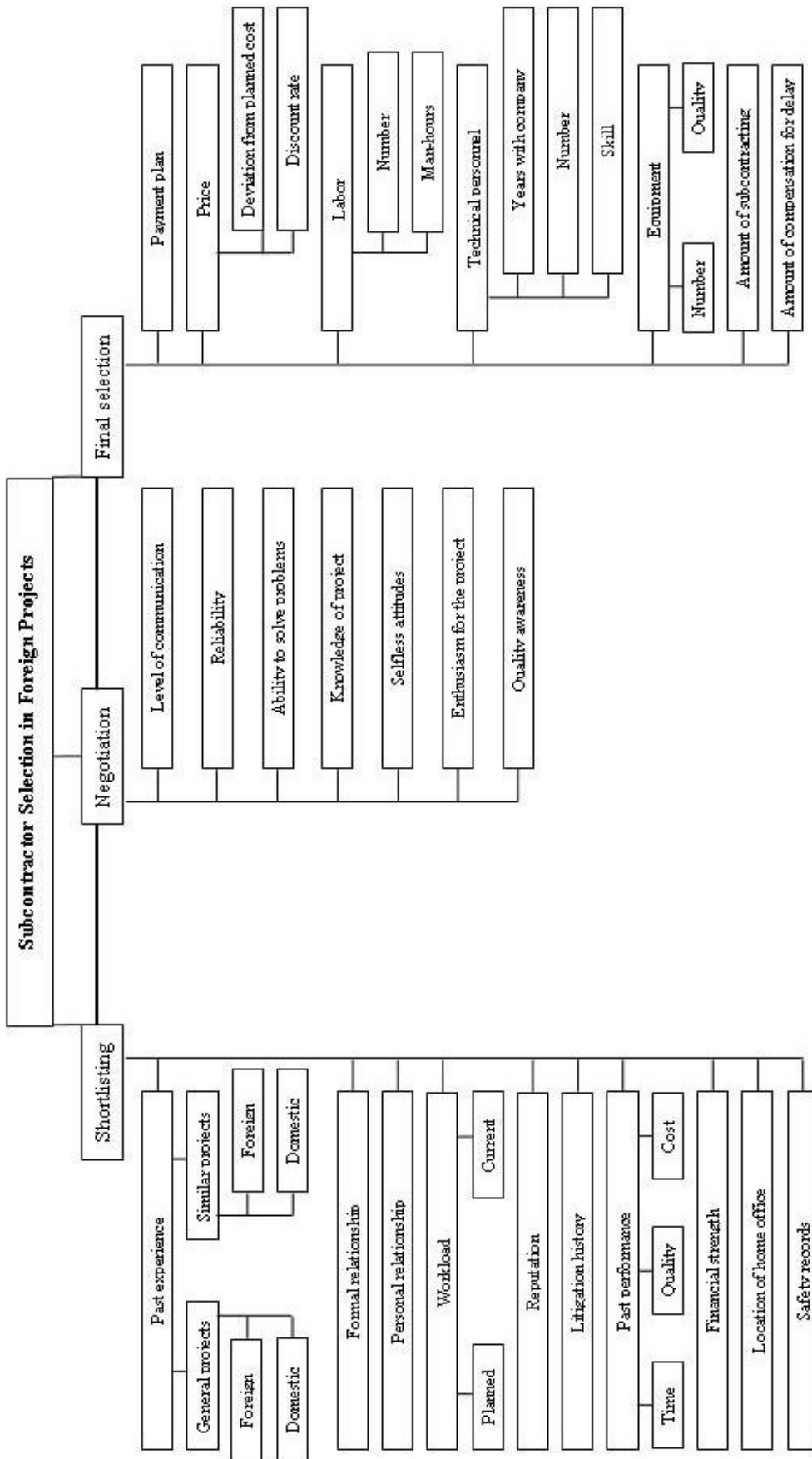


Figure 1. Subcontractor selection criteria in foreign projects

### 3.1. Shortlisting criteria

This initial appraisal step is a preliminary vetting or restricting process of potential subcontractors. It is therefore preferable to identify those subcontractors deemed to satisfy project requirements and only then invite them to submit a tender. In other words, a pre-tender screening allows a contracting authority to sort potential operators into those of high and low expected quality before the tendering actually takes place. Such separation is important because if low and high quality subcontractors bid simultaneously, difficulties will arise in distinguishing low bids that are due to cost efficiency from those that involve the reduced quality of service. In this phase, basic characteristics of candidates on their professional backgrounds are considered in particular. Aims of this pre-tender process used to investigate and to assess capabilities of subcontractors to carry out a subcontract satisfactorily if it is awarded to them are as follows:

- to determine the possible subcontractor's competence, ability, skill, and efficiency for participating in the project bid and thereby for providing an early warning of the subcontractor's likely performance,
- to remove the risk of the project failure,
- to minimize the amount of the unrealistic tendering of incapable subcontractors,
- to filter out incompetent subcontractors from the bidding process quickly and thus to identify subcontractors with whom a main contractor could enter into a subcontract. Also note that main contractors disqualified from bidding for a project in their own capacities due to prequalification criteria in the international bidding often end up as subcontractors,
- to minimize the possibility of the subcontractor default, together with the cost and time involved in the bidding. It is worth noting that costs of the bidding incurred by potential subcontractors are sunk – they cannot be recovered if the bid is unsuccessful. Hence, by screening out subcontractors who are unlikely to be selected irrespective of their bid prices, total sunk costs can be significantly reduced.

In the shortlisting stage, subcontractors are first invited to submit their bids. Information about criteria 'past experience', 'workload', 'financial strength', 'location of home office', and 'safety records' is obtained from firms wishing to be included on the project tendering list via an application form from the main contractor. For information concerning criteria 'reputation', 'litigation history', and 'past performance', main contractors and subcontractors that have previous working relationships with the related subcontractor are contacted. 'Formal relationship' and 'personal relationship' are evaluated by means of the main contractor's own experience. Candidates must get through this step to be eligible for second and third phases of the selection. Related tender documents of the package such as drawings and specifications are then given to qualified candidates. To find out the importance level of this first stage, respondents gave numerical weights between 0 (extremely unimportant) and 100 (extremely important). As can be seen from Table 1, main contractors assigned a weight of 69.69 as a mean value. Considering other two stages, shortlisting is the least important stage.

Table 1. Importance weight of the shortlisting stage

Mean	Standard deviation	Minimum value	Median	Maximum value	Error	%95 confidence interval	
						Lower limit	Upper limit
69.69	22.54	25	70	100	5.64	57.67	81.70

### 3.2. Negotiation criteria

In this step, candidates on the approved list are first interviewed. This and other two stages are executed by a selection committee including project manager, site manager, and other technical managers. To avoid individual biases, it is recommended that a minimum of three evaluators is required for each scoring activity. To come to a conclusion, it is aimed to make a group decision. Before proposal meetings, subcontractors submit their detailed project proposals and thus the committee has an opportunity of pre-appraisal. The related information should always be treated as a matter of utmost confidentiality. An importance weight of 72.81 was suggested for this stage by participants, as can be seen in Table 2.

Table 2. Importance weight of the negotiation stage

Mean	Standard deviation	Minimum value	Median	Maximum value	Error	%95 confidence interval	
						Lower limit	Upper limit
72.81	26.27	15	72.5	100	6.57	58.82	86.81

### 3.3. Final selection criteria

More specialized factors directly related with the project to be awarded are examined in this third stage whereas general capability levels of candidates are determined in former two stages. Therefore, ‘final selection’ is perceived as the most important stage by main contractors in the industry. A clear indicator of this judgment is that the mean value of the importance weight for this stage was calculated as 79.69, as given in Table 3. First steps of this stage are executed together with the negotiation stage. Respondents assigned a weight of 79.69 as a mean value. Given all three stages, the final selection was found to be the most significant stage.

Table 3. Importance weight of the final selection stage

Mean	Standard deviation	Minimum value	Median	Maximum value	Error	%95 confidence interval	
						Lower limit	Upper limit
79.69	26.68	20	90	100	6.67	65.47	93.90

## 4. Conclusions

This paper presents a structured selection process for subcontractors to take part in international construction investments. In conclusion, a three-step selection procedure and their criteria was determined. The steps are composed of (i) shortlisting of ten criteria, (ii) negotiation of seven criteria, and (iii) final selection of seven criteria. Also, it was found out that the final selection was found to be the most significant stage, followed by negotiation and shortlisting, respectively. Consequently, this research can have considerable implications on potential researchers, main contractors, and subcontractors.

### Acknowledgements

The authors gratefully acknowledge numerous chairpersons, managers, and other technical/administrative staff of surveyed companies for their generous collaboration and contributions. The authors also would like to thank financial supports provided by Committees on Research Grants of Bulent Ecevit University and Akdeniz University.

### References

- [1] S. Ulubeyli and A. Kazaz, “Fuzzy multi-criteria decision making model for subcontractor selection in international construction projects,” *Technological and Economic Development of Economy*, vol. 22, pp. 210-234, 2016.
- [2] S. Ulubeyli, “Fuzzy multiple criteria decision making model for subcontractor selection in international construction projects,” Ph.D. thesis, Istanbul University, Istanbul, Turkey, 2008.
- [3] E. Babbie, *The Practice of Social Research*, 11th ed., Belmont, USA: Wadsworth Publishing, 2007.
- [4] J. Curwin and R. Slater, *Quantitative Methods for Business Decisions*, 3rd ed., London, England: Chapman and Hall, 1992

**BIBLIOGRAPHY OF AUTHORS**

Serdar Ulubeyli is an Associate Professor in the Department of Civil Engineering at Bulent Ecevit University, Turkey. His areas of academic research interests include international subcontracting, decision-making, and construction economics. He has published many papers in various scientific journals and proceedings.



Aynur KAZAZ is a Professor in the Department of Civil Engineering at Akdeniz University, Turkey. Her areas of academic research interests include international subcontracting, decision-making, and construction economics. She has published many papers in various scientific journals and proceedings.



Volkan Arslan is a PhD student and a Research Assistant in the Department of Civil Engineering at Bulent Ecevit University, Turkey. His areas of academic research interests include international subcontracting, decision-making, and construction economics. He has published many papers in various scientific journals and proceedings.

## Multi-Objective Artificial Bee Colony Algorithm to Estimate Transformer Equivalent Circuit Parameters

Züleyha YILMAZ<sup>1</sup>, Musab OKŞAR<sup>2</sup>, Fatih BAŞÇİFTÇİ<sup>1</sup>

<sup>1</sup>Department of Computer Engineering, Selcuk University

<sup>2</sup>Electrical Engineer, Inonu University

### Article Info

#### Article history:

Received May 23<sup>th</sup>, 2017

Revised Aug 18<sup>th</sup>, 2017

Accepted Oct 18<sup>th</sup>, 2017

#### Keyword:

Multi-objective artificial bee colony algorithm  
Multi-objective optimization  
Transformer parameter estimation

### ABSTRACT

Real world problems such as scientific, engineering, industrial problems are in the form of the multi-objective optimization problems. In order to achieve optimum solutions of such problems, multi-objective optimization algorithms are utilized. In this study, the problem is estimation of single-phase transformer parameters which is one of the engineering problems. This estimation is provided by artificial bee colony (ABC) algorithm. ABC is developed as a metaheuristic method and simulates foraging of bees. Since the problem is a multi-objective optimization problem, multi-objective ABC (MOABC) is proposed to estimate parameters in the study. This study aims to estimate equivalent circuit parameters using current and voltage values at any known load. Through algorithm, difference between actual and estimated parameter values that is the error has been tried to minimize. The successful results show that the proposed method can be used for a single-phase transformer parameters estimation.

### Corresponding Author:

Züleyha YILMAZ,  
Department of Computer Engineering,  
Selcuk University,  
AlaeddinKeykubat Campus, 42075, Selcuklu, Konya, TURKEY.  
Email: zulehayilmaz@selcuk.edu.tr

## 1. Introduction

Many engineering problems in the world have more than one objective. The main goal of the problems is to find optimum solutions for all objectives simultaneously. For this reason, the results are a set of optimum solution. In multi-objective problems (MOPs), problem solvers suggest this set of solutions to decision makers generally and decision makers decide an optimum solution from the set according to importance of the problem type. The set of optimum solutions is named as Pareto-optimal set [1]. Pareto-optimal set stores solutions which are not worse than each other. Namely, a Pareto-optimal solution is better than at least one of all objectives. These solutions are also named as non-dominated solutions [1]. This domination term is described as detailed in Section II. At this point, at the stage of proposing set of solutions, multi-objective optimization algorithms (MOAs) are utilized. In order to solve MOPs, proposed optimization algorithms are generally meta-heuristic algorithms. For instance, Multi-objective genetic algorithm is proposed to solve many MOPs such as flow shop scheduling [2] and fuzzy rule selection [3]. Multi-objective particle swarm optimization is also proposed to solve MOPs such as job-shop scheduling problem [4] and electromagnetic absorber design [5].

This study is focused on parameter estimation problem of a single-phase transformer being one of the engineering problems. Transformers are used as an electric machine to convert energy from one voltage to another voltage. In order to estimate transformer parameters, two experimental tests and some computations

are required. This study provides parameters without any experimental test using proposed method with known current and voltage values at any known load.

So far, identification of the transformer parameter is realized as single optimization problem as [6], [7], [8]. However, in non-convex multi-objective optimization problems, results cannot be reached some optimum solutions when objectives of the problem are combined to do single objective problem [1]. Because of this reason, the transformer parameter estimation problem is solved as multi-objective optimization problem using Multi-Objective Artificial Bee Colony algorithm (MOABC) in this study. The algorithm is a population-based and stochastic optimization method. Foraging of real honey bees is simulated by the ABC. The original version of the ABC is for single optimization problems. Therefore, MOABC algorithm is utilized to identify transformer parameter being multi-objective problem.

In this paper, firstly described multi-objective optimization problems; then MOABC algorithm is described in detail; then introduced the problem and implementation of the MOABC to the problem. Finally, reported experimental results and conclusion.

## 2. Material and Methods

### 2.1. Multi-Objective Optimization Problems

MOPs involves more than one objective to find minimum or maximum solutions. In single objective optimization, there is sightful and only one purpose: to be minimized or maximized. On the contrary, in MOPs, there are conflicting objectives in some cases.

General form of MOPs can be expressed as (1), (2) and (3);

$$x = \{ x_1, x_2, \dots, x_D \} \quad (1)$$

$$\text{Minimize or Maximize } f(x) = \{ f_1(x), f_2(x), \dots, f_m(x) \} \quad (2)$$

$$s. t. g_p(x) \leq 0; \quad p = 1, 2, \dots, P$$

$$h_n(x) = 0; \quad n = 1, 2, \dots, N \quad (3)$$

where  $x$  is a solution vector,  $D$  is dimension of the problem. Also,  $f(x)$  is called objective vector,  $g$  and  $h$  functions are constraints of the problem.

In MOPs, unlike single objective problems, the optimum solution is a solution set. Because, the solutions are trade-off and are known as Pareto-optimal set. This set refers to Pareto dominance [9], [10], [11]. The term of dominance is frequently encountered term in MOPs. The states of dominance can be expressed by the following conditions [1];

If the solution  $x_1$  dominates  $x_2$ , both case 1 and case 2 are verified;

*Case 1:* The objective values ( $f_1$  and  $f_2$ ) are compared and the solution  $x_1$  is found no worse than the solution  $x_2$  for all objective.

*Case 2:* At least one objective, the solution  $x_1$  outperforms the solution  $x_2$ .

If the solution  $x_1$  dominates all other solutions in the population, it is called non-dominated solution. Desired of MOPs, the solution set consists of non-dominated solutions. Representing of Pareto-optimal set and concept of dominance are illustrated as Fig. 1 for two objectives ( $f_1$  and  $f_2$ ) to be minimized [12].



Figure 1. (a) Representing of Pareto-optimal set

(b) Concept of Dominance

To find optimal set of MOPs, the algorithm has some mechanisms. Two important parts of them are External Archive and Update External Archive.

### 2.1.1. External Archive (EA)

In MOPs, despite of the fact that more than one objective, the algorithms generate an optimal solution set. The set maintains non-dominated solutions. To store these solutions, external archive can be used as [13], [14]. The archive is initialized in the first phase. Then, objective values of the solutions are compared and non-dominated solutions are stored in the EA. Also, EA is updated in every cycle.

### 2.1.2. Update External Archive

In every cycle, the EA is updated. In this paper, updating procedure is associated with domination procedure. Every solution in population of the algorithm is respectively compared with the EA solutions. The solution in the EA dominated by population member is removed from the archive, and the dominant solution of the population is added into the EA. Not only dominant solutions are added, but also non-dominated solutions in the population are joined into the EA.

## 2.2. Multi-Objective Artificial Bee Colony Algorithm

The basic artificial bee colony algorithm (ABC) has been proposed by Karaboga [15] in 2005. ABC is a nature-inspired algorithm. In nature, honey bees search food sources and when they find any source, they share the knowledge about the source with the other bees by dancing. Inspired by this communication, ABC algorithm is developed. Employed, onlooker and scout bees are the types of artificial bee in the algorithm. Also, initially, the initial parameters of colony size, maximum cycle and limit value are set. Limit value is the abandonment value of the food source. Initial population is generated by randomly and other phases are follows;

*Employed bees:* This type of bees calculates nectar amounts of the neighbor food sources. After comparing existing source and neighbor source, employed bees select the better source.

*Onlooker bees:* Using the information about the quality of food sources, onlooker bees interpret the sources. Then, all onlooker bees choose a food source and are fed.

*Scout bees:* In the ABC, employed bee turns into a scout bee when the food source is consumed (reaches the limit value).

The basic form of the algorithm is introduced for single optimization problems. In this study, the optimization problem has three objectives to be minimized. Therefore, the focus of the study is multi-objective ABC (MOABC) algorithm.

In MOABC, defining initial values of the food sources are the same with the basic ABC. It can be showed as (4);

$$x_{ij} = x_j^{\min} + rand(0,1)(x_j^{\max} - x_j^{\min}) \quad (4)$$

$x_{ij}$  is  $j$ . dimension of  $i$ . food source where  $i = (1, \dots, FN (Food Number))$  and  $j = (1, \dots, D (Dimension))$ . The maximum and minimum bounds of the dimension is respectively  $x_j^{\max}$ ,  $x_j^{\min}$ .

One of the most important modification in MOABC is to determine neighbor food source. In the algorithm, each employed bee, which performs this part, utilizes EA member specified randomly to optimize its solution. It can be defined the following equation (5);

$$v_{ij} = x_{ij} + \phi_{ij}(x_{ij} - \mathbf{ExAr}_{kj}) \quad (5)$$

$V$  is neighbor solution of  $X_i$  and  $j$  is the random parameter of  $X$  food source, and  $k$  is the random member of the EA.  $\phi_{ij}$  is a value between  $[-1,1]$ . Whenever the neighbor solution is determined, space bound is controlled. If a parameter exceeds the bounds, the parameter pulls the limits.

After determining the parameters, fitness values for all objectives of the two solutions are compared. This process uses greedy selection mechanism. Namely, the solution dominating the other solution is selected. If the selected solution is neighbor solution, then the abandonment value of the source is reset. Vice versa, abandonment value of the source is incremented. Fitness value is determined as (6);

$$fitness_i = \begin{cases} 1/(1 + f_i) & , f_i \geq 0 \\ 1 + abs(f_i) & , f_i < 0 \end{cases} \quad (6)$$

$fitness_i$  is fitness value of  $i$ . food source for minimization problems. If the problem is maximization,  $f_i$  denotes the fitness value.

After employed bees, new tasks are realized by onlooker bees. The mission is to choose a food source to optimize the solution using tournament selection for each onlooker bee. In tournament selection, two random food source is chosen from the population and onlooker bee choses the solution has better fitness value, and the neighbor food source is determined as employed bee part. Then, greedy selection is applied in this part, too. Abandonment value is updated according to which source is selected.

The last type of bee is scout bee. Scout bee part is completely as basic ABC. If a food source reaching the limit value, then the food source is exhausted. The parameters of the food source are randomly determined again and abandonment value is reset.

After completing all bee parts, updating EA procedure occurs. Each bee in the population is compared with the EA members according to fitness values. If the solution  $x_i$  dominates the member of EA, the EA member is removed and the solution  $x_i$  is inserted into the EA. If the solution  $x_i$  and EA member are non-dominated solutions, then the solution  $x_i$  is inserted into the EA.

Pseudocode of MOABC algorithm can be expressed as Fig. 2.

```

Initialize the food source with random solutions
Evaluate fitness values of all objectives
Generate External Archive (EA) from non-dominated solutions in the population
While (stopping criteria not met)
  For each employed bee
    Choose randomly a parameter
    Choose randomly a solution as a neighbor from EA members
    Calculate fitness value of new solution
    Apply greedy selection on the solutions based on Pareto-optimality
  End for // employed bee part
  For each onlooker bee
    Choose a solution from the population using tournament selection
    Choose a neighbor solution as employed bee
    Calculate fitness value of new solution
    Apply greedy selection on the solutions based on Pareto-optimality
  End for // onlooker bee part
  If a food source reaching limit value
    Generate new solution randomly for the food source
  End if // scout bee part
  // Update Archive Procedure
  For each bee in the population
    Compare with EA members and solution of the population based on Pareto-optimality
    If the solution of the population dominates the member of EA
      Remove the member of EA
      Insert the solution of the population into EA
    End if
    If the member of EA and solution of the population are non-dominated solutions
      Insert the solution of the population into EA
    End if
  End for
End while

```

Figure 2. Pseudocode of the MOABC algorithm

### 3. Transformer Equivalent Circuit And Parameter Estimation Using MOABC

Transmission of electrical power from the place of production to other regions is provided by alternative current. Due to the high voltage of the alternating current electrical power, transformers are used. A transformer provides to transform from the high voltage of electrical power to low voltage or vice versa. While doing this transformation, no change in the frequency. A transformer structure consists of two windings being called primary and secondary winding. The transformers can be classified as single-phase and poly-phase transformers. In single-phase transformers, primary winding is for input signal with single phase, and secondary winding can be one or more according to aim. On the other hand, in poly-phase transformers, number of primary winding is two or more, and secondary winding can be one or more according to aim. Poly-phase transformers are often wrapped in three phases, and also this information can be found in detail in [16].

In this study, single-phase transformers are focused on and the equivalent circuit of a single-phase transformer is illustrated as Fig. 3. When estimation of the transformer parameters is examined, two tests are required: no-load and short-circuit operation. These tests are examined in detail in [16]. Owing to this study, only from current and voltage at any known load, the transformer parameters are obtained without any test. Each equation of transformer parameters is obtained from Kirchhoff's circuit laws and thereby three objectives of the problem are identified.

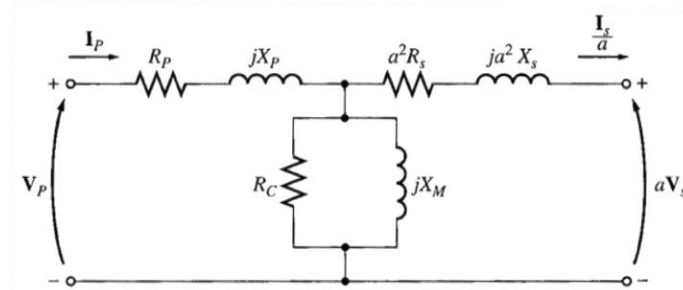


Figure 3. Equivalent transformer circuit referring to the primary

where  $R_p$  is primary winding resistance,  $X_p$  is primary winding leakage reactance,  $V_p$  is primary voltage,  $I_p$  is primary current,  $a$  is transforming ratio,  $R_s$  is secondary winding resistance,  $X_s$  is secondary winding leakage reactance,  $I_s$  is secondary current,  $V_s$  is secondary voltage,  $R_c$  is resistance of core and  $X_m$  is magnetizing reactance in the Fig. 2.

$$Err_1 = ||I_p| - Act_{I_p}| \quad (7)$$

$$Err_2 = ||I_s| - Act_{I_s}| \quad (8)$$

$$Err_3 = ||V_s| - Act_{V_s}| \quad (9)$$

where  $Err_1$  is the error of the  $I_p$ ,  $Err_2$  is the error of the  $I_s'$  ( $I_s/a$ ),  $Err_3$  is the error of the  $V_s'$  ( $aV_s$ ).  $I_p$ ,  $I_s$  and  $V_s$  are obtained by Kirchhoff Circuit Laws.

In this stage, MOABC creates randomly initial parameters which of  $R_p$ ,  $X_p$ ,  $R_s'$  ( $a^2R_s$ ),  $X_s'$  ( $a^2X_s$ ),  $R_c$  and  $X_m$  and calculates fitness values of the objectives benefiting from the parameters. Then, non-dominated solutions are stored in the EA. While stopping criteria is not met, each bee tries to improve the solutions. When reaching to stopping criteria, MOABC determines Pareto-optimal solutions of the problem in the archive. According to the Euclidean distance method, the best solution is selected through the EA members. Finding minimum solution in the EA is associated with parameters of the problem.

### 4. Experimental Results

MOABC is used to estimate transformer parameters according to current and voltage at any known load in this study. The performance of the MOABC is investigated in two different load.

In Case I, the transformer parameters ( $R_p$ ,  $X_p$ ,  $R_s'$ ,  $X_s'$ ,  $R_c$  and  $X_m$ ) are determined using MOABC at a  $Z_{L1}$  load ( $Z_{L1}=50+i30\Omega$ ). Actual data can be obtained by experimental tests which are no-load and short-circuit operation. This study assumes that the actual parameters are already known. Then, current and voltage ( $I_p$ ,  $I_s'$  and  $V_s'$ ) are calculated according to estimated parameters. Actual data, estimated data and error rate are

showed in Table I. The results show that proposed method is very satisfied for estimation parameters of the single-phase transformer.

This study is for estimation of the parameters even if at different load operations. Therefore, the results are demonstrated at the another  $Z_{L2}$  load ( $Z_{L2}=22.3607\Omega$ ) in Case II as Table II. The results show again superior performance of MOABC algorithm to estimate same parameters at another load.

Table 1. Case I: Estimated Parameters of the Single-Phase Transformer obtained by MOABC algorithm at  $Z_{L1}$  load.

Parameters and Transformer Data	Actual Data	Estimated Data by MOABC	Error (%)
Rp ( $\Omega$ )	1	1.054	-5.4
Xp ( $\Omega$ )	2	1.978	1.1
Rs' ( $\Omega$ )	1.4	1.433	-2.36
Xs' ( $\Omega$ )	1.8	1.870	-3.89
Rc ( $\Omega$ )	6400	6339.49	0.95
Xm ( $\Omega$ )	1100	1092.50	0.68
Ip (A)	3.65	3.6500	0
Is' (A)	3.50	3.6279	-3.65
Vs' (V)	205.37	211.42	-2.95

Table 2. Case II: Estimated Parameters obtained by MOABC at  $Z_{L2}$  load.

Parameters and Transformer Data	Actual Data	Estimated Data by MOABC	Error (%)
Rp ( $\Omega$ )	1	1.2320	-23.2
Xp ( $\Omega$ )	2	2.1693	-8.47
Rs' ( $\Omega$ )	1.4	1.1617	17.02
Xs' ( $\Omega$ )	1.8	1.6326	9.3
Rc ( $\Omega$ )	6400	6442.27	-0.66
Xm ( $\Omega$ )	1100	1088.43	1.05
Ip (A)	8.47	8.4648	0.06
Is' (A)	8.45	8.4514	-0.02
Vs' (V)	202.27	202.33	-0.03

## 5. Conclusion

This paper is focused on MOABC algorithm to estimate single-phase transformer parameters via current and voltage values at any known load. ABC algorithm simulates honey bee behavior. The reason for choosing this algorithm is simple implementation and minimum control parameters. In optimization process, the algorithm tries to minimize error between actual and estimated data. Proposed MOABC uses Pareto-optimality concept to achieve optimum solutions of the problem. Through the non-dominated solutions, one optimum solution is selected using Euclidian distance method. The results of the proposed method show that using MOABC algorithm to estimate transformer equivalent circuit parameters very satisfactory results is obtained.

## Acknowledgements

This study is supported by Academic Staff Training Program of Selcuk University, Konya, Turkey. The Project number is 2015-ÖYP-005.

## References

- [1]. K. Deb, *Multi-Objective optimization using evolutionary algorithms*, John Wiley & Sons, Inc. New York, NY, USA, 2001.
- [2]. T. Murata, H. Ishibuchi, and H. Tanaka, "Multi-objective genetic algorithm and its applications to flowshop scheduling," *Computers & Industrial Engineering*, vol. 30, pp. 957-968, 1996.
- [3]. H. Ishibuchi and T. Yamamoto, "Fuzzy rule selection by multi-objective genetic local search algorithms and rule evaluation measures in data mining," *Fuzzy sets and systems*, vol. 141(1), pp. 59-88, 2004.
- [4]. G. Zhang, X. Shao, P. Li, and L. Gao, "An effective hybrid particle swarm optimization algorithm for multi-objective flexible job-shop scheduling problem," *Computers & Industrial Engineering*, vol. 56 (4), pp. 1309-1318, 2009.
- [5]. S. Chamaani, S. A. Mirtaheri, M. Teshnehlab, and M. A. Shooredeli, "Modified multi-objective particle swarm optimization for electromagnetic absorber design," *In Applied Electromagnetics, 2007. APACE 2007. Asia-Pacific Conference on IEEE*, pp. 1-5, December, 2007.
- [6]. D. Meister and M. A. G. de Oliveira, "The use of the least squares method to estimate the model parameters of a transformer," *2009 10th International Conference on Electrical Power Quality and Utilisation, Lodz*, doi: 10.1109/EPQU.2009.5318853, pp. 1-6, 2009.
- [7]. S. A. Soliman, R. A. Alammari, and M. A. Mostafa, "On-line estimation of transformer model parameters," *2004 Large Engineering Systems Conference on Power Engineering (IEEE Cat. No.04EX819)*, doi: 10.1109/LESCPE.2004.1356295, pp. 170-178, 2004.
- [8]. S. H. Thilagar and G. S. Rao, "Parameter estimation of three-winding transformers using genetic algorithm," *Eng. Appl. Artificial Intell.*, vol. 15, no. 5, pp. 429-437, Sep. 2002.
- [9]. K. Deb, "A fast and elitist multiobjective genetic algorithm: NSGA-II", *IEEE Transactions On Evolutionary Computation*, vol. 6, pp. 182-197, 2002.
- [10]. A. H. F. Dias and J. A. de Vasconcelos, "Multiobjective genetic algorithms applied to solved optimization problems," *IEEE Transactions On Magnetism*, vol. 38, no. 2, pp. 1133-1136, Mar. 2002.
- [11]. A. Osyczka. "Evolutionary algorithms for single and multicriteria design optimization," New York: Physica Verlag., 2002.
- [12]. W. Zou, Y. Zhu, H. Chen, and B. Zhang, "Solving multiobjective optimization problems using artificial bee colony algorithm," *Discrete Dynamics in Nature and Society*, vol. 2011, 37 pages, 2011.
- [13]. J. D. Knowles and D. W. Corne, "Approximating the nondominated front using the pareto archived evolution strategy," *Evolutionary Computation*, vol. 8(2), pp. 149-172, 2000.
- [14]. C. A. Coello and G. T. Pulido, "A micro-genetic algorithm for multiobjective optimization," *in Proc. EMO 2001*, pp. 126-140, Mar. 2001.
- [15]. D. Karaboga, *An Idea Based On Honey Bee Swarm for Numerical Optimization*, Technical Report TR06, Erciyes University, Engineering Faculty, Computer Engineering Department, 2005.
- [16]. S. J. Chapman, *Electric Machinery Fundamentals*, McGraw-Hill, New York, 2003.

# Estimation of Projection Matrices from a Sparse Set of Feature Points for 3D Tree Reconstruction from Multiple Images

Štefan Kohek<sup>1</sup>, Damjan Strnad<sup>1</sup>, Borut Žalik<sup>1</sup>, Simon Kolmanič<sup>1</sup>

<sup>1</sup>University of Maribor, Faculty of Electrical Engineering and Computer Science

---

## Article Info

### Article history:

Received May 24<sup>th</sup>, 2017

Revised Aug 18<sup>th</sup>, 2017

Accepted Oct 18<sup>th</sup>, 2017

---

### Keyword:

3D reconstruction  
simulated annealing  
projection matrix

---

## ABSTRACT

3D reconstruction of trees is an important task for tree analysis but the most affordable approach to capture real objects is with a camera. Although, there already exist methods for 3D reconstruction of trees from multiple photographs, they mostly handle only self-standing trees captured at narrow angles. In fact, dense feature detection and matching is in most cases only the first step of the reconstruction and requires a large set of features and high similarity between individual pictures. However, capturing trees in the orchard is in most cases possible only at wider angles between the individual pictures and with overlapping branches from other trees, which prevents reliable feature matching. We introduce a new approach for estimating projection matrices to produce 3D point clouds of trees from multiple photographs. By manually relating a smaller number of points on images to reference objects, we substitute the missing dense set of features. We assign to each image a projection matrix and minimize the projection error between the images and reference objects using simulated annealing. Thereby, we produce correct projection matrices for further steps in 3D reconstruction. Our approach is tested on a simple application for 3D reconstruction of trees to produce a 3D point cloud. We analyze convergence rates of the optimization and show that the proposed approach can produce feasible projection matrices from a sufficiently large set of feature points. In the future, this approach will be a part of a complete system for tree reconstruction and analysis.

---

### Corresponding Author:

Štefan Kohek,

University of Maribor, Faculty of Electrical Engineering and Computer Science,

Smetanova ulica 17, 2000 Maribor, Slovenia

Email: stefan.kohek@um.si

---

## 1. Introduction

Reliable measurement of branches is important for successful examination of trees. However, manual measurement and examination of trees inside orchards is a tedious task, which is prone to errors and also requires extensive workforce. It is more preferable to capture real trees and perform examination on digitized trees inside the office. Therefore, numerous algorithms for automatic 3D reconstruction of trees have been developed. Many of them require special devices for tree capturing, e.g. terrestrial LIDAR [1] and Kinect [2], which are not widely deployed. On the other hand, cameras (e.g., on mobile phones) are the most affordable and widely adopted approach to capture real objects.

Pipelines for 3D reconstruction from images in most cases [3] consist of numerous steps: detecting feature points on a sequence of images, matching feature points between image pairs, camera calibration (i.e., pose estimation), and triangulation [4]. The biggest issue with this approach lies in the heavy dependence on detecting and matching feature points. Most commonly, SIFT [5] or SURF [6] are used for this task, but they require distinct features on images. When trying to perform 3D reconstruction of trees inside the orchards, we cannot easily produce enough distinct feature points because trees might be captured at wider angles, have

repeating patterns, look quite similar and therefore lack distinct features. Overlapping trees in the orchards further aggravate the aforementioned problem.

3D tree reconstruction inside orchards is a problem which cannot be easily solved with the standard 3D reconstruction pipeline. Although numerous approaches for 3D reconstruction of trees from photographs were developed, many of them are designed mostly for convincing visualization or animation of reconstructed 3D models and therefore perform more coarse reconstruction [7], [8], [9], [10]. On the other hand, other more exact approaches [11], [12] have specific requirements, such as clear background, no overlapping trees, or smaller recording angles. Because we cannot adhere to aforementioned requirements, we must use alternative approach for 3D reconstruction. In our case, an approach similar to voxel coloring [13] is used, which performs 3D reconstruction in inverse direction than ordinarily (i.e., with triangulation [3]) and it thus does not require matched feature points. On the other hand, it requires correct camera projection matrices in advance.

Evolutionary algorithms are useful tool for camera calibration when calculating intrinsic parameters [14] or even extrinsic parameters by considering relation between real 3D object with known coordinates and its occurrence on images [15]. However, considering solely relation between 3D object and its occurrence on images is not enough when 3D object covers only part of the image. In this case, the projective error on other parts of the image increases, which prevents correct 3D reconstruction.

In this work, we introduce new approach for estimating camera matrices which considers in addition to few correspondences between points on a known object and its occurrences on multiple images also correspondences between points on multiple images. We use simulated annealing [16] for calculating projection matrices because it requires only few parameters and is quite successful on various applications (e.g., automated tree pruning [17]). We show that consideration of direct relations between images lowers projective error and thus enables 3D reconstruction.

## 2. Overview of the method

Automatic feature extraction and matching from our photographs is not reliable, therefore we provide alternative data for estimating matrices of images. We can easily provide just a set  $P$  of few corresponding points between neighbor images and reference object. Thus before recording, we place a unit cube inside the scene. After taking pictures, we manually match each vertex of the cube with its occurrence on all pictures. For each vertex  $p$  of the cube, we thus define its 3D coordinates  $\mathbf{u}_p$  inside the scene and its 2D position  $\mathbf{v}_{p,i}$  on each picture  $i$ . Additional data are provided by manually relating few tips of branches between the images. Therefore, we provide  $\mathbf{v}_{p,i}$  for branch tips and thus match each point  $p$  on a branch tip between different pictures.

Our approach for estimating projection matrices is designed to consider input data which can be easily provided. To find  $3 \times 4$  camera projection matrix  $\mathbf{M}_i$  of each image  $i$  from a set of images  $I$ , two-step approach is used. In the first step, we calculate initial estimation of projection matrices, where relations between known object in 3D space and its projection in images are considered. Here, a draft approximation of metric reconstruction is obtained. In the second step, we refine matrices from the previous step by considering also the correspondences between points (tips of branches) on multiple images.

### 2.1. Initial projection matrix estimation

The objective of the first step is to find for each image  $i$  a coarse projection matrix for metric reconstruction. With simulated annealing [16], we calculate projection matrix  $\mathbf{M}_i$  of picture  $i$  by minimizing for vertices  $p \in P$  the distance between projection  $\mathbf{M}_i$  of 3D point  $\mathbf{u}_p$  and its 2D position  $\mathbf{v}_{p,i}$  on the image  $i$ . Criteria/energy function of matrix  $\mathbf{M}_i$  is:

$$f_1(\mathbf{M}_i) = \frac{\sum_{p \in P} g(\mathbf{M}_i, \mathbf{u}_p, \mathbf{v}_{p,i})}{\|P\|}, \quad (1)$$

where function  $g(\mathbf{M}, \mathbf{u}, \mathbf{v})$  calculates distance between point  $\mathbf{v}$  and projection  $\mathbf{M}$  of point  $\mathbf{u}$  (in pixels):

$$g(\mathbf{M}, \mathbf{u}, \mathbf{v}) = \left\| \mathbf{v} - \frac{(\mathbf{M}\mathbf{u})_{xy}}{(\mathbf{M}\mathbf{u})_z} \right\|. \quad (2)$$

The initial state of simulated annealing is for the first image a random matrix which has values in the range of a typical projection matrix:

$$\mathbf{M}_1 = \begin{bmatrix} 1000 r_1 & r_2 & r_3 & 1000 r_4 \\ r_5 & 1000 r_6 & r_7 & 1000 r_8 \\ 1000 r_9 & 1000 r_{10} & 1000 r_{11} & r_{12} \end{bmatrix}. \quad (3)$$

Here,  $r_i \in [0, 1]$  is a random number from the uniform distribution.

New candidate projection matrix  $\mathbf{M}'_i$  is calculated from  $\mathbf{M}_i$ . One random element at row  $r$  and column  $c$  of matrix  $\mathbf{M}_i$  is in each iteration of simulated annealing perturbed according to parameter  $F$  and current temperature  $T$ :

$$\mathbf{M}'_{i,r,c} = \mathbf{M}_{i,r,c} + T F \mathbf{M}_{i,r,c} (2r - 1). \quad (4)$$

Other elements are perturbed with probability  $C$ . If candidate  $\mathbf{M}'_i$  is better solution than  $\mathbf{M}_i$ , it is accepted as the new state ( $\mathbf{M}_i$ ), otherwise it is accepted with Metropolis criterion [18].

The best estimated projection matrix of image  $i-1$  is used as the initial state of image  $i$  in order to speed up the estimation of subsequent matrices.

## 2.2. Final estimation of matrices

In this step, we refine matrices from the first step by considering also the correspondence between points on multiple images. With simulated annealing from the previous step we produce a set of projection matrices  $\mathbf{M}$ . Initial state of simulated annealing is thus a set of matrices from the first step  $\mathbf{M} = \{\mathbf{M}_1, \dots, \mathbf{M}_{|I|}\}$ . Criteria function for minimization in the second step is:

$$f_2(\mathbf{M}) = \frac{\sum_{i \in I} f_1(\mathbf{M}_i)}{2 \|I\|} + \frac{\sum_{p \in P} \sum_{i \in I} g(\mathbf{M}_i, t(p, \mathbf{M}), \mathbf{v}_{p,i})}{2 \|P\| \|I\|}. \quad (5)$$

Here, function  $t(p, \mathbf{M})$  calculates 3D position from correspondences  $\mathbf{v}_p$  of point  $p$  by averaging triangulated positions between image-pairs [19].

Unlike the first step, each iteration of simulated annealing changes one random element of randomly chosen matrix. Other elements are perturbed with probability  $C$ .

## 3. Results and discussion

Our approach for estimating projection matrices was tested on a set of 8 orchard images (Fig. 1) which are obtained synthetically from EduApple [21]. For each test we executed simulated annealing 10 times. At first, we estimated coarse projection matrix of the first image. Here, we used next parameters for simulated annealing:  $T_0=1$ ,  $F=0.5$ , and  $C=0$ . Fig. 2 displays convergence curves of median, highest, and lowest errors. Results indicate successful estimation as best solution had errors (i.e. average distance of pixels) smaller than 10 pixels.

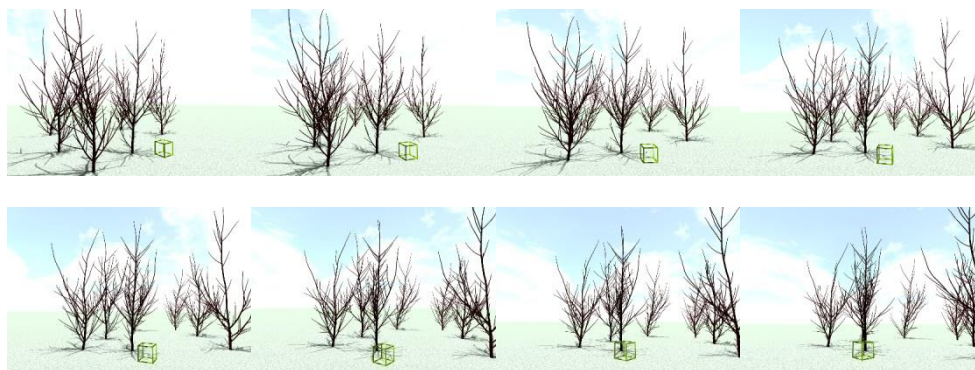


Figure 1. A sequence of images used in 3D reconstruction.

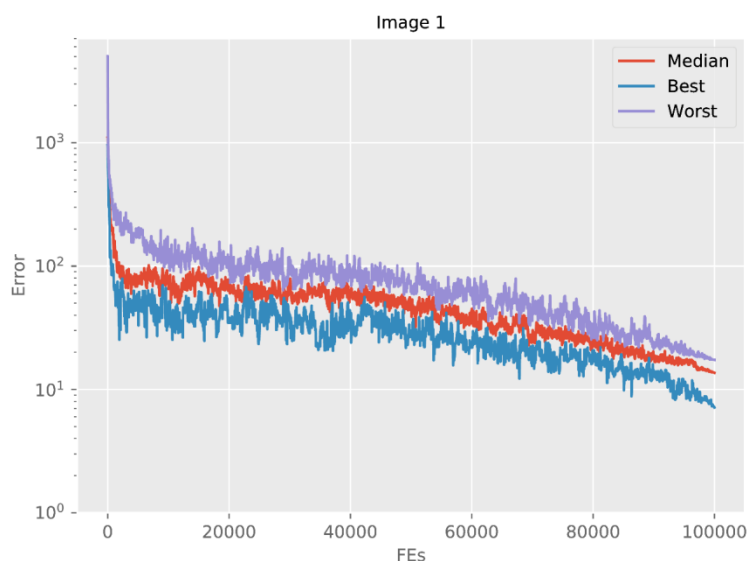


Figure 2. Convergence curves of initial projection matrix estimation (median/best/worst estimations).

The best solution of each estimation of  $\mathbf{M}_i$  was used for each subsequent image (Fig. 3). Here, the parameters of simulated annealing were:  $T_0=1$ ,  $F=0.1$ , and  $C=0.5$ . For the first image, we again used previous estimation and lowered the error even further. The errors of other images were also significantly lowered from the initial estimation, although initial errors were not so high because projection matrices of consecutive images are already similar to final estimation.

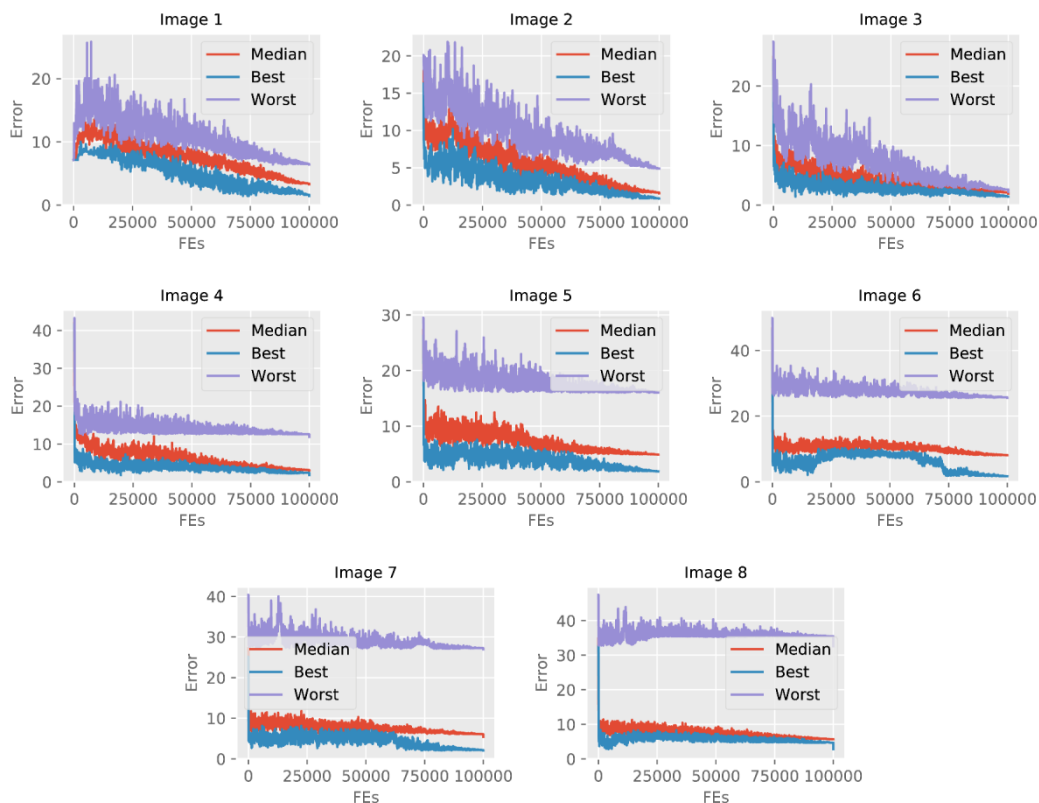


Figure 3. Convergence curves of initial estimation of all projection matrices (median/best/worst estimations).

Fig. 4 shows convergence rates of the second step of matrix estimation. Here, we used next parameters:  $F=0.1$ ,  $T_0=0.01$ , and  $C=0.05$ . Lower initial temperature was used because matrices were in most cases already oriented towards the optimal solution. Smaller variations between best and worst estimation confirm the aforementioned fact. The final error was just few pixels, which enables further steps of 3D reconstruction. Here, we used resulting matrices for initial version of 3D reconstruction pipeline, which works similar to voxel coloring [13]. Fig. 5 shows result of successful 3D reconstruction, where produced tree is similar to the tree at the cube (Fig. 1).

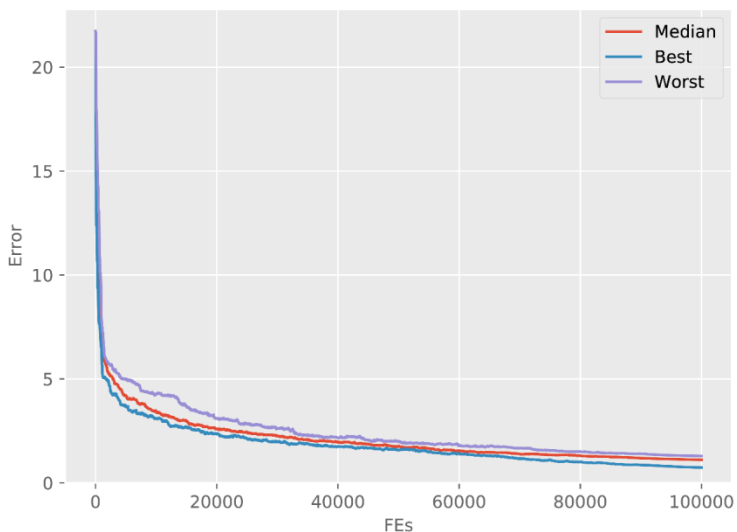


Figure 4. Convergence curves of final optimization of all eight matrices (median/best/worst estimations).

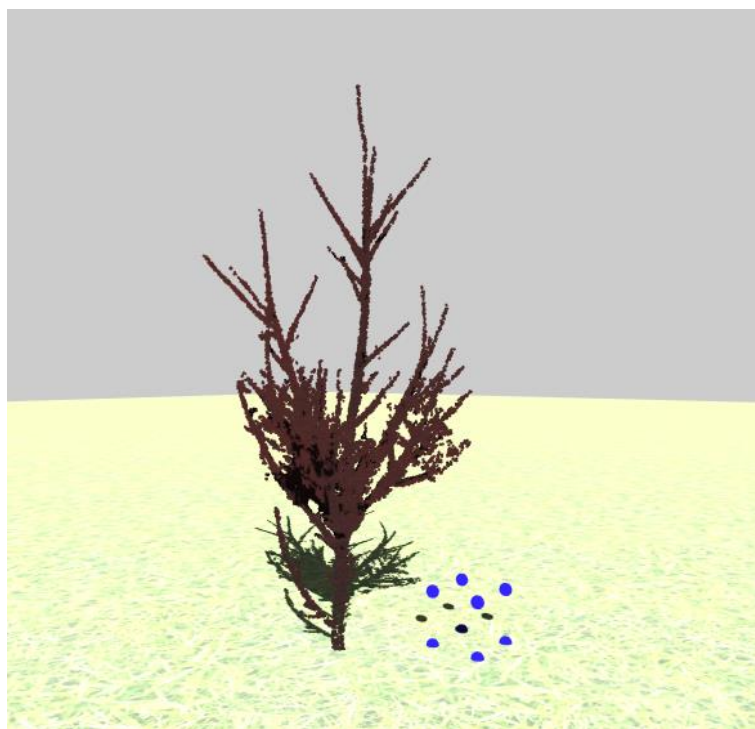


Figure 5. Resulting 3D structure of the reconstructed tree.

#### 4. Conclusions

In this paper, we presented alternative approach for estimating projection matrices and show that two-step approach was able to correctly estimate projection matrices and enable further steps of 3D reconstruction. Simulated annealing supported steady convergence of our optimization problem. Initial estimation of projection matrices lowered complexity of the problem for the second step and thus increased estimation speed of final projection matrices. Finally, we have successfully produced 3D point cloud of simple tree from multiple images inside the orchards. 3D structure was similar to input images and thus appropriate for subsequent analyses.

In the future, we plan to develop a complete framework for tree reconstruction. Matching corresponding branches manually is tedious, therefore we want to automate this task to a greater extent. Simulated annealing in current version requires large number of criteria function evaluations. Therefore, we plan to increase convergence speed of the presented approach by tuning input parameters. Simulated annealing is also only one of the algorithms for global optimization. We plan to verify other algorithms for global optimization, e.g., DE [22] or jDE [23], or even multi-criteria optimization algorithms [24]. Finally, we plan to use our approach for further growth analysis.

#### Acknowledgements

The authors acknowledge the project J2-6764 and research program P2-0041 were financially supported by the Slovenian Research Agency.

#### References

- [1] J. R. Rosell, J. Llorens, R. Sanz, J. Arno, M. Ribes-Dasi, J. Masip, A. Escolà, F. Camp, F. Solanelles, F. Gràcia, et al., “Obtaining the Three-Dimensional Structure of Tree Orchards from Remote 2D Terrestrial Lidar Scanning,” *Agricultural and Forest Meteorology*, vol. 149, no. 9, pp. 1505–1515, 2009.
- [2] N. M. Elfiky, S. A. Akbar, J. Sun, J. Park, and A. Kak, “Automation of Dormant Pruning in Specialty Crop Production: An Adaptive Framework for Automatic Reconstruction and Modeling of Apple Trees,” in *Proceedings of the IEEE Conference on Computer Vision and Pattern Recognition Workshops*, pp. 65–73, 2015.

- [3] C. Li, J. Zheng, C. Dang, and H. Zhou, “A Method of 3D Reconstruction from Image Sequence,” in *Image and Signal Processing, 2009. CISP'09. 2nd International Congress on*, pp. 1–5, IEEE, 2009.
- [4] R. I. Hartley and P. Sturm, “Triangulation,” *Computer Vision and Image Understanding*, vol. 68, no. 2, pp. 146–157, 1997.
- [5] D. G. Lowe, “Object Recognition from Local Scale-Invariant Features,” in *Computer Vision, 1999. The proceedings of the seventh IEEE international conference on*, vol. 2, pp. 1150–1157, Ieee, 1999.
- [6] H. Bay, A. Ess, T. Tuytelaars, and L. Van Gool, “Speeded-up Robust Features (Surf),” *Computer Vision and Image Understanding*, vol. 110, no. 3, pp. 346–359, 2008.
- [7] P. Tan, G. Zeng, J. Wang, S. B. Kang, and L. Quan, “Image-Based Tree Modeling,” *ACM Transactions on Graphics*, vol. 26, 2007.
- [8] P. Tan, T. Fang, J. Xiao, P. Zhao, and L. Quan, “Single Image Tree Modeling,” *ACM Transactions on Graphics*, vol. 27, pp. 1081–1087, 2008.
- [9] B. Neubert, T. Franken, and O. Deussen, “Approximate Image-Based Tree-Modeling Using Particle Flows,” *ACM Transactions on Graphics*, vol. 26, no. 3, 2007.
- [10] A. Zamuda, J. Brest, B. Bošković, and V. Žumer, “Differential Evolution for Parameterized Procedural Woody Plant Models Reconstruction,” *Applied Soft Computing*, vol. 11, no. 8, pp. 4904–4912, 2011.
- [11] C. Wu, L. He, X. Du, S. Chen, and K. Ni, “3D Reconstruction of Chinese Hickory Tree for Dynamics Analysis,” *Biosystems Engineering*, vol. 119, pp. 69 – 79, 2014.
- [12] D. Zhang, N. Xie, S. Liang, and J. Jia, “3D Tree Skeletonization from Multiple Images Based on PyrLK Optical Flow,” *Pattern Recognition Letters*, vol. 76, pp. 49 – 58, 2016.
- [13] S. M. Seitz and C. R. Dyer, “Photorealistic Scene Reconstruction by Voxel Coloring,” *International Journal of Computer Vision*, vol. 35, no. 2, pp. 151–173, 1999.
- [14] A. Whitehead and G. Roth, “Estimating Intrinsic Camera Parameters from the Fundamental Matrix using an Evolutionary Approach,” *EURASIP Journal on Advances in Signal Processing*, vol. 2004, no. 8, p. 412751, 2004.
- [15] Q. Ji and Y. Zhang, “Camera Calibration with Genetic Algorithms,” *IEEE Transactions on Systems, Man, and Cybernetics*, vol. 31, no. 2, pp. 120–130, 2001.
- [16] S. Kirkpatrick, C. D. Gelatt, M. P. Vecchi, et al., “Optimization by Simulated Annealing,” *Science*, vol. 220, no. 4598, pp. 671–680, 1983.
- [17] D. Strnad and Š. Kohek, “Novel Discrete Differential Evolution Methods for Virtual Tree Pruning Optimization,” *Soft Computing*, pp. 1–13, 2015.
- [18] N. Metropolis, A. W. Rosenbluth, M. N. Rosenbluth, A. H. Teller, and E. Teller, “Equation of State Calculations by Fast Computing Machines,” *The Journal of Chemical Physics*, vol. 21, no. 6, pp. 1087–1092, 1953.
- [19] R. Hartley, R. Gupta, and T. Chang, “Stereo from Uncalibrated Cameras,” in *Computer Vision and Pattern Recognition, 1992. Proceedings CVPR'92., 1992 IEEE Computer Society Conference on*, pp. 761–764, IEEE, 1992.
- [20] P. C. Schuur, “Classification of Acceptance Criteria for the Simulated Annealing Algorithm,” *Mathematics of Operations Research*, vol. 22, no. 2, pp. 266–275, 1997.
- [21] Š. Kohek, N. Guid, S. Tojnko, T. Unuk, and S. Kolmanič, “Eduapple: Interactive Teaching Tool for Apple Tree Crown Formation,” *HortTechnology*, vol. 25, no. 2, pp. 238–246, 2015.
- [22] R. Storn and K. Price, “Differential Evolution— A Simple and Efficient Heuristic for Global Optimization over Continuous Spaces,” *Journal of Global Optimization*, vol. 11, no. 4, pp. 341–359, 1997.
- [23] J. Brest, S. Greiner, B. Boskovic, M. Mernik, and V. Žumer, “Self-adapting Control Parameters in Differential Evolution: A comparative Study on Numerical Benchmark Problems,” *IEEE Transactions on Evolutionary Computation*, vol. 10, no. 6, pp. 646–657, 2006.
- [24] T. Robič and B. Filipič, “Demo: Differential Evolution for Multiobjective Optimization,” in *International Conference on Evolutionary Multi-Criterion Optimization*, pp. 520–533, Springer, 2005.



## A scrutiny study on wave energy potential and policy in TURKEY

Muhammet Kaan YEŞİLYURT<sup>1</sup>, İlhan Volkan ÖNER<sup>1</sup>, Gökhan ÖMEROĞLU<sup>2\*</sup>, Efe Çetin YILMAZ<sup>3</sup>

<sup>1</sup>Ataturk University Pasinler Vocational School, Department of Electricity and Energy

<sup>2</sup>Ataturk University Engineering Faculty, Department of Mechanical Engineering

<sup>3</sup>Ataturk University Pasinler Vocational School, Department of Electronics and Automation

---

### Article Info

#### *Article history:*

Received May 26<sup>th</sup>, 2017

Revised Aug 20<sup>th</sup>, 2017

Accepted Oct 18<sup>th</sup>, 2017

#### *Keyword:*

Electricity generation from wave energy, Wave energy, Wave energy potential in Turkey

### ABSTRACT

Recently new and renewable energy sources began to become prominent as alternatives to fossil fuels. Among these are wind, solar, hydraulic, biomass, geothermal and wave energies. As for Turkey, the least accounted and less applied of these sources is wave energy. The government has established a short-term outlook on utilization of renewable energy sources, named "National Renewable Energy Action Plan" which is a part of Vision 2023 targets. Nonetheless, there is no planned utilization of and/or investment into wave energy in Turkey's agenda up to the year 2023. This might be mainly because of the complex structure of wave energy conversion systems, marine conditions, mechanical difficulties and high initial investment costs. However, this type of energy is environmentally friendly, cheap and clean, and a great potential is available especially in Turkey which is surrounded on three sides by sea. Although Turkey has neither coasts to oceans nor a long stretch of west coastline, which have the highest energetic waves thanks to the prevailing west-to-east winds; the Black Sea basin, as well as the southwestern Mediterranean region, may offer a good potential for development as an energetic regime, often comparable to oceanic sites in terms of wave heights, induced by strong wind patterns. In this study, wave energy potential in Turkey and recent studies made on determination of suitable sites for evaluation of wave energy in Turkey are discussed.

---

#### *Corresponding Author:*

Third Author,

Engineering Faculty, Department of Mechanical Engineering Ataturk University 25200 Erzurum, Turkey

Email: [gomeroglu@atauni.edu.tr](mailto:gomeroglu@atauni.edu.tr)

---

## 1. Introduction

The total theoretical potential of renewable is huge, insomuch that it is deemed to be infinite when compared to the total energy need of man, which is around 12 TW max [1]. Wave energy is not one of the richest, or the most prominent among renewable. For certain areas, it has a considerable potential. Why Turkey is not one of these areas, while it is surrounded by sea on three sides. One of the objectives of this study is to seek an answer to this question.

Wave energy, actually, is the buoyant force of the water together with the kinetic energy of the moving water column, which can be regarded as a concentrated form of wind energy generated by wind blowing over the ocean surface. Wave energy can be regarded as a concentrated form of wind energy generated by wind blowing over the ocean surface [2]. But when considered in terms of earth's energy balance, wave power is a byproduct of wind power, which is in turn a minor byproduct of solar power [3]. The net power transferred from wind to waves is seldom as much as  $1 \text{ W/m}^2$ , however, waves are far more powerful.

Wave energy and extracting energy from waves attracted a great deal of attention recently. But this is not a new phenomenon. The first patent dates back to 1799[4]. The oil crisis of the 1970s led to greater interest in utilization from waves and researches on concepts and technologies have been being carried out since then [5]. Finally, it led to the world's first commercial wave farm (2.25 MW) built in 2005 in Portugal.

Wave energy is deemed to be one of the renewable energy sources with the greatest potential for development in the near future [6].

Reviews by [7] and [8] have shown that there are numerous projects at different stages of development. A number of pilot and demonstration projects, serving as research and development or proof of concept, applied around the world counts up to hundreds, with few contributing electricity to local grids.

## 2. Wave Energy

Oceans, which may be regarded as the largest solar collectors in the world, cover more than 70 percent of the surface of earth. Besides being that huge, they are the untapped and uninterrupted energy supply on the planet. The power density of wave energy is much higher than that of wind or solar energy. The environmental concerns in the use of wave systems for electricity generation are also less[4]. Marine based energy potential in the World is almost one fourth of wind energy and is more than those of hydraulic and biomass energies [9].

Oceans present innumerable benefits but in terms of energy harvesting, they might be seen as a non-stop machine that generate mechanical energy. Electricity generation is possible by capturing the energy of ocean waves by means of oscillating water columns, oscillating body converters or overtopping converters. Trapped air pockets in a water column, up-down, forwards-backwards or side to side wave motions as well as reservoirs to create a head can be utilized to drive turbines. Energy from each of the aforementioned can be converted into pneumatic/mechanical energy as rotation or translation force. Structures and positioning within the ocean may vary. Fixed, floating, submerged systems can be installed at shoreline, near shore or off shore [10].

Wave energy potential is estimated based on certain assumptions and these assumptions are always open to discussion. In order to make a more realistic determination, years-lasting and quite costly measurements are needed in the target region. Considering time and cost, in lieu of these measurements, more economical wind measurements are made and using empirical formulas, obtained from previously made researches, which gives the relationship between wind energy and wave energy can be used to estimate wave energy potential. Thus,

the amount of electrical energy that can be obtained can be determined according to the number and specifications of WECS to be positioned at that measuring location [9].

### 3. Wave Energy Technologies

As can be seen in Fig. 1, there are different approaches and solutions to extract and absorb the energy of ocean waves developed considering different conditions and potentials such as the water depth and installation location [11, 7].

In this regard, devices can be categorized for many aspects. Location wise categorization can be made as shoreline, near shore (adapted into the shore), and offshore (away from the shore and in open sea). For wave energy conversion, channel/reservoir/turbine and air-driven turbine methods are applied [4]. Another categorization is made according to what characteristics the harvesting system makes use of. In this regards systems are designed to make use of:

- the salinity difference between the surface waters and deep waters,
- mechanical energy of the tides,
- buoyant force or kinetic energy of the waves,
- or water streams [12].

It is better to consider and take advantage of the power that emerges between the buoyant force of the waves and water and gravity, rather than the kinetic energy that varies depending on many parameters [5].

According to how they are put in place, they might be grouped as fixed, submerged, floating, isolated, in-breakwater, rotating (or hinged), shoreline etc. With regards to how they interact with the water column, we can classify WECs as Oscillating Water Column (OWC), Oscillation Bodies (OB) and Overtopping (OT). Each system has various advantages and disadvantages. For instance, while land installed systems are easier to construct and maintain, there may be few locations suitable to install an OWC system. Likewise, while shoreline wave devices are advantageous in terms of installation and maintenance, energy potential is lower compared to other schemes. Near shore devices are positioned in shallow waters (<20m) while offshore devices are more typical in deep waters (>40 m) [4].

Although there is an interest for Wave Energy applications, and in many countries community and government support for wave energy projects has raised in parallel to technological development in wave energy converters (WECs) which achieved a big growth recently[13,14], there is also a big handicap; cost.

Therefore, many technologies and approaches are far from being commercial and affordable because of the high cost of deployment. Full commercial Wave Energy Conversion systems (WECs) require more effort and research on the basic components to represent a solution that accelerates wave technology development by reducing costs and increase the performance [10].

Hybrid or multiplatform concepts seem to represent a solution. Platforms to combine wave energy technologies with offshore wind turbines or with aquaculture farms are considered to cast a solution for making wave energy more affordable by sharing foundation system costs, lowering operation and management costs as well as providing environmental benefits[15,1].

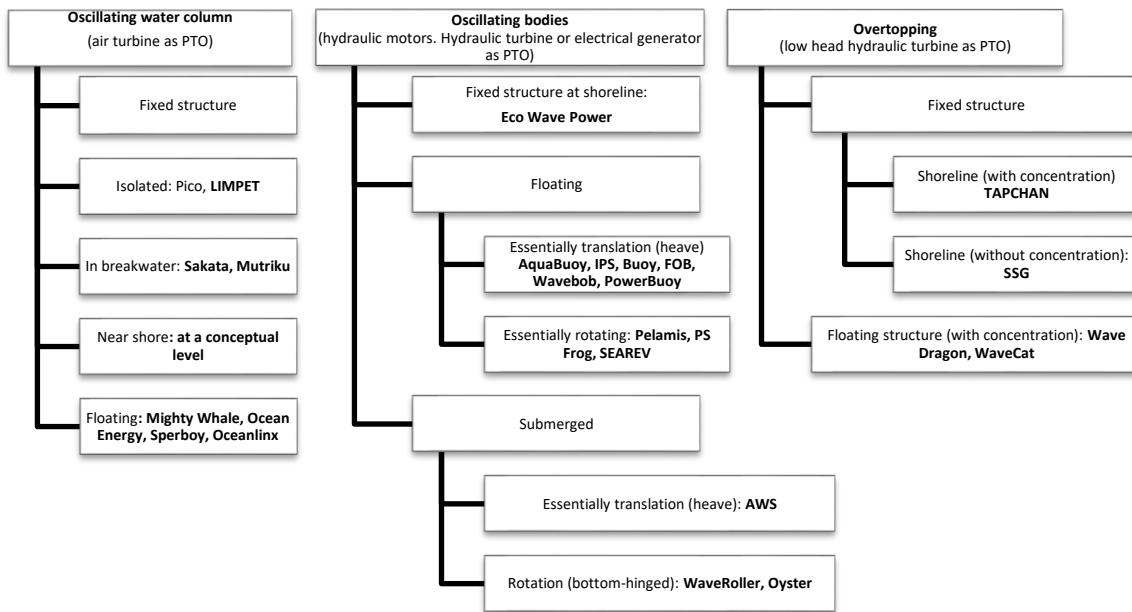


**Figure 1** Classification of Wave Energy Conversion systems based on recent researches

A typical WEC consists of (1) foundation or mooring keeping the structure and prime mover in place, (2) the structure and prime mover that captures the energy of the wave, (3) the power take-off (PTO) system which converts mechanical energy into electrical energy, and (4) the control systems to safeguard and optimize performance in operating conditions.[10]published an elaborated list of wave energy technologies which Fig. 1 is based on.

Lastly, the power corresponding to the unit length of three-dimensional wave front at a location is simply calculated using Eq. (1)

$$P = \rho g H^2 C_g / 8 [kW] \tag{1}$$

Whereas;

$\rho$ : is the density of the sea water ( $kg/m^3$ ),  $g$  is gravitational acceleration ( $m/sn^2$ ),  $C_g$  is group velocity ( $m/sn$ ),  $H$  is mean significant wave height ( $m$ )[5]

#### 4. Case For Turkey

Western coasts of the continents in the 40-60 latitude range, both north and south, have the highest energetic ocean waves as they are bigger and more powerful thanks to the prevailing west-to-east winds. In these areas, the annual average power in the wave fronts varies between 30 and 70 kW/m, peaking up to 100 kW/m at some locations. Researchers have shown that countries located at relatively high latitude and having a coastline of ocean immediately to the west have substantial wave power potential [16].

On the other hand, some researchers have reported that the average wave powers acting in unit width in Northeast Atlantic, at coasts of Portugal, in Canada, in South Africa and in China are 100 kW/m, 5-26 kW/m, 0.6 - 101.6 kW/m, 10-14 kW/m and 0.7-4.5 kW/m respectively [9].

The power of the wave fronts at non-oceanic coasts varies between 10 - 40 kW/m, and for Mediterranean coasts it is given to be around 13 kW/m. In measurements made outside of Turkey in the Mediterranean region, this figure varies between 8.4 - 15.5 kW/m throughout the year [1].

#### 4.1 Wave Energy Potential and Situation in Turkey

Although Turkey does not have coasts to oceans and does not have a long stretch of west coastline the Black Sea basin may offer a good potential for development as an energetic regime, often comparable to oceanic sites in terms of wave heights, is induced by strong wind patterns [16].

Renewable of sea origin available in Turkey; are wave energy, marine temperature gradient energy, sea currents (in the straits of Istanbul and Canakkale) as there is no tidal energy potential in Turkey. Although there are strong sea currents in straits of Canakkale and Istanbul, marine traffic limits making use of this energy.

For Turkey, the most important energy of this group is wave energy and marine wave converters are not arranged in a single row, wave converters are not limited by coastal length. Yet, longer coastline is still a pro. Turkey's coastline is about 8,200 km excluding coasts of the Sea of Marmara. It is an undeniable fact that Turkey has a great potential of wave energy.

As of the year 1998, in his very precious piece-of-art work, [1] had stated that Turkey had no wave observations and relevant data. He urged that relevant measurements should be made and applications that could be done within the framework of technological possibilities should be sought and complained of the absence of institutions or organizations to carry out the work.

At that time, the use of marine wave energy had not yet entered the agenda of Turkey, despite the fact that numerous power plants had already been established around the world. Turkey's estimated total wave power potential was given to be 75.000 MW and wave energy potential was given to be 150 billion kWh per annum, nevertheless the technical potential was struck through and given as "none" or "not applicable"[1]. But other researchers claim that the technical potential of wave energy that can be harvested by taking utilizing only one-fifth of Turkey's coastline is 18.5 billion kWh [5].

Later, there have been a number of studies on determining the wave energy potential of Turkey. Within the scope of NATO TU WAVE, a project related to Wind Energy, an Atlas of Turkish Coastal Winds and Deep Water Waves was formed.

Figure 2 and Figure 3, taken from this Atlas, show approximate significant wave height (H) and wave period (T) values, and the approximate minimum and maximum levels of wave energy ready for use [17,18].

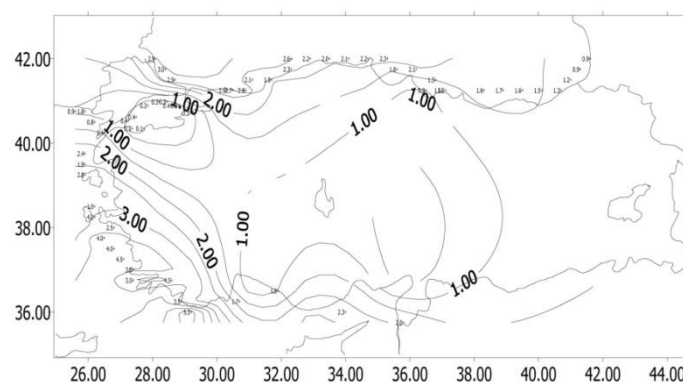


**Figure 2.** Approximate significant wave height (H) and wave period (T) values

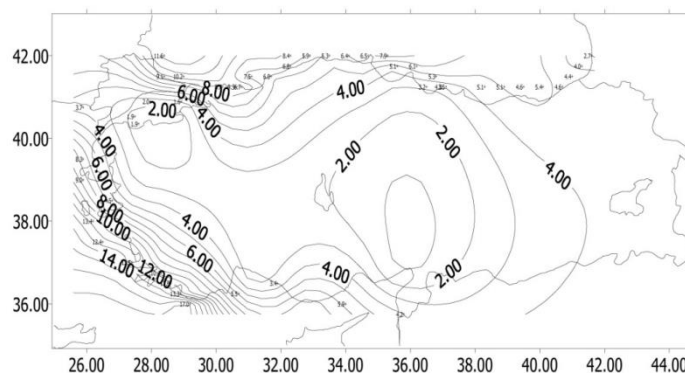


**Figure 3.** Approximate minimum and maximum levels of wave energy ready for use

In the contrary to the claims that Black Sea is wavier than any other sea surrounding Turkey, the prevailing wind potential in Aegean and Mediterranean seas intensify particularly in the south-western region between İzmir and Antalya, more precisely from Dalaman in west to Finike in east [17,18].

**Table 1.** Wave intensities as reported by [17,18].

Region	Wave Intensity
İzmir-Antalya	3.91-12.05 kWh/m
Aegean Sea	2.86-8.75 kWh/m
Mediterranean	2.59-8.26 kWh/m
Black Sea	1. 96-4.22 kWh/m
Marmara	0.31-0.69 kWh/m

[19] have investigated wave energy potential at a total of 7 study points in south-east coast of Black Sea using a third generation wave model, SWAN. The investigation area covers Hopa, Rize, Trabzon, Giresun, Ordu, Samsun and Sinop.

**Table 2.** Wave energy potential and average wave power findings by [19]

Pointname	(Hs)mean ± std. dev. (m)	(Hs) max(m)	Jmean (kW/m)	Jmax (kW/m)	Annual wave energy (MWh/m yr)
Sinop	0.533 ± 0.442	4.566	1.123	83.664	9.841
Samsun	0.399 ± 0.316	4.295	0.524	73.333	4.592
Ordu	0.403 ± 0.365	4.614	0.702	93.412	6.153
Giresun	0.384 ± 0.348	4.619	0.629	97.638	5.518
Trabzon	0.414 ± 0.372	4.186	0.689	72.031	6.036
Rize	0.383 ± 0.358	4.249	0.646	77.755	5.665
Hopa	0.361 ± 0.347	3.886	0.597	64.907	5.231

In another study carried out in Çeşme, İzmir, [9] has found that the average wave powers acting in unit width

varies between 7.16 – 39.66 kW/m with an average of 14.84 kW/m. This potential suggests that Turkey can compete with other countries in terms of evaluation of wave energy [9].

Both studies shown that WECs with a nominal power of 15 kW/m is suitable for Çeşme, and as for South East Black Sea region more than 15 kW/m is affordable.

## 4.2 Challenges

There are different assessments of wave energy potential; the amount of available energy as found in the nature is called natural potential, the utilizable amount of natural potential through the instrumentality of practical information and technical capacity we have is called technical potential, and the unit cost of technical potential as compared to that of other energy sources is called economic potential [5]. While natural potential and/or technical potential is important in terms of the diversity in energy supply and non-dependence on foreign sources, economic potential is crucial in financial aspect. Therefore, the major concern must be the economic potential rather than the natural potential.

Period of the waves in the sea varies between 3 to 5 second. The energy which can't be converted into useful work or into another type of energy in the course of this small time span will wither away under effects of successive waves, the buoyancy of the water and gravity. Therefore, selection of WECs is particularly important.

In determination of the nominal power of wave turbines enabling the conversion of wave energy into electrical energy, the current average wave power potential plays the primary role. In electric power generation, the use of turbines having a nominal power greater than available average wave power will result in the excess part of the turbine power remaining idle. While this increases the unit cost of electric energy generated from waves, the contrary, that is the nominal power of the wave turbine is less than the available average, will result in non-utilized wave power, which poses negative impact on the economy of power conversion. Therefore, the average wave power needs to be determined and turbine selection should be done accordingly.

On the other hand, other challenges that need to be overcome and/or bore in Wave Energy Conversion include but not limited to:

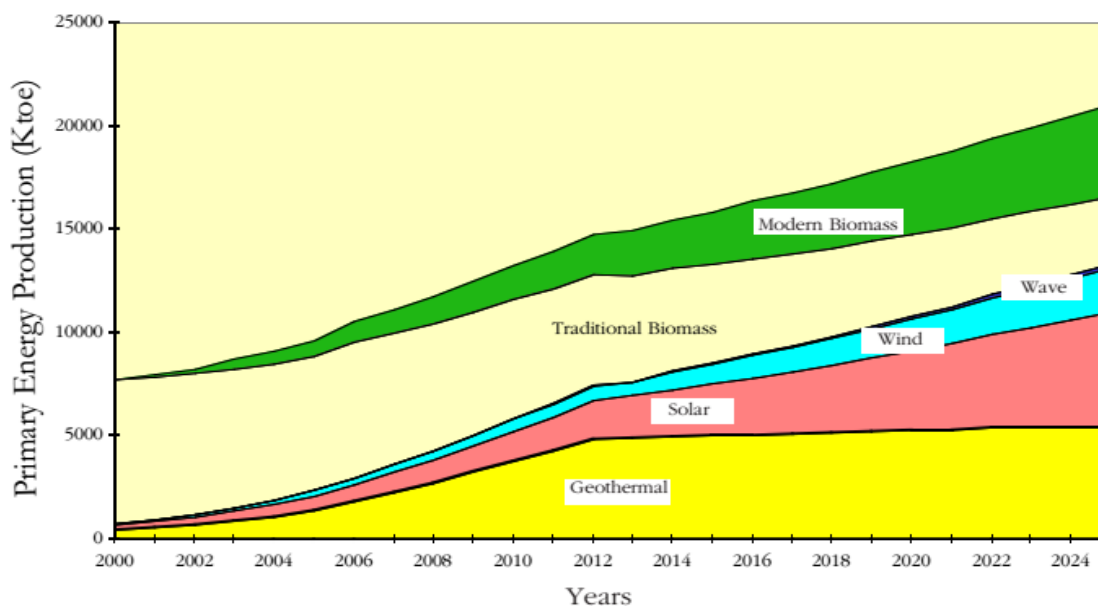
- Some devices are susceptible to be destroyed by the forces of tides, waves and strong storms,
- Accessibility, maintenance and repair can also be costly,
- The typical efficiency of a wave energy device at the moment is only about 30%. Waves generate about 2,700 gigawatts of power, only about 500 gigawatts of which can be captured with the current technology.
- There is a potential impact on the marine environment.
- Noise pollution, for example, could have negative impact if not monitored, although the noise and visible impact of each design varies greatly.
- The major competitor of wave power is offshore wind power.
- Wave farms can result in the displacement of commercial and recreational fishermen from productive fishing grounds hence lead to a socio-economic challenge.
- Other biophysical impacts (flora and fauna, sediment regimes and water column structure and flows) are being studied [20].

## 4.3 Policies and Politics

In 1998, using Energy Simulation Model (ESM) and Energy Optimization Model (EOM), a 25-years energy production scenario for Turkey, starting from year 2000, has been prepared.

**Table 3.** Turkey’s domestic primary energy production scenario (in ktoe) for years 2000 to 2025[1].

Years	2000	2005	2010	2015	2020	2023	2025
Coal / Lignite / Asphaltite	18.253	23.452	28.819	35.059	42.169	46.852	51.136
Petrol + Natural Gas	3.408	2.127	2.155	2.155	2.580	2.580	2.580
Central Heat	253	495	884	1.336	2.018	2.427	2.748
Hydraulic	3.763	6.268	7.695	9.219	9.989	10.726	11.585
Nuclear (1st alt.)	-	-	3.657	9.143	18.286	26.988	29.200
Nuclear (2nd alt.)	-	-	3.657	10.972	21.943	32.386	35.040
Geothermal	432	1.380	3.760	5.000	5.250	5.400	5.400
Solar	287	716	1.458	2.514	3.882	4.854	5.564
Wind	58	263	629	995	1.519	1.883	2.167
<b>Sea Wave</b>	-	-	<b>10</b>	<b>25</b>	<b>125</b>	<b>175</b>	<b>175</b>
Traditional Biomass	6.963	6.461	5.734	4.789	3.980	3.560	3.307
Modern Biomass	17	765	1.652	2.500	3.515	4.049	4.406
<b>Total</b>	<b>33.434</b>	<b>41.957</b>	<b>56.453</b>	<b>72.735</b>	<b>93.313</b>	<b>109.495</b>	<b>118.268</b>

**Figure 4:** New and renewable energy sources in Turkey’s domestic energy production according to the EOM model outputs.

As seen in Table 3 and Figure 4, Wave energy utilization had been in the agenda, and by the year 2010 and 2015, 10 ktoe and 25 ktoe wave energy production had been estimated. Before going any further, let’s have a look at the latest National Renewable Energy Action Plan (REAP) published by [21].

In “The Law on the Utilization of Renewable Energy Resources for the Purpose of Generating Electrical Energy” (Law No: 5346), among defined Renewable Energy sources is wave energy. In this action plan optimistic, realistic as well, targets are set and trajectories defined in order to meet the targets. Financial support for the promotion for Tidal/Wave, sea thermal, and marine current energy technologies is said to be

considered and planned within the scope of REAP. It also states that wave energy has a promising future in Turkey, as the country has an extensive surface and a large coastline, suitable to develop and install WECs. Therefore, financial support for R&D and the promotion of these technologies will be established. For wave energy, in terms of trajectories, financial support to the investors for the promotion for wave energy technologies is planned, but the launching date is still under consideration. Nevertheless, analyzing the ten-year look-ahead chart for the renewable for electricity generation, under concrete obligations/targets per year (per technology) from year 2013 to 2023, we can see no projection for wave energy. Both installed capacity and electricity generation targets for wave energy is neglected up to the year 2023, as seen in Fig. 5. and Fig.6.

Renewable energy technology	Installed power capacity (MW)			Electricity generation (GWh)		
	2013	2023	Δ	2013	2023	Δ
Hydro	22,289	34,000	53%	59,420	91,800	54%
Wind	2,759	20,000	625%	7,558	50,000	562%
Geothermal	310	1,000	223%	1,364	5,100	274%
Solar	0	5,000	-	0	8,000	-
Biomass	224	1,000	346%	1,171	4,533	287%

Figure 5: Electricity generation and installed capacity: 2013 data, 2023 forecast and increases [21]

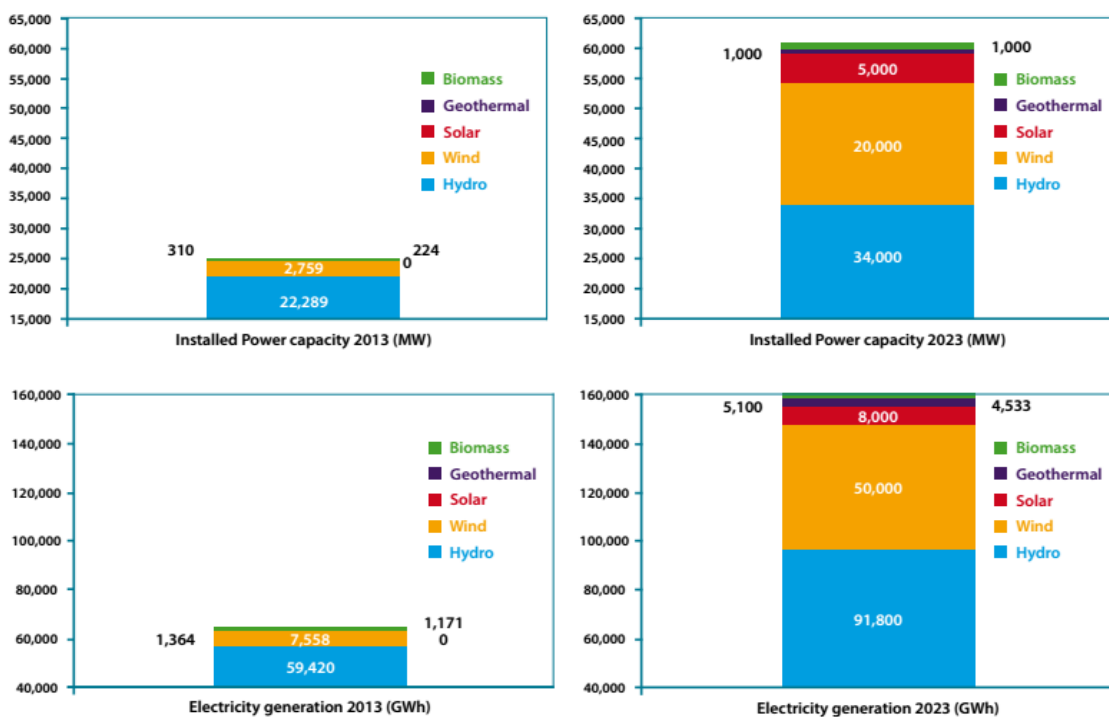


Figure 6: Electricity generation and installed capacity from renewable sources: 2013 data and 2023 forecast (Ministry of Energy and Natural Sources, Republic of Turkey, 2014)

What made the policy-makers change their mind is unknown, but what is clear is that wave energy seems to have not been in Turkey’s agenda at present.

## 5. Discussion

Among renewable, one with the greatest potential for development and promising for the near future is surely the wave energy. With regards to predictability, high power density, offering relatively high utilization factor, and environmental and visual friendliness; wave energy presents numerous advantages [19].

In terms of environmental sensitivity, wave energy is expected to reduce the dependence on fossil fuels in producing electricity, directly and indirectly. Yet, WECs can be used to produce hydrogen, thus adverse impacts of energy supply may be decreased at a certain level, which in turn help decrease global warming, acid rains, and other contamination in a way[24].

Although many studies have been carried out for the determination of wave energy potential along the shores of the country throughout the last decade, comparative experimental and theoretical studies on selection of appropriate turbine systems to take advantage of available potential in the most economical way is also required. The target on the use of alternative energy sources of Vision 2023, recently declared by the government, is very hard to be met neglecting wave energy, an alternative renewable energy source with a high potential.

**Table 4.** General Energy Balance for years for Turkey (based on data by MENR)

Year	Hydro	Biomass	Wind	Geothermal	Solar	Total	Ren. Share in Tot.	Hydro share in Ren.
<b>2007</b>	<b>3217</b>	<b>12</b>	<b>31</b>	<b>914</b>	<b>420</b>	<b>27373</b>	<b>17%</b>	<b>70%</b>
<b>2014</b>	<b>3495</b>	<b>81</b>	<b>733</b>	<b>3524</b>	<b>803</b>	<b>31049</b>	<b>28%</b>	<b>40%</b>

While the share of renewable energy sources in electricity production reached 17% in the last decade, more than 70% of renewable energy-based electricity was supplied from hydropower [22]. As of the year 2014, share of renewable rose to 28 percent while share of hydropower in renewable decreased to 40% [23]. Other renewable energy sources, with a share of less than 1%, are almost non-utilized in annual total electricity production. Although there are recent investments along with subsidies and incentives on solar-based electricity production projects, majority of new renewable energy investments is focused in wind, solar, biomass and geothermal energy, and so far, wave energy is still not considered.

The most suitable sites for WEC installation and energy production are reported to be the Black Sea, in the north of Istanbul strait and off the southwestern and western coasts in Aegean/Mediterranean region. When coasts not having enough potential for commercialization and other facility sites are excluded, WECs set up at three main regions off the coasts of Turkey, having annual wave power between 3 and 17 kW/m, would convert a total of around 10 TWh/year, which is 7.8% of the current economically feasible hydro electrical potential [24].

The characteristics of a WEC should be in conformity with the characteristics of the sea, in other words, the marine conditions and climate of the sea. A WEC perfect for North Sea may not perform as good in a mild climate sea, such as the Mediterranean. The fore an index called Wave Energy Development Index (WEDI) is defined for sites and being used in design and selection phases at the beginning of a project. In light of the findings from researches, the characteristics of Baltic Sea seem to conform to Turkish waters hence devices designed for that sea can be good samples for the studies in Turkey [24].

The Black Sea basin and South-west Mediterranean region, which may often be comparable to oceanic sites in terms of wave heights, are induced by strong wind patterns and may offer a good potential for development as an energetic regime.

## 6. References

- [1] M. Ö. Ültanır, *21. Yüzyıla Girerken Türkiye'nin Enerji Stratejisinin Değerlendirilmesi [Evaluation of Turkey's 21<sup>st</sup>-Century Energy Strategy]*, Lebib, 1998.
- [2] L. H. Holthuijsen, *Waves in oceanic and coastal waters*, Cambridge University Press, Cambridge, 2007.
- [3] D. Mollison, “Wave Climate and the Wave Power Resource,” in *Hydrodynamics of Ocean Wave-Energy Utilization: IUTAM Symposium Lisbon/Portugal 1985*, D. V. Evans and A. F. O. Falcão, Eds., pp. 133–156, Springer Berlin Heidelberg, Berlin, Heidelberg, 1986.
- [4] E. Özkop, *An Intelligent Controlled Novel Power Conditioning For Wave Energy Converter Systems*, Ph.D. Thesis, Karadeniz Technical University, 2012.
- [5] İ. Uygur, R. Demirci, H. Saruhan et al., “Batı Karadeniz Bölgesindeki Dalga Enerjisi Potansiyelinin Araştırılması [An Investigation of Wave Energy Potential in Western Black Sea Region],” *PAJES - Pamukkale University Journal of Engineering Sciences*, vol. 12, no. 1, pp. 7–13, 2006.
- [6] G. Iglesias and R. Carballo, “Wave energy potential along the Death Coast (Spain),” *Energy*, vol. 34, no. 11, pp. 1963–1975, 2009.
- [7] A. F. d. O. Falcão, “Wave energy utilization: A review of the technologies,” *Renewable and Sustainable Energy Reviews*, vol. 14, no. 3, pp. 899–918, 2010.
- [8] A. S. Bahaj, “Generating electricity from the oceans,” *Renewable and Sustainable Energy Reviews*, vol. 15, no. 7, pp. 3399–3416, 2011.
- [9] A. Özdamar, “Dalga Enerjisinden Elektrik Enerjisi Eldesi Üzerine Bir Araştırma: Çeşme Örneği [An Investigation on Electricity Generation from Wave Energy: Çeşme Example],” *Ege Journal of Fisheries and Aquatic Sciences*, vol. 17, 1-2, pp. 201–213, 2000.
- [10] International Renewable Energy Agency, “IRENA Ocean Energy Technology Brief 4 June 2014: Wave Energy Technology Brief,” 2014.
- [11] J. Cruz, *Ocean wave energy: Current status and future prepectives [i.e. perspectives]*, Springer, Berlin, 2008.
- [12] A. Okur, *Karadeniz Ereğli'de Dalga Enerjisi Üretimine Bir Yaklaşım [An Approach to Wave Energy Conversion in Karadeniz Ereğli]*, Master Thesis, Karaelmas Üniversitesi, 2011.
- [13] A. Clément, P. McCullen, A. Falcão et al., “Wave energy in Europe: Current status and perspectives,” *Renewable and Sustainable Energy Reviews*, vol. 6, no. 5, pp. 405–431, 2002.
- [14] M. G. Hughes and A. D. Heap, “National-scale wave energy resource assessment for Australia,” *Renewable Energy*, vol. 35, pp. 1783–1791.
- [15] C. Perez-Collazo and G. Iglesias, “Integration of Wave Energy Converters and Offshore Windmills,” in *Conference Proceedings*, 2012.
- [16] E. Rusu, “Wave energy assessments in the Black Sea,” *Journal of Marine Science and Technology*, vol. 14, no. 3, pp. 359–372, 2009.
- [17] E. Özhan and S. Abdalla, *Türkiye Kıyıları Rüzgar ve Derin Deniz Dalga Atlası [Atlas of Turkish Coastal Winds and Deep Water Waves]*, Turkish National Committee on Coastal Zone Management / MEDCOAST, Ankara, 2002.
- [18] M. Sağlam and T. S. Uyar, “Wave Energy and Technical Potential of Wave Energy for Turkey,” in *Conference Proceedings*, 2005.
- [19] A. Akpınar and M. İ. Kömürcü, “Wave energy potential along the south-east coasts of the Black Sea,” *Energy*, vol. 42, no. 1, pp. 289–302, 2012.
- [20] “Wave Energy: Renewable Energy Research,” Bluebird Marine Systems, Ltd., [http://www.bluebird-electric.net/wave\\_power\\_energy\\_generation.htm](http://www.bluebird-electric.net/wave_power_energy_generation.htm).
- [21] “National Renewable Energy Action For Turkey,” Ministry of Energy and Natural Sources, Republic of Turkey, 2014, [http://www.eigm.gov.tr/File/?path=ROOT%2f4%2fDocuments%2fEnerji%20Politikas%2fC4%B1%2fNational\\_Renewable\\_Energy\\_Action\\_For\\_Turkey.pdf](http://www.eigm.gov.tr/File/?path=ROOT%2f4%2fDocuments%2fEnerji%20Politikas%2fC4%B1%2fNational_Renewable_Energy_Action_For_Turkey.pdf).
- [22] “General Energy Balance for the Year 2007 for Turkey,” Ministry of Energy and Natural Resources, Republic of Turkey, 2011, [http://www.eigm.gov.tr/File/?path=ROOT%2f4%2fDocuments%2fDenge+Tablosu%2f2007\\_Denge\\_Tablosu.xlsx](http://www.eigm.gov.tr/File/?path=ROOT%2f4%2fDocuments%2fDenge+Tablosu%2f2007_Denge_Tablosu.xlsx).

- [23] “General Energy Balance for the Year 2014 for Turkey,” Ministry of Energy and Natural Resources, Republic of Turkey, 2016, <http://www.eigm.gov.tr/File/?path=ROOT%2f4%2fDocuments%2fSayfalar%2f2014+Genel+Enerji+De+nge+Tablosu.xlsx>.
- [24] M. Sağlam, E. Sulukan, and T. S. Uyar, “Wave Energy and Technical Potential of Turkey,” *Journal of Naval Science and Engineering*, vol. 6, no. 2, pp. 34–50, 2010.

## BIOGRAPHY OF AUTHORS



**Muhammet Kaan YEŞİLYURT** was born in 1979. After he received his Bsc in 2003, he worked for many international companies, especially in oil and gas sector. Then he returned his academic career and received his MSc at Ataturk University in 2015. He is working as an Instructor at Pasinler Vocational School in Electric and Energy Department. He is now a PhD student at Ataturk University in Turkey.



**İlhan Volkan ÖNER** was born in 1979. He received MSc degree in Mechanical Engineering at Ataturk University, Erzurum, Turkey, in 2009. Later, he received his Ph.D. degree also at Ataturk University in 2014. Since 2015, he has been working as an Assistant Professor in Department of Alternative Energy Sources at Ataturk University. His areas of interest are renewable energy, internal combustion engines and alternative fuels.



**Gökhan ÖMEROĞLU** was born in 1982. He received Bsc, MSc and Ph.D degrees at Ataturk University in 2003, 2009, and 2012 respectively. He has started his career at Bayburt University as an Instructor. After receiving his Ph.D he has been assigned the Assistant Professor position at the same university, and shifted to Ataturk University the same year. Since then, he has been working as an assistant professor at Ataturk University Engineering Faculty, Department of Mechanical Engineering, Thermodynamics division.



**Efe Çetin YILMAZ** was born in 1989. He received MSc degree from Mechanical Engineering the Ataturk University, Erzurum, Turkey, in 2014. Now, he is continuing from same University Ph.D. degree since in 2014. For five years, he has been working as a Lecturer in the Department of electronics and automation at Ataturk University. His areas of interest are control system design and programming, wear of biomaterials, corrosion and renewable energy.

**Note:** This study has been extended and revised after been presented in 3rd International Conference on Sustainable Development held on 19 - 23 April 2017 in Sarajevo, Bosnia Herzegovina. It was previously published as Abstract in the Book of Abstracts of the conference under the name of "Wave Energy as a Renewable Energy For Turkey".

## Condition Monitoring of the Uncoated Carbide Cutting Tool in Turning Process of the Aluminum Alloy 6061 via Vibration

Othman Inayatullah<sup>1</sup>, Vickneswaran Sinnasamy<sup>2</sup>

<sup>1</sup>Departement of Mechanical and Manufacturing Engineering, School of Engineering and Technology, University College of Technology Sarawak

<sup>2</sup>Departement of Mechanical and Manufacturing Engineering, Faculty of Engineering, Universiti Putra Malaysia (9 pt)

---

### Article Info

#### Article history:

Received May 29<sup>th</sup>, 2017

Revised Aug 20<sup>th</sup>, 2017

Accepted Oct 18<sup>th</sup>, 2017

#### Keyword:

Cutting tool

Turning

Vibration

Aluminum Alloy 6061

Tool life

---

### ABSTRACT

This study have been conducted in an attempt to monitor the changing of tool wear caused by increasing the cutting speed, depth of cut and feed rate. The signal processing analysis was done on the raw signal, the vibration signal then which is analyses by using MATLAB software. The relationship among several parameter of vibration signal, such as energy and maximum amplitude with cutting speed and depth of cut was studied. The material machined was Aluminum Alloy 6061 and uncoated carbide as a cutting tool. At the same time, the cutting temperature was also monitored. The results show that vibration signal can be one of the method to monitor tool wear in turning process via in-situ and therefore can be obtained useful for establishing the end of tool life in these operation. Based on the results the suitable speed and depth of cut range was identified to maximize the tool life

---

### Corresponding Author:

First Author,

Departement of Mechanical and Manufacturing Engineering,

School of Engineering and Technology,

University College of Technology Sarawak,

868 Persiaran Brooke 96000, Sibul, Sarawak, Malaysia.

Email: drothman@ucts.edu.my

---

## 1. Introduction

Turning is a form of machining; a material removal process which is used to create rotational parts by cutting away unwanted material. Lathes are designed for turning operations, so the precise control of the cutting results in tight tolerances. However, the desired dimensions and its precision are highly influenced by a critical phenomenon which is the cutting tool wear property. Due to the worm cutting tool, it causes vibration in the cutting tool affects due lifespan of the cutting tool and functional behaviour. There are three parameters influence the cutting tool lifespan, the cutting speed, depth of cut and tool feed rate. On other parts, the cutting speed also depends on the length, type of material and diameter of the object and problem occurs when we encounter unknown material.

The objectives of this study is to evaluate the mechanical behaviour of the cutting tool during turning by analysing the vibration signal and the relationship percentage of tool wear with vibration signal. The vibration signal propagates by the cutting tool during the cutting of the turning aluminium alloy. The amplitude and energy produced by the system increased as the vibration increase. In the thermographic testing, an images shown the worm cutting tool create more heat compared to the good one.

The cutting tool selection in turning process is among the most essential factors in machining process. The cutting tools must possess certain characteristics as they subject to high temperature, high contact stresses and rubbing along the machined surface. The important mechanical property with respect to the workpiece to be machined is the cutting tool's hot hardness as shown in Figure 1 [1].

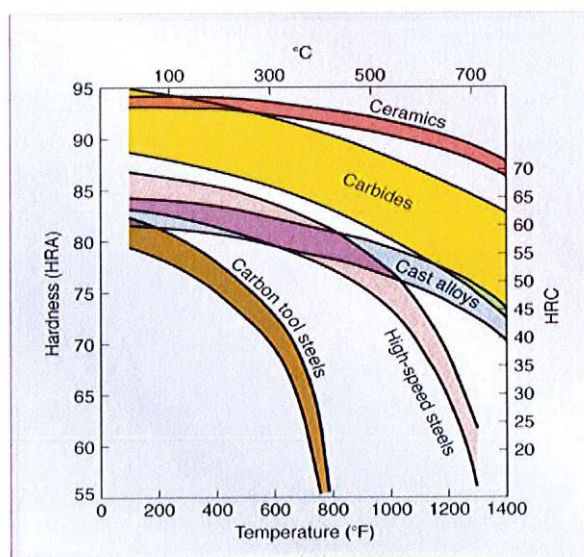


Figure 1. Hot hardness of cutting tool according to the materials [1]

It is vital so that the hardness, strength and wear resistance of the tool are maintained at any temperature encountered in the process. This property ensure that the tool stays in its shape and sharpness without undergoing plastic deformation [2-3]. Since there are so many materials used in machining, the tool life varies from the material used. As the time of cutting increase. The tool wear increase as shown on Figure 2 [4].

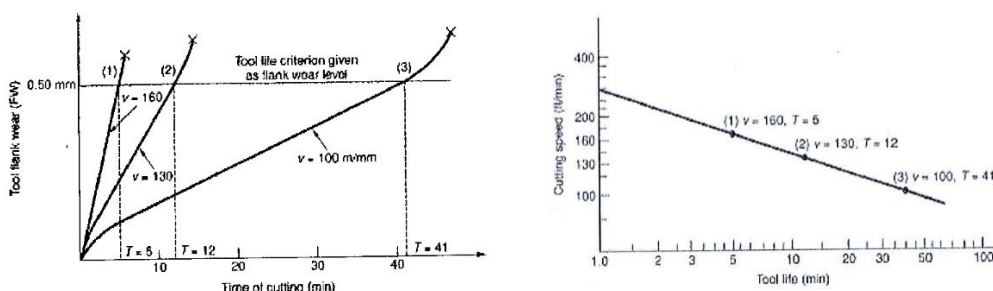


Figure 2. Relationship between time of cutting and cutting speed with tool life [4]

Typically, there are two methods of detecting tool wear, indirect and direct method. As one of the widely used, due to low price, easy to work on and online continuous testing characteristic vibration measurement, is the indirect sensor based method. Many of experiments has been carried out to correlate tool wear and the vibration signal produced. The results does show the tool wear are sensitive to the vibration signature features extracted from the time and frequency domain [5-7].

In previous study, the main purpose of vibration analysis is to identify the features indicative of tool wear. In the experiment done by Baojia Chan, a total of 12 cutting tools vibration signal and wear data were measured [8] and it is that all investigated tools have the same wear mechanism and vibration characteristics with increasing tool wear. This study shown, the on-line vibration signals at the sampling frequency 32.768 Hz, is the frequency characteristics of tool vibration. After running 78 mins, the vibration spectrum of the tool divided by two frequency ranges of 2-4 kHz and 7-10 kHz as shown in Figure 3 [8].

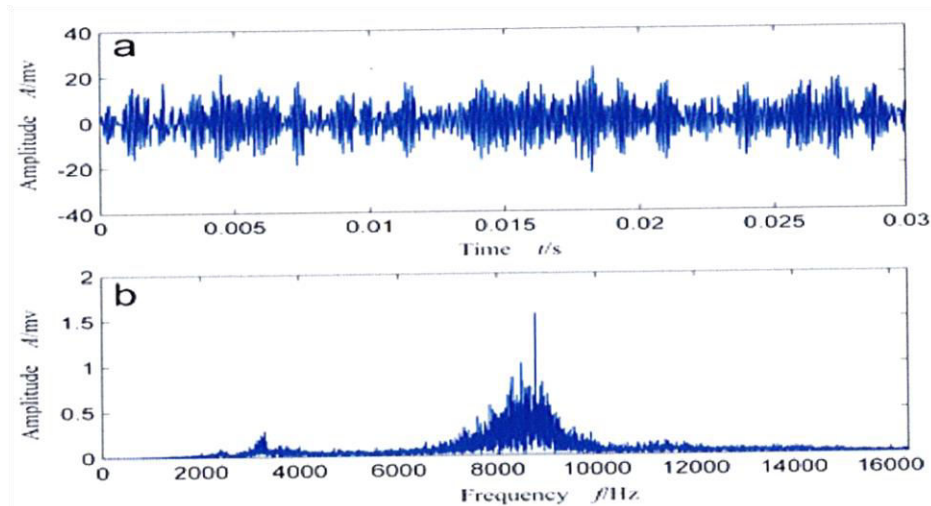


Figure 3. Vibration signal in time domain and frequency domain [8]

## 2. Methodology

The turning experiment is conducted by using Aluminum Alloy 6061 as the specimen. During the turning process the specimen rotating in high revolution and this will generate the vibration signal even before cutting tool contact the specimen. The main purpose of this process is to identify the vibration level of the turning lathe machine. The vibration signal of the turning lathe machine in free of contact will be recorded, and it is followed by contact between cutting tool and specimen, and during cutting process with different depth and speed.

The setup of the equipment, the speed of spindle rotation, location of the transducer, and the cutting first point should be considered thoroughly as these are the important factors that will influence the result of the experiment. A piezoelectric accelerometer was attached to the cutting tool holder to measure the vibration during cutting process and convert the signal into another form readable by the data acquisition system (DAQ). For each depth, the vibration of the cutting tool holder was recorded when it is being cut. The vibration signals were analyzed using MATLAB in time domain to obtain the required parameters such as maximum amplitude and vibration energy.

In this study, the specimen is Aluminum Alloy 6061 with ultimate tensile strength 124 MPa and Hardness 30. The measurement of the cutting tool vibration will be done at cutting speeds of 72 rpm and 1750 rpm with depths of cut of 2 mm and 5 mm. The transducer used for this study was a sub-miniature Charge Amplifier, Type 4374 with Bruel&Kjaer Portable Pulse 3560-C used to analyze the signal converted by the accelerometer. The vibration signal was analyzed and visualized by using B&K Pulse LabShop software. For heat measurement, a HotShot thermography camera was used. This thermography camera incorporates a high performance micro bolometer infrared focal plane array with accurate temperature measurement from -20°C to 250°C.

## 3. Result and Discussion

Results of this study will be started with vibration wave propagation for rotation speeds of 72 rpm and 1750 rpm in different conditions. Figure 4 shows the time domain vibration wave at rotation without cutting, Figure 5 shows the time domain vibration wave during point of cutting, Figure 6 shows the time domain vibration wave during cutting process with a 2 mm depth of cut, Figure 7 shows the time domain vibration wave during cutting process with a 5 mm depth of cut, and Figure 8 shows the time domain vibration wave during 1750 rpm, 5 mm depth of cut with a worm cutting tool.

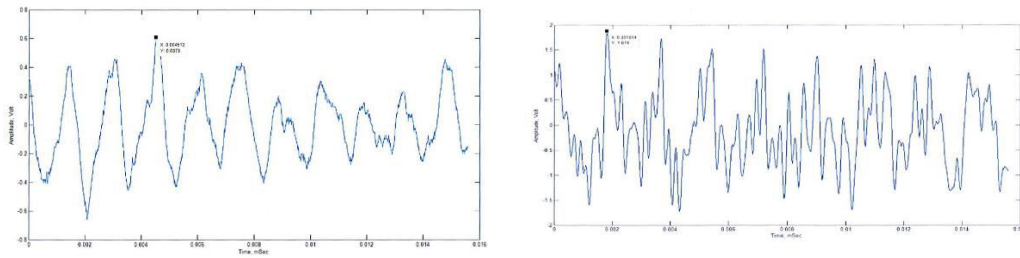


Figure 4. Time domain vibration wave at rotation speed 72 and 1750 rpm without cutting process

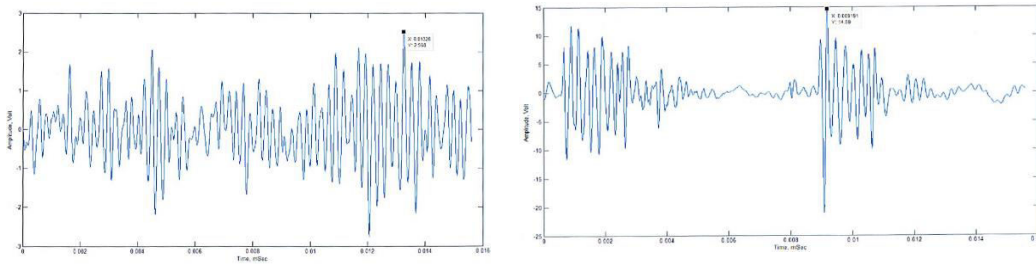


Figure 5. Time domain vibration wave at rotation speed 72 and 1750 rpm during position point of cutting

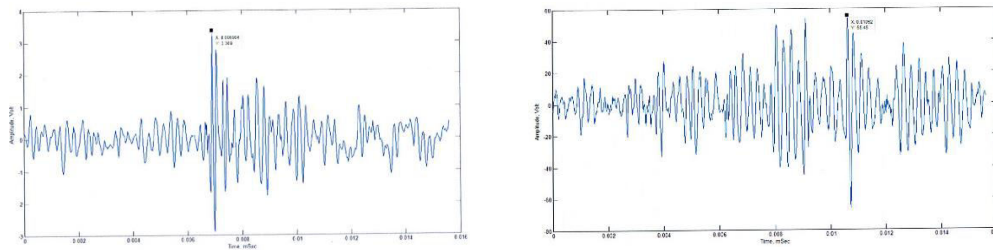


Figure 6. Time domain vibration wave at rotation speed 72 and 1750 rpm during 2 mm depth of cut

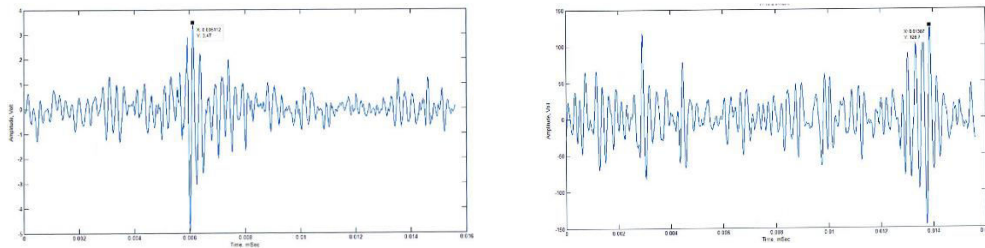


Figure 7. Time domain vibration wave at rotation speed 72 and 1750 rpm during 5 mm depth of cut

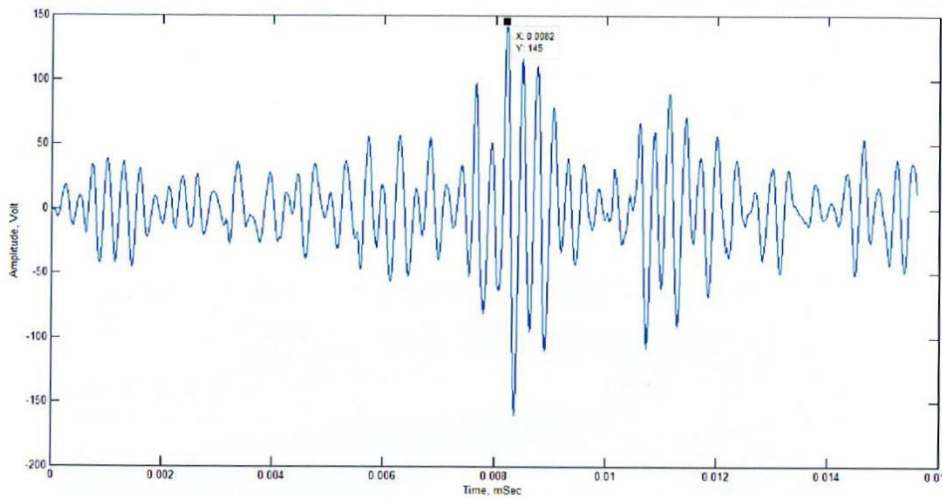


Figure 8. Time domain vibration wave at rotation speed 1750 rpm, 5 mm depth of cut with worm cutting tool

In thermal analysis, Figure 9 shown the thermal image of rotation speed 72 and 1750 rpm during 2 mm depth of cut. Figure 10 shown the thermal image of rotation speed 72 and 1750 rpm during 5 mm depth of cut, and Figure 11 shown the thermal image of rotation speed 1750 rpm, 5 mm depth of cut with worm cutting tool.

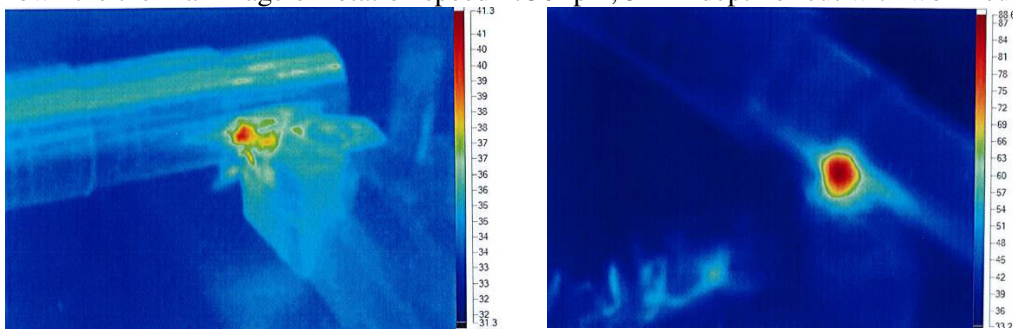


Figure 9. Thermal image during 72 and 1750 rpm, 2 mm depth of cut

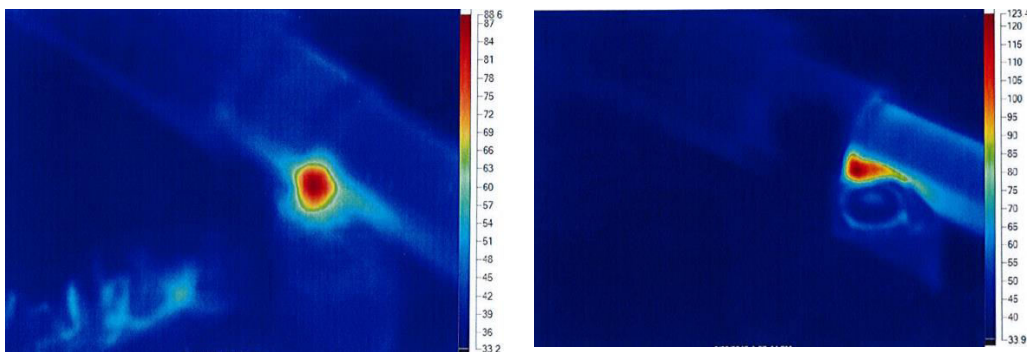


Figure 10. Thermal image during 72 and 1750 rpm, 5 mm depth of cut

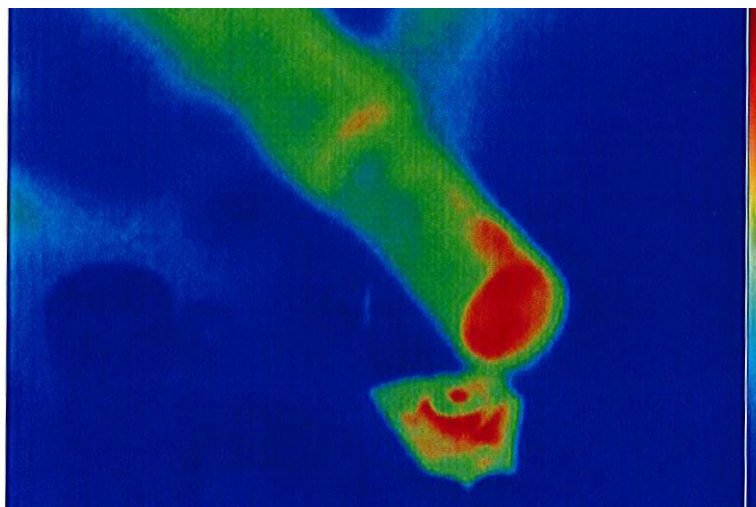


Figure 11. Thermal image of worm cutting tool during 1750 rpm and 5 mm depth of cut

The value of maximum amplitude, vibration energy, and temperature for lathe machine, when the cutting tool touched the surface of the aluminum, when cutting processes of 2 and 5 mm depth of cut, and when worm cutting tool is tabulated in Table 1.

Table 1 shown the vibration energy increase with the depth of cut for 72 rpm and 1750 rpm spindle rotation speed. Due to increasing of depth of cut, force imposed by cutting tool on specimen experience increase. This will be the main cause the increasing of pressure towards specimen. The resistance of the point of contact between cutting tool and specimen increased and it is produced more vibration activities. The cause of wear is due to the abrasion and adhesion which occurs when cutting tool and specimen are enforced in cutting process.

Table 1. Maximum amplitude, vibration energy and temperature for each processes

Speed (rpm)	Position	Maximum Amplitude (Volt)	Vibration Energy (Joule)	Temperature (°C)
72	Without cut	0.6079	205.2137	-
	Cutting point	2.5077	291.6156	-
	Depth cut 2 mm	3.3689	423.3078	41.30
	Depth cut 5 mm	3.4703	477.0082	88.60
1750	Without cut	1.8744	616.1857	-
	Cutting point	14.590	2108.400	-
	Depth cut 2 mm	55.448	12324.00	104.3
	Depth cut 5 mm	126.70	23871.00	123.4
	Depth cut 5 mm (worm)	147.25	25680.00	167.1

Increasing the degree of wear of cutting tool, led to an increase in the control area owing to crumbled of cutting edges. The transition of friction from static to sliding owing increasing of the contact area which generated the strong vibration waves [9]. This will be form instabilities before the structure started develop the crack point at the cutting tool especially in contact area. These instabilities results also form existence of plastic deformation and propagation of crack.

In high speed of cutting of cutting it is noticeable, the rate of increment of vibration energy via increment depth of cut is higher compared to vibration energy produced in lower speed turning. This shown the vibration energy is significant increment as the spindle speed increase. During free run or turning with cutting process, shown the vibration produced at low speed is relatively small due to damper of the rotating motor. In other way, increasing the spindle speed will be increase the lathe machine vibration internally. This discovery useful to re-location test and identified the suitable vibration damper pad to reduce the machine vibration in high speed operation.

When the cutting tool touches the turning specimen it creates vibrations due to the roughness of the specimen. Once cutting tool touches that point, the oxide layer of specimen establish the friction and produced the vibration wave. This scenario will be happen for all speed of spindle and vibration energy increased in trend of exponential. This trend almost same for cutting process with the different depth of cut. In other part, increasing of vibration energy it is directly proportional to temperature of heat release. It is clearly shown between good cutting tool and worm cutting tool.

#### 4. Conclusion

In this study, the experiment was mainly to study the mechanical behavior of the cutting tool during turning, the relationship of cutting speed and depth of cut to the tool wear by analyzing vibration wave and for early detection of tool wear. However, the differences values and trend of maximum amplitude and vibration energy does give us an overview of the effect of the cutting speed and the depth of cut which related to the tool wear. There are two important similarities can be observed by this experiment. The minimum tool wear occurs at the optimum cutting speed and optimum depth of cut since the vibration energy is directly proportional to the tool wear.

#### References(11 PT)

- [1]. S. Kalpakjian, and S. Schmid, *Manufacturing Process for Engineering Materials*, New Jersey, USA: Pearson Education, 2017, 6th Editions.
- [2]. R. F. Brito, S. R. Carvalho, S. M. M. L. Silva, and J. R. Ferreira, "Thermal Analysis in Coated Cutting Tools," *Int. Communications in Heat and Mass Transfer*, vol. 36 (4), pp. 314-321, April 2009
- [3]. Y. Cerci, P. Pemiroioglu, I. Bogrekei, C. Denis, and N. M. Durakbasa, "Case Study in Thermal and Wear Analysis for Cutting Tool," in *Proc. 11th Int. Symposium on Measurement and Quality Control*, 2013.
- [4]. M. P. Groover, *Principles of Modern Manufacturing*, USA: John Wiley and Sons, 2013, 5th Editions.
- [5]. W. Rmili, R. Serra, A. Ouahabi, C. Gontier, and M. Kisio, "Tool Wear Monitoring in Turning Process Using Vibration Measurement," in *Proc. 13th Int. Congress on Sound and Vibration*, 2008.

- 
- [6]. S. Orhen, A. Osman, N. Camuscu, and E. Aslan, "Tool Wear Evaluation by Vibration Analysis during End Milling of AISI D3 Cold Work Tool Steel with 35 HRC Hardness," *NDT&E Int.*, vol. 40 (2), pp 121-126, 2007.
- [7]. M. S. H. Bhuriyan, and I. A. Choudhury, "Investigation of Tool Wear and Surface Finish by Analyzing Vibration Signals in Turning Assab-705 Steel," *Marching Sensor and Technology*, vol. 19 (2), pp 236-251, 2015.
- [8]. B. Chen, "Reliability estimate for cutting tools based on logistic regression model using vibration signals," *Journal of Mechanical Systems and Signal Processing*, vol. 25 (7), pp 2526-2537, 2011.
- [9]. D. E. Dimla, "The Correlation of Vibration Signal Features to Cutting Tool Wear in a Metal Turning Operation," *The Int. Journal of Advanced Manufacturing Technology*, vol. 19 (10), pp 705-713, 2002.

## A high resolution DDFS design on VHDL using Bipartite Table Method

Yunus Emre ACAR<sup>1</sup>, Ercan YALDIZ<sup>1</sup>

<sup>1</sup>Departement of Electrical and Electronics Engineering, Selcuk University

---

### Article Info

#### Article history:

Received May 29<sup>th</sup>, 2017

Revised Aug 20<sup>th</sup>, 2017

Accepted Oct 18<sup>th</sup>, 2017

#### Keyword:

Bipartite Table Method  
Quadratic Compression  
DDFS  
DDS  
VHDL

---

### ABSTRACT

In this study, a Look Up Table (LUT) based Direct Digital Frequency Synthesizer (DDFS) is designed on VHDL. Bipartite Table Method, an advance memory compression method, is used together with quadratic compression method. 23 mHz frequency resolution is achieved with 100MHz clock input. The required memory is obtained 585 times smaller than traditional DDFSs. A MATLAB code is revealed to select the best design which provides the smallest required memory for 100 dB Spurious Free Dynamic Range (SFDR) level. The contents of the LUTs are also evaluated by using MATLAB software. The design is simulated for multiple frequencies between 23mHz-30MHz with VIVADO 2016.3 software. The simulation results perfectly match with calculations.

---

#### Corresponding Author:

Yunus Emre ACAR,  
Departement of Electrical and Electronics Engineering,  
Selcuk University, Alaeddin Keykubat Campus, 42075, Selcuklu, Konya, TURKEY.  
Email: [yacar@selcuk.edu.tr](mailto:yacar@selcuk.edu.tr)

---

### 1. Introduction

Frequency synthesizers are the systems that generate signals with new frequencies from one or more reference signal. In the history of frequency synthesizers, several approaches are proposed to synthesize new frequencies and these approaches are divided in three major groups. These are Direct Analog, Direct Digital and Indirect Frequency Synthesizers.

Direct Digital Synthesis is the one which provides fast switching speed, very high frequency resolution, low phase noise, ease to control output frequency precisely and utilized in several areas such as communication [1]-[3] test and measurement systems [4], [5], image processing [6] and medical applications [7].

A typical Direct Digital Frequency Synthesizer (DDFS) uses ROMs as Look Up Tables (LUTs) to convert the phase values to amplitude values. The ROMs contains the digital samples of the desired signal form. A counter is used as a phase accumulator. The phase accumulator controls the frequency of the output signal with a digital Frequency Tuning Word (FTW). The word changes the step size of the address counter of the ROM. Thus, the desired frequency is adjusted digitally. The output frequency is evaluated by the following equation where  $f_{clk}$  is the reference clock signal and  $2^N$  is the number of phase values on the counter.

$$f_{out} = FTW \times \frac{f_{clk}}{2^N} \quad (1)$$

A Digital to Analog Converter (DAC) is used to get the analog signal. Principle stages of a DDFS are given in Fig. 1.

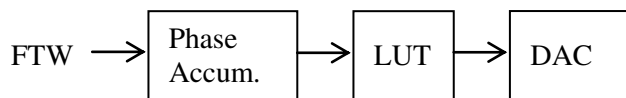


Figure 1. Principal stages of a traditional LUT based DDS

In DDS designs, many improvements are revealed to achieve better spectral performance [8], lower power dissipation [9], [10], higher frequency resolution [11] and smaller required area [12]-[14].

This paper presents a high resolution, LUT based DDS design on VHDL. Bipartite Table Method (BTM) which is offered by Dinechin and Tisserand in 2005 is used to lessen the LUT size while keeping the Spurious Free Dynamic Range (SFDR) above 100 dB.

### 1.1. LUT Based DDSs

In DDS, the phase to amplitude conversion is done in several ways. LUT based [12]-[14], iterative approaches [15] and LUT free approaches [16] are the most common ones of these ways. LUTs are the tables that store the sampled data of a signal form. The size of the LUT determines the resolution and the spectral performance of the signal to be generated. Table 1 shows the content of a 32x8 bits LUT for a sine.

Table 1. Contents of a typical 32x8 bits LUT for a sine

0	49	71	91	106	118	126	128
126	118	106	91	71	49	25	0
-25	-49	-71	-91	-106	-118	-126	-128
-126	-118	-106	-91	-71	-49	-25	0

As shown from the Table 1, the LUT stores 32 digital data represented with 8 bits signed numbers. When a sine is generated from this small LUT, the approximate SFDR value of the generated signal is evaluated as 53.62 dB with the *sfdr(x)* command in MATLAB. Although the spectral performance seems good, the phase and amplitude resolutions are both unsatisfactory. The generated sine is shown in Fig. 2.

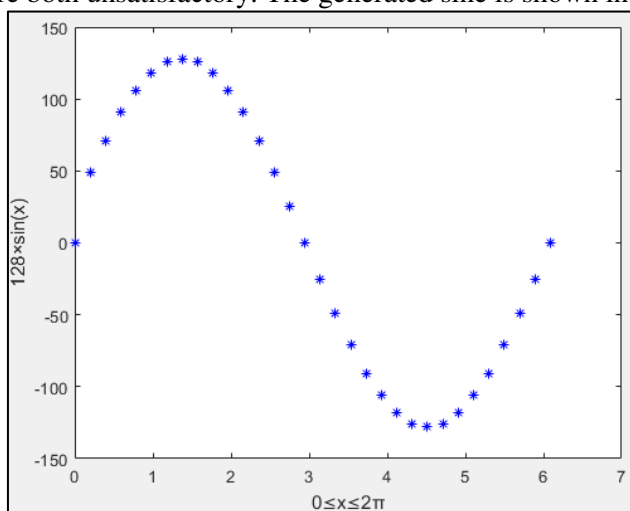


Figure 2. The sine generated from the 32x8 bits LUT

The increase in resolution or spectral performance requires an increase in the LUT size. De Caro and his friends claim that their design requires only 208 bits to provide higher SFDR level with 11 bits phase and 9 bit amplitude resolution. To obtain this much phase and amplitude resolution, a 18,432 bits-LUT is required in a traditional DDS structure. There are several LUT based studies providing 100 dBc and higher SFDR levels with very high phase and amplitude resolution [14], [17]. The common idea behind these studies is to compress the ROM size as much as possible while keeping the SFDR level and the resolutions good enough. In this design, BTM is used to compress the ROM while keeping the SFDR above the predetermined levels.

## 2. Method

### 2.1. Bipartite Table Method (BTM)

In this part of the paper BTM which is the one of the LUT based approaches is introduced. The method uses piecewise linear approach. In this method two different LUT is used. Firstly,  $2^a$  initial values are evaluated and stored in the first LUT. This table is called table of initial values (TIV). Fig. 3 shows the initial values for the one fourth of a sine period for 32 initial values with the 8 bit amplitude resolution (R). The TIV size is calculated as

$$TIV_{size} = R \times 2^a \quad (2)$$

Secondly, some offset values are evaluated and stored in the second LUT. The table is called as table of offsets (TO). The TO values are calculated by using piecewise linear approach with the following equations.

$$m_i = \frac{f(x_{i+1}) - f(x_i)}{x_{i+1} - x_i} \quad (3)$$

$$f(x) = m_i (x - x_i) \quad (4)$$

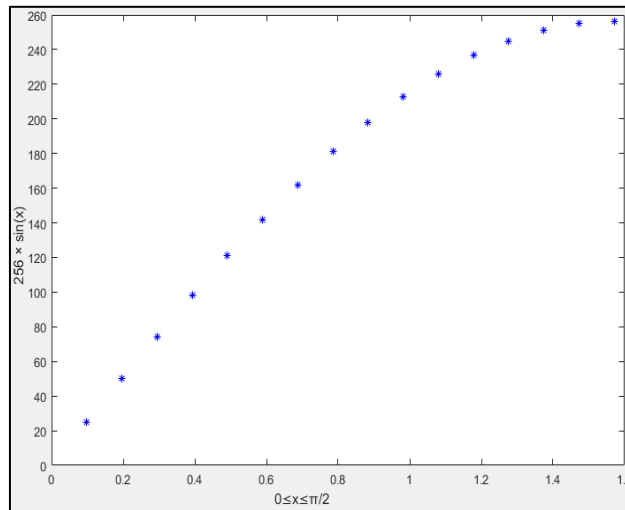


Figure 3. The initial values for the one fourth of sine period

In BTM, the idea is to use same slope value for some adjacent points. Thus, the  $x$  axis is divided into  $2^b$  equal intervals where  $b < a$ . The same slope value is used for the  $2^{a-b}$  adjacent points in each  $2^b$  interval. The TO size is calculated as

$$TO_{size} = (R - a) \times 2^{b+c} \quad (5)$$

where  $2^c$  is the number of offset value for each initial value. Fig. 4 gives the approximated  $\sin(x)$  where  $0 \leq x \leq \pi/2$  with BTM. The function is evaluated as

$$f_{app}(x) = TIV(x) + TO(x) \quad (6)$$

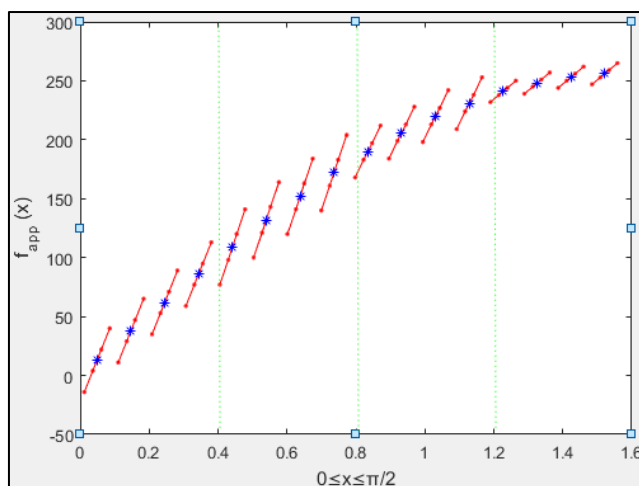


Figure 4. Approximated sine using BTM with R=8, a=4, b=2, c=2

As previously mentioned, LUT stage of a DDS converts the phase value from the phase accumulator to amplitude values. To do this, it uses the P bit phase information as the address counter of both the TIV and the TO. First a bits of the word is used for the TIV, and the rest c bits and the most significant b bits of the word is also used for the TO. The decomposition of phase the word is given in Fig. 5.

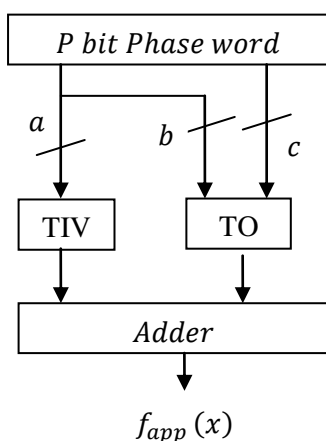


Figure 5. Phase word decomposition

### 3. Design

In this study, BTM was used together with the quadrant compression technique which uses the sine symmetry. In this technique, only one fourth of a sine sampled data is stored in the tables, and the rest of the function is generated by using these values.

#### 3.1. Phase Accumulator

A 32 bit counter is created as the phase accumulator. The counter counts with every rising edge of the clock signal up to  $2^N$ . FTW, the step size of the counter, changes the output frequency of the DDS. The 32 bit counter value is truncated to 20 bits. The most significant 2 bits of these data is used to generate the hidden quarters of the sine values, and the rest represents the 18 bit phase word. The block scheme of the counter is given in Fig. 6.

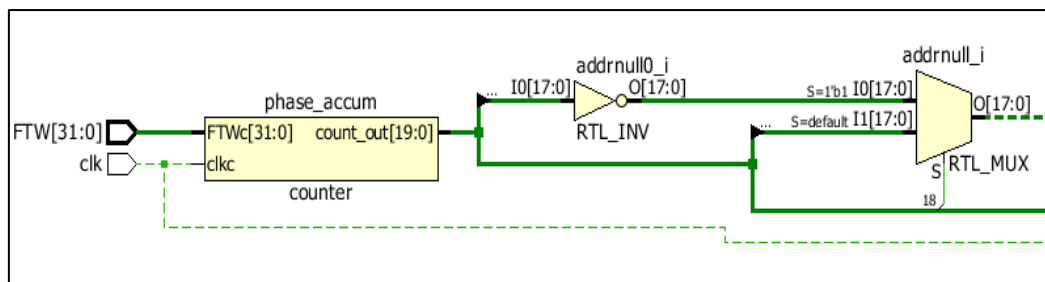


Figure 6. Block scheme of the counter

### 3.2. Best Decomposition of the Phase Word

The goal is to design a DDFS with 18 bits phase and 16 bits amplitude resolution and a SFDR level over 100 dB. An algorithm is created to find out the best decomposition of the phase word to obtain the target SFDR with the minimum size of the required memory. The Matlab code of the algorithm is given in Fig. 7. By using the algorithm, the parameters a, b and c are found as 10, 3 and 8, respectively.

```

R=16; %% The amplitude resolution
Q=18; %% The phase word to address the tables
a_max=Q-2;
a_min=round(Q/2);
desired_SFDR=100;
parameters=[R Q 0 0]; %% [R Q a b]
b_min=2;
min_size=R*2^Q; %% possible max table size
%% for each (a,b) pair calculate sfdr and total table size
for i=a_min:a_max
    parameters(3)=i;
    for j=b_min:parameters(3)
        parameters(4)=j;
        [SFDRx,size]=calculations(parameters);
        if SFDRx>desired_SFDR
            if size<min_size
                min_size=size;
                best_decomposition=parameters;
                obtained_SFDR=SFDRx;
            end
        end
    end
end
end
    
```

Figure 7. Matlab code of the best decomposition algorithm

### 3.3. LUTs (Phase to Amplitude Conversion)

As the phase to amplitude conversion stage, two Block Random Access Memories (BRAMs) are used. The dimensions of the tables are determined as  $16 \times 2^{10}$  and  $6 \times 2^{11}$  with the equations (2) and (5). The block scheme of the phase to amplitude part is given in Fig. 8. The contents of the tables are evaluated by using a MATLAB code. The code is given in Fig. 9.

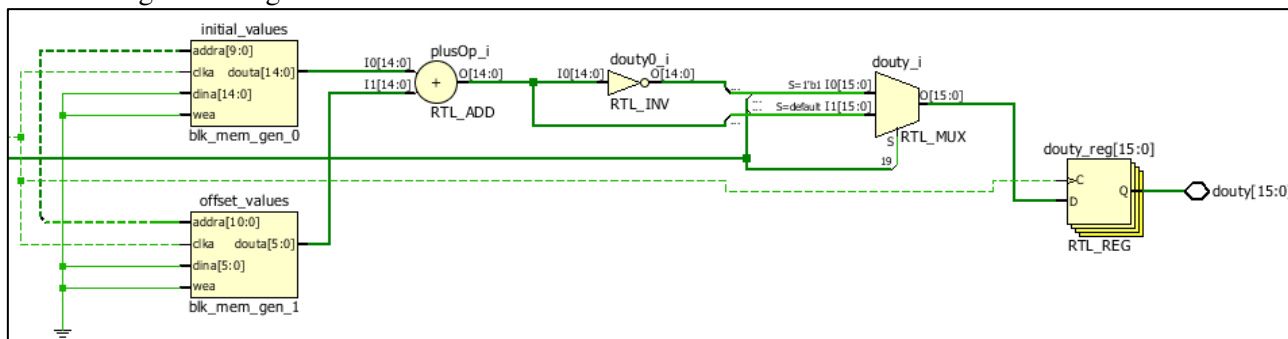


Figure 8. Block scheme of the phase to amplitude conversion stage

```

s=2^a;
max_genlik=(2^R)-1;
x_incr=(pi/2)/s;
x_incr_TO=x_incr/2^b;
K=2^(a-c);
x(1)=0;
y(1)=round(max_genlik*sin((x(1)+x_incr/2)));

for i=1:s
    x(i+1)=x(i)+x_incr;
    y(i+1)=round(max_genlik*sin((x(i+1)+x_incr/2)));
    m(i)=(y(i+1)-y(i))/(x(i+1)-x(i));
end
for i=1:s/K;
    sum=0;
    for j=1:K
        sum=m((i-1)*K+j)+sum;
    end
    M(i)=sum/K;
end
for i=1:2^c
    for j=1:2^b
        TO(i,j)=round((-M(i)*x_incr/2+M(i)*j*x_incr_TO));
    end
end
k=1;
for i=1:2^c
    for j=1:2^(a-c)
        TIV(i,j)=floor(y(k));
        k=k+1;
    end
end
end

```

Figure 9. MATLAB code to evaluate the LUT contents

#### 4. Simulation Results

The created design is simulated in VIVADO 2016.3 software. The design is tested under 100 MHz and 400 MHz reference clock input. The output frequency is adjusted to various frequencies between 23 mHz and 30 MHz. FTW is calculated by (1). Table 2 gives some FTW values for some frequencies.

Table 2. FTW values for some frequencies

$f_{clk}$	FTW		$f_{out}$	$T_{out}$
	Decimal	hex		
100 MHz	1	1	23 mHz	43.48 s
	43	2B	1 Hz	1 s
	42950	A7C6	1 kHz	1 ms
	42949673	28F5C29	1 MHz	1 $\mu$ s
	214748365	CCCCCD	5 MHz	200 ns
400 MHz	107374182	6666666	10 MHz	100 ns
	214748365	CCCCCD	20 MHz	50 ns
	322122547	13333333	30 MHz	33.3 ns

The output signal is named as *douty* in the design. The signal has 4.5 clock delay which is 45 ns for 100 MHz input and 11.25 ns for 400 MHz input. The input clock has 1  $\mu$ s delay. Thus, the period of the *douty* is showed between two markers. The blue one is the start of the signal and fixed at 1045 ns. The yellow one is the end of the signal and fixed at the last digital value of the *douty* for one period. The figures Fig.10 to Fig.16 show that the period of the *douty* is exactly same with the calculations.

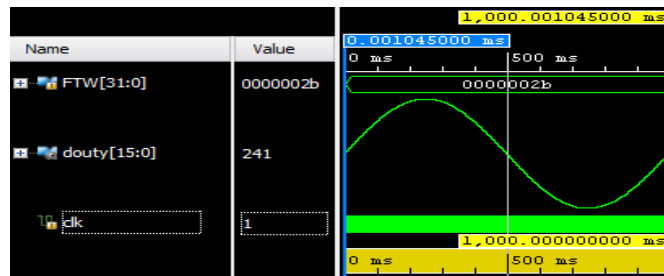


Figure 10. The Generated 1 Hz sine wave (clk =100 MHz)



Figure 11. The Generated 1 kHz sine wave (clk =100 MHz)

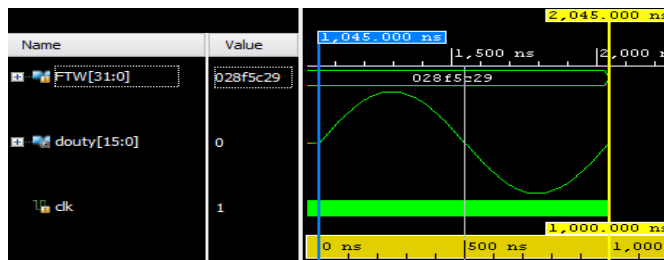


Figure 12. The Generated 1 MHz sine wave (clk =100 MHz)

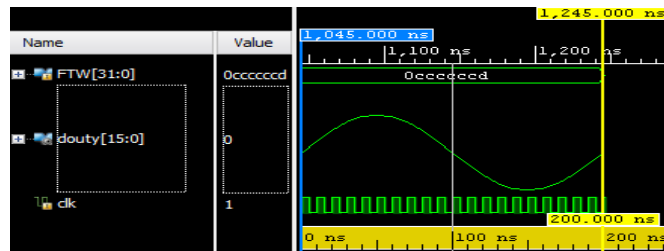


Figure 13. The Generated 5 MHz sine wave (clk =100 MHz)

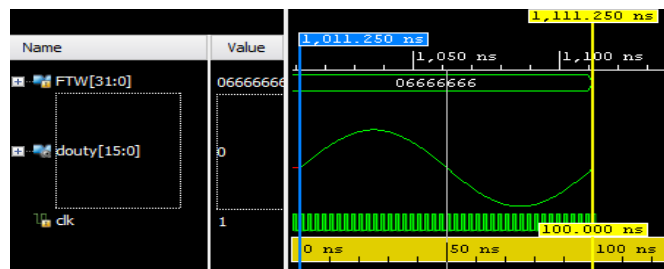


Figure 14. The Generated 10 MHz sine wave (clk =400 MHz)

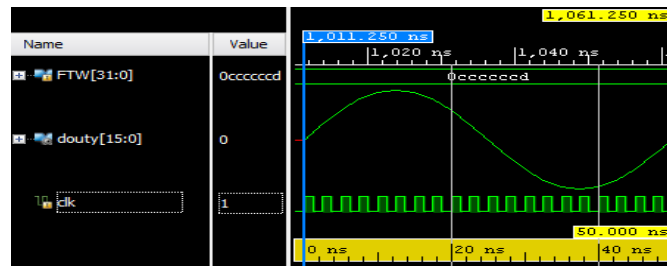


Figure 15. The Generated 20 MHz sine wave (clk =400 MHz)

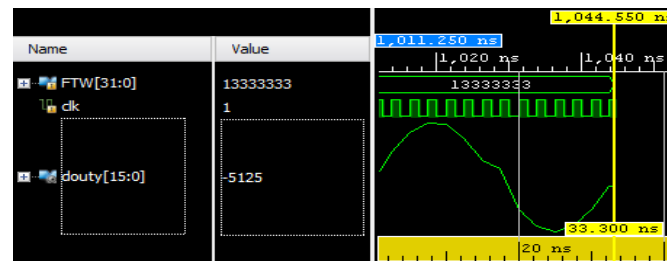


Figure 16. The Generated 30 MHz sine wave (clk =400 MHz)

## 5. Conclusion

A LUT based DDFS design has been proposed in this study. Bipartite table method and quadratic compression method are used together to lessen the LUT size. Firstly, the DDFS is briefly introduced and BTM is handled. Later on, the details of the design is focused, block schemes and related codes are given. Finally, simulation results of the design are shared.

The design provides 100 dB SFDR level with the LUTs whose size are  $16 \times 2^{10}$  and  $6 \times 2^{11}$ , respectively. 32 bit phase and 16 bit amplitude resolution are also provided. By using BTM and quadratic compression method, the LUT size is less than 585 times than a traditional DDFS which provides the same SFDR and resolution values. The design is tested with 100 MHz and 400 MHz input clocks. The output frequency is adjusted between 23 MHz and 30 MHz. Noticeable distortions are observed for 30 MHz and higher frequencies.

## Acknowledgements

This study is supported by Academic Staff Training Program of Selcuk University, Konya, Turkey.

## References

- [1] C. Nie, X. Wang, H. Zhao, "W-band Transceiver Design of FMCW Radar with High Resolution", *5th IEEE International Symposium on Microwave, Antenna, Propagation and EMC Technologies for Wireless Communications*, 2013, pp. 691-693.
- [2] A. Al Safi, B. Bazuin, "FPGA Based Implementation of BPSK and QPSK Modulators Using Address Reverse Accumulators", *IEEE 7th Annual Ubiquitous Computing, Electronics & Mobile Communication Conference (UEMCON)*, 2016, pp. 1-6.
- [3] D. Sarriá, O. Pallarés, J. del-Río Fernández, A. Manuel-Lázaro, "Low Cost OFDM Based Transmitter for Underwater Acoustic Communication", *MTS/IEEE OCEANS, Bergen*, 2013, pp. 1-4.
- [4] S. Yunxia, C. Bingyan, Z. Juan, T. Yingying, G. Yuan and S. Minglei, "Design of Time-Delay Detection Equipment for Signal Circuit", *12th International Conference on Electronic Measurement & Instruments*, 2015, pp. 824-830.
- [5] C. Lv, D. Fan, B. Shi, W. Wang and Z. Liu, "A Distortion Tester of Geophone Based on FPGA", *IEEE International Conference on Automation and Logistics (ICAL)*, 2009, pp. 1289-1092.
- [6] X. Cheng, H. Zhao, Y. Dai and X. Liu, "Image Acquisition Design of the AOTF Imaging Spectrometer Based on SOPC", *International SoC Design Conference (ISOCC)*, 2011, pp. 266-269.

- [7] K. Peng ,X. Liu and P. Huang, “Study on The Wireless Energy Supply System in The Implantable Cardiac Pacemaker”, *6th International Conference on Intelligent Systems Design and Engineering Applications (ISDEA)*, 2015, pp. 778-781.
- [8] R. Storch and T. Musch, “Synthesis Concepts of Signals With High Spectral Purity for the Use in Impulse Radar Systems”, *IEEE Transactions on Instrumentation and Measurement*, vol. 64, pp. 2574-2582, Sept. 2015.
- [9] S. Thuries, E. Tournier and J. Graffeuil, “A 3-bits DDS Oriented Low Power Consumption 15 GHz Phase Accumulator in a 0.25  $\mu\text{m}$  BiCMOSSiGe:C Technology”, *13th IEEE International Conference on Electronics, Circuits and Systems (ICECS)*, 2006, pp. 991-994.
- [10] H. Jafari, A. Ayatollahi, and S. Mirzakuchaki, ” A Low Power, High SFDR, ROM-less Direct Digital Frequency Synthesizer”, *IEEE Conference on Electron Devices and Solid-State Circuits*, 2005, 829-832.
- [11] S. Yanbin, G. Jian and C. Ning, “High Precision Digital Frequency Signal Source Based on FPGA”, *International Conference on Solid State Devices and Materials Science*, 2012, pp. 1342-1347.
- [12] F. Dinechin and A. Tisserand, “Multipartite Table Methods”, *IEEE Transactions On Computers*, vol.54, pp. 319-330, Mar. 2005.
- [13] A. G. M. Strollo, D. De Caro and N. Petra, “A 630 MHz, 76 mW Direct Digital Frequency Synthesizer Using Enhanced ROM Compression Technique”, *IEEE Journal of Solid-State Circuits*, vol.42, pp. 350–360, Feb. 2007.
- [14] D. De Caro, N. Petra, and A. G. M. Strollo, “Reducing Lookup-Table Size in Direct Digital Frequency Synthesizers Using Optimized Multipartite Table Method”, *IEEE Transactions On Circuits And Systems*, vol.55, pp. 2116-2127, Aug. 2008.
- [15] T. Menakadevi and M. Madheswaran, “Direct Digital Synthesizer using Pipelined CORDIC Algorithm for Software Defined Radio”, *International Journal of Science and Technology*, vol. 2, pp.372-378, June 2012.
- [16] Y.H. Chen and Y. A. Chau, “A Direct Digital Frequency Synthesizer Based on a New Form of Polynomial Approximations”, *IEEE Transactions on Consumer Electronics*, vol.56, pp. 436-440, May. 2010.
- [17] Y. Song and B. Kim, “A 14-b Direct Digital Frequency Synthesizer With Sigma-Delta Noise Shaping”, *IEEE J. Solid-State Circuits*, vol. 39, no. 5, pp. 847–851, May 2004.

# Numerical Modelling of the In-Plane Loaded Homogenized Masonry Walls

Sedat Kömürçü<sup>1</sup>, Abdullah Gedikli<sup>2</sup>

<sup>1</sup>Department of Civil Engineering, Istanbul Technical University

<sup>2</sup>Department of Civil Engineering, Istanbul Technical University

---

## Article Info

### Article history:

Received May 30<sup>th</sup>, 2017

Revised Aug 20<sup>th</sup>, 2017

Accepted Oct 18<sup>th</sup>, 2017

---

### Keyword:

Crack

Fracture

Homogenization

Masonry

Modelling

---

## ABSTRACT

Masonry structures are one of the oldest structures in the world and have a considerable place among all the structures. Modelling of the masonry structures has become a significant requirement to evaluate the strengths of existing masonry structures and to build modern masonry structures. In this study, in-plane behaviors of the walls which constituting masonry structures are numerically modelled and analyzed. The homogenization technique is applied to obtain the material parameters used in the models. Unreinforced solid masonry wall and masonry wall with an opening are analyzed. The propagations of the cracks which may occur under the in-plane loads on the walls are investigated numerically. Fracture mechanisms occurring in the walls under the effect of in-plane loads are determined as a result of the analyzes.

---

### Corresponding Author:

Sedat Kömürçü,

Department of Civil Engineering,

Istanbul Technical University,

Ayazağa Campus Civil Engineering Faculty Building, Maslak, 34469 Sarıyer / Istanbul

Email: komurcus@itu.edu.tr

---

## 1. Introduction

Masonry is a composite material that consists of units and mortar. It is necessary to model and analyze the masonry structures to understand them which exposed to many natural hazards especially earthquakes and to construct safe and modern masonry structures. There are several modelling techniques for modelling of walls constituting the masonry structures. Homogenous modelling techniques are suitable and widespread techniques reflecting general masonry behavior. In this study, nonlinear behaviors of walls under the effect of in-plane loads are numerically modelled and analyzed. The homogenization technique is used to model the masonry walls with their composite structures. Masonry walls were modelled and analyzed to determine the fracture mechanisms of the walls. In addition, in-plane behaviors of unreinforced masonry walls were analyzed numerically.

There are many studies about homogenous modelling of masonry structures. Researches have worked for producing homogenous damage models for masonry structures. The effects of in-plane effects on the masonry walls have been investigated by many scientists. Masonry units and mortar are modelled as a single material in the macro modelling technique. The macro modelling technique was studied in [1] and [2]. Researches were created orthotropic damage models in studies [3] and [4]. Lourenço worked on computational modelling of masonry structures using macro modelling technique [5]. Oller were studied on the numerical modelling of masonry walls [6]. Masonry panel wall behavior was studied in [7] and numerical study about strength of masonry was presented in [8]. Macro modelling is a significant modelling method for masonry structures and studies have continued to model masonry walls with homogeneous techniques.

## 2. Homogenization of Masonry Walls

Modelling of the masonry walls is a special issue because of the different characteristics of masonry units and mortar. There are various techniques to characterize structural behavior of masonry. Masonry structures can be generally modelled as heterogeneous and homogeneous models. Macro modelling technique is known as homogeneous modelling technique. Masonry units (brick, stone etc.) and mortar are represented as a single material with homogenization of masonry wall parts. The homogenous modelling procedure is shown in Figure 1. Composite structure is produced after the homogenization process.

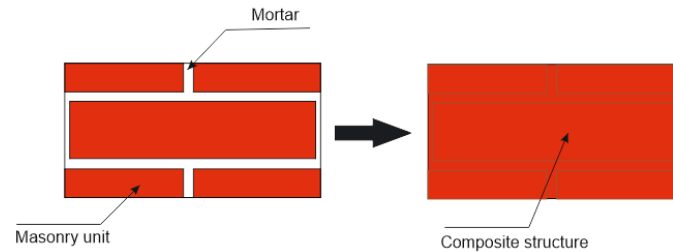


Figure 1. Macro modelling procedure.

Masonry walls are composite structures that can be homogenized using advanced techniques according to the macro modelling technique. It is beneficial to use masonry wall parts which periodically repeat themselves on the wall to model the masonry walls by homogenization. Some periodically repeated masonry wall parts that can be used for homogenization are shown in Figure 2. All the numbered wall parts in Figure 2 is called as elementary wall parts.

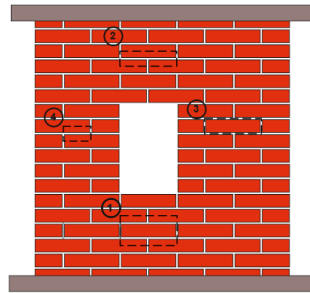


Figure 2. Determination of periodically repeated elementary wall parts.

Elementary wall parts are shown in Figure 3. These elementary wall parts can be used to determine material parameters of the masonry wall using in numerical analysis.

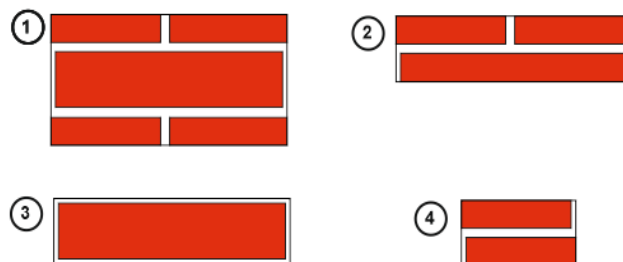


Figure 3. Elementary wall parts.

Homogenization procedure is applied on an elementary wall part. Application of the homogenization technique is shown in Figure 4. There are two different directions to apply homogenization because of the orthotropic structure of the masonry walls. Elementary wall part can be divided into continuous parts both vertically and horizontally. Finally, a composite structure is obtained at the end of the homogenization procedure.

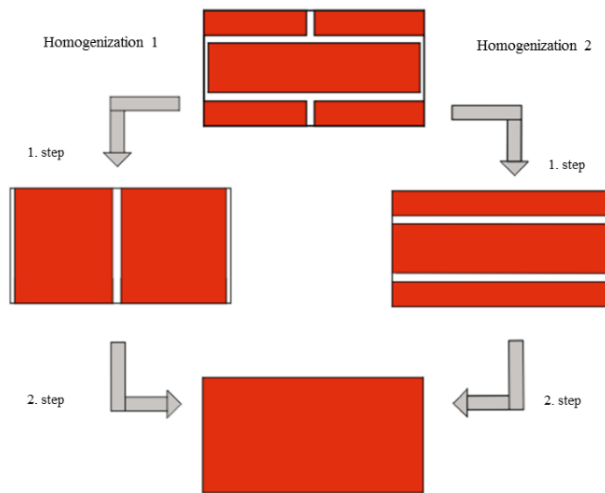


Figure 4. Application of the homogenization technique.

### 3. Finite Element Models of Homogenized Masonry Walls

In this study, finite element analysis was performed in ANSYS software by using homogenization technique on unreinforced masonry walls without and with an opening. Experimental studies were used to build numerical models in the literature [9], [10]. The periodically repeated masonry wall part used in the analysis and the masonry unit using in the wall are shown in Figure 5.

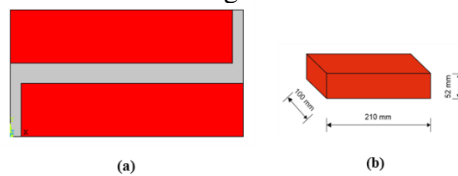


Figure 5. (a) Elementary wall part (b) Masonry unit.

Elementary wall part was divided to slices as shown in Figure 6.

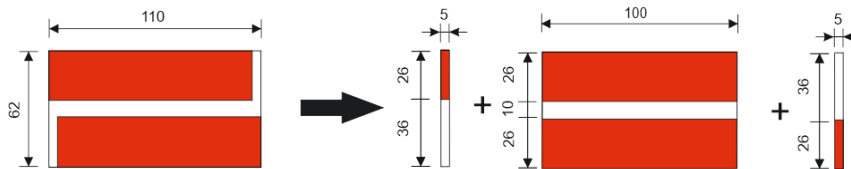


Figure 6. Slicing of the elementary wall part.

All the material units in the slices which obtain from the masonry elementary wall part can be considered as elastic springs as shown in Figure 7.

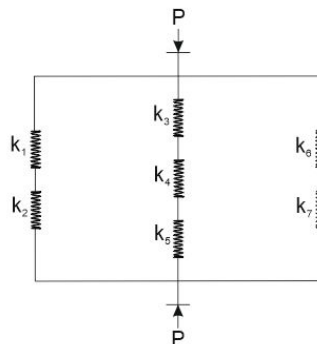


Figure 7. Spring representation of the elementary wall part.

The modulus of elasticity of the homogenized wall can be calculated by using spring model. SOLID 65 finite element in the ANSYS software was used for the finite element analysis. This element has 8 node points and each node point has 3 displacement degree of freedom in x, y and z directions. It can

showcollapsemechanismsboth tensile andcompression. Brittlematerials can be modelledsuch as rock, stone, brick, concreteetc. This element is suitableformodelling of nonlinearbehavior of structuresandcracks can be determined in thestructure. Thestructure of the SOLID 65 element is shown in Figure 8.

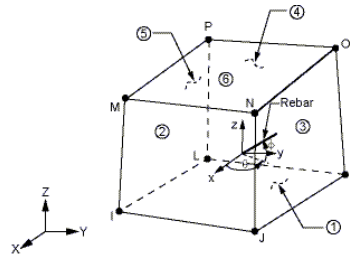


Figure 8. SOLID 65 element.

Materialparametersused in themodelsareshown in Table 1. Wall materialparameterswereobtainedwithhomogenization of themasonrywallandwereimplementedtothefinite element model.

Table 1. Material properties.

Material	Modulus of Elasticity [MPa]	Poisson's Ratio	Tensile Strength [MPa]	Compressive Strength [MPa]
Brick	16700	0.15	2	10.5
Mortar	780	0.15	0.25	3
Wall (Homogenous)	3655	0.15	0.25	9

In the numerical analysis, the Willam-Warnke fracture hypothesis is used for nonlinear behavior of the masonry wall. Willam-Warnke hypothesis is a suitable hypothesis for materials having different compressive strength and tensile strength such as masonry materials. The wall is loaded in two steps. In the first load step, the wall was loaded with a vertical pressure of 0.3 MPa to top nodes of the wall. In the second load step, horizontal displacement is given to the top nodes of the walls. The first load step is implemented by dividing by 10 equal sub-steps. The second load step is divided into 40 sub-steps.

### 3.1. Masonry Wall without Opening

In ANSYS software the geometry of the masonry wall was created by using the macro modelling technique. Masonry units and mortar were produced as a single material. Figure 9 shows the geometry and loading for the masonry wall without opening.

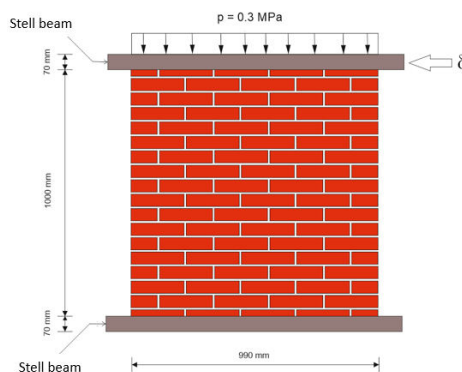


Figure 9. Masonry wall geometry and loading.

Total displacement at the end of the 1. load step, minimum principal stresses at the end of the 1. load step, minimum principal stresses at  $\delta=1$ , total displacement at  $\delta=1$ mm and shear stresses at  $\delta=1$ mm are shown in Figure 10. Continuous stress distribution is determined between the bricks and mortar.

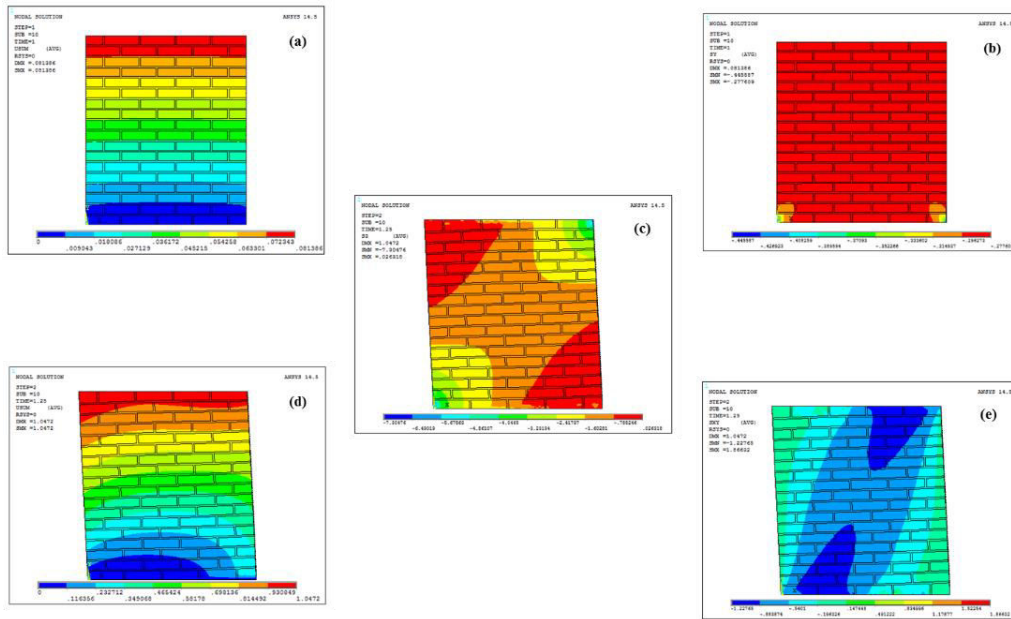


Figure 10. Masonry without opening: (a) total displacement at the end of the 1. load step, (b) minimum principal stresses at the end of the 1. load step, (c) minimum principal stresses at  $\delta=1$ , (d) total displacement at  $\delta=1$ mm, (e) shear stresses at  $\delta=1$ mm.

The crack distribution of the unreinforced masonry wall from  $\delta=0.1$  mm to  $\delta=1$  mm is given in Figure 11. Continuous cracks are obtained with the macro modelling technique according to finite element analysis.

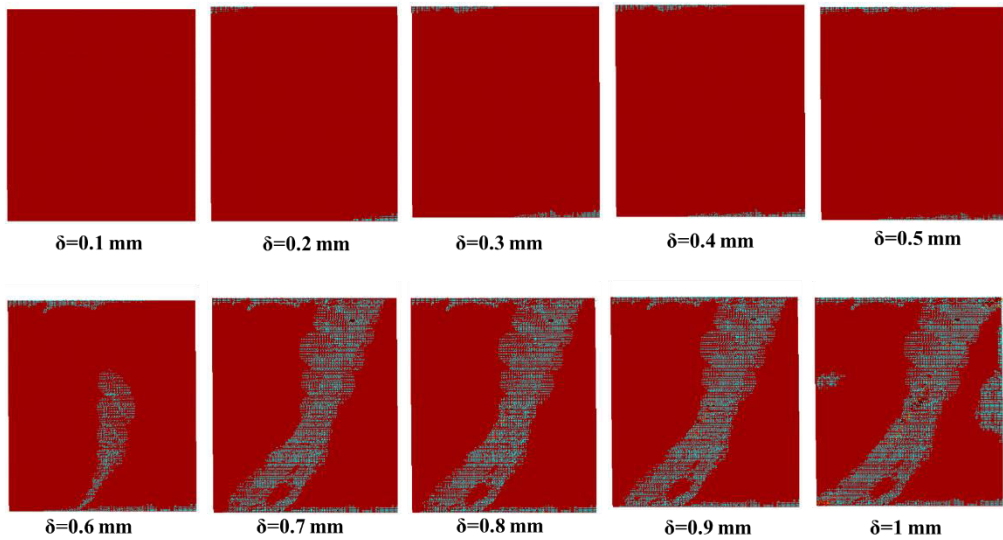


Figure 11. Crack distributions for masonry wall without opening.

It is seen that the cracks first started from the upper left and lower right corners of the wall. Next, diagonal cracks occurred on the wall.

### 3.2. Masonry Wall with an Opening

Second homogenization example worked on the masonry wall with an opening. Figure 12 shows the geometry and loading for the masonry wall with an opening.

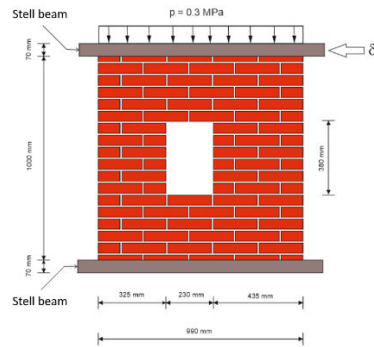


Figure 12 . Masonry wall with an opening geometry and loading.

Total displacement at the end of the 1. load step, minimum principal stresses at the end of the 1. load step, minimum principal stresses at  $\delta=1$ , total displacement at  $\delta=1$ mm and shear stresses at  $\delta=1$ mm according to finite element analysis are shown in Figure 13.

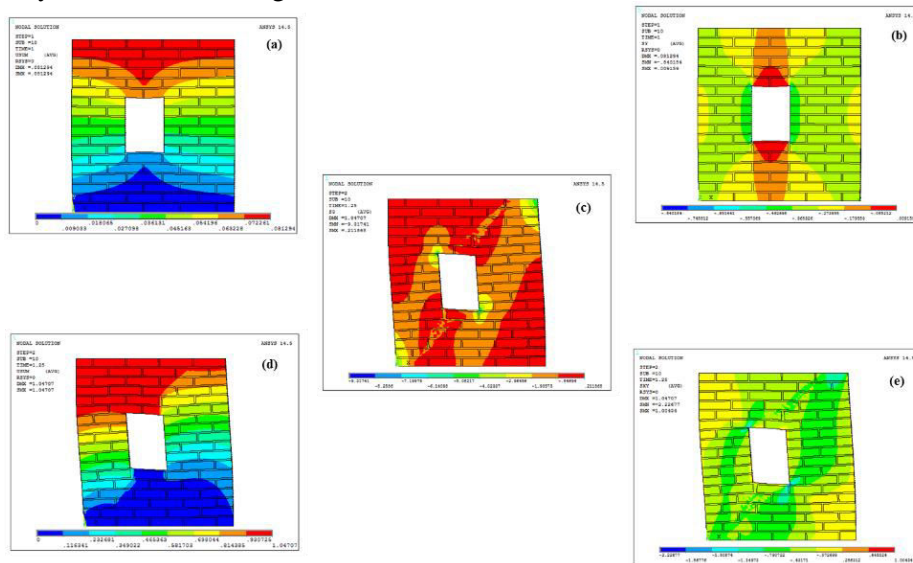


Figure 13 . Masonry with opening: (a) total displacement at the end of the 1. load step, (b) minimum principal stresses at the end of the 1. load step, (c) minimum principal stresses at  $\delta=1$ , (d) total displacement at  $\delta=1$ mm, (e) shear stresses at  $\delta=1$ mm.

The crack distributions of the unreinforced masonry wall with an opening are given from  $\delta=0.1$  mm to  $\delta=1$  mm in Figure 14.

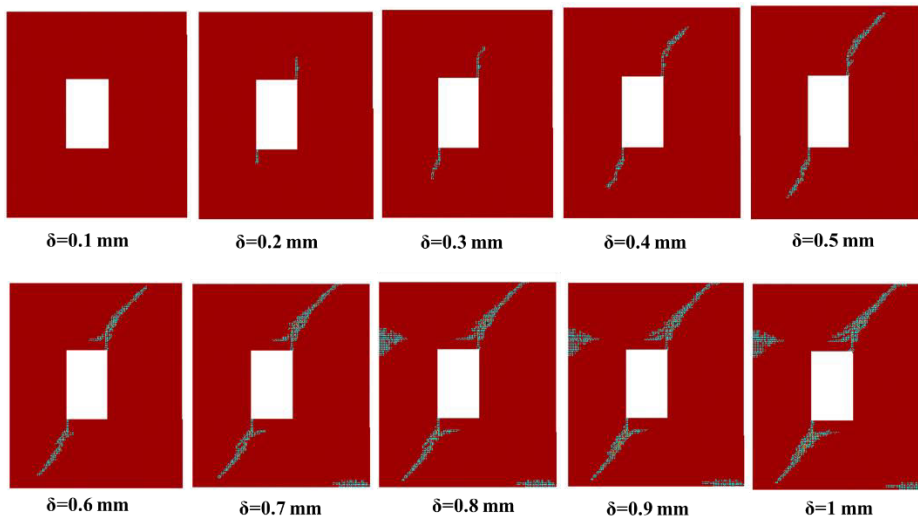


Figure 14 . Crack distributions for masonry wall with opening.

It is seen that the cracks first started from the lower left and upper right corners of the gap in the wall. In addition to the diagonal cracks on the wall, cracks are formed in the lower right part of the wall and in line with the upper left part of the opening. Finally, diagonal cracks spread to the left lower and right upper portions of the wall. And horizontal cracks spread towards to upper left and lower right corner of the wall. Finally, failure mechanism of the masonry wall with an opening idealized as four rigid blocks connected by four joints.

**4. ResultsAndDiscussion**

In this study, unreinforced masonry walls without and with an opening were modelled and analyzed using finite element method. Crack distributions were investigated step by step on the walls. The reason of the cracks can be explained in terms of internal effects. Figure 15 (a) shows the reasons of the cracks on the unreinforced masonry wall. Firstly, horizontal cracks that occur in the upper left and lower right parts of the wall shown with number (1) are tensile or shear cracks. Secondly, the cracks that occur in the upper right and lower left parts of the wall shown with number (2) are compressive cracks. Next, the diagonal cracks that occur in the middle region of the wall are represented by number (3) are caused by multiple influences.

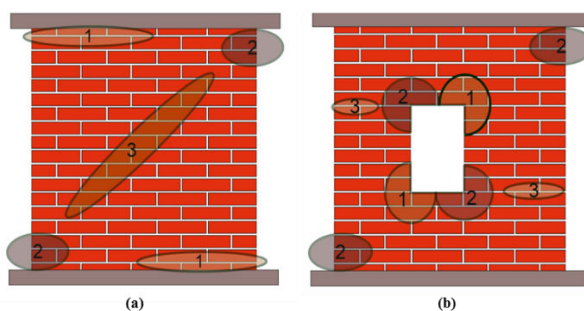


Figure 15 . The reasons of the cracks on the masonry walls.

Figure 15 (b) showsthereasons of thecracks on theunreinforcedmasonrywallwith an opening. Thecracksformed in theupperrightandleftlowercorners of thegapshownwithnumber (1) are tensile cracks. Thecracks in thelowerleftandupperrightcorners of thewallandthe cracks in thelowerrightandleftuppercorners of theopeningshownwithnumber (2) arepressurecracks. Horizontalcracksstartedfromtheedge of thewallandcontinuetowardstheopeningshownwithnumber (3) areshearcracks.

Horizontal displacement of the top of the wall and horizontal reaction force of the wall diagrams of the two wall models are shown in Figure 16. It is seen that the masonry wall without opening has higher strength than the masonry wall with opening. But, masonry wall with an opening represents more ductile behavior than the masonry wall without opening.



Figure 16 . Load – displacement curves of the masonry wall models after the analysis.

**5. Conclusion**

The modelling technique, the material model and the fracture hypothesis form a combination for the modelling of the masonry walls. In homogenous modelling technique, single material parameters are used as an average property for masonry unit and mortar. Continuous cracks can be obtained with using homogenization technique on the walls. The strength of a masonry wall with an opening is dramatically at a lower level than masonry wall without opening but masonry wall with an opening represents more ductile behavior.

## Acknowledgements

This research has been supported financially by the ITU scientific research projects unit.

## References

- [1] R.D. Quinteros, S. Oller, L.G. Nallim, “Nonlinear homogenization techniques to solve masonry structures problems,” *Composite Structures.*, vol. 94, pp. 724–730, 2012.
- [2] H.O. Köksal, B. Doran, A.O. Kuruscu, A. Kocak, “Elastoplastic finite element analysis of masonry shear walls,” *KSCE Journal of Civil Engineering.*, vol. 20, pp. 784-791, 2016.
- [3] L. Pela, M. Cervera, P. Roca, “An orthotropic damage model for the analysis of masonry structures,” *Construction and Building Materials.*, vol 41, pp. 957-967, 2012.
- [4] P.B. Lourenço, “An Orthotropic Continuum Model for The Analysis of Masonry Structures,” The Netherlands, TU Delft, Report 03-21-1-31-27, 1995.
- [5] Lourenço, “Computational Strategies for Masonry Structures” Doctoral dissertation, Delft University of Technology, The Netherlands, 1996.
- [6] S. Oller, *Numerical Simulation of Mechanical Behavior of Composite Materials*, Barcelona, Spain, Springer, 2014.
- [7] A.Th. Vermeltoort, T.M.J. Raijmakers, “Deformation controlled meso shear tests on masonry piers,” The Netherlands: Building and Construction Research, Eindhoven, Report B-92-1156, TNO-BOUWrrU, 1992.
- [8] A.Th. Vermeltoort, T.M.J. Raijmakers, “Deformation controlled meso shear tests on masonry piers,” The Netherlands: Building and Construction Research, Eindhoven, Report B-92-1156, TNO-BOUWrrU Part 2 Draft report, 1993.
- [9] L. Berto, A. Saetta, R. Scotta, R. Vitaliani, “Shear behaviour of masonry panel: parametric FE analyses,” *International Journal of Solids and Structures.*, vol. 41 pp. 4383–4405, 2004.
- [10] A. Drougkas, P. Roca, C. Molins, “Numerical prediction of the behavior, strength and elasticity of masonry in compression,” *Engineering Structures.*, vol 90, pp. 15–28, 2015.

# The Effects of Nanosilica on Charpy Impact Behavior of Glass/Epoxy Fiber Reinforced Composite Laminates

Ömer Yavuz Bozkurt<sup>1</sup>, Özkan Özbek<sup>1</sup>, Atban Rafea Abdo<sup>2</sup>

<sup>1</sup>Mechanical Engineering Department, Gaziantep University, Gaziantep, Turkey

<sup>2</sup>Ministry of Industry and Minerals, The State Company for Textile Industries and Leather Cotton Factory, Anbar, Iraq

## Article Info

### Article history:

Received May 30<sup>th</sup>, 2017

Revised Aug 20<sup>th</sup>, 2017

Accepted Oct 18<sup>th</sup>, 2017

### Keyword:

Charpy impact

Glass fiber

Nanosilica

## ABSTRACT

Desire to improve the efficiency of composite materials for engineering applications has led to the use of nano-sized additives or fillers such as nanoclay, nanosilica, nano-graphene, carbon nanotubes. The effect of nanoparticle inclusion on mechanical properties of fiber reinforced composite materials has been investigated by many researchers and crucial effects have been reported in several papers. In this work, the effects of nanosilica content on the low velocity impact behaviors of glass/epoxy fiber reinforced composite laminates are determined using Charpy impact tests. The composite laminates are fabricated via hand lay-up followed by hot press molding. The nanosilica particles with different weight percentages are dispersed in epoxy resins using mechanical stirring. The absorbed impact energy values of flatwise-unnotched and edgewise-notched beam specimens, and impact damages are analyzed as a measure of impact behavior. The results show that the incorporation of nanosilica particles have significant effects on the Charpy impact behavior.

## Corresponding Author:

Özkan Özbek,

Mechanical Engineering Department,

Gaziantep University,

27310, Gaziantep, Turkey.

Email: ozkanozbek@gantep.edu.tr

## 1. Introduction

In the past few decades, fiber reinforced composite materials have become promising materials in aerospace, automotive, marine and defense industries due to their outstanding performance-to-weight ratio, better damping characteristics, good fatigue resistance, high resistance to corrosion when compared to conventional engineering materials. However, they have low intensity on the impact behavior because its brittle characteristics. Heavier design, so reduction in strength of the materials, may be necessary to satisfy requirement of the system safety. One of the techniques to improve the impact damage resistance of fiber reinforced polymer composites are the addition of small amounts of nanoparticles into the matrix of composites.

Desire to improve the efficiency of composite materials for engineering applications, has led to the use of nano-sized additives or fillers such as nanoclay, nanosilica, nano-graphene, carbon nanotubes. The effect of nanoparticle inclusion on mechanical properties of fiber reinforced composite materials has been investigated by many researchers and crucial effects have been reported in several papers [1]. Nano silica particle is the one of the common nanoparticles used in literature studies to improve behaviors of fiber reinforced composite materials. Due to better mechanical properties, nanosilica inclusion in polymer composite has been used in many areas such as automotive, electronics, aerospace industries [2-3].

Several studies related to nanosilica incorporation on polymer based composite materials are present in the literature. Kuzmin et al. [4] conducted a study related to surface modification of basalt fibers by coating the

fibers with nanosilica particles. 23% increase in tensile strength was obtained from the sample having 0.1 wt.% nanosilica inclusion when compared to non-coated fibers. Different weight percentages of nano silica particles were considered as between the 0.1 wt.% and 1 wt.%. Huang and Tsai [5] researched the effect of nanosilica and rubber particles on the vibration and damping behavior of E-glass fiber reinforced composite laminates. The samples having different stacking sequences and nanoparticle incorporation in epoxy component were prepared and the obtained results were compared with the pure ones. Zeng et al. [6] examined the fracture toughness characteristics of carbon fibre/epoxy laminates by adding the nanosilica and rubber particles. The highest improvement comparing to sample without nanoparticle was obtained from 10 wt. % rubber addition as 2.5 times. Nanosilica incorporation showed the 20-30% increase in fracture toughness. Manjunatha et al. [7] investigated the tensile fatigue behavior of glass fibre reinforced epoxy composites having 10 wt. % nanosilica particles. Fatigue life of samples having nanosilica was improved with three or four times compared to pure samples. Kang et al. [8] derived an advanced proof material for body armor materials. Kevlar fiber reinforced composites were prepared with incorporation of the fumed silica. Kevlar/silica composite fabric exposed to quasi-static stab testing and impact tests. The samples having silica particles showed the better results than pure ones. Rosso et al. [9] employed the well-dispersed silica nanocomposites for tensile and fracture tests. The author indicated that the addition of ratio of 5% silica nanoparticles from the total volume of composite material could be developed the stiffness and fracture energy at the range from 20% to 140%. Zamanian et al. [10] noticed that the mechanical characteristics of an epoxy resin have been improved drastically by the addition of silica nanoparticles with various sizes, the best improvements being approached with the smaller nanoparticles.

In this work, the effects of nanosilica content on the low velocity impact behaviors of glass/epoxy fiber reinforced composite laminates are determined using Charpy impact tests. The nanosilica particles with different weight percentages are dispersed in epoxy. Absorbed impact energy values of beam specimens, and impact toughness are analyzed as a measure of impact behavior.

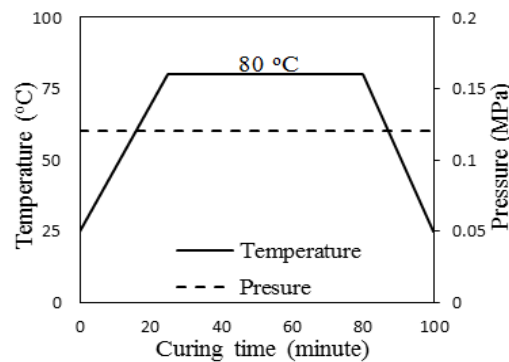
## 2. Materials & Methods

Plain weave E-glass fabrics having 202 g/m<sup>2</sup> areal density, epoxy resin (MOMENTIVE-MGS L285) and hardener (MOMENTIVE-MGS H285) were purchased from DOST Chemical Industrial Raw Materials Industry, Turkey. Nanosilica particles having average particular dimension, specific surface area, mass density and high purity as 15 nm, 300 m<sup>2</sup>/g, 0.05 g/cm<sup>3</sup>, 99.5%, respectively, were supplied by Grafen Chemical Industries, Turkey. Firstly, epoxy resin/nanosilica mixtures were prepared in a beaker according to different weight percentages of nanosilica particles as 0.5, 1.0, 1.5, 2.0 and 3.0. The mixture were blended by mechanical stirring to provide homogeneous mixture. Then, hardener was added to mixture in the weight ratio of mixture/hardener as 100:40 and stirred again.

Step by step representation of fabrication procedure are given in Fig. 1a. Hand layup technique, shown in Fig. 1b, was conducted to obtain composite laminates. For this purpose, a thin release agent and a layer of glass fabric were placed on the below mold plate. Then, resin mixture was applied on the fabric layer with a help of brush. Afterwards, second fabric layer was placed and resin mixture was applied, respectively. This process was repeated until twelve layers were stacked. Lastly, top mold plate was deposited on the wet fabric layers. After finishing the preparation of combination of resin mixture and fabric layers, curing process was performed as shown in Fig. 1c in a hot press. Charpy impact test specimens were cut on the mini CNC machine. All this procedure was applied for each nanosilica content.



a) b)



c)

Figure 1. Fabrication Process; a) step by step representation of fabrication, b) hand layup technique, c) curing process.

Charpy impact tests were conducted by Köger 3/70 Charpy impact test machine, which is shown in Fig. 2 and Fig.3, for determining the impact behavior of composite laminates having nanosilica particles. The specimens with dimensions of 55 mm x 10 mm were prepared in accordance with ISO 179/92 standard [12]. Notched and unnotched specimens were exposed to edgewise and flatwise impact loading, respectively. Five specimens were tested for each configuration. All experiments carried out at standard room temperature.

Absorbed impact energy and impact toughness for each specimen are determined by following equation (1) and (2);

$$E = E_a - E_b \tag{1}$$

$$a_{cu} = E / (bh) \tag{2}$$

where, E, E<sub>a</sub>, E<sub>b</sub>, a<sub>cu</sub>, b and h represents the absorbed impact energy, potential energy of the weighted pendulum before and after impact, impact toughness, width and thickness of the specimen.

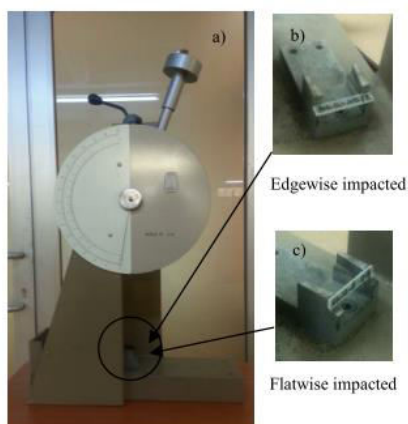


Figure 2. Köger 3/70 Charpy impact tester; a) the calibrated dial on the impact tester, b) edgewise impacted notched test specimen, c) flatwise impacted unnotched test specimen.

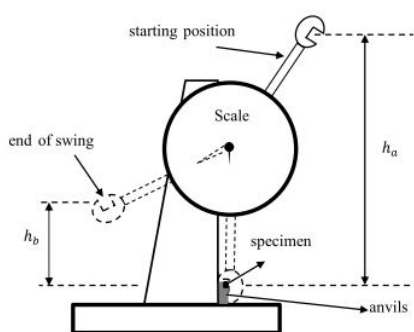


Figure 3. Schematic illustration of Charpy impact test.

### 3. Results & Discussions

The Charpy impact test was performed to observe effects of nanosilica inclusion of the impact behavior of glass/epoxy fiber reinforced composite laminates.

The impact energy and impact toughness values for edgewise (notched) were plotted versus nanosilica contents in Fig. 4 and Fig. 5. GFRE means the pure epoxy laminates that has no addition of silica particles in all figures. For the edgewise specimens, the maximum impact energy and toughness values are obtained from the specimen having 1.5% nanosilica inclusion as 3.34 J and 156.84 kJ/m<sup>2</sup>. All silica particles inclusions have the increase comparing to pure one. The results for impact energy and toughness give an idea that there is an improvement trend up to 1.5% and afterwards decreasing trend happens. This can be related to some agglomerations resulted with a weak interfacial adhesion between the matrix and nanoparticles.

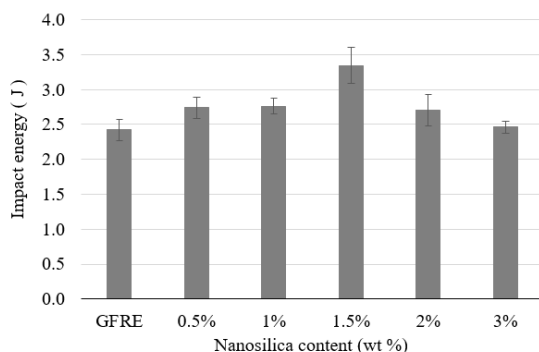


Figure 4. Impact energy of edgewise-notched impacted with respect to nanosilica content.

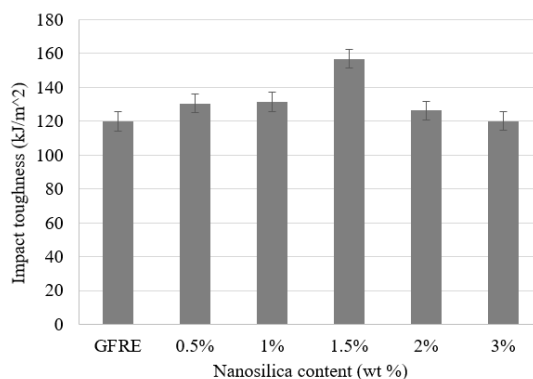


Figure 5. Impact toughness of edgewise-notched impacted with respect to nanosilica content.

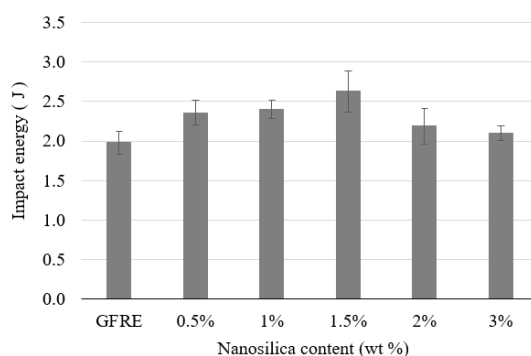


Figure 6. Impact energy of flatwise-unnotched impacted with respect to nanosilica content.

The Figures 6 and 7 are represent the impact energy and toughness results that belong the flatwise (unnotched) specimens. For the results belong the flatwise specimens, they have similar fashion with the edgewise results. The best improvement are obtained from the 1.5% nanosilica incorporation again as 2.63 J and 124.67 kJ/m<sup>2</sup>. At this point, 32.8% and 27.1% increase in impact energy and toughness are ensured against to pure ones. In the literature, several similar results were reported for the decreasing trend after a certain value of nanoparticle inclusion [11].

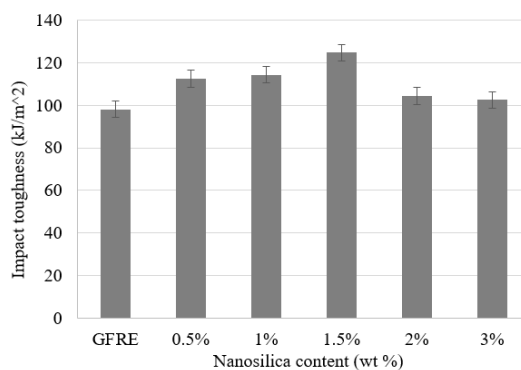


Figure 7. Impact toughness of flatwise-unnotched impacted with respect to nanosilica content.

#### 4. Conclusions

In this study, the effects of nanosilica inclusion on the impact behavior of glass/epoxy fiber reinforced composite laminates were investigated by conducting Charpy impact tests. For each nanosilica content, five specimens as notched and unnotched were exposed to edgewise and flatwise impact loading. Impact energy and impact toughness results were obtained and compared to specimens having pure epoxy matrix. 38.02%, 30.86% for edgewise-notched specimens and 32.83%, 27.1% for flatwise-unnotched specimens increase in impact energy and toughness were obtained from the test results. The best improvements were achieved on the addition of 1.5 wt.% nanosilica inclusion for both situations. Also, all addition of nanosilica weight percentages gave the improvements compared to pure ones.

As seen in the results, nanosilica addition in the matrix the crucial effects on the impact behavior of the fiber reinforced composite laminates even the usage of very small amounts. It can be recommended in the engineering applications.

#### **Acknowledgements(11 PT) (Optional)**

Some glass fiber data was benefited from a M.Sc. thesis studies of AtbanRafeaAbdo supported by the Gaziantep University Scientific Research Projects (B.A.P) under grant number MF.YLT.16.14.

#### **References(11 PT)**

- [1] M. Jawaid, A. el Kacem Qaiss, R. Bouhfid, “Nanoclay Reinforced Polymer Composites: Natural Fibre/Nanoclay Hybrid Composites,” *Springer*, 2016.
- [2] A. Moisala, Q. Li, I. A. Kinloch, A. H. Windle, “Thermal and electrical conductivity of single- and multi-walled carbon nanotube-epoxy composites,” *Composite science and technology*, 66(10), pp. 1285-1288, 2006.
- [3] R. Goyal, M. Sharma, U. K. Amberiya, “Innovative nano composite materials and applications in automobiles,” *International Journal of Engineering Research and Technology*, 3(1), 2014.
- [4] K. L. Kuzmin, I. A. Timoshkin, S. I. Gutnikov, E. S. Zhukovskaya, Y. V. Lipatov, B. I. Lazoryak, “Effect of silane/nano-silica on the mechanical properties of basalt fiber reinforced epoxy composites,” *Composite Interfaces*, 24(1), pp. 13-34, 2017.
- [5] C. Y. Huang & J. L. Tsai, “Characterizing vibration damping response of composite laminates containing silica nanoparticles and rubber particles,” *Journal of Composite Materials*, 49(5), pp. 545-557, 2015.
- [6] Y. Zeng, H. Y. Liu, Y. W. Mai, X. S. Du, “Improving interlaminar fracture toughness of carbon fibre/epoxy laminates by incorporation of nano-particles,” *Composite Part B: Engineering*, 43(1), pp. 90-94, 2012.
- [7] C. M. Manjunatha, A. C. Taylor, A. J. Kinloch, S. Sprenger, “The tensile and fatigue behaviour of a silica nanoparticle-modified glass fibre reinforced epoxy composite,” *Composite Science and Technology*, 70(1), pp. 193-196, 2010.
- [8] T. J. Kang, K. H. Hong, M. R. Yoo, “Preparation and properties of fumed silica/Kevlar composite fabrics for application of stab resistant material,” *Fibers and Polymers*, 11(5), pp. 719-724, 2010.
- [9] P. Rosso, L. Ye, S. Sprenger, “A toughened epoxy resin by silica nanoparticle reinforcement,” *Journal of Applied Polymer Science*, 100(3), pp. 1849-1855, 2006.
- [10] M. Zamanian, M. Mortezaei, B. Salehnia, J. E. Jam, “Fracture toughness of epoxy polymer modified with nanosilica particles: Particle size effect,” *Engineering Fracture Mechanics*, 97, pp. 193-206, 2013.
- [11] J. K. Pandey, K. R. Reddy, A. K. Mohanty, M. Misra, “Handbook of Polymer nanocomposites. Processing, Performance and Application Volume A: Layered Silicates,” *Germany: Springer-Verlag Berlin Heidelberg*, 2014.
- [12] ISO, EN. "179: 72." *Plastics -- Determination of Charpy impact properties -- Part 1: Non-instrumented impact test.*

## Performance Comparisons of Current Metaheuristic Algorithms on Unconstrained Optimization Problems

Umit Can<sup>1</sup>, Bilal Alatas<sup>2</sup>

<sup>1</sup> Computer Engineering Department, Munzur University, 62000, Tunceli, Turkey, ucan@munzur.edu.tr

<sup>2</sup> Software Engineering Department, Firat University, 23119, Elazig, Turkey, balatas@firat.edu.tr

### Article Info

#### Article history:

Received May 30<sup>th</sup>, 2017

Revised Aug 20<sup>th</sup>, 2017

Accepted Oct 18<sup>th</sup>, 2017

#### Keyword:

Metaheuristic Algorithms,  
Global Optimization,  
Performance

### ABSTRACT

Nature-inspired metaheuristic algorithms have been recognized as powerful global optimization techniques in the last few decades. Many different metaheuristic optimization algorithms have been presented and successfully applied to different types of problems. In this paper; seven of newest metaheuristic algorithms namely, Ant Lion Optimization, Dragonfly Algorithm, Grey Wolf Optimization, Moth-Flame Optimization, Multi-Verse Optimizer, Sine Cosine Algorithm, and Whale Optimization Algorithm have been tested on unconstrained benchmark optimization problems and their performances have been reported. Some of these algorithms are based on swarm while some are based on biology and mathematics. Performance analysis of these novel search and optimization algorithms satisfying equal conditions on benchmark functions for the first time has given important information about their behaviors on unimodal and multi-modal optimization problems. These algorithms have been recently proposed and many new versions of them may be proposed in future for efficient results in many different types of search and optimization problems.

### Corresponding Author:

Umit Can,  
Computer Engineering Department,  
Munzur University, 62000, Tunceli, Turkey,  
ucan@munzur.edu.tr

## 1. Introduction

Optimization is the process of searching for the optimal solution. Analytical, enumeration, and heuristic methods can be used for optimization task. Heuristic refers to experience-based techniques for problem-solving and learning. Heuristics are problem-dependent and designed only for the solution of a specific problem. A metaheuristic is a higher level heuristic that may provide a sufficiently good solution to any optimization problem [1]. Metaheuristic algorithms are simple to implement and faster than the classical calculus based optimization algorithms, they are capable of achieving good approximation to the global optimum, and they are robust to problem changes.

Metaheuristics are recently getting stronger and increasing their popularity due to their advantages. They are used extensively in various fields such as management, computer, engineering due to advantages such as not having difficult mathematical models to set up, good computing powers, and requiring no change on the interested problems like classical algorithms [2]. The different properties of metaheuristic algorithms cause them to perform unequivocally in different optimization problems, and for this reason none of them can be superior to others in all situations. Each has different solutions and superiorities. Their modified new versions

or novel metaheuristic algorithms are still proposed due to the absence of the most efficient method for all types of problems [3].

There are many metaheuristic optimization methods that are based on biology, physics swarm, sociology, music, chemistry, sports, mathematics and plants. In this paper, seven of newest metaheuristic algorithms namely, Ant Lion Optimization (ALO) [4], Dragonfly Algorithm (DA) [5], Grey Wolf Optimization (GWO) [6], Moth-Flame Optimization (MFO) [7], Multi-Verse Optimizer (MVO) [8], Sine Cosine Algorithm (SCA) [9], and Whale Optimization Algorithm (WOA) [10] have been tested on unconstrained benchmark optimization problems and their performances have been reported.

Organization of this paper has been as follows: Section 2 gives brief explanations of the current algorithms with pseudo-codes. Section 3 gives the descriptions of the unconstrained unimodal and multi-modal benchmark functions. Section 4 reports the experimental results obtained from these metaheuristic algorithms on unconstrained benchmark optimization problems. Section 5 concludes the paper along with future research directions.

## 2. Current Metaheuristic Algorithms

As a constant source of inspiration, nature continues to offer researchers new ideas for new efficient optimization algorithms. In the past decades, various metaheuristic intelligence optimization algorithms have been proposed to solve complex search and optimization problems. These algorithms have shown an outstanding performance on the problems. Hence, while many researchers have focused in adapting them on different problems or to improve their performances, some researchers have proposed novel algorithms inspired from biology, swarm, physics, and etc.

ALO is a nature-inspired algorithm mimicking the hunting behavior of antlions in nature [4]. ALO is implemented in five main steps: random walks of ants, building pits, entrapment of ants, catching preys, and lastly rebuilding pits. Pseudo-code of ALO is depicted in Figure 1.

```

Initialize problem parameters
Initialize algorithm parameters
Initialize the first population of ants and ant lions
Determine the best ant lion and assume it as the elite
While termination criteria not satisfied
For each ant
  Select an ant lion with roulette wheel method
  Create a random walk normalize it
  Update the position of ant
End For
  Compute the fitness of all ants
  Replace an ant lion with its corresponding fitter ant
  Update elite if ant lion becomes fitter than the elite
End While
Return elite

```

**Figure 1.** Pseudo-code of ALO

DA is inspired from the static and dynamic swarming behaviors of dragonflies in nature [5]. Two essential phases in optimization, namely exploration and exploitation, are designed by modelling the social interaction of dragonflies in navigating, searching for foods, and avoiding enemies when swarming dynamically or statistically [5]. Pseudo-code of DA is shown in Figure 2.

```

Initialize problem parameters
Initialize algorithm parameters
Initialize swarm of dragonflies, the initial velocity vector, food source, and enemy.
Compute fitness function
While termination criteria not satisfied
  Update the food source and enemy
  For each dragonfly
    Compute the Euclidean distance of each dragonfly with other members in the swarm and
    select the number of neighbors
    Based on the number of neighbors, update the velocity and position vectors
  End For
End While
Return best food source

```

**Figure 2.** Pseudo-code of DA

GWO mimics the leadership hierarchy and hunting mechanism of gray wolves in nature [6]. GWO has three main steps of hunting, searching for prey, encircling prey, and attacking prey. Pseudo-code of GWO is shown in Figure 3.

MFO is inspired from navigation method of moths in nature called transverse orientation [7]. Spiral flying path of moths around artificial lights (flames) has been mathematically modeled in MFO. Main steps of this algorithm are demonstrated in Figure 4.

```

Initialize problem parameters
Initialize algorithm parameters
Initialize the initial positions of grey wolves
Initialize the vectors for mathematically modelling encircling behavior
Compute the fitness of each grey wolf
Get the first three best wolves
While termination criteria not satisfied
  For each search agent
    Update the position of the current grey wolf
  End For
  Update the vectors
  Compute the fitness of all grey wolves
  Update the first three best wolves
End While
Return grey wolf with the first maximum fitness

```

**Figure 3.** Pseudo-code of GWO

```

Initialize problem parameters
Initialize algorithm parameters
Initialize the initial positions of moths
Compute the fitness
While termination criteria not satisfied
For each moth
Update positions
Compute the fitness
End While
Return the best flame

```

**Figure 4.** Pseudo-code of MFO

MVO is a novel search and optimization algorithm main inspirations of which are based on three concepts in cosmology: white hole, black hole, and wormhole [8]. The mathematical models of these three concepts are developed to perform exploration, exploitation, and local search, in optimization respectively. Main steps of MVO are demonstrated in Figure 5.

```

Initialize problem parameters
Initialize algorithm parameters
Initialize galaxy
While termination criteria not satisfied
Apply Black/White Hole mechanism
Apply Wormholes mechanism
End While
Return best universe position

```

**Figure 5.** Pseudo-code of MVO

SCA is an interesting math inspired search and optimization algorithm and uses mathematical model based on sine and cosine functions. SCA adaptively balances the exploration and exploitation phases in optimization quickly [9]. Main steps of SCA are demonstrated in Figure 6.

```

Initialize problem parameters
Initialize algorithm parameters
Initialize search agents
While termination criteria not satisfied
Compute the fitness
Update the next position region between solution and destination, parameters that tells
how far the movement should be towards or outwards the destination, random weight for
destination, and value controlling switches between sine and cosine component.
Update the positions
End While
Return best result

```

**Figure 6.** Pseudo-code of SCA

WOA is inspired from the bubble-net hunting strategy [10]. The mathematical model of WOA is based on encircling prey, bubble net hunting, and searching the prey. Main steps of WOA are demonstrated in Figure 7.

```
Initialize problem parameters
Initialize algorithm parameters
Initialize search agents
Compute the fitness of all search agents
While termination criteria not satisfied
Encircle prey
Bubble net hunt
Search the prey
Compute the fitness
End While
Return best result
```

**Figure 7.** Pseudo-code of WOA

### 3. Benchmark Functions

To evaluate the performance of these seven current metaheuristic algorithm, five benchmark test functions with different characteristics have been used. These benchmark functions are frequently used to evaluate and compare the characteristics of optimization algorithms in terms of convergence, precision, robustness, and general performance. The nature, complexity, and other properties of these benchmark functions can be easily obtained from their definitions and the difficulty levels of these benchmark functions can be adjusted by changing their dimension and interval parameters [11].

Chung Reynolds function is a unimodal function with less complexity and it can be used to evaluate the converging behaviors of algorithms [12]. Its graph with two dimensions has been shown in Figure 8. Griewank function is a multi-modal function with many local optima and it can be used to test the global search ability of the optimization algorithms in avoiding premature convergence [13]. Its graph with two dimensions has been shown in Figure 9. Rastrigin function is highly multi-modal, but locations of the minima are regularly distributed. Its graph with two dimensions has been shown in Figure 10. Ackley is a multi-modal function with deep local optimizations and the variables are independent of each other [14]. Its graph with two dimensions has been shown in Figure 11. Rosenbrock function is unimodal with two dimensions however multi-modal with higher dimensions [15]. Two dimensional Rosenbrock function has been shown in Figure 12. Schwefel's 2.22 is another unimodal function. It is separable, non-differentiable, continuous, and convex function [16]. Its graph with two variables has been shown in Figure 13. Schwefel is multimodal, asymmetric and separable test function [17] and its graph with two dimensions has been shown in Figure 14.

The selected benchmark functions and their properties have been demonstrated in Table 1. The dimensions ( $n$ ) for all benchmark functions have been determined as 10.

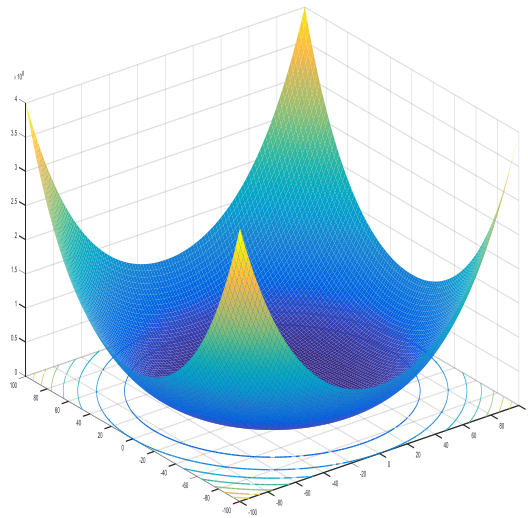


**Figure 8.** Chung Reynolds function with two variables

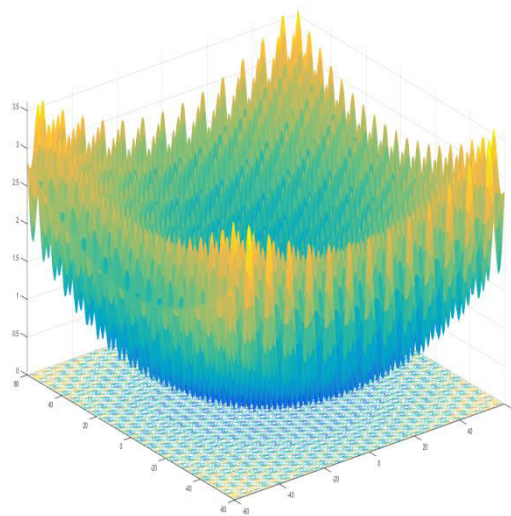


**Figure 9.** Griewank function with two variables

**Table 1.** Benchmark function

Function Name	Definition	Interval	Characteristics
Chung Reynolds	$f_1(x) = \left(\sum_{i=1}^n x_i^2\right)^2$	$-100 \leq x_i \leq 100$	Unimodal
Griewank	$f_2(x) = 1 + \frac{1}{4000} \sum_{i=1}^n x_i^2 - \prod_{i=1}^n \cos\left(\frac{x_i}{\sqrt{i}}\right)$	$-600 \leq x_i \leq 600$	Multi-modal
Rastrigin	$f_3(x) = 10 \times n + \sum_{i=1}^n x_i^2 - 10 \cos(2\pi x_i)$	$-5 \leq x_i \leq 5$	Multi-modal
Ackley	$f_4(x) = 20 + e - 20 \cdot e^{-0.2 \cdot \sqrt{\frac{1}{n} \sum_{i=1}^n x_i^2}} - e^{\frac{1}{n} \sum_{i=1}^n \cos(2\pi x_i)}$	$-32 \leq x_i \leq 32$	Multi-modal
Rosenbrock	$\sum_{i=1}^{n-1} \left(100(x_i^2 - x_{i+1})^2 + (x_i - 1)^2\right)$	$-30 \leq x_i \leq 30$	Multi-modal
Schwefel's 2.22	$f_6(x) = \sum_{i=1}^n  x_i  + \prod_{i=1}^n  x_i $	$-100 \leq x_i \leq 100$	Unimodal
Schwefel	$f_7(x) = 418.9829 \times n - \sum_{i=1}^n x_i \sin\left( x_i ^{\frac{1}{2}}\right)$	$-500 \leq x_i \leq 500$	Multi-modal

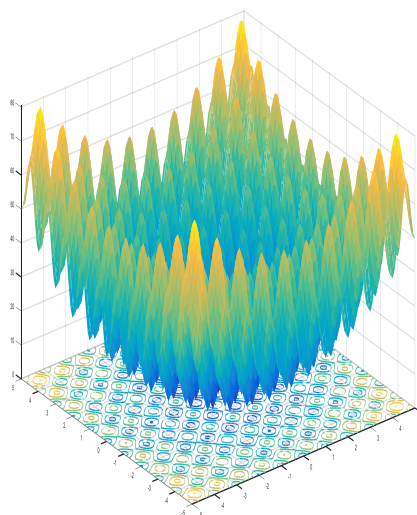


**Figure 10.** Rastrigin function with two variables

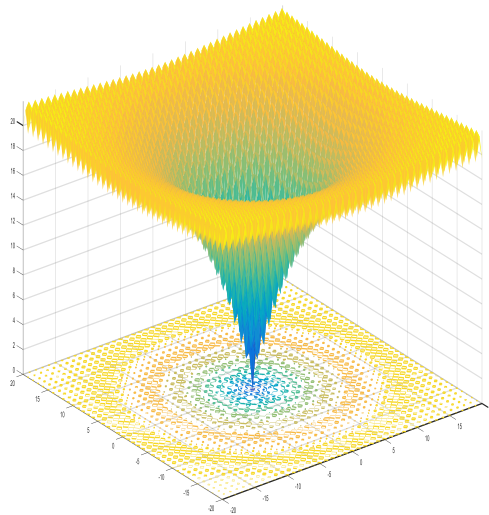


**Figure 11.** Ackley function with two variables

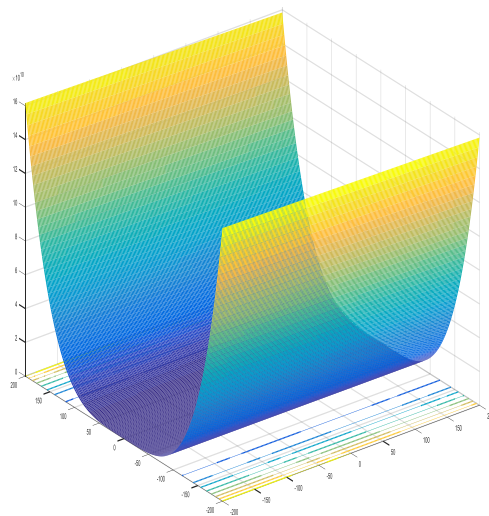


**Figure 12.** Rosenbrock function with two variables

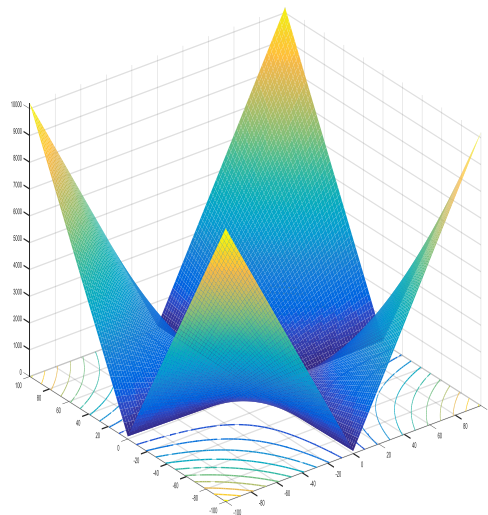


**Figure 13.** Schwefel's 2.22 function with two variables

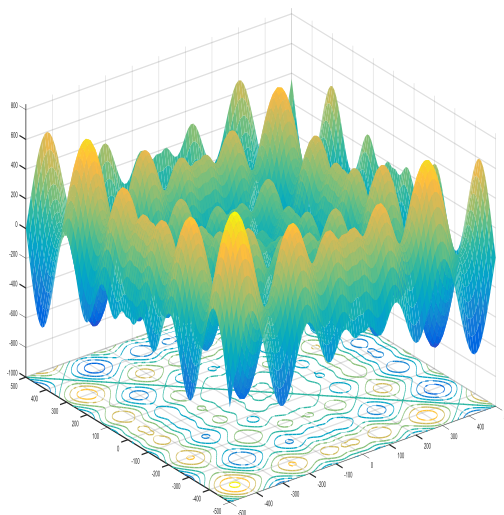


**Figure 14.** Schwefel function with two variables

#### 4. Experimental Results

The performances of algorithms have been tested on Chung Reynolds function with 10 dimensions. Initial population size of all algorithms is selected as 30 and maximum iteration number for termination criteria is determined as 100. All algorithm parameters have been selected as their original values. All algorithms have been run 10 times. The results obtained from this problem have been demonstrated in Table 2. From these results, it can be concluded that WOA is the best algorithm within this unimodal problem. GWO is the second best algorithm. MFO seems the worst algorithm within this function using this dimension and interval of the problem and iteration number for the algorithms.

**Table 2.** Performances of algorithms on Chung Reynolds function

<i>Algorithm</i>	<i>Mean optimum</i>
ALO	0.3793
DA	50.2239
GWO	8.3804e-18
MFO	88.5679
MVO	0.0478
SCA	0.2782
WOA	2.7393e-28

The performances of algorithms have been tested on Griewank function with 10 dimensions. Initial population size of all algorithms is selected as 30 and maximum iteration number for termination criteria is determined as 100. All algorithm parameters have been selected as their original values. All algorithms have been run 10 times. The results obtained from this problem have been demonstrated in Table 3. From these results, it can be concluded that WOA is the best algorithm within this multi-modal problem. GWO is the second best algorithm. SCA seems the worst algorithm within this function in the selected dimension and interval for the problem and iteration number for the algorithms.

**Table 3.** Performances of algorithms on Griewank function

<i>Algorithm</i>	<i>Mean optimum</i>
ALO	0.0913
DA	0.9221
GWO	0.0319e-4
MFO	1.0425
MVO	0.6848
SCA	1.0809
WOA	5.4877e-7

The performances of algorithms have also been tested on another multi-modal problem, namely Rastrigin function, with 10 dimensions. Initial population size of all algorithms is selected as 30 and maximum iteration number for termination criteria is determined as 100. All algorithm parameters have been selected as their original values. All algorithms have been run 10 times. The results obtained from this problem have been demonstrated in Table 4. From these results, it can be concluded that again, WOA is the best algorithm within this multi-modal problem. GWO is the second best algorithm. SCA seems the worst algorithm within this function in the selected dimension and interval for the problem and iteration number for the algorithms.

**Table 4.** Performances of algorithms on Rastrigin function

<i>Algorithm</i>	<i>Mean optimum</i>
ALO	22.9145
DA	42.7102
GWO	4.4678
MFO	15.5878
MVO	33.9496
SCA	47.6633
WOA	1.0747e-06

The performance comparisons of the algorithm on another multi-modal problem, namely Ackley function, with 10 dimensions have been demonstrated in Table 5. Initial population size of all algorithms is selected as 30 and maximum iteration number for termination criteria is determined as 100. All algorithm parameters have been selected as their original values. All algorithms have been run 10 times. From these results, it can be concluded that again, WOA is the best algorithm within this multi-modal problem. GWO is the second best algorithm. DA seems the worst algorithm within this function using the selected dimension and interval for the Ackley function and iteration number for the algorithms.

The performance comparisons of the algorithm on Rosenbrock with 10 dimensions have been demonstrated in Table 6. Initial population size of all algorithms is selected as 30 and maximum iteration number for termination criteria is determined as 100. All algorithm parameters have been selected as their original values. All algorithms have been run 10 times. From these results, it can be concluded that again, GWO is the best algorithm within this multi-modal problem. WOA is the second best algorithm. DA seems the worst algorithm within this function in the selected dimension and interval for the Rosenbrock function and iteration number for the algorithms.

**Table 5.** Performances of algorithms on Ackley function

<i>Algorithm</i>	<i>Mean optimum</i>
ALO	4.1785
DA	5.6896
GWO	1.1195e-05
MFO	3.4870
MVO	0.3215
SCA	0.4256
WOA	1.9207e-06

**Table 6.** Performances of algorithms on Rosenbrock function

<i>Algorithm</i>	<i>Mean optimum</i>
ALO	12.7817
DA	573.5498
GWO	8.0282
MFO	299.0972
MVO	12.7262
SCA	238.4051
WOA	8.6148

The performance comparisons of the algorithm on unimodal Schwefel's 2.22 with 10 dimensions have been demonstrated in Table 7. Initial population size of the algorithm is selected as 30 and maximum iteration number for termination criteria is determined as 100. All algorithms have been run 10 times. According to the obtained experimental results, it can be concluded that, WOA is the best algorithm within this unimodal problem. GWO is the second best algorithm. MVO seems the worst algorithm within this function in the selected dimension and interval for the Schwefel's 2.22 function and iteration number for the algorithms.

**Table 7.** Performances of algorithms on Schwefel's 2.22 function

<i>Algorithm</i>	<i>Mean optimum</i>
ALO	332.3281
DA	210.4979
GWO	4.5780e-05
MFO	9.5452
MVO	1.5024e+03
SCA	1.4083
WOA	1.0563e-08

The performance comparisons of the algorithm on multi-modal Schwefel with 10 dimensions have been demonstrated in Table 8. Initial population size of the algorithm is selected as 30 and maximum iteration number for termination criteria is determined as 100. All algorithms have been run 10 times. According to the obtained experimental results, it can be concluded that, MFO is the best algorithm within this multi-modal function. DA is the second best algorithm. SCA seems the worst algorithm within this function in the selected dimension and interval for the Schwefel function and iteration number for the algorithms.

**Table 8.** Performances of algorithms on Schwefel function

<i>Algorithm</i>	<i>Mean optimum</i>
ALO	1.2240e+03
DA	955.3876
GWO	1.8975e+03
MFO	792.3943
MVO	1.2647e+03
SCA	2.1515e+03
WOA	1.1430e+03

Table 9 demonstrates the total successes of these algorithms. According to this table, WOA has performed better in five of the seven benchmark functions. GWO has performed better only one and MFO has also performed in only one of the seven functions.

**Table 9.** General evaluations

<b>Function Name</b>	<b>Characteristics</b>	<b>Best Algorithm</b>	<b>Worst Algorithm</b>
Chung Reynolds	Unimodal	WOA	MFO
Griewank	Multi-modal	WOA	SCA
Rastrigin	Multi-modal	WOA	SCA
Ackley	Multi-modal	WOA	DA
Rosenbrock	Multi-modal	GWO	DA
Schwefel's 2.22	Unimodal	WOA	MVO
Schwefel	Multi-modal	MFO	SCA

## 5. Conclusions

Novel metaheuristic algorithms are still proposed due to the absence of the most efficient method for all types of search and optimization problems. In this paper, performances of current metaheuristic search and optimization methods have been tested and seven new algorithms, namely Ant Lion Optimization, Dragonfly Algorithm, Grey Wolf Optimization, Moth-Flame Optimization, Multi-Verse Optimizer, Sine Cosine Algorithm, and Whale Optimization Algorithm have been selected for this goal. They have been executed on unconstrained unimodal and multi-modal benchmark optimization problems. According to the obtained results within the benchmark functions, WOA is the best algorithm and GWO is the second best algorithm. WOA has performed better in five of the seven benchmark functions. GWO has performed better in only one and MFO has also performed in only one of the seven functions.

These algorithms are very new computational methods and they can be improved in many ways. More validation studies should be performed to discover the capabilities of these algorithms in dealing with the search and optimization problems. There are positive challenges in terms of efficiency and best possible usage of these algorithms.

## References

- [1] Du, Ke-Lin, Swamy, M. N. S. (2016) Search and Optimization by Metaheuristics. Springer.
- [2] Akyol, S., Alatas, B. (2012). Güncel Sürü Zekası Optimizasyon Algoritmaları, Nevşehir Bilim ve Teknoloji Dergisi, 1(1), 36-50
- [3] Altunbey, F., Alatas, B. (2015). Overlapping community detection in social networks using parliamentary optimization algorithm. International Journal of Computer Networks and Applications, 2(1), 12-19.
- [4] Mirjalili, S. (2015). The ant lion optimizer. Advances in Engineering Software. 83. 80-98.
- [5] Mirjalili, S. (2016). Dragonfly algorithm: a new meta-heuristic optimization technique for solving single-objective, discrete, and multi-objective problems. Neural Computing and Applications, 27(4), 1053-1073.
- [6] Mirjalili, S., Mirjalili, S. M., & Lewis, A. (2014). Grey wolf optimizer. Advances in Engineering Software, 69, 46-61.
- [7] Mirjalili, S. (2015). Moth-flame optimization algorithm: A novel nature-inspired heuristic paradigm. Knowledge-Based Systems, 89, 228-249.
- [8] Mirjalili, S., Mirjalili, S. M., & Hatamlou, A. (2016). Multi-verse optimizer: a nature-inspired algorithm for global optimization. Neural Computing and Applications, 27(2), 495-513.
- [9] Mirjalili, S. (2016). SCA: a sine cosine algorithm for solving optimization problems. Knowledge-Based Systems, 96, 120-133.
- [10] Mirjalili, S., Lewis, A. (2016). The whale optimization algorithm. Advances in Engineering Software, 95, 51-67.
- [11] Alatas, B. Akin, E. Ozer, A. B (2009) Chaos Embedded Particle Swarm Optimization Algorithms, Chaos, Solitons & Fractals, vol. 40, pp. 1715-1734.
- [12] (2017) C. J. Chung, R. G. Reynolds, "CAEP: An Evolution-Based Tool for Real-Valued Function Optimization Using Cultural Algorithms", International Journal on Artificial Intelligence Tool, 7(3), 239-291, 1998
- [13] (2017) GEATbx: Examples of Objective Functions. Available: <http://www.pg.gda.pl/~mkwies/dyd/geadocu/fcnfun8.html>
- [14] Ackley, D. (1987) An Empirical Study of Bit Vector Function Optimization. Genetic Algorithms and Simulated Annealing, 170-215.
- [15] Shang, Y. W., Qiu, Y. H. (2006). A note on the extended Rosenbrock function. Evolutionary Computation, 14(1), 119-126.
- [16] (2017) Ardeh, M. A. Well-known optimization benchmark functions. Available <http://benchmarkfns.xyz/benchmarkfns/schwefel222fcn.html>
- [17] (2017) GEATbx: Examples of Objective Functions. Available: <http://www.pg.gda.pl/~mkwies/dyd/geadocu/fcnfun7.html>

# Charpy Impact Response of Glass Fiber Reinforced Composite with Nano Graphene Enhanced Epoxy

Ahmet Erklig<sup>1</sup>, Nurettin Furkan Dogan<sup>2</sup>, Mehmet Bulut<sup>3</sup>

<sup>1</sup> University of Gaziantep, Engineering Faculty, Mechanical Engineering Department

<sup>2</sup> University of Gaziantep, Engineering Faculty, Mechanical Engineering Department

<sup>3</sup> University of Hakkari, Engineering Faculty, Mechanical Engineering Department

## Article Info

### Article history:

Received May 30<sup>th</sup>, 2017

Revised Aug 20<sup>th</sup>, 2017

Accepted Oct 18<sup>th</sup>, 2017

### Keyword:

Graphene nano platelets, epoxy, glass, composite, low velocity impact

## ABSTRACT

Fiber reinforced polymer composite materials show several superior properties over conventional engineering materials; on the other hand, most of composite materials also have some drawbacks such as brittle behavior of matrix. This study is aimed to improve the impact response of composite material by adding nano particle into epoxy matrix. For this purpose; an experimental study was conducted to investigate the effect of graphene nano particles inclusion in epoxy resin with glass fiber reinforced composite plate on the Charpy impact response. Glass fiber reinforced (GFR) epoxy composite plates were produced with various graphene nano platelets content such 0, 0.1, 0.25 and 0.5 wt%. Low velocity impact response was investigated by using Charpy impact test method. Impact energy and impact damage results presented in detail.

## Corresponding Author:

Nurettin Furkan Dogan,  
University of Gaziantep,  
Engineering Faculty,  
Mechanical Engineering Department,  
Turkey,  
Email: [nfurkandogan@gantep.edu.tr](mailto:nfurkandogan@gantep.edu.tr)

## 1. Introduction

In the past few decades, composite materials have been focused more by the engineering and research world due to their superior performance to weight ratio compared to conventional engineering materials. With these superior performance characteristics, fiber reinforced polymer (FRP) composites have seized the supremacy of usage in marine, aerospace, automobile, and construction industries. In fiber reinforced polymer composites, as the name suggests, fibers are used as a reinforcement materials into resins. Glass fibers are widely used reinforcement type due to their low cost (compared to Kevlar, carbon) and good mechanical properties. And, resin material can be polymer, ceramic or metal based. Epoxy is one of the most used polymer type as resin material. The brittle and poor impact resistance nature of resin has led the researchers to improve these properties of resin with adding micro and nano-sized particles to resin material. Riley et al [1, 2] found that the inclusion of large particle in matrix adversely affects the impact properties of material, since

they can act like a crack initiation site. Also, they stated that the presence of nanosized fillers can affect the morphology of polymers and improve the toughness of materials in consequence of crack deviating processes.

Carbon nano materials have attracted a huge attention because of their remarkable mechanic, thermal and electrical properties since their discovery [3]. Graphene nano platelets (GnPs) which has been recently developed single layered carbon nano material is a useful polymer reinforcement material which has a large surface area led to increase the stress transfer between polymer and nano material [4, 5, 6, 7]. Graphene has a 2-D nanostructure and leads an enhancement in toughness of fibers [8, 9]. Several researchers reported that the graphene nano material addition in the fiber reinforced composites significantly affects the mechanical [10, 11], dynamic [12], thermal [13] and electrical [14] properties materials. Madhukar et al. [15] stated that GnPs inclusion in unidirectional composites significantly increased the interfacial adhesion and interlaminar shear strength as well as the flexural and tensile properties. Rafiee [16] concluded that the 0.125 wt% GnPs incorporation in graphene/epoxy nanocomposite the fracture energy was increased about 115%. Bulut [17] studied the effect of GnPs on the tensile, flexural and impact properties of Basalt fiber reinforced epoxy composite and stated that the addition of 0.1 wt% GnPs resulted the increase in impact strength of composite material.

In this study, the influence of graphene nano platelets on the low velocity impact behavior of glass fiber reinforced polymer composites will be investigated experimentally by conducting Charpy impact test. The change in energy absorption property and impact strength will be characterized at different weight ratios of nano material.

## 2. Materials and specimen preparation

### 2.1 Materials

Glass plain fabric having areal weight of 202 g/m<sup>2</sup> and thickness of 0.15 ( $\pm 5\%$ ) mm produced by Hexcel Corporation, Italy was used as reinforcement phase. Chemical products of epoxy (MOMENTIVE-MGS L285) and hardener (MOMENTIVE –MGS H285) were supplied from DOST Chemical Industrial Raw Materials Industry in Turkey. Graphene nano Glass plain fabric having areal weight of 202 g/m<sup>2</sup> and thickness of 0.15 ( $\pm 5\%$ ) mm produced by Hexcel Corporation, Italy was used as reinforcement phase. Chemical products of epoxy (MOMENTIVE-MGS L285) and hardener (MOMENTIVE –MGS H285) were supplied from DOST Chemical Industrial Raw Materials Industry in Turkey. Graphene nano platelets were supplied from GrafNano Technological Materials Industry & Trade Ltd. Co., Turkey. Nanomaterial has purity of 99.5%, bulk density of  $\sim 0.05$  g/cm<sup>3</sup>, 5  $\mu$ m diameter of graphene, thickness of 5–8 nm, and specific surface area of 150 m<sup>2</sup>/g, as well as Raman spectra ID/IG Ratio of 0.08 and XRD 2-theta of 26° peak.

Table 1. Material properties

Material	Density	Thickness
Glass Fabric	202 g/m <sup>2</sup>	0.15 mm
Graphene Nano Platelets	50 kg/m <sup>3</sup>	5-8 nm
Epoxy Resin	1.18 g/m <sup>3</sup>	-

### 2.2 Sample Preparation

The composite material preparation was carried out by vacuum infusion method in Fig.1. Twelve plies of glass fabric were cut into a certain size and laid by [0/90] lay-up sequence. Matrix phase was prepared by mixing the epoxy with hardener in the 100:40 weight ratio as well as different amounts of GnPs (0.1, 0.25 and 0.5 wt%). After epoxy was mixed with GnPs filler, the mixture was stirred for 20 min to reach a good dispersity. Following this step, the mixture was stirred with hardener for 10 min. During composite production, first, all twelve plies were laid on to a thin release agent on production desk, then peel ply and resin infusion mesh were laid on the fabrics. And finally, vacuum bag was sealed onto mesh. After these steps, resin mixture was transferred with the help of vacuumed bag. When the resin mixture impregnated, the

composite material subjected vacuum 10 h curing time and under temperature of 45 °C for 5 h. Nominal thickness of samples was measured as  $2.1 \pm 0.1$  mm.

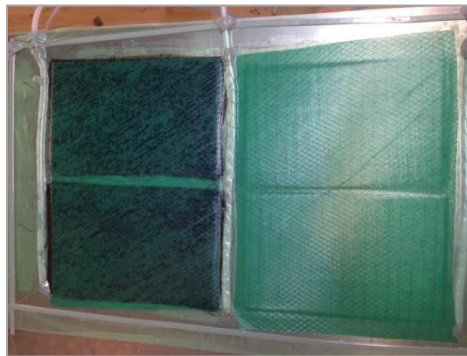


Figure 1. Composite plate production

### 2.3 Charpy Impact Test

In this test, Charpy tests were performed following ISO 179/92 standard [18] with Köger 3/70 Charpy impact test device shown in Fig.2. Both notched and unnotched test specimens with dimensions of 55 x 10 mm as seen in Fig. 2(b) were subjected to impact loads flatwise and edgewise respectively. In Charpy impact test device, a pendulum with a defined mass attached to a rotating arm connected to device body. Pendulum falls from a certain height and hits the test specimen and specimen absorbs part of pendulums kinetic energy. The absorbed impact energy and impact strength of material were calculated as follows:

$$E = E_1 - E_2 \tag{1}$$

$$U = E / (bh) \tag{2}$$

where  $E$  is the absorbed energy after impact,  $U$  is the impact strength,  $E_1$  and  $E_2$  are initial and final potential energies,  $b$  and  $h$  are width and thickness of the specimen respectively.

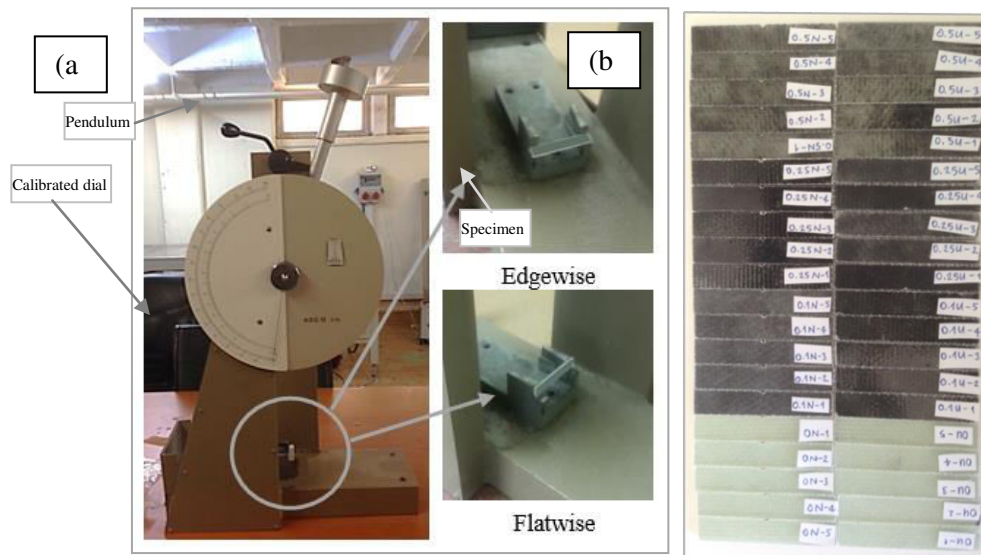


Figure 2. (a) Charpy impact test device and specimen positions, (b) Test specimens

### 3. Results and Discussions

Impact resistance of glass reinforced composite samples was investigated by using Charpy impact test. In experiments notched and unnotched specimens were subjected to impact energy of 15 J at room temperature. Fig. 3 presents the absorbed energy values of specimens with respect to GnPs contents. It can be seen that subsequent the inclusion of nano particle to matrix, absorbed impact energy values increases drastically. Maximum absorbed energy was reached with the 0.5 wt% GnPs inclusion. It was 123% greater for notched

and 41% greater for unnotched specimens than the neat epoxy/glass specimens. In case of impact strength, the variation had the same increasing profile with the absorbed energy variation with respect to GnPs contents. Increase in impact strength can be interpreted as enhancement in bonding between fiber-matrix and nanoparticle. This enhancement also leads to the increase in energy absorption capacity.

The fractured notched and unnotched test specimens after impact load can be seen in Fig. 5. And, it can be observed from figures, delamination failure first decreased 0.25 wt% GnPs content, until 0.5 wt%. Also, multiple fiber breakage failure decreased with the GnPs inclusion.

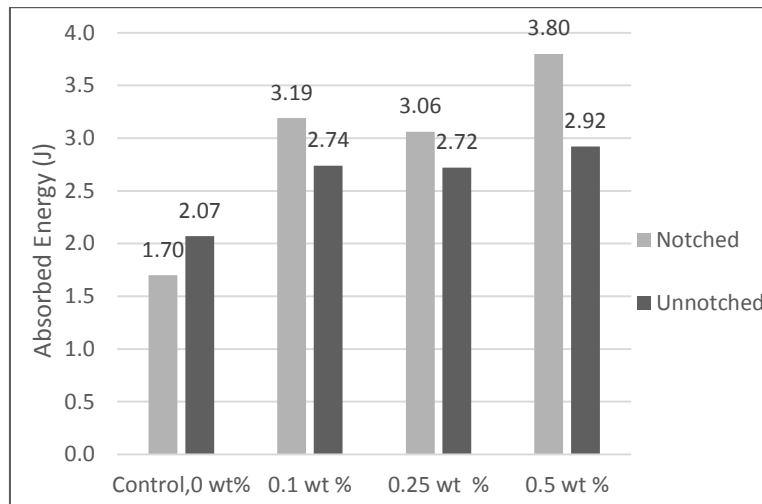


Figure 3. Absorbed energy of notched/unnotched impacted glass fiber reinforced epoxy composites with respect to GnPs content

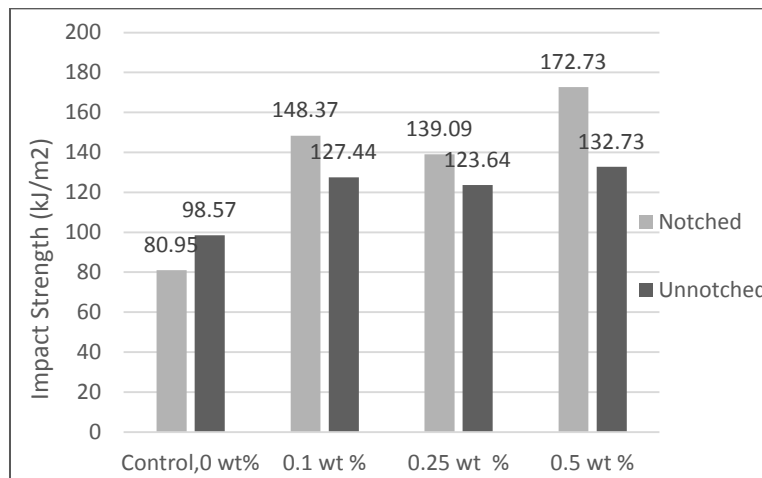


Figure 4. Impact strength of notched/unnotched impacted glass fiber reinforced epoxy composites with respect to GnPs content

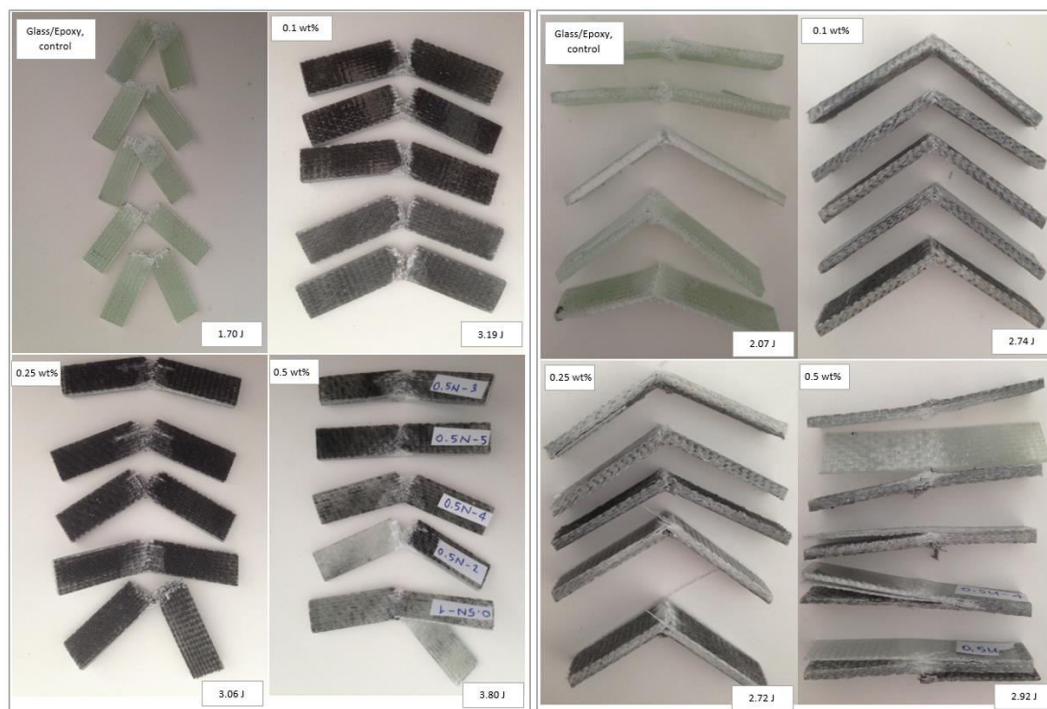


Figure 5. Fractured notched and unnotched specimens

#### 4. Conclusions

During experimental study, the Charpy impact properties of glass fiber reinforced (GFR) composite under graphene nano platelets inclusion were studied using notched and unnotched specimens. It can be concluded as the GnPs inclusion in GFR composite improves the impact strength of the material as well as the energy absorption capacities. For notched specimens, this improvement was 123% and 41% for unnotched specimens in terms of absorbed energy by 0.5 wt% GnPs content. However, presence of delamination failure increased with this content, and it can be interpreted because of nano materials' nature, the agglomeration in particles takes place with the higher content of nano materials.

#### References

- [1]. A. M Riley., et al. "Factors affecting the impact properties of mineral filled polypropylene", *Plastics and rubber processing and applications*, (1990), 14.2, pp. 85-93.
- [2]. M., Hussain, A., Nakahira, K Niihara, "Mechanical property improvement of carbon fiber reinforced epoxy composites by Al<sub>2</sub>O<sub>3</sub> filler dispersion", *Materials Letters*, 26(3), (1996), pp. 185-191.
- [3]. X. Ji, Y. Xu, W. Zhang, L. Cui, J. Liu, "Review of functionalization, structure and properties of graphene/polymer composite fibers", *Compos Part A*, 87 (2016), pp. 29–45.
- [4]. Rawat, P., Singh, Kalyan Kumar, "An impact behavior analysis of CNT-based fiber reinforced composites validated by LS-DYNA: A review", *Polymer Composites*, 2015.
- [5]. G. Mittal, Y.R. Kyong, J.P. Soo, D. Hui, "Generation of the pores on graphene surface and their reinforcement effects on the thermal and mechanical properties of chitosan-based composites", *Compos Part B Eng*, 114 (2017), pp. 348–355.
- [6]. M.R. Zakaria, M.H.A. Kudus, H.M. Akil, M.Z.M. Thirmizir, "Comparative study of graphene nanoparticle and multiwall carbon nanotube filled epoxy nanocomposites based on mechanical, thermal and dielectric properties", *Compos Part B Eng*, 119 (2017), pp. 57–66.
- [7]. H.S. Shen, Y. Xiang, Feng Lin, D. Hui, "Buckling and postbuckling of functionally graded graphene-reinforced composite laminated plates in thermal environments", *Compos Part B Eng*, 119 (2017), pp. 67–78.

- [8]. B. Zhang, R. Asmatulu, S.A. Soltani, L.N. Le, S.S.A. Kumar, “Mechanical and thermal properties of hierarchical composites enhanced by pristine graphene and graphene oxide nano-inclusions”, *J Appl Poly Sci*, 131 (2014), p. 40826.
- [9]. X. Du, H. Zhou, W. Sun, H.Y. Liu, G. Zhou, “Graphene/epoxy interleaves for delamination toughening and monitoring of crack damage in carbon fibre/epoxy composite laminates”, *Compos Sci Technol*, 140 (2017), pp. 123–133.
- [10]. W. Qin, F. Vautard, L.T. Drzal, J. Yu, “Mechanical and electrical properties of carbon fiber composites with incorporation of graphene nanoplatelets at the fiber–matrix interphase”, *Compos Part B Eng*, 69 (2015), pp. 335–341.
- [11]. X.Q. Zhang, X.Y. Fan, C. Yan, H.Z. Li, Y.D. Zhu, X.T. Li, *et al.*, “Interfacial microstructure and properties of carbon fiber composites modified with graphene oxide”, *ACS Appl Mater Interfaces*, 4 (3) (2012), pp. 1543–1552.
- [12]. L.W. Zhang, Y. Zhang, K.M. Liew, “Vibration analysis of quadrilateral graphene sheets subjected to an in-plane magnetic field based on nonlocal elasticity theory”, *Compos Part B Eng*, 118 (2017), pp. 96–103.
- [13]. S.Y. Huang, G.P. Wu, C.M. Chen, Y. Yang, S.C. Zhang, C.X. Lu, “Electrophoretic deposition and thermal annealing of a graphene oxide thin film on carbon fiber surfaces”, *Carbon*, 52 (2013), pp. 613–616.
- [14]. X. Du, I. Skachko, A. Barker, E.Y. Andrei, “Approaching ballistic transport in suspended graphene”, *Nat Nanotech*, 3 (2008), pp. 491–495.
- [15]. M.S. Madhukar, L.T. Drzal, “Fiber–matrix adhesion and its effect on composite mechanical properties: I. In plane and interlaminar shear behavior of graphite/epoxy composites”, *J Compos Mater*, 25 (1991), pp. 932–957.
- [16]. M.A. Rafiee, J. Rafiee, I. Srivastava, Z. Wang, H. Song, Z.Z. Yu, *et al.*, “Fracture and fatigue in graphene nanocomposites”, *Small*, 6 (2010), pp. 179–183.
- [17]. ISO 179–181 Plastics – Determination of Charpy impact properties – Part 1: non-instrumented impact test (2010)
- [18]. Bulut, M., “Mechanical characterization of basalt/epoxy composite laminates containing graphene nanopellets”, *Composites Part B: Engineering*, 2017.

# Combined Natural Convection and Thermal Radiation in an Inclined Cubical Cavity with a Rectangular Pins Attached to Its Active Wall

Z. Sert<sup>1</sup>, M. Tekkalmaz<sup>1</sup>, C. Timuralp<sup>1</sup>

<sup>1</sup>Departement of Mechanical Engineering, Eskisehir Osmangazi University

---

## Article Info

### Article history:

Received May 30<sup>th</sup>, 2017

Revised Aug 20<sup>th</sup>, 2017

Accepted Oct 18<sup>th</sup>, 2017

---

### Keyword:

Heat transfer  
Inclined cubic enclosure  
Natural convection  
S2S radiation

---

## ABSTRACT

Three dimensional combined natural convection and thermal radiation in an inclined cubic enclosure with pins attached to the active wall is investigated numerically. The vertical opposing walls are heated and cooled while the other walls are assumed to be adiabatic. The governing flow, momentum equations and the radiative transfer are solved using Fluent® 6.3 CFD software. In the discretization of the convection terms, the second order upwind scheme and for the solution algorithm SIMPLE is used. The cubic enclosure is filled with air and the flow is considered to be laminar. The properties of air are assumed to be constant except for the density variation for which the Boussinesq approximation is used. The surface to surface (S2S) heat model is used as the radiation transfer model. The computations are performed for Rayleigh number in the range  $10^3 \leq Ra \leq 10^6$  and for the surface emissivity ( $\epsilon$ )  $0 \leq \epsilon \leq 1$  while the inclination angle is varied  $0^\circ \leq \phi \leq 75^\circ$ . The mean Nusselt number for convection and radiation transfer were evaluated as a function of Rayleigh number, emissivity and inclination angle and for some cases, the fluid flow and the temperature distributions were analyzed. The results showed that the mean total and radiative Nusselt number increases monotonically with increasing Ra number and the surface emissivity.

---

### Corresponding Author:

C. Timuralp,  
Department of Mechanical Engineering,  
Eskisehir Osmangazi University,  
Bati-Meselik 26480 Eskisehir, Turkey.  
Email: [cisil@ogu.edu.tr](mailto:cisil@ogu.edu.tr)

---

## 1. Introduction

The natural convection and thermal radiation heat transfer in fluid filled cavities has received considerable attention in recent years due to its relation to the thermal performance of engineering applications such as cooling of electronic components, electrical boxes, solar energy collector designs and heat exchanger designs so on. Thus, the combined characteristic of natural convection and thermal radiation heat transfer are more important.

Baig and Masood [1], numerically studied the two-dimensional natural convection phenomena in a rotating and differentially heated square enclosure. The results are presented in terms of the Rayleigh, Taylor numbers and rotational Rayleigh number. It is found that a significant enhancement in heat transfer can be achieved due to rotational effects. Rahman and Sharif [2], numerically investigated laminar natural convection in rectangular enclosures of different aspect ratios and at various angles of inclination. At certain inclinations the local heat flux ratios increased initially and then decreased. Jin et al. [3], investigated the effects of rotation on natural convection cooling in a rectangular cavity. It is observed that rotation reduced oscillation in Nusselt number and improved heat transfer in the weak stages. Cheng and Liu [4], performed the effects of cavity inclination, Richardson number and the aspect ratio on the mixed convection heat transfer in two-dimensional

cavity flows. The results indicated that in a forced convection dominated regime, the increase of inclination angle does not affect the flow structures and heat transfer; but for  $Ri=100$  it has a significant impact on the flow and thermal fields. Saleh and Hashim [5], studied the problem of conjugate convection heat transfer in a rotating square enclosure numerically. They presented the results for flow fields and heat transfer performance of rotating enclosure in graphical forms.

Impacts of inclination in natural convection was studied three-dimensional enclosures. Li and Tong [6], carried out natural convective heat transfer in the inclined rectangular cavities using three-dimensional numerical simulations and experimental measurements. With the increase in the aspect ratio and the cavity inclination angle resulted in accelerated natural convection and enhanced the convective heat transfer in the cavity. Awasarmol and Pise [7], experimentally investigated natural convection heat transfer enhancement of perforated rectangular fin array at different angles of inclination. They observed that the perforation of fins enhances the heat transfer dissipation rates and the optimum perforation diameter depends the inclination angle.

The thermal radiation heat transfer plays an important role in cases where it cannot be ignored or neglected. Ramesh and Venkateshan [8], experimentally examined the effect of surface radiation on the natural convection in a square 2D enclosure. Correlations for convective Nusselt number, radiative Nusselt number, and total Nusselt number are given in terms of Grashof number. Bouali et.al [9], analyzed the radiation-natural convection interactions in an inclined rectangular enclosure with and without inner body numerically. The results showed that the inclination angle affects the isotherms and streamline values for both cavities and radiation heat transfer increases the average Nusselt number without body case. The radiation-natural convection heat transfer in inclined rectangular enclosures containing multiple partitions was investigated by Rabhiet. al. [10]. The results showed that the radiation increases the Nusselt number significantly. Nouanegueet. al. [11], investigated the effect of the surface radiation on the conjugate heat transfer by natural convection and conduction in an inclined square enclosure. They observed that the radiation affected the flow and temperature fields. Interaction effects between laminar natural convection and surface radiation in tilted square and shallow enclosures have been determined by Vivek et.al. [12]. They found that interaction effects are much stronger in shallow enclosures compared to square enclosures.

The present study investigates numerically combined laminar natural convection and thermal radiation heat transfer in an inclined cubic enclosure. The enclosure is assumed to be cubical in form. The enclosure is heated on one vertical wall and cooled from an opposite wall, while the other walls are adiabatic.

## 2. Mathematical Formulation

The studied geometry and coordinate system of the considered enclosure in the present study are depicted in Figure 1. Pins with dimensions are  $(0.1H \times 0.1H \times 0.6H)$  are attached to hot wall of the cubical enclosure whose dimensions are  $H \times H \times H$ . The hot wall (with the pins) and cold wall are isothermal while the side walls are adiabatic. The enclosure is filled with air ( $Pr=0.71$ ).

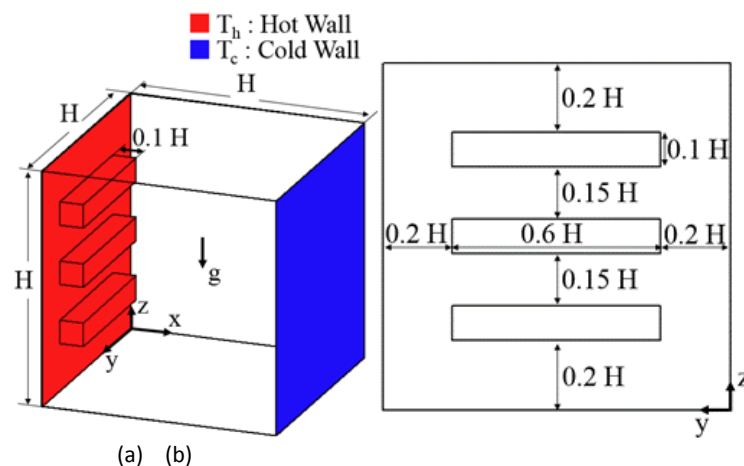


Figure 1. Schematic diagram of the computational domain. a) isometric, b) front view.

The governing continuity, flow and energy equations are given respectively,

for the continuity,

$$\frac{\partial u}{\partial x} + \frac{\partial v}{\partial y} + \frac{\partial w}{\partial z} = 0 \quad (1)$$

for the x, y and z momentum equations

$$u \frac{\partial u}{\partial x} + v \frac{\partial u}{\partial y} + w \frac{\partial u}{\partial z} = -\frac{1}{\rho} \frac{\partial P}{\partial x} + \nu \left[ \frac{\partial^2 u}{\partial x^2} + \frac{\partial^2 u}{\partial y^2} + \frac{\partial^2 u}{\partial z^2} \right] \quad (2)$$

$$u \frac{\partial v}{\partial x} + v \frac{\partial v}{\partial y} + w \frac{\partial v}{\partial z} = -\frac{1}{\rho} \frac{\partial P}{\partial y} + \nu \left[ \frac{\partial^2 v}{\partial x^2} + \frac{\partial^2 v}{\partial y^2} + \frac{\partial^2 v}{\partial z^2} \right] \quad (3)$$

$$u \frac{\partial w}{\partial x} + v \frac{\partial w}{\partial y} + w \frac{\partial w}{\partial z} = -\frac{1}{\rho} \frac{\partial P}{\partial z} + \nu \left[ \frac{\partial^2 w}{\partial x^2} + \frac{\partial^2 w}{\partial y^2} + \frac{\partial^2 w}{\partial z^2} \right] - g\beta(T - T_0) \quad (4)$$

for the energy

$$u \frac{\partial T}{\partial x} + v \frac{\partial T}{\partial y} + w \frac{\partial T}{\partial z} = \alpha \left[ \frac{\partial^2 T}{\partial x^2} + \frac{\partial^2 T}{\partial y^2} + \frac{\partial^2 T}{\partial z^2} \right] \quad (5)$$

where  $u, v, w$  is the velocity,  $\rho$  is the density,  $P$  is the pressure,  $\nu$  is the kinematic viscosity,  $\beta$  is the thermal expansion coefficient,  $T$  is the temperature,  $\alpha$  is the thermal diffusivity. Prandtl and Rayleigh numbers are defined as  $Pr = \nu/\alpha$  and  $Ra = g\beta(T_h - T_c)H^3/\nu\alpha$  respectively.

The boundary conditions can be written as follows:

a) At the cold wall

$$T = T_c, u = v = w = 0 \quad (6)$$

b) At the hot wall

$$T = T_h, u = v = w = 0 \quad (7)$$

c) At the insulated walls (The adiabatic walls)

$$q_c + q_r = 0 \text{ or } -k \frac{\partial T}{\partial n} + q_r = 0 \quad (8)$$

where  $n$  is the perpendicular direction to pertinent wall,  $q_r$  is also the radiation heat flux on the corresponding insulated wall.

The mean total Nusselt number for cold wall is calculated by,

$$Nu_t = Nu_c + Nu_r = \frac{q_c + q_r}{k(T_h - T_c)/H} \quad (9)$$

where  $q_c$  convection heat flux.

### 3. Numerical Methodology And Validation Of The Numerical Code

In this study, the continuity, momentum and the energy equations are solved using the commercially available code Fluent® 6.3. The flow field in the computational domain is solved using SIMPLE algorithm with the second order upwind scheme. The convergence criterion for the inner iterations was  $10^{-5}$  for the continuity, momentum and energy equations while under-relaxation factors are set to the default values in the program. The analysis is performed for the Rayleigh number which is varied between  $10^3$  and  $10^6$  while the emissivity is  $0 \leq \epsilon \leq 1$ . The inclination angle is taken  $0^\circ$ ,  $15^\circ$ ,  $30^\circ$ ,  $60^\circ$  and  $75^\circ$  respectively.

The present numerical scheme was validated against various numerical results available in the literature. To determine the grid independent solutions, a comparison of the mean convective Nusselt numbers (or the mean total Nu numbers – pure natural convection ( $\epsilon=0$ )) with the published results for a bare cubic enclosure (with no pins) for various Rayleigh numbers is provided in Table 1.

The variation of the mean total Nusselt number at cold wall for various grids are shown in Figure 2. For verification of the numerical solutions validations with solved problems in the literature have been carried out. The independence of the solution with respect to the grid size has been examined for different Rayleigh numbers,  $\epsilon=1$  and  $\phi=0^\circ$ . Three grid configurations consisting of  $50 \times 50 \times 50$ ,  $80 \times 80 \times 80$  and  $100 \times 100 \times 100$  have been used. As can be observed from the Figure 2, a uniform  $80 \times 80 \times 80$  grid was found to be sufficiently fine for the numerical analysis.

Table 1. Effect of the grid size on  $Nu_t$  for the bare cubic enclosure (without no pins)

Ra	Nu				
	Colomer et. al. [13]	Böcü and Altaç [14]	Present Study		
			$50 \times 50 \times 50$	$80 \times 80 \times 80$	$100 \times 100 \times 100$
$10^3$	1.055	1.0706	1.071	1.071	1.071
$10^4$	2.030	2.0575	2.064	2.059	2.058
$10^5$	4.334	4.3598	4.399	4.363	4.354
$10^6$	8.862	8.7945	9.038	8.801	8.744

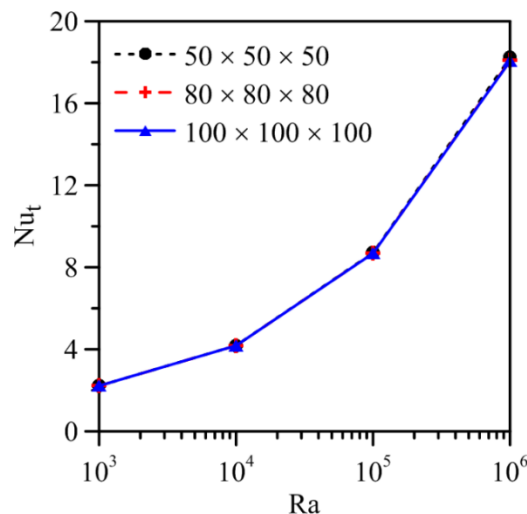


Figure 2. Variation of the mean total Nusselt number at cold wall with mesh parameters.

#### 4. Results And Discussions

The presented results are generated for different dimensionless groups, such as the Rayleigh number ( $10^3 \leq Ra \leq 10^6$ ), the surface emissivity ( $0 \leq \epsilon \leq 1$ ) and the inclination angle of cubical enclosure ( $0^\circ \leq \phi \leq 75^\circ$ ). The enclosure is filled with air where constant Pr number is kept at 0.71. The predicted hydrodynamic and thermal fields variables are depicted through the streamlines, the temperature iso-surfaces, and the corresponding velocity and temperature profiles. The mean total, radiative and convective Nusselt number is also represented in order

to supply useful information about the influence of each parameter, quoted above, on heat transfer enhancement.

Figure 3 shows the effects of  $Ra = 10^4, 10^5, 10^6$ , on isotherms and path lines (colored by temperature) as well as on temperature field (along  $x/H=0.05$  and  $z/H=0.1$  planes) for the present configuration at  $\varepsilon=0.75, \varphi=0^\circ$ . The flow for all  $Ra$  numbers in this work have been affected by the buoyancy force. For  $Ra=10^4$ , the buoyancy force is not so significant. However, when  $Ra$  number is increased to  $10^5$  and  $10^6$ , the buoyancy force becomes more pronounced, and the difference caused by the inhomogeneity of medium declines. While increased Rayleigh number, as evidenced by the value of path lines, the circulation becomes stronger. Thus, more energy is transported into the medium from the hot wall. When examined the temperature fields (along  $x/H=0.05$  and  $z/H=0.1$  planes) for high  $Ra$  numbers, the temperature gradients around the pins increase. Hence the heat flux augments.

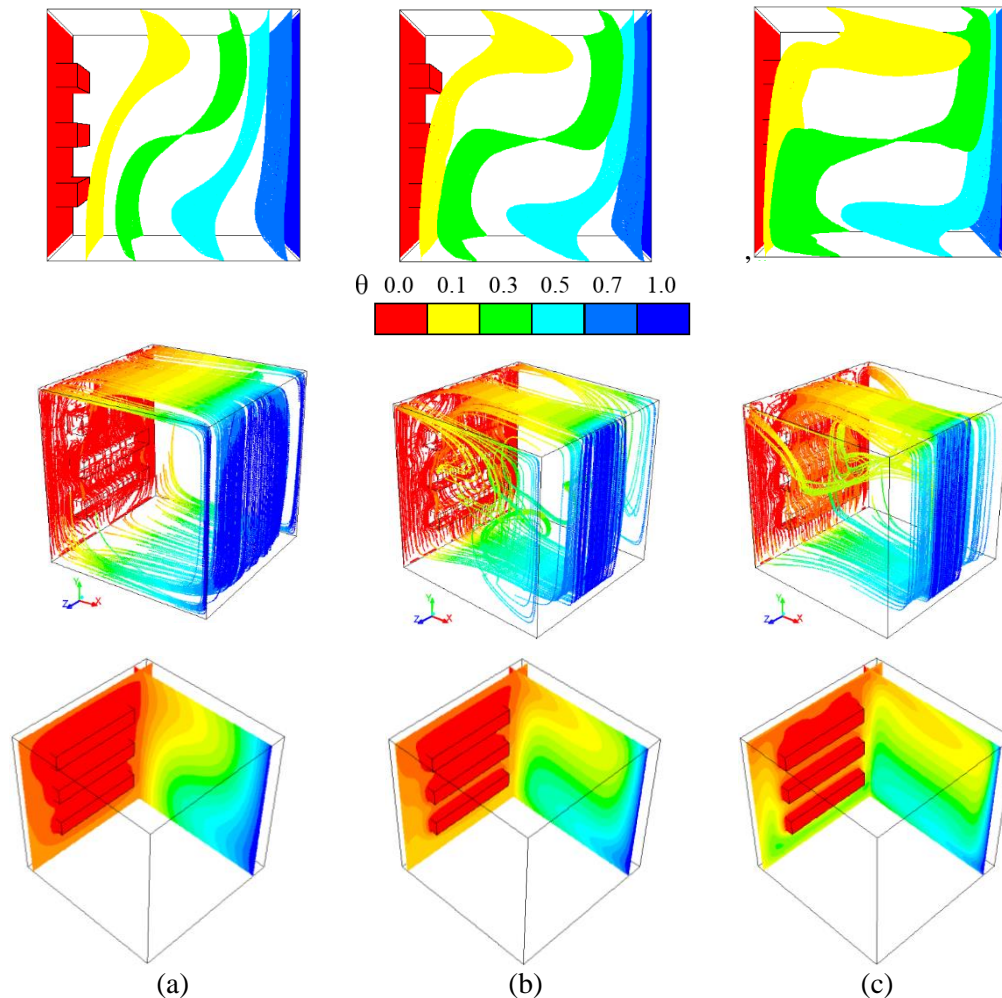


Figure 3. The effect of Rayleigh number on isothermal surfaces (top), path lines (colored by temperature) (middle) and temperature field along  $x/H=0.05$  and  $z/H=0.1$  planes (below) for  $\varepsilon=0.75, \varphi=0^\circ$  and a)  $Ra=10^4$ , b)  $Ra=10^5$ , c)  $Ra=10^6$ .

Figure 4 shows a three-dimensional velocity and temperature fields for different values of the inclination angle ( $\varphi=0^\circ, 30^\circ$  and  $60^\circ$ ) at  $\varepsilon=0.5$  and  $Ra=10^5$ . The fluid flow patterns are reported using pathlines graphs, whereas the temperature fields are shown using isotherms graphs. The isotherms and streamlines are concentrated on the surface of hot and cold wall. Further, it is observed that the nature of the streamlines and isotherms do not change significantly as the angle of inclination changes. When the enclosure has an inclination angle of  $30^\circ$ , the velocity magnitude of the airflow is larger values than those of the flow when the enclosure is not inclined.

The variation of the mean total, radiative and convective Nusselt number with the Rayleigh number for several surface emissivities is briefly sketched in Figure 5. Independently of surface radiation, the mean all Nu numbers increases with increasing Ra number. Moreover, the surface thermal radiation in the heat transfer problems plays an important role. The mean total and radiative Nusselt number increase considerably with increasing the surface emissivity. In comparison with pure natural convection, when the surface emissivity is existed, the total and radiative heat flux increase. The mean total Nu number is two times higher when the surfaces are black ( $\epsilon=1$ ) only in case of pure natural convection. But with the effect of surface radiation, the mean convective Nu number changes. With increasing surface radiation, at high Ra numbers, the mean convective Nu number decrease modestly.

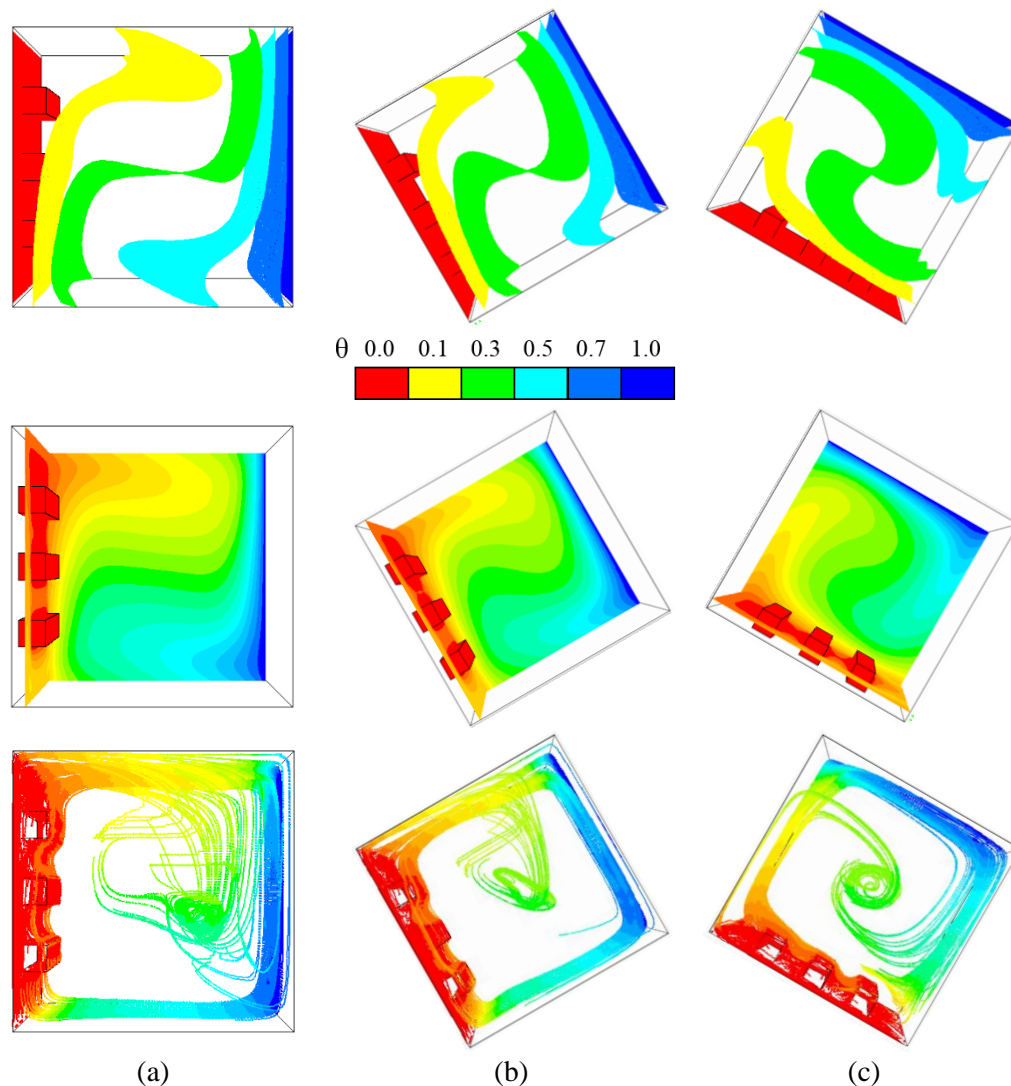


Figure 4. The effect of inclination angle on isothermal surfaces (top), temperature field along  $x/H=0.05$  and  $z/H=0.1$  planes (middle) and path lines (colored by temperature) (below) for  $\epsilon=0.5$ ,  $Ra=10^5$  and a)  $\varphi=0^\circ$ , b)  $\varphi=30^\circ$ , c)  $\varphi=60^\circ$ .

The effect of inclination angle and the surface emissivity on the mean total Nusselt number is depicted in Figure 6. The analysis has been conducted in a wide range of the inclination angle:  $\varphi=0^\circ$ ,  $15^\circ$ ,  $30^\circ$ ,  $45^\circ$ ,  $60^\circ$  and  $75^\circ$ . It is also observed that the heat transfer increases at first and then decreases with increasing inclination of the enclosure, therefore the total mean Nusselt number reaches its maximum at a specific inclination angle where the maximum heat transfer is detected at about  $\varphi = 30^\circ$ . Within the three surface emissivities provided, the relationship between the inclination angle of the enclosure and the mean total Nu number shows similar characteristics.

Figure 7 shows the mean total Nu numbers versus Ra numbers for cubical enclosure with rectangular pins and bare cubical enclosure. As shown in Figure 7, the slope of the mean total Nu numbers versus Ra is greater for the enclosure with rectangular pins compared with bare enclosure, which means a considerable enhancement of heat transfer due the addition of pins. For high surface emissivity, relative difference is nearly %10-6.5, but also for low surface emissivity, relative difference is nearly %3-4.5.

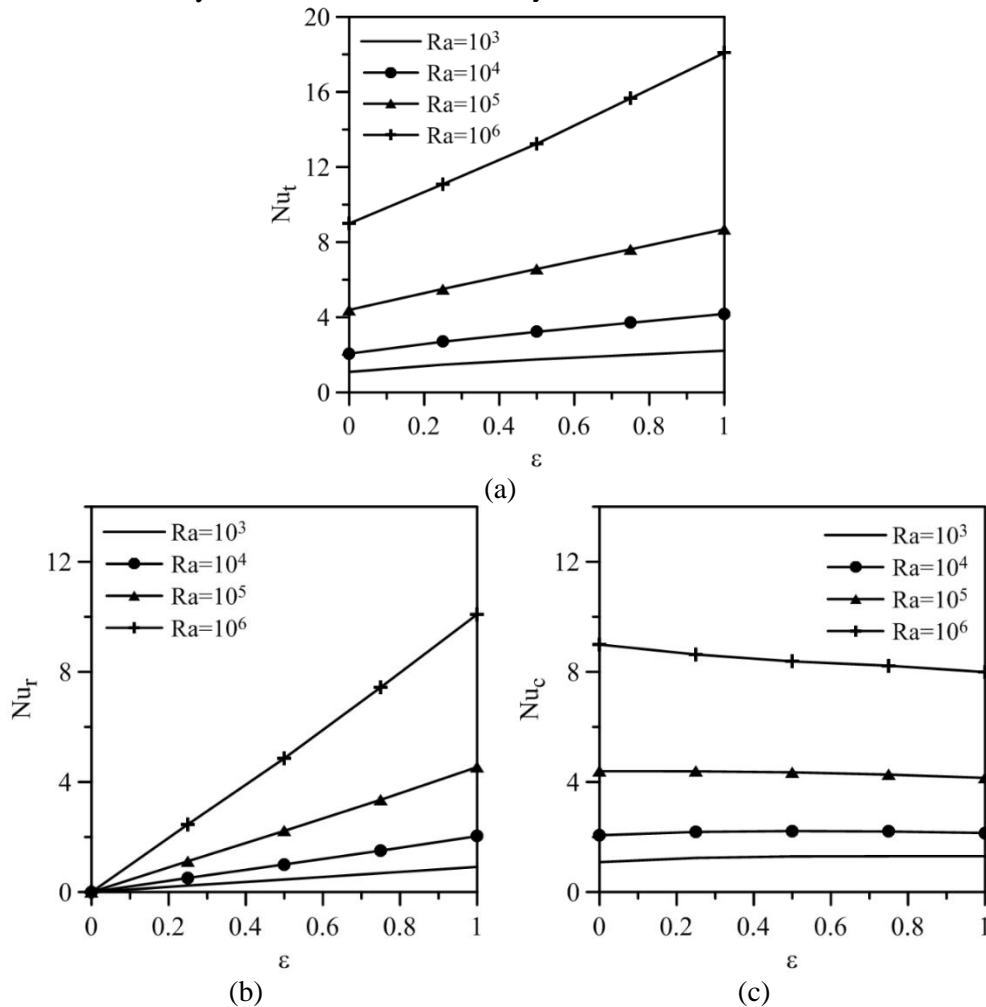


Figure 5. Variation of the mean a) total, b) radiative and c) convective Nusselt number with the surface emissivity and Rayleigh number at  $\phi=0^\circ$ .

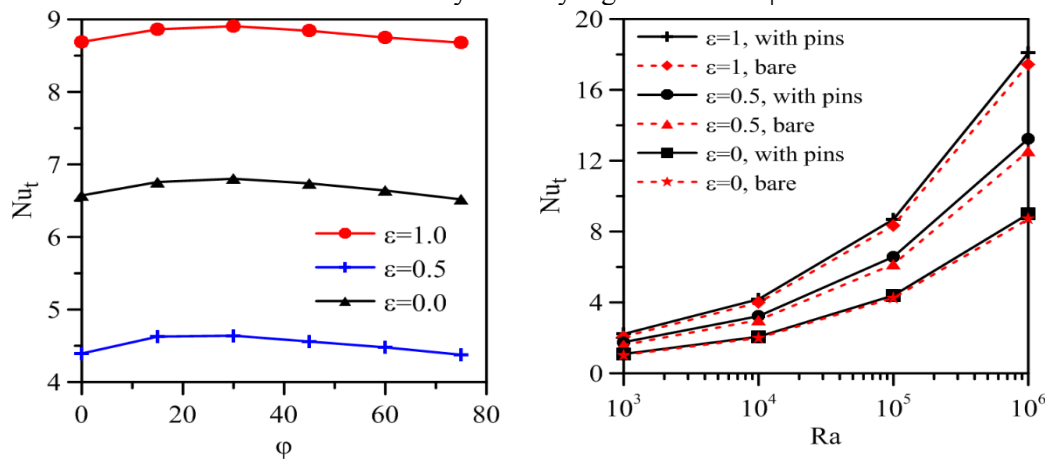


Figure 6. Variation of the mean total Nusselt number with inclination angle for different surface emissivity at  $Ra = 10^5$ .

Figure 7. Comparison of the mean Nu number in bare and with pins cubic enclosure at  $\phi=0^\circ$ .

## 5. Conclusion

Based on these results, the following results was obtained:

- Independently of surface radiation, the mean total, radiative and convective Nusselt number increases monotonically with increasing Rayleigh number and a major part of the enclosure is employed by the flow, especially at high Rayleigh numbers.
- The mean total and radiative Nusselt number increase considerably with increasing the surface emissivity.
- The mean total and convective Nusselt number increases first then decreases, with increasing inclination of the cubic enclosure for all cases.
- The presence of the rectangular pins has significant effects on heat and flow characteristics in the cubic enclosure.

## References

- [1]. M. F. Baigand A. Masood, “Natural convection in a two-dimensional differentially heated square enclosure undergoing rotation”, *Numerical Heat Transfer Part A: Applications*, vol. 40, pp. 181-202, 2001.
- [2]. M. Rahmanand M. A. R. Sharif, “Numerical study of laminar natural convection in inclined rectangular enclosures of various aspect ratios”, *Numerical Heat Transfer Part A*, vol. 44, pp. 355-373, 2003.
- [3]. L.F. Jin, K.W. Tou, C.P. Tso, “Effects of rotation on natural cooling from three rows of heat sources in a rectangular cavity”, *International Journal of Heat and Mass Transfer*, vol. 48, pp. 3982-3994, 2005.
- [4]. T.S. Cheng and W.H. Liu, “Effects of cavity inclination on mixed convection heat transfer in lid-driven cavity flows”, *Computers & Fluids*, vol.100, pp.108-122, 2014.
- [5]. H. Saleh and I. Hashim, “Conjugate natural convection heat transfer in a rotating enclosure”, *Journal of Applied Fluid Mechanics*, vol. 9, pp. 945-955, 2016.
- [6]. H. Li, S. Tong, “Natural convective heat transfer in the inclined rectangular cavities with low width-to-height ratios”, *International Journal of Heat and Mass Transfer*, vol. 93, pp. 398-407, 2016.
- [7]. U. V. Awasarmol and A. T. Pise, “An experimental investigation of natural convection heat transfer enhancement from perforated rectangular fins array at different inclinations”, *Experimental Thermal and Fluid Science*, vol. 68, pp. 145-154, 2015.
- [8]. N. Ramesh and S.P. Venkateshan, “Effect of surface radiation on natural convection in a square enclosure”, *Journal of Thermophysics and Heat Transfer*, vol. 13, pp. 299-301, 1999.
- [9]. H. Bouali, A. Mezrhab, H. Amaoui, M. Bouzidi, “Radiation-natural heat transfer in an inclined rectangular enclosure”, *International Journal of Thermal Sciences*, vol. 45, pp. 553-566, 2006.
- [10]. M. Rabhi, H. Bouali, A. Mezrhab, “Radiation-natural convection heat transfer in inclined rectangular enclosures with multiple partitions”, *Energy Conversion and Management*, vol. 49, pp. 1228-1236, 2008.
- [11]. H.F. Nouanegue, A. Muftuoglu, E. Bilgen, “Heat transfer by natural convection, conduction and radiation in an inclined square enclosure bounded with a solid wall”, *International Journal of Thermal Sciences*, vol. 48, pp. 871-880, 2009.
- [12]. V. Vivek, A.K. Sharma, C. Balaji, “Interaction effects between laminar natural convection and surface radiation in tilted square and shallow enclosures”, *International Journal of Thermal Sciences*, vol. 60, pp.70-84, 2012.
- [13] G. Colomer, M. Costa, R. Consul, A. Oliva, “Three dimensional numerical simulation of convection and radiation in a differentially heated cavity using the discrete ordinates method”, *International Journal of Heat and Mass Transfer*, vol. 47, pp. 257-269, 2004.
- [14] Z. Böcü and Z. Altaç, “Laminar natural convection heat transfer and air flow in three-dimensional rectangular enclosures with pin arrays attached to hot wall”, *Applied Thermal Engineering*, vol. 31, pp. 3189-3195, 2011.

## Kinetic Study of the Thermal Decomposition for Mixed Municipal Solid Waste Using Thermogravimetric Analysis

Nzioka Antony Mutua<sup>1</sup>, Alunda Benard Ouma<sup>2</sup>, Odero Shirley Atieno<sup>3</sup>

<sup>1</sup>Department of Environmental and Energy Engineering, Kyungpook National University, Republic of Korea

<sup>2</sup>Department of Mining and Mineral Processing Engineering, Taita Taveta University, Kenya

<sup>3</sup>World Food Programme, Kenya

### Article Info

#### Article history:

Received May 30<sup>th</sup>, 2017

Revised Aug 20<sup>th</sup>, 2017

Accepted Oct 18<sup>th</sup>, 2017

#### Keyword:

Thermal decomposition

Temperature

Municipal solid waste

ANOVA

Composition

Activation Energy

### ABSTRACT

Thermal conversion of wastes is one of the perspectivesolution to ‘municipal solid waste’ problem. Thermal conversion process entails thermal decomposition of material with an increase in temperature. This experimental analysis investigated thermal decomposition of municipal solid waste using the thermogravimetric technique. The objective of the analysis was to analyze the changes in kinetic characteristics with changes in the composition of content in sample waste and temperature. Sample waste analyzed consisted of plant organic waste, paper, plastics, wood and inert substance. Proximate and elemental analyses were determined and calorific values determined experimentally using bomb calorimeter. Thermogravimetric curves were derived using thermogravimetric analyzer (TGA) at different temperature rates. Activation energy and preexponential factor were derived using Flynn-WallOzawa, KissingerAkahiraSunose and Kissinger model equations. Additional statistical analyses of variance using ANOVA was conducted for the different sets of composition analyzed. Results showed kinetic parameter values for different model free models used in analysis as well as the level of variance in activation energies for different composition of waste and temperature rates used.

### Corresponding Author:

Nzioka Antony Mutua

Department of Environmental and Energy Engineering,

Kyungpook National University,

Daehak-ro 80, Buk-gu, College of Engineering, Daegu, 41566, Republic of Korea

Email: [manymutua@knu.ac.kr](mailto:manymutua@knu.ac.kr)

## 1. Background

There are different solutions proposed by researchers seeking to reduce the adverse effects of accumulating municipal solid wastes (MSW) in countries with developing and emerging economies. One of the perspective solutions is thermal conversion processes which may such processes such as pyrolysis, waste-to-energy, aerobic/anaerobic conversion processes among others [1]–[4]. Previous research showed that recycling and conversion of MSW with high moisture content to refuse derived fuel is feasible and may require minimal treatment [1],[5],[6].

Thermal decomposition process may provide sufficient information so as to understand the thermal conversion process. Thermogravimetric analysis is one of the perspective methods of studying the thermal decomposition process of any material including MSW. Some researchers have presented valuable data related to the thermogravimetric analysis of the MSW [7]–[9]. Research presented in the publications mentioned above focussed on the kinetic characteristics of the components or a combination of components in the MSW. It is, in our opinion, of utmost importance to study the sample material (i.e. MSW) with all the components combined.

Therefore, the objectives of this research are to study the thermal decomposition of MSW, derive the kinetic characteristics as well as study the effect of changes in the composition of MSW on the kinetic characteristics of the thermal decomposition process.

## 2. Materials and methods

### 2.1. Materials

Sample MSW consisted of plant wastes, shredded plastics and paper and wood chips. In this research, we used combustible materials and excluded all possible inert materials (glass, soil, metals etc.) We prepared two sets of samples as shown in Table 1 based on other references [5], [10], [11]. The particle size of sample MSW was <20 mm recommended by Athanaopolous [12], and reference [13] provided mathematical formulation for determining the particle size of our sample MSW. The sample MSW used in this research was prepared on as received basis. We conducted this experimental study based on the workflow presented in Figure 1.

We prepared sample MSW and used approximately 200 g. We dried the sample MSW at a temperature of 80°C for 24 hours. We used ASTM E955 – 88 standards to determine ash content on “dry material” basis [14].

Table 1. Composition of the sample MSW used in the experimental study

Mixing proportion, (% weight basis) for “as received” MSW		
Component	Set 1	Set 2
Plant wastes	73	52
Shredded paper	11	21
Shredded plastics	11	21
wood	5	6
Proximate analysis		
Ash content, (%)	6 ∞ 12	10 ∞ 12
*Moisture content, (%)	55 ∞ 56	35 ∞ 38
*Bulk Density, (kg/m <sup>3</sup> )	85 ∞ 109	60 ∞ 76

#### Remark:

Mixing proportion provided in this table is based on previous research [5]

\* - “as received” basis

References [4], [5] provided formula for calculating the bulk density for “as-received” MSW. We calculated the gross calorific values using bomb calorimeter (plain-jacket oxygen bomb-type, Parr Instrument Company-USA). Calorific standard (Benzoic acid pellets) used were in accordance with Parr Instrument Company’s (USA) specification. We calculated appropriate corrections from the “after-combustion” remains of the bomb calorimeter: these corrections are specified in the analytical equipment’s manual. Net calorific values were determined using empirical formulas provided by Ilinkh [15] as well as ASTM E955-88 standards [14]. The formula (1) was suggested by Ilinkh while (2) by ASTM E955 – 88 standards. Calorific values were converted to MJ/kg SI unit. The formulas for calculating the net calorific values are shown below:

$$Q_N = 4600 - 4A - 51.85X \quad (1)$$

$$Q_N = \frac{[100 - (X + A)]Q_g}{100} \quad (2)$$

In the formulas above,  $Q_g$ ,  $Q_N$  represent gross and net calorific values respectively (MJ/kg) while variables  $A$ ,  $X$  represent ash content and moisture content shown in Table 1. We calculated the gross calorific values on “dry material” basis and the net calorific values on “as received” basis.

We analysed the thermal decomposition process using TGA-50 supplied by Shimadzu Scientific (USA) equipped with the thermal analysis workstation (Shimadzu TA-60WS). We reduced the particle size of the sample MSW and prepared pellets using laboratory press machine and a roundshape tablet press(4 mm diameter). TGA analysis was conducted up to 900°C (1173 K) for four different temperature rates (5, 10, 20 and 50 K/min) under inert conditions sustained using argon gas (gas flowrate=10 ml/min).

### 3. Thermal decomposition theory and calculation

General formula used to describe reaction kinetics (i.e. thermal decomposition process) can be written as follows [16]:

$$\frac{dc}{dt} = k(T) f(c) \tag{3}$$

From the equation above, function  $k(T)$  represents the rate constant which conforms with the Arrhenius law. We may express the rate constant as follows:

$$k(T) = Ae^{\frac{-E}{RT}} \tag{4}$$

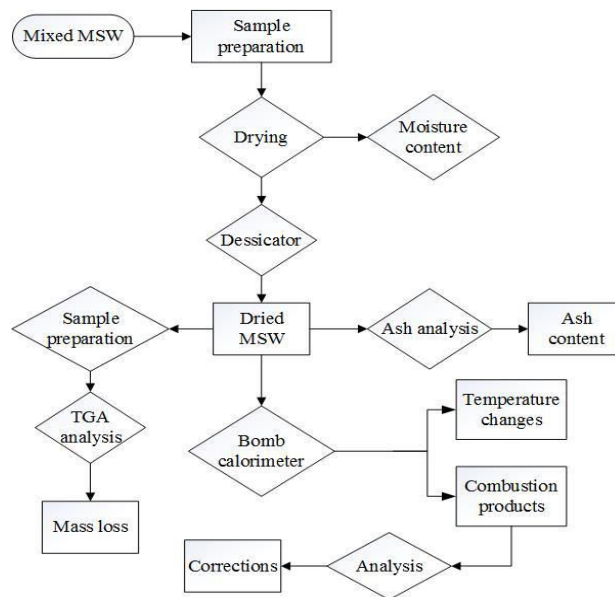


Figure 1. Experimental analysis workflow

where variable  $E$  represent the activation energy(kJ/mol),  $R$  - universal gas constant (j/mol K),  $A$  - pre-exponential factor (/min) and  $T$  - temperature (K). We might justify (3) by assuming that the sample MSW would undergo complex decomposition process generating volatile substances and char[16]. Therefore, we may determine the degree of conversion ( $c$ ) using the following expression[17]:

$$c = \frac{m_{t-start} - m_{t-i}}{m_{t-start} - m_{t-final}} \quad (5)$$

where variables  $m_{t-start}$ ,  $m_{t-final}$ ,  $m_{t-i}$  represent initial, final and mass at the time (i). If we assume that our reaction is first-order ( $n=1$ ), then (3) may be rewritten as follows:

$$\frac{dc}{dt} = (1-c)^n A e^{\frac{-E}{RT}} \quad (6)$$

Formula (6) corresponds to isothermal conditions. Thermogravimetric analysis is conducted under non-isothermal conditions whereby the actual temperature is expressed as a function of heating rates. Therefore, we will rewrite (6) to satisfy the non-isothermal conditions as follows [16]:

$$\frac{dc}{dT} = (1-c)^n \frac{A}{\beta} e^{\frac{-E}{RT}} \quad (7)$$

From the formula above,  $\beta$  represents the rate of heating (K/min) that we will use in thermogravimetric analysis.

In this study, we will use several non-isothermal model equations, namely: Kissinger, Kissinger – Akahira – Sunose and Flynn – Wall – Ozawa. The Kissinger model equation can be described as follows[18]:

$$\ln\left(\frac{\beta}{T_m^2}\right) = \ln\left(\frac{AR}{E}\right) - \frac{E}{RT_m} \quad (8)$$

From the formula above, variable  $T_m$  represent the peak temperature (K) where  $dm_{t-i}/dt = 0$ . We may calculate the activation energy by plotting a graph of  $\ln(\beta/T_m^2)$  versus  $1000/T_m$ . The Kissinger – Akahira – Sunose model equation can be expressed as follows:

$$\ln\left(\frac{\beta}{T_{\alpha(i)}^2}\right) = \ln\left(\frac{A_{\alpha(i)}R}{E_{\alpha(i)}g[\alpha(i)]}\right) - \frac{E_{\alpha(i)}}{RT_{\alpha(i)}} \quad (9)$$

We can calculate the activation energy using model equation (9) mentioned above by plotting a graph of  $\ln(\beta/T_{\alpha(i)}^2)$  versus  $1000/T_{\alpha(i)}$ . From formula (9) variable  $E_{\alpha(i)}$ ,  $T_{\alpha(i)}$  represent activation energy and temperature at conversion value  $\alpha(i)$  respectively. Santos et al. [17] provided precise formulation and explanation of the integral function  $g[\alpha(i)]$ . The final model that we will use in our study (Flynn – Wall – Ozawa) can be expressed as follows:

$$\ln(\beta) = \ln\left(\frac{A_{\alpha(i)}E_{\alpha(i)}}{Rg[\alpha(i)]}\right) - 5.331 - 1.052 \frac{E_{\alpha(i)}}{RT_{\alpha(i)}} \quad (10)$$

From formula (10) we can determine activation energy from the graphical dependence of  $\ln(\beta)$  versus  $1000/T_{\alpha(i)}$ . In this experiment, we will analyse the level of variance for our samples (i.e set 1 and 2). We will use one-way ANOVA analysis for the activation energy values obtained for all the model equation used. The following conditions were considered for the one-way ANOVA test:

- Levene test of variance
- Actual power analysis
- Tukey range test
- Number of Tests = 5

#### 4. Results and discussion

##### 4.1. Gross and net calorific value

Table 2 shows the gross and net calorific values of the mixed MSW. Experimental and empirical results showed that the mixed MSW with low plant wastes content (MSW set 2) had higher calorific value than that with high plant wastes content (i.e. MSW set 1). We obtained these calorific values without including the soil content. Soil, just like many inert compounds, are bound to have an adverse effect the calorific values of MSW since a significant amount of heat may be used in the oxidation /formation of other compounds from the inert substances. Our preliminary analysis coupled with previous research supported our conclusion [19]. The net calorific values calculated using the empirical formulas chose did not differ significantly.

Table 2. Calorific values for mixed MSW

<b>Gross calorific values, MJ/kg</b>		
	<b>Set 1</b>	<b>Set 2</b>
$Q_g$	$14.5 \pm 0.5$	$16.9 \pm 1.2$
<b>Net calorific values, MJ/kg</b>		
Ilinykh (2013)	$6.1 \pm 0.15$	$10 \pm 0.3$
ASTM E955 (2009)	$5.1 \pm 0.3$	$8.6 \pm 0.25$

##### 4.2. Thermal decomposition

Thermal decomposition process was analyzed from the temperature of 300 K to 1073 K. Decomposition reaction showed similar decomposition characteristics for all the temperature rates. These decomposition characteristics were in three stages, namely: dehydration; fast decomposition of high molecular substances such as cellulose, lignin, etc. and subsequent and slow degradation of lower molecular compounds with the formation of char. Dehydration phase ended at a temperature range of 500 – 568 K for MSW set 1 and 495 – 560 K for MSW set 2. The second phase characterising the fast degradation process of high molecular compounds ended at a temperature range of 788 – 872 K for MSW set 1. The final stage began from the temperatures mentioned above till 1173 K. Solid residue for MSW was between 6 – 10% for MSW set 1 and 11 - 12 for MSW set 2 which corresponds to the values obtained from the proximate analysis. Preliminary analysis indicated that the presence of impurities such as inert substances might lead to the formation of anomalous/irregular decomposition behaviour of the MSW.

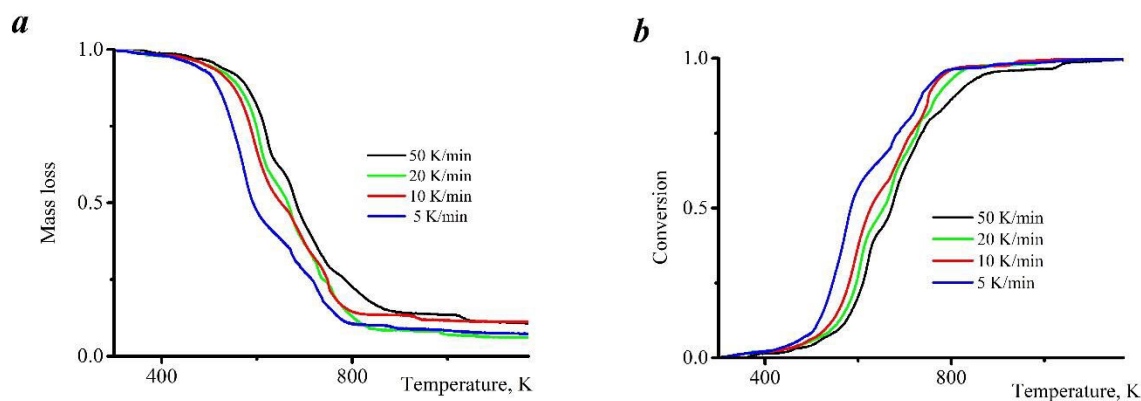


Figure 2. TGA mass loss and conversion curves for MSW set 1. Graph a: TGA mass loss and b: conversion curves.

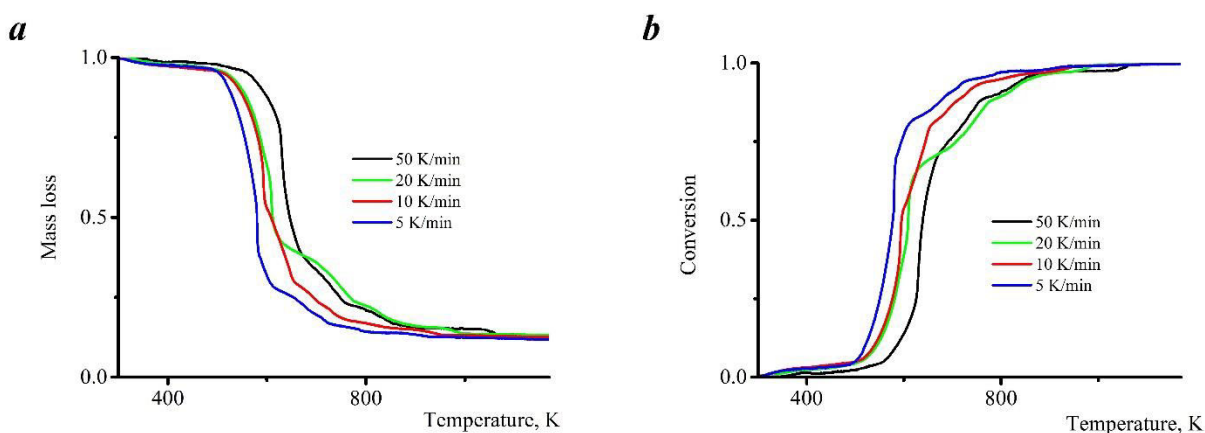


Figure 3. TGA mass loss and conversion curves for MSW set 2: Fig. a - TGA mass loss and b - conversion curves

#### 4.3. Kinetic study and statistical analysis

We derived the linear regression equations for conversion values ranging from 0.1 to 0.8 for Kissinger – Akahira – Sunose / Flynn – Wall – Ozawa model equations and Kissinger Model equations to determine the activation energy values. From the Kissinger model equation, the activation energy values for MSW set 2 were higher than those of MSW set 1: MSW set 2 had a mean activation value of 122.5 kJ/mol while MSW set 1 had 135.6 kJ/mol.

From Kissinger – Akahira – Sunose model equation, the activation energy values ranged from 76 – 90 kJ/mol for MSW set 1 and 78 – 105 kJ/mol for MSW set 2. From the Flynn – Wall – Ozawa model equation, the activation energy values ranged from 75 – 96 kJ/mol for MSW set 1 and 83 – 109 kJ/mol for MSW set 2. From these two model equation, it is evident that MSW set 2 had the average activation energy greater than MSW set 1. This result is in contrast with the values we obtained using the Kissinger model equation.

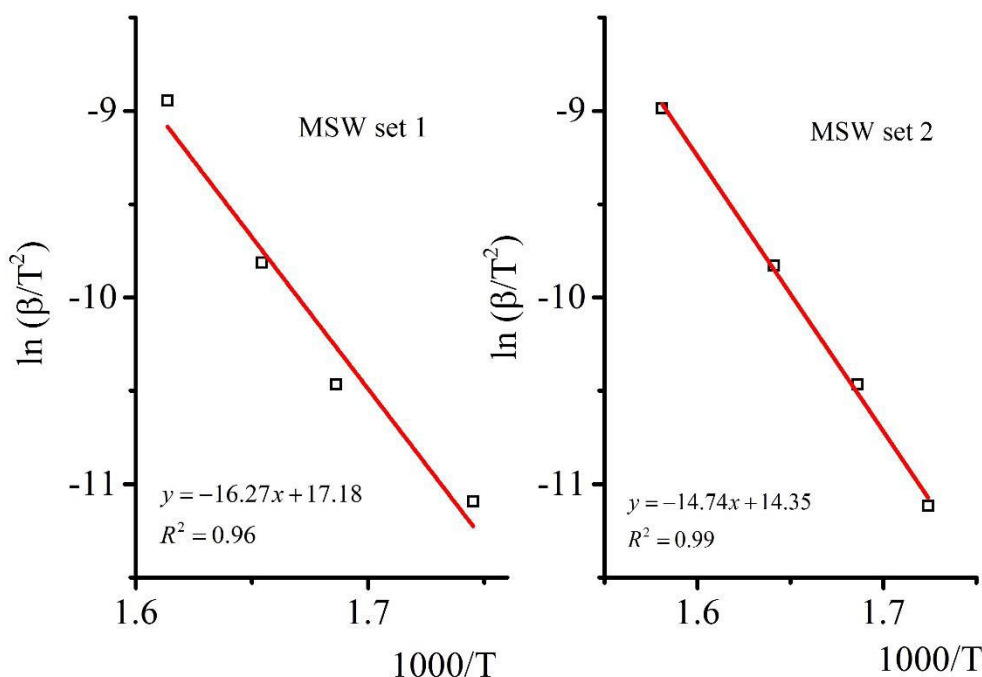


Figure 4. Graphicplots derived using the Kissinger model equation for MSW set 1 and 2

We conducted preliminary thermal decomposition analysis of MSW with inert substances (soil) with the objective of investigating the feasibility of correlating the differences between activation energy values and the organic plant wastes composition. Even though we might correlate such differences with the composition of organic plant wastes in this experimental study, the irregular characteristics of the thermal decomposition of MSW+inert substances from our preliminary analysis with MSW did not support our theory.

Table 3. Linear regression equations derived using Kissinger – Akahira – Sunose model equation

	MSW Set 1			MSW set 2		
	$y = ax + b$	$R^2$	E	$y = ax + b$	$R^2$	E
<b>0.1</b>	$y = -10.84x + 10.9$	0.95	90	$y = -9.51x + 7.58$	0.94	78.9
<b>0.15</b>	$y = -9.95x + 7.97$	0.95	83	$y = -9.25x + 6.55$	0.93	76.9
<b>0.2</b>	$y = -9.7x + 7.02$	0.92	80.6	$y = -9.14x + 5.97$	0.93	76.1
<b>0.25</b>	$y = -9.78x + 6.8$	0.93	81.4	$y = -9.4x + 6.15$	0.93	78.2
<b>0.3</b>	$y = -10.26x + 7.34$	0.92	85.4	$y = -10.18x + 7.28$	0.94	84.8
<b>0.35</b>	$y = -11.06x + 8.44$	0.93	91.2	$y = -10.96x + 8.43$	0.95	91.2
<b>0.4</b>	$y = -11x + 8.06$	0.91	91.5	$y = -11.9x + 9.8$	0.97	98.9
<b>0.45</b>	$y = -8.43x + 3.43$	0.93	67.9	$y = -12.58x + 10.72$	0.99	104.3
<b>0.5</b>	$y = -8.42x + 3.14$	0.93	69.8	$y = -12.58x + 10.72$	0.99	104.5
<b>0.55</b>	$y = -8.3x + 2.62$	0.9	68.8	$y = -12.57x + 10.6$	0.97	104.8
<b>0.6</b>	$y = -9.17x + 3.61$	0.87	76.4	$y = -11.2x + 8.14$	0.91	92.9

Table 4. Linear regression equations derived using Flynn – Wall – Ozawa model equation

	MSW set 1			MSW set 2		
	$y = ax + b$	$R^2$	E	$y = ax + b$	$R^2$	E
<b>0.1</b>	$y = -12.12x + 25.45$	0.96	95.6	$y = -10.61x + 22.2$	0.96	83.6
<b>0.15</b>	$y = -11.05x + 25.6$	0.93	87.5	$y = -10.4x + 21.23$	0.94	82.1
<b>0.2</b>	$y = -10.84x + 21.7$	0.92	85.7	$y = -10.3x + 20.69$	0.96	81.6
<b>0.25</b>	$y = -10.93x + 21.53$	0.92	86.5	$y = -10.58x + 20.9$	0.96	83.7
<b>0.3</b>	$y = -11.43x + 22.1$	0.92	90.4	$y = -11.37x + 22$	0.96	90
<b>0.35</b>	$y = -12.24x + 23.2$	0.93	96.7	$y = -12.16x + 23.21$	0.97	96.2
<b>0.4</b>	$y = -12.2x + 22.86$	0.94	96.5	$y = -13.1x + 24.61$	0.98	103.5
<b>0.45</b>	$y = -10.6x + 19.84$	0.96	83.8	$y = -13.66x + 25.44$	0.99	107.6
<b>0.5</b>	$y = -9.67x + 18$	0.95	76.2	$y = -13.8x + 25.54$	0.99	109.4
<b>0.55</b>	$y = -9.55x + 17.53$	0.91	75.2	$y = -13.8x + 25.4$	0.97	98

We conducted one-way ANOVA test analysis so as to determine the level of similarity/variance between MSW set 1 and 2. ANOVA test for all the cases and model equations showed significant differences between MSW set 2 and MSW set 1

## 5. Conclusion

We investigated the thermal decomposition of MSW, and the following conclusions would be made:

1. Calorific values of MSW set 2 were higher than that of MSW set 1. We could attribute these differences to the composition of MSW.
2. Net calorific values calculated empirically exhibited some similarity
3. The thermal decomposition process for MSW showed similar decomposition characteristics
4. Activation energy values derived using Kissinger model ranged from 135 kJ/mol for MSW set 1 and 122 kJ/mol for MSW set 2.
5. Activation energy using Kissinger – Akahira – Sunose model equation ranged from 76 – 90 kJ/mol for MSW set 1 and 78 – 105 kJ/mol for MSW set 2. MSW set 2 had an average activation energy value greater than that of MSW set 1
6. Activation energy using Flynn – Wall - Ozawa model equation ranged from 75 – 96 kJ/mol for MSW set 1 and 83 – 109 kJ/mol. MSW set 2 had an average activation energy value greater than that of MSW set 1
7. Measurement of variance showed a significant difference in activation energy values.

## References

- [1] A. G. Troshin and A. M. Nzioka, "Method of processing unsorted municipal solid waste utilising heat energy from reciprocating grate cooler during the cooling process," Ukraine Patent № 83321 C1, 2013.
- [2] L. B. Pavlovich, N. Y. Solovyova, E. D. Pavlovskaya, and V. M. Strakhov, "Using polymer waste in coke production," *Coke and Chemistry*, vol. 59, pp. 287–295, Aug. 2016. doi: 10.3103/S1068364X16080068
- [3] K. Miezah, K. Obiri-Danso, Z. Kádár, S. Heiske, B. Fei-Baffoe, M. Mensah and A. S. Meyer, "Municipal Solid Waste Management in a Low Income Economy Through Biogas and Bioethanol Production," *Waste and Biomass Valorization*, vol. 8, pp. 115–127, 2017. doi: 10.1007/s12649-016-9566-5
- [4] L. F. Diaz, G. M. Savage, L. L. Eggerth and L. Rosenberg, *Solid waste management*. Paris: Cal. Recovery Inc. and United Nations Environment Programme, 2005.

- [5] A. M. Nzioka, H. U. Hwang, M. G. Kim, C. Z. Yan, C. S. Lee, and Y. J. Kim, "Effect of storage conditions on the calorific value of municipal solid waste," *Waste Management and Research*, "2017, in press".
- [6] E. L. Morton, L. Szabo, R. Nobis, and S. Alesi, "Method and apparatus for drying wet bio-solids using excess heat from a cement clinker cooler," US Patent № 20050274067, 2008.
- [7] M. Kple, P. Girods, M. Anjorin, B. Fagla, and Y. Rogaume, "Thermal Degradation of Household Solid Waste in the Town of Abomey-Calavi in Benin: Kinetic Study," *Waste and Biomass Valorization*, vol. 7, no. 1, pp. 59–70, Feb. 2016. doi: 10.1007/s12649-015-9441-9
- [8] D. Q. Zhang, P. J. He, and L. M. Shao, "Sorting efficiency and combustion properties of municipal solid waste during bio-drying," *Waste Management*, vol. 29, pp. 2816–2823, 2009. doi: 10.1016/j.wasman.2009.06.024
- [9] F. Jiang, Z. Pan, S. Liu, and H. Wang, "Experimental studies on combustion characteristics of mixed municipal solid waste," *Journal of Thermal Science*, vol. 12, pp. 367–370, Nov. 2003. doi: 10.1007/s11630-003-0046-4
- [10] A. M. Nzioka, M. G. Kim, H. U. Hwang, C. Z. Yan, V. E. Ved, V. P. Meshalkin and Y. J. Kim, "Experimental investigation on the drying of loosely-packed and heterogeneous municipal solid waste," *Theoretical Foundations of Chemical Engineering*, vol. 50, pp. 414–421, Jul. 2016. doi: 10.1134/S0040579516040448
- [11] H. K. Rotich, Y. Zhao and J. Dong, "Municipal solid waste management challenges in developing countries – Kenyan case study," *Waste Management*, vol. 26, pp. 92–100, 2006. doi: 10.1016/j.wasman.2005.03.007
- [12] G. A. Athanasopoulos, "Laboratory Testing of Municipal Solid Waste," in *International Symposium on Waste Mechanics "Geotechnical Characterization, Field Measurement, and Laboratory Testing of Municipal Solid Waste"*, 2008, pp. 195–205. doi: 10.1061/41146(395)7
- [13] R. B. Keey, *Drying of loose and particulate materials*. New York: Hemisphere, 1992.
- [14] *ASTM E955 - 88(2009)e1 Standard Test Method for Thermal Characteristics of Refuse-Derived Fuel Macrosamples*. .
- [15] G. V. Ilinykh, "Evaluation of MSW thermotechnical properties based on its composition," *PNRPU. Applied Ecology and Urban Development*, vol. 3, pp. 125–137, 2013.
- [16] M. Heydari, M. Rahman, and R. Gupta, "Kinetic Study and Thermal Decomposition Behavior of Lignite Coal," *International Journal of Chemical Engineering*, vol. 2015, pp. 1–9, 2015. doi: 10.1061/41146(395)7
- [17] N. A. V. Santos, Z. M. Magriotis, A. A. Saczk, G. T. A. Fássio, and S. S. Vieira, "Kinetic Study of Pyrolysis of Castor Beans (*Ricinus communis* L.) Presscake: An Alternative use for Solid Waste Arising from the Biodiesel Production," *Energy & Fuels*, vol. 29, pp. 2351–2357, Apr. 2015. doi: 10.1021/ef401933c
- [18] H. Hwang, M. Kim, A. Nzioka, Y. Kim, I. Tahir, and C. Yan, "Kinetic characteristics in pyrolysis of RPF with additives," *Journal of Wuhan University of Technology, Material Science Edition*, vol. 31, pp. 1144–1148, 2016. doi: 10.1007/s11595-016-1503-8
- [19] L. L. Baxter, T. R. Miles, T. R. Miles Jr., B. M. Jenkins, T. Milne, D. Dayton, R. W. Bryers and L. L. Oden, "The behavior of inorganic material in biomass-fired power boilers: field and laboratory experiences," *Fuel Processing Technology*, vol. 54, pp. 47–78, 1998.

## Autonomous Car Parking System with Various Trajectories

Bunyamin Esiyok<sup>1</sup>, Anil Can Turkmen<sup>2</sup>, Ozgur Kaplan<sup>2</sup>, Cenk Celik<sup>2</sup>

<sup>1</sup>Department of Electrical and Electronics Engineering, Yeditepe University

<sup>2</sup>Department of Mechanics Engineering, Kocaeli University

---

### Article Info

#### Article history:

Received May 30<sup>th</sup>, 2017

Revised Aug 20<sup>th</sup>, 2017

Accepted Oct 18<sup>th</sup>, 2017

---

#### Keyword:

Autonomous vehicle

Trajectory

Parallel parking

Ultrasonic sensor

Path planning

---

### ABSTRACT

In this study, an algorithm presents a solution to 4-wheel-car parking. This algorithm is suitable for parallel parking between two objects or two cars. Firstly the system verifies whether enough space. After finding a valid parking space, system makes the suitable movements for a perfect parking. This parking operation is tested in a simulation environment using MatLab-Simulink.

---

#### Corresponding Author:

Anil Can Turkmen,

Department of Mechanical Engineering,

Kocaeli University,

Umuttepe Yerleskesi, 41380, Izmit, Kocaeli, Turkey

Email: anilcan.turkmen@hotmail.com

---

### 1. Introduction

New generation cars have serious developments and automobile brands are in competition. Due to this competition, intelligent driver assistance systems are playing a key role while automotive industry is being more automated. Researches show that finding a solution to parallel parking is one of the most needed improvements for drivers. Because parking is a very difficult topic for novice drivers. Especially in crowded cities this problem is getting bigger because number of the car is increasing every day. [1]

The goal of the park assistant system is to help the drivers have more enjoyable and more productive driving experiences. Also another aim is decreasing damages during the parking operation. Parking damages have very bad effect on World's economy. Because countries and insurance companies pays money for simple parking damages and also owners of the cars' sell their cars below its value because of damage history.

System needs ultrasonic sensors that located on the corners of the car. These sensors needed not only for doing parking movements, but also scanning the park area. There are some problems about ultrasonic sensors. For example, thin objects are not seen by this sensors and some environmental changes as temperature, pressure, humidity, air turbulence, airborne particles etc. effect on ultrasonic response. Despite these disadvantages ultrasonic sensors are the most suitable sensor for these systems.

### 2. Literature Survey

In recent years, parking assistance systems were improved in the automotive industry to make perfect movements for perfect parking instead of drivers. Path planning is one of the important problems for parking

operation. For this reason, trajectory planning algorithm needs to be good and creative for a collision-free path starting from the first point to last position, which is described as parking area. Of course this trajectory needs to satisfy all kinematic conditions and limitations of the car model. This kind of problem belongs to the most frequently considered examples in robotics literature, where various solution approaches are available, e.g. planning based on neural-networks, fuzzy-techniques, dynamic programming, numerical continuation methods and two-step algorithms making use of small-time controllability. In any case, rather experimental techniques are connected for this assignment in application. One reason might be that lots of authors analyzed the case of full autonomous-maneuvering, though most versions of assistant systems just control the steering system of the car, but driver still need to control the velocity. One more issue of the systematic technique is that frequently complicated calculations are included which are difficult to achieve progressively. Besides, some of features required by the automotive industry, like that the path founded by the car should be same as the behavior of a real driver or that steering at standstill should be avoided, are rather difficult to integrate into the systematic-frameworks.

In this contribution, a usable type of an algorithm is developed and this algorithm ensures the requirements for some real-life applications. Besides, the methodology is based on a strong hypothesis guaranteeing that a solution is always found provided that one exists. In principle, the proposed strategy is a combination of the crash-free planned path algorithm created in and the path planner for a vehicle presented in. Parking operation has special requirements such as velocity controlling, steering controlling, trajectory finding etc. These processes have to be in progress together and final position of the vehicle should be where it is demanded. Besides, it is indicated how sensible calculation times can be accomplished by performing real parts of required costly figuring offline. In this setting, some point of interest on a keen usage structure of the algorithm is given. In the following section a suitable dynamic model of a vehicle is presented and the considered trajectory planning issue is defined all the more definitely. Besides, some essential outcomes coming about because of the uncommon structure and basic properties of the vehicle model are expressed. [2]

## 2.1. Previous Parking Algorithms

In 1999, M. Wada, K. Yoon, H. Hashimoto, and S. Matsuda proposed a paper in an International Conference named “Development of advanced parking system using human guidance”. This paper offers not only parallel but also vertical parking with an increased complexity in maneuvers and numerous direction changes. In this solution, parking time lasts longer and needs parking space around 1.55 times of the vehicle length for the parking process. [3]

In 2001, F. Gomez-Bravo, F. Cuesta and A. Ollero, proposed a paper named “Parallel and diagonal parking in nonholonomic autonomous vehicles”. This study presents collision-free trajectories from initial position to final position. There are several trajectories determined before and the algorithm based on fuzzy logic controller. Researchers tested that method in a small electrically powered car model. But testing with a real car model was unsuccessful because of the less ability of parking the car in small distance areas. Real car kinematics is not appropriate for this method. [4]

In 2008, T.-H. Hsu, J.-F. Liu, P.-N. Yu, W.-S. Lee proposed a paper named “Development of an automatic parking system for vehicle,” in Vehicle Power and Propulsion Conference. This paper focuses on steering motor controller. In the project, main idea is parking the car with the path which has the minimum length from the possible trajectories. This parking system just working for the back parking process. [5]

In 2006, I. Song, K. Gowan, J. Nery, H. Han, T. Sheng, H. Li, and F. Karray proposed a paper “Intelligent parking system design using fpga” in an international conference which is also a fuzzy-control based solution. This study concentrates on initial and final positions of the trajectories and does not care about the comfortable drive. But instead of comfortable drive, that study presents fast car parking for the drivers. [6]

In 2000, J. Xu, G. Chen, and M. Xie proposed a vision guided automatic parking paper named “Vision-guided automatic parking for smart car” in Intelligent Vehicles Symposium. In this system video data needed to find a space and calculate a collision-free parking path. Neural network and hybrid fuzzy logic algorithms are used to find solution. This parking operation is useful for parallel parking operation. [7]

In 2012, N.Scicluna,E.Gatt,O.Casha,I.Grech,andJ.Micallef proposed a paper for autonomous parking using fuzzy logic control in International conference named “Fpga-based autonomous parking of a car-like robot using fuzzy logic control”[8]

After having knowledge about these algorithms, generally systems need parking space more than 1.4 times of the vehicle length for the parking process. [9]

### 3. Parking Problem

Parking is the process that leaving the car temporarily in a parking area until it required. Parking process seems easy but it has some difficulties especially for novice drivers. There are a lot of factors that effect on parking process. For example; length of the car, steering angle, size of the tires, angle of the road etc. Also there is a problem about the parking area, because parking could be between two cars, by the side of the road, or in a parking space between poles etc. There is no standard parking space set in the world. Every countries and local governments have their rules. This problem starts from that not every car has the same length. That’s why there is no standard variable for parking. Sometimes it’s not easy to park these places even for experienced drivers.

### 4. Vehicle Model

#### 4.1. Bicycle Model

Bicycle model is widely used in this kind of research as autonomous systems. This model can be modified to four-wheel car.

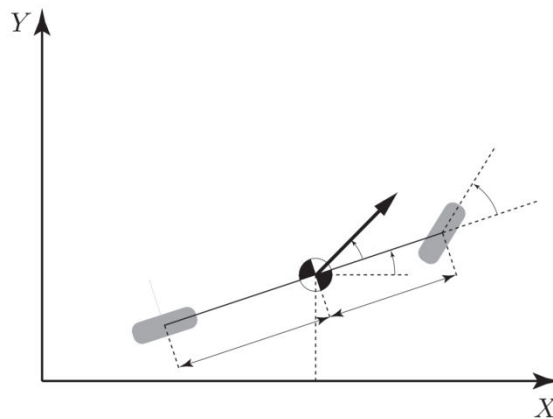


Figure 1. An example of a bicycle model. [10]

Center of gravity is one of the important point for automotive engineering. Bicycle model is flexible and realistic. Any model can be built up to this dynamic. A usable car which has a great load distribution between front and rear wheels is found for this study.

In this study, the model is consist on the following variables:

Length: 4491 mm

Width: 1852 mm

Wheelbase: 2450 mm

Turning circle diameter: 11100 mm

### 5. Simulations

In this system, realistic conditions were used as soon as possible. These conditions were entegrated to simulation environment. Assumptions distances were set from parked car to autonomous car as 0.57, 1.416, 2.262 meters and tested successfully in Simulink.

Fig. 2. shows the initial position of the autonomous car. Driver presses the button for autonomous parking at this time. Time is equal to 5 seconds (Fig 3). Car started to search a free space and at that time parking light turned into yellow. That means car found a free space but still searching for the right distance. Also car keeps going at that time. In Fig. 4., time is equal to 11 seconds, parking light turned into red because car did not detect a suitable area for parking. The 35th second of the simulation seems at Fig 5., sensors detected that free space on the right of the car and parking light turned into yellow. Car changed the shift at that time and now gear is “R” and car started to parking.

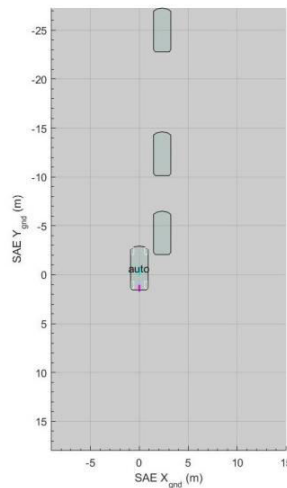


Figure 2. Simulation step 1

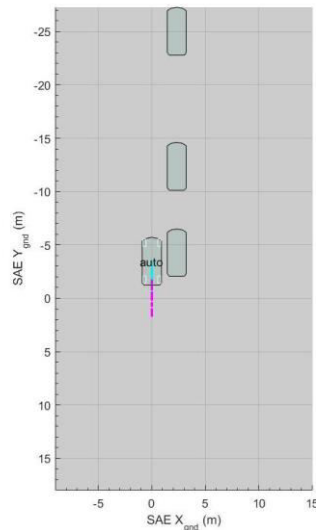


Figure 3. Simulation step 2

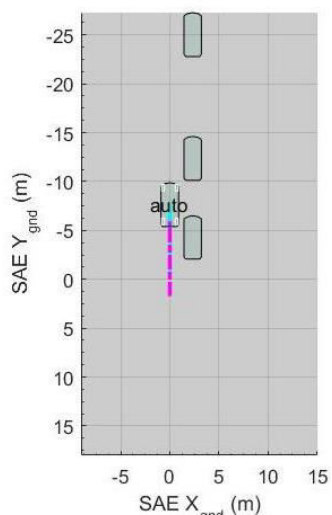


Figure 4. Simulation step 3

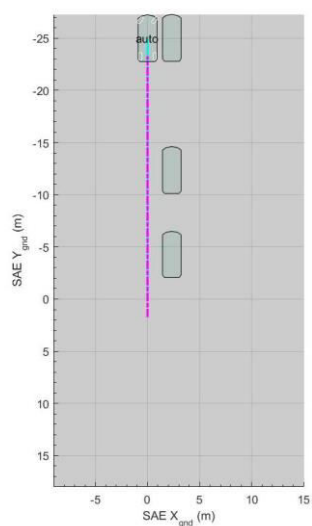


Figure 5. Simulation step 4

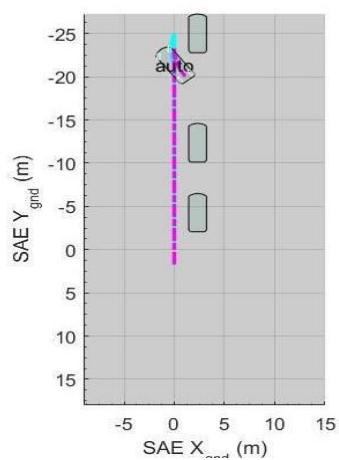


Figure 6. Simulation step 5

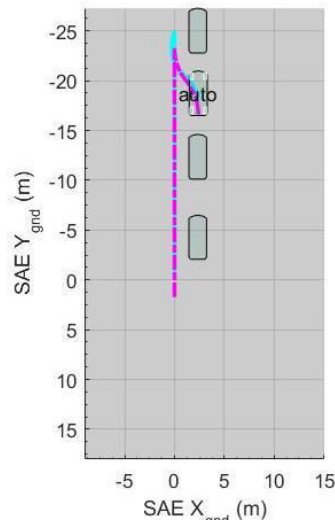


Figure 7. Simulation step 6

Fig. 6 shows the 40th second of the parking process. Now wheels are 40 degrees turned to right side. Car keeps going rear. Car turned the wheel to the left side with 40 degrees and reached to this position in 45th second (Fig. 7). For the final position car goes forward for 1 second and then finishes the process.

In this system, motivation is parking the car with less maneuvering with no crash. Firstly, less maneuvering decreases the fault possibility during parking process. Secondly less maneuvering gives the possibility of parking the car in a shorter time.

## 6. Conclusion

Due to driver does not controlling anything, this system is much more comfortable comparing to other parking assistance systems. System dynamics could be integrated any car model in the future. In the system required parking area is found as 1.6 times of the vehicle length. In the system, required free space for parking area is optimum for a comfortable parking space. Because car can leave the parking area with one move and other cars' drivers do not have any potential problem. Due to less maneuvering, possibility of crashing to a car or an object is less and system reduces the possibility of making mistake. Fuel consumption is directly related to shift. From first to top gear fuel consumption decreases. Also rear shift's consumption is as high as first shift. During parking process first and rear shifts are used. That's why during parking process, car consumes much more fuel. If we decrease the maneuvering move steps, car consumes less. A regular driver parks the car about 600 times during the whole year. But there are numerous drivers that work with car and park it more than 5 times during a day. This means less maneuvered car parking systems saves money and contributes the economy.

## References

- [1] M. U. Rafique, K. Faraz, "Guidance Based Autonomous Parking Assistant", *2<sup>nd</sup> International Conference on Industrial Mechatronics and Automation*, Wuhan-China, 30 May-31 May 2010, pp. 320-324, China, 2010.
- [2] B. Muller, J. Deutscher, S. Grodde, "Continuous Curvature Trajectory Design and Feedforward Control for Parking a Car", *IEEE Transactions on Control Systems Technology*, Vol. 15, No.3, May 2007, pp. 541-553.
- [3] M. Wada, K. Yoon, H. Hashimoto, S. Matsuda, "Development of advanced parking assistance system using human guidance," in *Advanced Intelligent Mechatronics, 1999. Proceedings. 1999 IEEE/ASME International Conference on*, 1999, pp. 997-1002.
- [4] F. Gomez-Bravo, F. Cuesta, A. Ollero, "Parallel and diagonal parking in nonholonomic autonomous vehicles," *Engineering Applications of Artificial Intelligence*, vol. 14, no. 4, pp. 419 – 434, 2001.

- 
- [5] T.-H. Hsu, J.-F. Liu, P.-N. Yu, W.-S. Lee, J.-S. Hsu, “Development of an automatic parking system for vehicle,” in Vehicle Power and Propulsion Conference, 2008. VPPC '08. IEEE, 2008, pp. 1–6.
- [6] I. Song, K. Gowan, J. Nery, H. Han, T. Sheng, H. Li, F. Karray, “Intelligent parking system design using fpga,” in Field Programmable Logic and Applications, 2006. FPL '06. International Conference on, 2006, pp. 1–6.
- [7] J. Xu, G. Chen, M. Xie, “Vision-guided automatic parking for smart car,” in Intelligent Vehicles Symposium, 2000. IV 2000. Proceedings of the IEEE, 2000, pp. 725–730.
- [8] N.Scicluna,E.Gatt,O.Casha,I.Grech,J.Micallef,“Fpga-basedautonomousparking of a car-like robot using fuzzy logic control,” in Electronics, Circuits and Systems (ICECS), 2012 19th IEEE International Conference on, 2012, pp. 229–232.
- [9] H. Ertugrul, “An FPGA Implementation of two-step Trajectory Planning for Automatic Parking”, Middle East Technical University, Sept 2013, pp. 6-7.
- [10] R. Rajamani, Vehicle Dynamics and Control, ser. Mechanical Engineering Series. Springer, 2011 pp. 26.

## Determination of Appropriate Axial Vibration Dampers for a Naval Vessel Driven by CODAG Propulsion

Abdullah Gokturk<sup>1,2</sup>, Osman Azmi Ozsoysal<sup>1</sup>

<sup>1</sup>Departement of Naval Architecture and Marine Engineering, Istanbul Technical University

<sup>2</sup>Departement of Naval Architecture and Marine Engineering, Iskenderun Technical University

---

### Article Info

#### Article history:

Received May 30<sup>th</sup>, 2017

Revised Aug 20<sup>th</sup>, 2017

Accepted Oct 18<sup>th</sup>, 2017

---

#### Keyword:

Axial dampers

Vibration

Naval vessel

Codag propulsion

Simulink

---

### ABSTRACT

The objective of this study is to reduce the vibration oscillations on a naval vessel propulsion system driven by CODAG. Within vibration analysis of the system firstly; physical model of the naval ship's propulsion system consist of mass, spring and damping elements developed properly and the effects of dynamic forces, which are consisted of main engine stresses, and the hydrodynamic forces that come from water effect are also taken into consideration. Afterwards, equation of motions derived for each mass and consequently by solving these equations, employing matrix approach, natural frequencies and modes of the axial vibration obtained. Finally, a model for propulsion system formed in Matlab/Simulink program. The axial vibrations caused by internal and external forces that excite the system examined and illustrated with graphs how the model respond in the face of undamped and under different axial damping ratios. Then which is also our goal; axial damping ratios that can absorb vibrational motions of the system successfully determined.

---

### Corresponding Author:

First Author,

Departement of Naval Architecture and Marine Engineering,

Istanbul Technical University,

Ayazaga Campus, MaslakSariyer, Istanbul31200, Turkey.

Email: goktura@itu.edu.tr

---

## 1. Introduction

Recent advances in ship design has led to build greater in size and more flexible vessels employ more powerful diesel engines with larger strokes. Flexibility in these structures brings about vibration problems. The main sources of ship vibration can be classified into two major groups; internal and external sources. Internal sources are main & auxiliary machines and propulsion system components and the external sources are hydrodynamic loadings by direct action or induced by the ship motions.

Vibration aboard ship may result in fatigue failure of local structural members or major machinery components, adversely effect the performance of vital shipboard equipment, increase maintenance costs and greatly increase discomfort or annoyance to passengers and crew. These all are why excessive ship vibrations must be taken under control. However, when ship is sailing, corrections on the vessel to decrease vibration problems is too difficult and causes great costs. Therefore, it is very important to identify and make corrections of vibration problems in design stage[1].

Antonides [2], made measurements on the propulsion system of the USS Simon Lake (AS-33) as a part of a program to improve analysis procedures used by the navy for predicting the longitudinal vibration of shaft

propulsion system. The objective was to find the axial exciting forces and damping associated with the propulsion system of the ship, as well as to determine how the gear case, turbines, condenser, and machinery foundation effect longitudinal vibration. Alternating thrust in the shaft and longitudinal displacement of the gear case, low-pressure turbine condenser and machinery foundation was measured. A resonance was found to exist in the operating range, but is not considered detrimental. The gear case, turbines and condenser move essentially as one unit. A mass-elastic system derived from measured data includes a level effect acting on the foundation mass. The exciting forces were lower than usual, except at or near full power.

Alarcin et al. [3], on their study were concerned with the decrease of vibration oscillations on ship main engine shaft system. The mathematics model of system was composed by Lagrange method and the effect of dynamics forces, which are consisted of main engine stresses, and the hydrodynamic forces that come from water effect were taken into consideration. The axial and torsional vibration are the factors during the analyze. Matlab–Simulink was used to obtain the oscillation of axial and torsional vibrations and to make these oscillations less different types of damping coefficient effects were investigated.

Zhang et al. [4] by modelling of the propeller shaft crankshaft with piston under the influence of angular and axial forces acting on the propeller was investigated. Between propeller and 1<sup>st</sup> order crankshaft journal, 5<sup>th</sup> and 6<sup>th</sup> order piston-crank journal's shaft torsional vibrations have been observed frequency change. Axial vibrations, except for the amplitude, a change of frequency components are expressed almost the same. Considering of coupled vibrations a nonlinear behavior effect was observed. They determined that when the propeller crankshaft vibration analysis approaches to linearity, a large error would be experienced.

Jiang et al. [5] studied the vibration performance of the propulsion shaft introduced by the coupling effect of the propeller and diesel engine. Firstly, the empirical formulas of the exciting force introduced by the diesel and propeller were given. Then a finite element model of propulsion shaft was established with ANSYS. Meanwhile the dynamic responses of the shaft introduced by the diesel excitation, the propeller excitation and the coupling effect of the two excitation were obtained respectively. The research results show that well matched diesel-propeller contributes to the vibration reduction of the propulsion shaft.

Several operations can be done at the ship design stage to reduce the excessive ship vibrations:

- reducing exciting forces amplitude,
- increasing stiffness,
- avoid values of frequency ratio near resonant condition and
- increasing damping ratios.

Avoiding vibrations by increasing damping ratios is the main objective of this study

## 2. CODAG Propulsion System Vibration Modelling

The main sources of axial vibrations in ship propulsion systems are the diesel engine crank mechanism, which produces the power needed for propeller propulsion and propulsion systems. Therefore, when axial vibration analysis is carried out, propeller characteristics, thrust generated and diesel engine characteristics must be well determined.

CODAG (Combined Diesel and Gas) is a type of propulsion system for ships which need a maximum speed that is considerably faster than their cruise speed, particularly warships like modern frigates or corvettes. It consists of diesel engines for cruising and gas turbines that can be switched on for high-speed transits. In figure 1, a simplified 3D model for CODAG propulsion system is represented and relevant to this model, idealized mass, spring and damping system for axial vibration analysis is shown in figure 2.

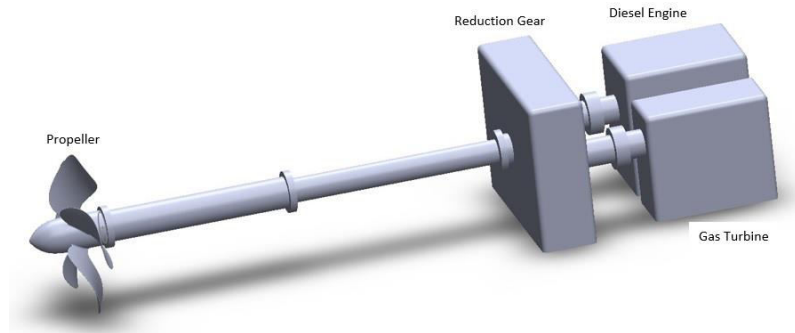


Figure 1. CODAG propulsion system simplified 3D model.

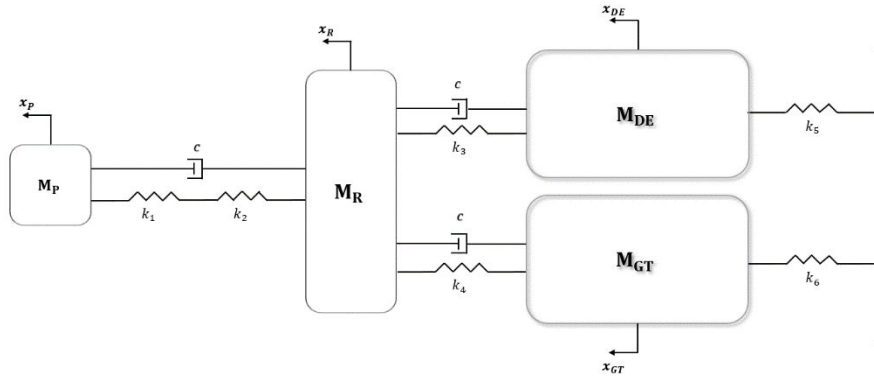


Figure 2. Idealized mass, spring, damping system.

Equations of motion for the system derived from mass spring damping system, as shown below:

$$\begin{aligned}
 M_P \ddot{x}_P + c(\dot{x}_P - \dot{x}_R) + k_e(x_P - x_R) &= T \\
 M_R \ddot{x}_R - c(\dot{x}_P - \dot{x}_R) + c(\dot{x}_R - \dot{x}_{DE}) + c(\dot{x}_R - \dot{x}_{GT}) - k_e(x_P - x_R) + \\
 + k_3(x_R - x_{DE}) + k_4(x_R - x_{GT}) &= F_R \\
 M_{DE} \ddot{x}_{DE} - c(\dot{x}_R - \dot{x}_{DE}) - k_3(x_R - x_{DE}) + k_5 x_{DE} &= 0 \\
 M_{GT} \ddot{x}_{GT} - c(\dot{x}_R - \dot{x}_{GT}) - k_4(x_R - x_{GT}) + k_6 x_{GT} &= 0
 \end{aligned} \tag{1}$$

In order to write differential equations expressing the dynamic behavior of the system in matrix form, it is necessary to specify the mass, damping and stiffness matrices of these equations. The matrix expression for the equations of motion is:

$$\begin{bmatrix} M_P & 0 & 0 & 0 \\ 0 & M_R & 0 & 0 \\ 0 & 0 & M_{DE} & 0 \\ 0 & 0 & 0 & M_{GT} \end{bmatrix} + \begin{bmatrix} \ddot{x}_P \\ \ddot{x}_R \\ \ddot{x}_{DE} \\ \ddot{x}_{GT} \end{bmatrix} + \begin{bmatrix} c & -c & 0 & 0 \\ -c & 3c & -c & -c \\ 0 & -c & c & 0 \\ 0 & -c & 0 & c \end{bmatrix} \begin{bmatrix} \dot{x}_P \\ \dot{x}_R \\ \dot{x}_{DE} \\ \dot{x}_{GT} \end{bmatrix} + \begin{bmatrix} k_e & -k_e & 0 & 0 \\ -k_e & k_e + k_3 + k_4 & -k_3 & -k_4 \\ 0 & -k_3 & k_3 + k_5 & 0 \\ 0 & -k_4 & 0 & k_4 + k_6 \end{bmatrix} \begin{bmatrix} x_P \\ x_R \\ x_{DE} \\ x_{GT} \end{bmatrix} = \begin{bmatrix} T \\ F_R \\ 0 \\ 0 \end{bmatrix}$$

T is the thrust, which is obtained at maximum power in the case of attaching to a fixed point. F<sub>R</sub> is the force generated by the reduction gear. The natural frequency is a value that depends on its own mass and rigidity. Therefore, these values are not taken into account since there is no effect of force and damping on the calculation of natural frequency.

$$\begin{bmatrix} M_P & 0 & 0 & 0 \\ 0 & M_R & 0 & 0 \\ 0 & 0 & M_{DE} & 0 \\ 0 & 0 & 0 & M_{GT} \end{bmatrix} + \begin{bmatrix} \ddot{x}_P \\ \ddot{x}_R \\ \ddot{x}_{DE} \\ \ddot{x}_{GT} \end{bmatrix} + \begin{bmatrix} k_e & -k_e & 0 & 0 \\ -k_e & k_e + k_3 + k_4 & -k_3 & -k_4 \\ 0 & -k_3 & k_3 + k_5 & 0 \\ 0 & -k_4 & 0 & k_4 + k_6 \end{bmatrix} \begin{bmatrix} x_P \\ x_R \\ x_{DE} \\ x_{GT} \end{bmatrix} = \begin{bmatrix} 0 \\ 0 \\ 0 \\ 0 \end{bmatrix}$$

In order to calculate natural frequency we should solve the eigenvalue problem for the system.

$$[K] - \omega^2[M] = 0 \tag{2}$$

$$\begin{bmatrix} k_e & -k_e & 0 & 0 \\ -k_e & k_e + k_3 + k_4 & -k_3 & -k_4 \\ 0 & -k_3 & k_3 + k_5 & 0 \\ 0 & -k_4 & 0 & k_4 + k_6 \end{bmatrix} - \omega^2 \begin{bmatrix} M_P & 0 & 0 & 0 \\ 0 & M_R & 0 & 0 \\ 0 & 0 & M_{DE} & 0 \\ 0 & 0 & 0 & M_{GT} \end{bmatrix} = \begin{bmatrix} 0 \\ 0 \\ 0 \\ 0 \end{bmatrix}$$

We need the values of parameters to solve eq. (2) and find natural frequencies for the system. Table 1 represents shaft characteristics for the propulsion system and there is mass and force values shown in Table 2. Additionally, shaft rigidity values (k) are calculated based on shaft properties and shown in Table 2.

Table 1. Shaft dimensions.

Shaft Type	Shaft Diameter (mm)	Shaft Length (mm)
Propeller shaft	480	14250
Intermediate shaft	420	14900
Diesel engine thrust shaft	400	3600
Gas turbine thrust shaft	400	3600

Table 2. Mass, spring system parameters.

M <sub>P</sub>	M <sub>R</sub>	M <sub>DE</sub>	M <sub>GT</sub>	T	F <sub>R</sub>	k <sub>e</sub>
13400	32300	13400	15000	197137	2.67x10 <sup>9</sup>	1.13x10 <sup>9</sup>
kg	kg	kg	kg	N	N/m	N/m
k <sub>1</sub>	k <sub>2</sub>	k <sub>3</sub>	k <sub>4</sub>	k <sub>5</sub>	k <sub>6</sub>	
2.67x10 <sup>9</sup>	1.95x10 <sup>9</sup>	7.33x10 <sup>9</sup>	7.33x10 <sup>9</sup>	1.29x10 <sup>9</sup>	1.87x10 <sup>9</sup>	
Ns/m	Ns/m	Ns/m	Ns/m	Ns/m	Ns/m	Ns/m

By solving the eq. (2), frequencies of the system is found and shown in Table 3.

Table 3. Natural frequency of the system.

	Frequency (Hz)
w <sub>1</sub>	2.306
w <sub>2</sub>	14.592
w <sub>3</sub>	468.792
w <sub>4</sub>	1256.433

### 3. Simulation

The vibrations of the CODAG propulsion system components in axial directions are analyzed by simulating various damping values with m-file and Simulink model files created in Matlab/Simulink program as shown in Figure 3.

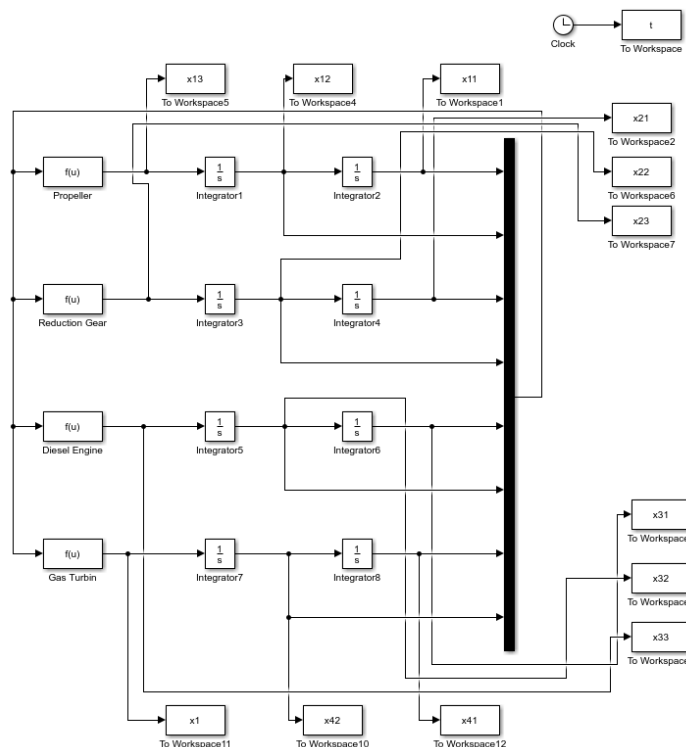


Figure 3. CODAG propulsion system Simulink model.

As a result of the analysis of the axial vibrations of the CODAG propulsion system elements at undamped and different damping ratios, the amplitude variations of axial displacements and the velocities of the propeller, reduction gear, diesel engine and gas turbine are illustrated in graphs respectively.

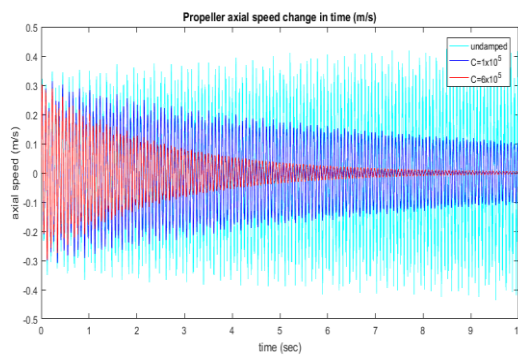
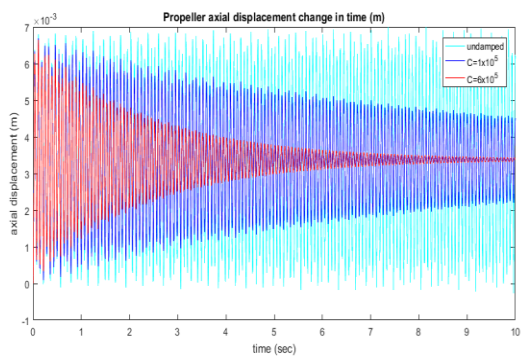


Figure 4. (a) Propeller axial displacement change in time(m)

(b) Propeller axial speed change in time(m/sec).

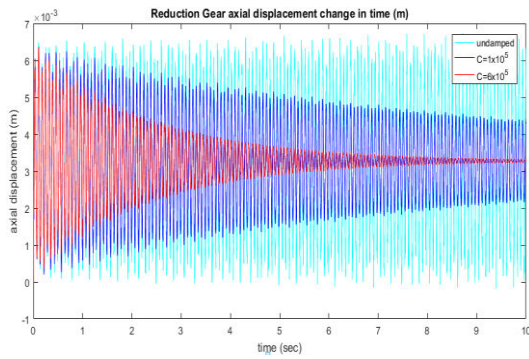
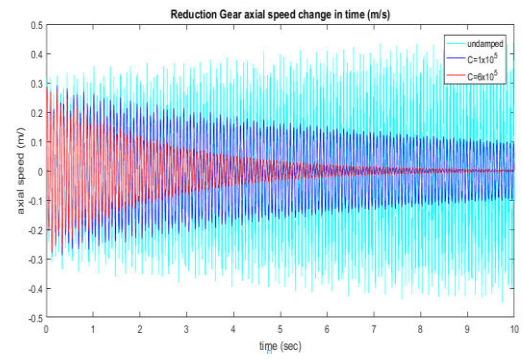


Figure 5. (a) Reduction Gear axial displacement change in time (m).



(b) Reduction Gear axial speed change in time (m/sec).

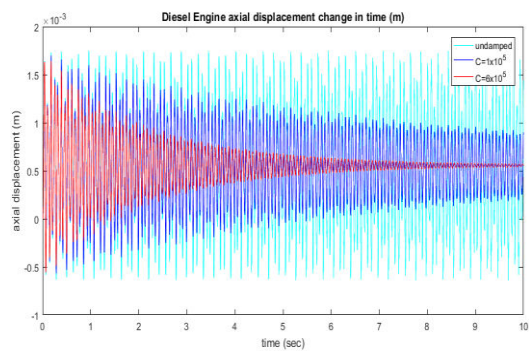
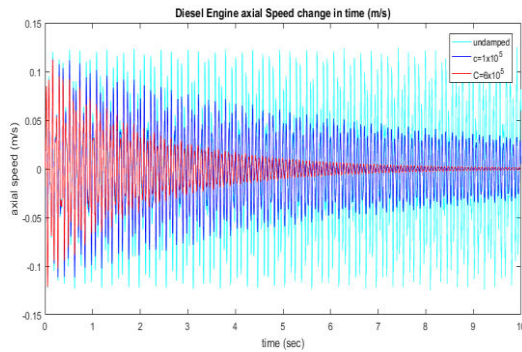


Figure 6. (a) Diesel Engine axial displacement change in time(m).



(b) Diesel Engine axial speed change in time (m/sec).

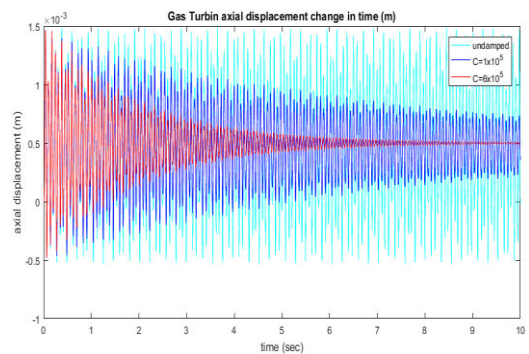
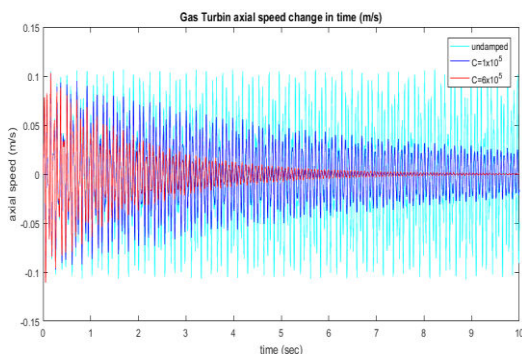


Figure 7. (a) Gas Turbin axial displacement change in time (m).



(b) Gas Turbin axial speed change in time (m/sec).

Considering the simulation, by applying the axial damping coefficients from  $1 \times 10^5 \text{Ns/m}$  to  $6 \times 10^5 \text{Ns/m}$ , the damping ratios changes from 27.34% to 45.46% for propeller axial displacement, and changes from 76.2% to 88.3%. for propeller axial velocity. Damping ratios for reduction gear axial displacement, changes from 30.7% to 47.2% and for reduction gear axial velocity, changes from 77.3% to 89.7%. Damping ratios for diesel engine axial displacement, changes from 36.7% to 55.3% and for diesel engine axial velocity, changes from 79.4% to 93.6%. Damping ratios for diesel engine axial displacement, changes from 39.8% to 56.7% and for diesel engine axial velocity, changes from 81.2% to 94.9%.

#### 4. Conclusion

In this study, the propulsion system vibrations of a naval vessel driven by CODAG are investigated. Firstly, the propulsion system is modeled separately as mass-spring-damping element, equations of motion for each

mass are obtained and dynamic behavior of the system in nature is observed by neglecting the effect of force and damping elements. The system is also modeled using Matlab/Simulink program for the case when the system is in operation, that is, the system is under the influence of excitations and damping elements. Axial vibrations due to internal and external forces acting on the system are analyzed and how the model responds to undamped and different damping conditions is illustrated. The axial damping coefficient,  $C=6 \times 10^5 \text{Ns/m}$ , that can successfully absorb the oscillatory motion of the system in the axial direction has been determined.

### References

- [1]. American Bureau of Shipping, "Guidance Notes on Ship Vibration." 2006.
- [2]. G. Antonides, "Longitudinal vibration of propulsion system on USS Simon Lake (AS-33)." *Acoustics and Vibration Laboratory Research and Development Report*, Report 2147, S-F0131108 Task 01351, 1966.
- [3]. F. Alarcin and F.C. Korkmaz "Vibration analysis of ship main engine and shaft system," *Journal of Engineering and Natural Sciences, Sigma 3*, 2012, pp.310-319.
- [4]. G. Zhang, Y. Zhao, T. Li, and X. Zhu, "Propeller excitation of longitudinal vibration characteristics of marine propulsion shafting system," *Hindawi Publishing Corporation Shock and Vibration*, 2014, Article ID 413592, 19 pages.
- [5]. X. Jiang, X. Zhou and K. Chen, "Vibration characteristics of a marine propulsion shaft excited by the effect of propeller and diesel," *Transportation Information and Safety (ICTIS, International Conference on, Whuan*, 2015, pp. 893-897.
- [6]. MTU, "Technical Sales Documentations," Friedrichshafen, Germany, 2011.

# Solving Constrained Optimization Problems with Sine-Cosine Algorithm

*Simge Ekiz<sup>1</sup>, Pakize Erdoğmuş<sup>1</sup>, Büşra Özgür<sup>1</sup>*

<sup>1</sup>University, Department of Computer Engineering, Duzce, Turkey

---

## Article Info

### Article history:

Received Jun 1<sup>st</sup>, 2017

Revised Aug 20<sup>th</sup>, 2017

Accepted Oct 18<sup>th</sup>, 2017

---

### Keyword:

Sine-Cosine  
Optimization  
Algorithm,  
Constrained  
Optimization  
Problems,  
Penalty Method

---

## ABSTRACT

Optimization algorithms aim to find the optimum values that give the maximum or minimum result of a function under given circumstance.

There are many approaches to solve optimization problems. Stochastic population-based optimization approaches tend to give the best results in a reasonable time. Two of the state-of-art stochastic optimization algorithms are Genetic Algorithms (GA) and Particle Swarm Optimization (PSO). In addition, Sine-Cosine Algorithm is one of the recently developed stochastic population-based optimization algorithms. It is claimed that Sine-Cosine has a higher speed than the counterparts of it. Moreover, Sine-Cosine Algorithm occasionally outperforms other optimization algorithms including GA and PSO. This algorithm is successful because it can balance exploration and exploitation smoothly.

In the previous studies, the above-mentioned algorithms were evaluated and compared to each other for the unconstrained optimization test functions. But there is no study on constrained optimization test problems. In this study, we aim to show the performance of Sine-Cosine Algorithm on constrained optimization problems. In order to achieve this, we are going to compare the performances by using well-known constrained test functions.

---

### Corresponding Author:

Simge Ekiz,

Duzce University, Department of Computer Engineering, Duzce, Turkey.

Email: [simgeekiz@duzce.edu.tr](mailto:simgeekiz@duzce.edu.tr)

---

## 1. Introduction

Optimization can be defined as finding the most effective and highest achievable performance under the given limitations. Mathematically speaking, Optimization is finding the minimum or maximum of a function subject to the constraints. A set of values that satisfies all the constraints of an optimization problem creates a feasible solution. The optimization technique tries to find the optimum solution from all of these feasible solutions [1].

Optimization problems can be found in every area of life because all living things tend to do the best. For example, Birds fly in 'V' shape to reduce the energy consumption, another example fish moves in flocks to benefit from defense against predators [2]. Optimization problems have been a topic since 1960's. In these

years optimization problems have been tried to solve by classical mathematical methods. Deterministic methods have a great advantage that they find global optima. Unfortunately, they cannot solve all nonlinear problems. With classical optimization, only limited problems can be solved. The inadequacy of classical methods has forced scientists to search for new methods. To find the optimum, solution stochastic algorithms are developed. These algorithms sample the search space without exploring it thoroughly. Stochastic computation techniques have received a great deal of attention regarding their potential as optimization techniques for complex problems. As a result, the development of stochastic algorithms has begun.

It is impossible to develop one way to solve all the nonlinear problems. There are a lot of methods proposed. Stochastic algorithms can find promising solutions for difficult optimization problems, but there is no guarantee that optimal solutions can be reached all the time. Stochastic algorithms are good at solving most of the real world problems which are nonlinear and multimodal[1].

The general nonlinear programming problem is defined as follows[3];

$$\text{Minimize} \quad f(x), \quad x = (x_1, \dots, x_n) \in R^n$$

$$\text{Subject to the constraints } g_i(X) \geq 0$$

$$h_i(X) = 0$$

Where  $g_i(X)$  and  $h_i(X)$  are constraints that are required to be satisfied.

The optimization problem is based on finding the optimum value of the objective function, and if there are no constraints on the variables, these problems are called unconstrained optimization problems. The solution of unconstrained optimization problems is easier than the constrained ones. However, most real-life problems are constrained. It is necessary to find the best value of a constraint optimization problem such as resource constraint, time constraint, cost constraint, design constraint according to these conditions.

### 1.1. Related Works

In 1994 Joines and Houck solve four test cases of constrained optimization problems with the genetic algorithm. They transform constrained optimization problems to the unconstrained optimization by using the penalty method. They aim at reaching the feasible solution of genetic algorithm by giving appropriate value according to the number of generations[4]. In 1996 Michalewicz and Schoenauer present several constraint-handling techniques for optimization problems. The first one based on feasibility of solutions, the second one is penalty based, the third method makes a clear distinction between feasible and infeasible and fourthly hybrid methods. Moreover, they provide 11 test cases which we use in this study to make our experiments[3]. In 2002 Hu and Eberhart applied one of the constraint handling methods which based on preserving feasibility of solutions. They test particle swarm optimization algorithm on the same test cases[5]. In 2005 Yeniay go over all constraint handling penalty based techniques for the genetic algorithm. He mentions their advantages and disadvantages. He emphasizes the importance of setting appropriate values of the penalty parameters[6].

### 1.2. Dealing with constraints

All the stochastic algorithms are directly suited to unconstrained optimization problems. Applying these algorithms to constrained optimization problems has always been a problem. In real life problems such as engineering design problems are constrained optimization problems and constraints has a great effect on the optimization performance[7]. Fortunately, many constrained optimization algorithms can be transformed to the unconstrained case, often with the use of a penalty method.

Penalty function method is common because of its simple principle and easy implementation. We modify the objective function in such a way that it penalizes any violation of the constraints.

Penalty function method can be formulated as follows[8];

$$\text{Minimize} \quad f(x)$$

$$\text{Subject to the constraints } g_i(X) \geq 0 \quad i = 1, 2, 3, \dots, m$$

The equivalent unconstrained optimization problem can be stated as;

$$\text{Minimize} \quad F(x) = f(x) + P(x)$$

Maximize  $f(x)$

Subject to the constraints  $g_i(X) \geq 0 \quad i = 1, 2, 3, \dots, m$

The equivalent unconstrained optimization problem can be stated as;

Maximize  $F(x) = f(x) - P(x)$

In minimization problems, we include the penalty function which adds a high cost to the objective function. In maximization problems, we subtract the penalty function from the objective function.

In this study, we implement two of the state-of-art algorithms that we mentioned to the well-known constraint test cases. In addition to these algorithms, we also implement Sine Cosine Algorithm that developed in 2016[9]. The above-mentioned algorithms were directly suited to unconstrained optimization test functions. To deal with constraints we use the penalty function method due to its popularity and easy implementation [7]. Penalty method adds the penalty term to the objective function for any violation of the constraints [8], [10]. We aim to show the performance of Sine-Cosine Algorithm on constrained optimization problem and compare results with genetic algorithm and particle swarm optimization algorithm.

## 2. Background theories

### 2.1. Genetic Algorithm (GA)

Pseudo code for Genetic Algorithm;
<pre> Begin   t ← 0;   InitializePopulation[P(t)];   EvaluatePopulation[P(t)];   while not termination do     P'(t) ← Selection[P(t)];     P(t+1) ← ApplyGeneticOperators[P'(t)uQ];     EvaluatePopulation[P(t+1)];     t ← t+1;   end while   return BestSolution end </pre>

Genetic algorithm mimics the biological evaluation. It starts with creating a population randomly. And population can be described as a group of individual solutions. In each iteration, the algorithm chooses some solutions from the current population as parents according to their fitness values to form a new generation. The new generation is created by applying genetic operators such as crossover and mutation. Next, these new generations are evaluated, and this process is going on until the termination condition is met. And the population evolves toward an optimal solution.

## 2.2. Particle Swarm Optimization Algorithm (PSO)

Pseudo code for Particle Swarm Optimization Algorithm;
<pre> Begin   t ← 0;   InitializeParticles[P(t)];   EvaluateParticles [P(t)];   while not termination do     t ← t+1;     Select pBest for each Particle;     Select gBest from P(t-1);     CalculateParticleVelocity[P(t)];     UpdateParticlePosition[P(t)];     EvaluateParticles [P(t)];   end while   return BestSolution end </pre>

Particle Swarm Optimization is another population optimization technique developed by Eberhart and Kennedy in 1995. It starts with initializing the population of random solutions called particles. In PSO the particles have velocity values alongside the fitness values. In every iteration, gbest and pbest are selected. Pbest is the best solution has achieved so far by a particle. Gbest is the best value obtained so far by any particle in the population. Next, the velocities of the particles are calculated using pbest and gbest values. Then particle positions are updated based on the velocities. Thus, the particles follows the best particle in the search space.[11]

## 2.3. Sine Cosine Algorithm (SCA)

Pseudo code for Sine Cosine Algorithm;
<pre> begin   InitializeSearchAgents[X];   while t&lt;maximum number of iterations do     EvaluateSearchAgents[X];     UpdateBestSolution(P=X*);     Update r<sub>1</sub>r<sub>2</sub>r<sub>3</sub>r<sub>4</sub> ;     UpdateSearchAgentPosition;   end while   return BestSolution end </pre>

Sine cosine algorithm can be described as the following formula;

$$X_i^{t+1} = \begin{cases} X_i^t + r_1 * \sin(r_2) * |r_3 P_i^t - X_i^t|, & r_4 < 0.5 \\ X_i^t + r_1 * \cos(r_2) * |r_3 P_i^t - X_i^t|, & r_4 \geq 0.5 \end{cases}$$

As another population-based optimization algorithm sine cosine algorithm also starts with initializing random solutions called search agents. Sine cosine algorithm uses 4 variables to tune. These are r variables.  $r_1$  decides that search agent is going to do whether exploration or exploitation. All stochastic algorithms are both exploration and exploitation but it is important to balance these.  $r_2$  decides how far the solution's movement should be.  $r_3$  assign a random weight and  $r_4$  decided whether sine or cosine formula is going to be used.

In every iteration, the solutions are evaluated by using the fitness function and the algorithm assigns the best solution obtained so far as the destination point. Next, the r variables are updated.

Search agent positions are updated based on the  $r$  variables and the best solution. Thus the potential solutions follow the best solution in the search space [9].

### 3. Experiments

We use global optimization toolbox in Matlab© which includes both genetic algorithm and particle swarm optimization algorithms with default values. And we implement Sine cosine algorithm with 30 search agents and 1000 iterations. The algorithms are run 30 times on the popular constraint optimization test problems that Michalewicz and Schoenauer first presented. We get these test problems from Kyoto University global optimization test problems web site[13]. We implement penalty method to these test cases.

The test problems are given below;

G1	$\text{Min } f(x) = \sum_{i=1}^4 x_i - 5 \sum_{i=1}^4 x_i^2 - 5 \sum_{i=5}^{13} x_i$
G2	$\text{Max } f(x) = \left  \frac{\sum_{i=1}^n \cos^4(x_i) - 2 \prod_{i=1}^n \cos^4(x_i)}{\sqrt{\sum_{i=1}^n i x_i^2}} \right $
G4	$\text{Min } f(x) = 5.3578547x_3^2 + 0.8356892x_1x_5 + 37.293239x_1 - 40792.141$
G5	$\text{Min } f(x) = 3x_1 + 10^{-6}x_1^3 + 2x_2 + \frac{2}{3} * 10^{-6}x_2^3$
G6	$\text{Min } f(x) = (x_1 - 10)^3 + (x_2 - 20)^3$
G7	$\text{Min } f(x) = x_1^2 + x_2^2 + x_1x_2 - 14x_1 - 16x_2 + (x_3 - 10)^2 + 4(x_4 - 5)^2 + (x_5 - 3)^2 + 2(x_6 - 1)^2 + 5x_7^2 + 7(x_8 - 11)^2 + 2(x_9 - 10)^2 + (x_{10} - 7)^2 + 45$
G8	$\text{Max } f(x) = \frac{\sin^3(2\pi x_1) \sin(2\pi x_2)}{x_1^3(x_1+x_2)}$
G9	$\text{Min } f(x) = (x_1 - 10)^2 + 5(x_2 - 12)^2 + x_3^4 + 3(x_4 - 11)^2 + 10x_5^6 + 7x_6^2 + x_7^4 - 4x_6x_7 - 10x_6 - 8x_7$
G10	$\text{Min } f(x) = x_1 + x_2 + x_3$
G11	$\text{Min } f(x) = x_1^2 + (x_2 - 1)^2$
G13	$\text{Min } f(x) = e^{x_1x_2x_3x_4x_5}$

### 4. Experimental Results

Results are shown in figures. The red lines represent the best-known values gathered in Kyoto University Global Optimization Website.

Sine cosine algorithm, genetic algorithm, and particle swarm optimization algorithm are represented by respectively by orange, pink and blue bars. In terms of accuracy mostly genetic algorithm gives the best results. SCA algorithm is outperformed by the others or results as the same.

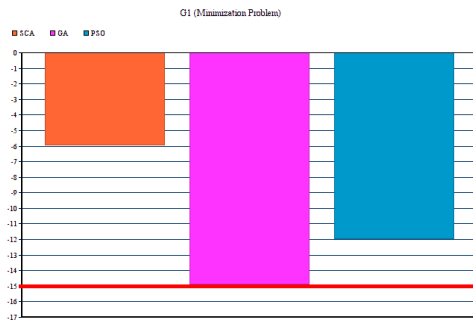


Figure 1. G1 Test Function(Minimization)



Figure 2. G2 Test Function(Maximization)

In G1 global optimization test case, genetic algorithm outperforms the other two algorithms. G1 is minimization problem and GA reaches the minimum value which is -15.

In G2 is maximization problem and in these experiments, any of the algorithms reach the maximum value gathered in Kyoto University Global Optimization Website so far.

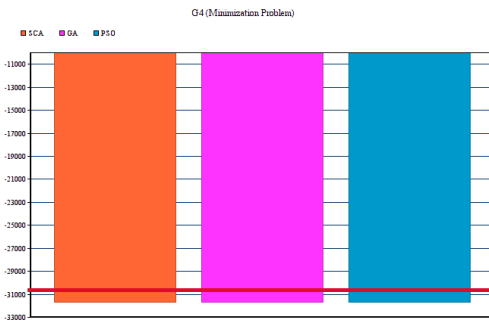


Figure 3. G4 Test Function(Minimization)

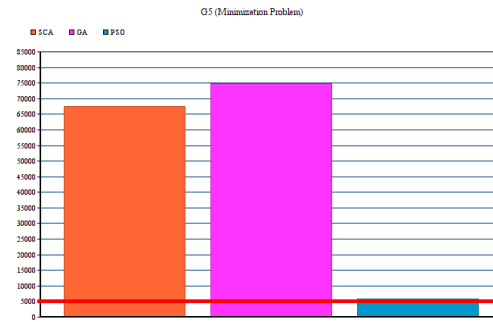


Figure 4. G5 Test Function(Minimization)

All the algorithms find the optimum value in G4 and G11 test cases. Like in these situations it is better to choose the algorithm which takes a shorter time. In G5 only PSO find the minimum optimal value. In G6, SCA and GA are both find the minimum value which updates the minimum value found up to now. Moreover, SCA is not good at solving problems like G7 but in the G8 test case, SCA outperforms both GA and PSO. In G9, G10, G13 test cases SCA is outperformed by the others.

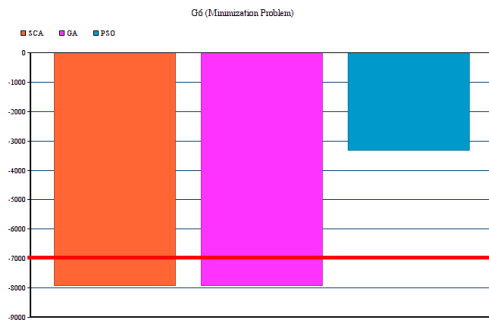


Figure 5. G6 Test Function(Minimization)

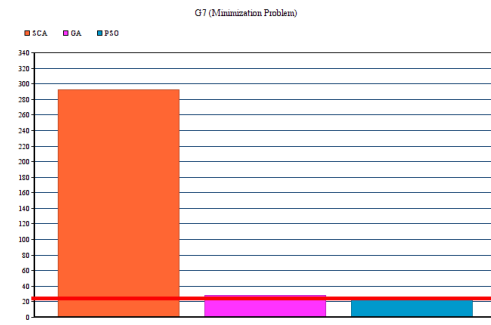


Figure 6. G7 Test Function(Minimization)



Figure 7. G8 Test Function(Maximization)

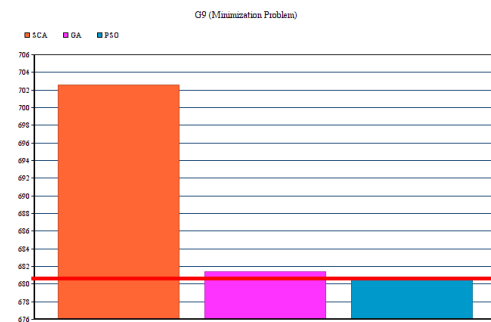


Figure 8. G9 Test Function(Minimization)



Figure 9. G10 Test Function(Minimization)

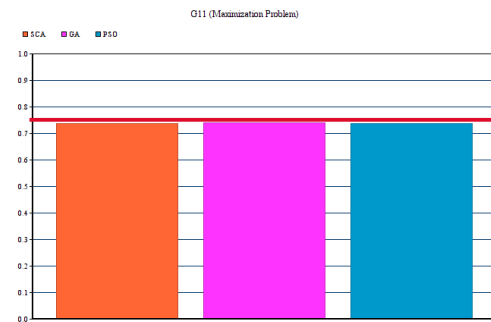


Figure 10. G11 Test Function(Maximization)

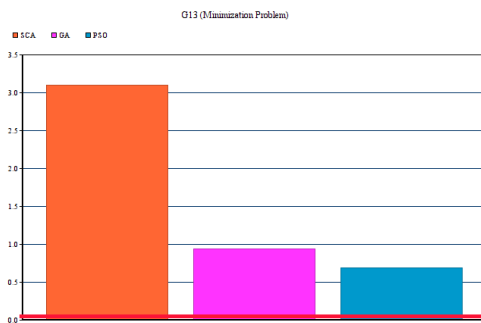


Figure 11. G13 Test Function(Minimization)

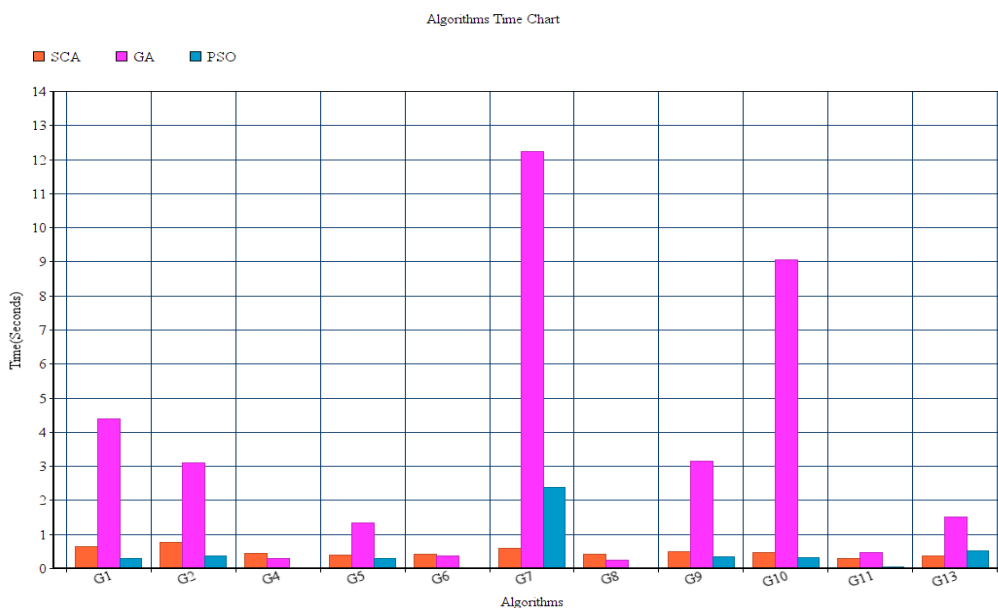


Figure 12. The time taken by the algorithms for each test case

This graph demonstrates the time taken by the algorithm for each problem. In most of the cases, the slowest algorithm is a genetic algorithm. Except two of the cases, PSO is the fastest one. And SCA takes slightly more time than the PSO. Mostly both PSO and SCA finish under a second.

**5. Conclusions and Discussion**

In this study, we optimized well known constrained optimization problems with using the recently developed sine cosine algorithm. We deal with constraints with the help of penalty method. Then we compared SCA algorithm results with GA and PSO. In terms of accuracy GA gives the best results but in terms of speed PSO and SCA are faster. Although SCA gives better result in unconstrained optimization problems, it does not perform well on constrained optimization problems. But SCA is a new algorithm and it might give better results by making further improvement in the algorithm. Also, it might give better results when we change the method of handling constraints.

## REFERENCES

- [1] A. Askarzadeh, "A novel metaheuristic method for solving constrained engineering optimization problems: Crow search algorithm," *Comput. Struct.*, vol. 169, pp. 1–12, 2016.
- [2] "Swarm Behaviour." [Online]. Available: [https://en.wikipedia.org/wiki/Swarm\\_behaviour](https://en.wikipedia.org/wiki/Swarm_behaviour).
- [3] Z. Michalewicz and M. Schoenauer, "Evolutionary Algorithms for Constrained Parameter Optimization Problems," *Evol. Comput.*, vol. 4, no. 1, pp. 1–32, 1996.
- [4] J. A. Joines and C. R. Houck, "On the use of non-stationary penalty functions to solve nonlinear constrained optimization problems with GA's," in *Evolutionary Computation, 1994. IEEE World Congress on Computational Intelligence., Proceedings of the First IEEE Conference on*, 1994, pp. 579–584.
- [5] X. Hu and R. Eberhart, "Solving Constrained Nonlinear Optimization Problems with Particle Swarm Optimization," *Optimization*, vol. 2, no. 1, pp. 1677–1681, 2002.
- [6] O. Yeniay, "Penalty function methods for constrained optimization with genetic algorithms," *Math. Comput. Appl.*, vol. 10, no. 1, pp. 45–56, 2005.
- [7] Q. He and L. Wang, "An effective co-evolutionary particle swarm optimization for constrained engineering design problems," *Eng. Appl. Artif. Intell.*, vol. 20, no. 1, pp. 89–99, 2007.
- [8] A. Homaifar, C. X. Qi, and S. H. Lai, "Constrained Optimization Via Genetic Algorithms," *Simulation*, vol. 62, no. 4, pp. 242–253, 1994.
- [9] S. Mirjalili, "SCA: A Sine Cosine Algorithm for solving optimization problems," *Knowledge-Based Syst.*, vol. 96, pp. 120–133, 2016.
- [10] R. Courant, "Variational methods for the solution of problems of equilibrium and vibrations," *Bull. Am. Math. Soc.*, vol. 49, no. 1, pp. 1–24, 1943.
- [11] J. Kennedy and R. Eberhart, "Particle swarm optimization," *Neural Networks, 1995. Proceedings., IEEE Int. Conf.*, vol. 4, pp. 1942–1948 vol.4, 1995.
- [12] J. Brownlee, "Particle Swarm Optimization." [Online]. Available: <http://www.cleveralgorithms.com/nature-inspired/swarm/pso.html>. [Accessed: 26-Apr-2017].
- [13] A. R. Hedar, "Global Optimization Test Problems." [Online]. Available: [http://www-optima.amp.i.kyoto-u.ac.jp/member/student/hedar/Hedar\\_files/TestGO.htm](http://www-optima.amp.i.kyoto-u.ac.jp/member/student/hedar/Hedar_files/TestGO.htm).

# An Investigation on Deformation Behaviors of Energy Absorbers for Passenger Coaches

Ramazan ÖZMEN<sup>1</sup>, Mustafa GÜNAY<sup>2</sup>

<sup>1</sup>Department of Mechatronics Engineering, Karabük University

<sup>2</sup>Department of Mechanical Engineering, Karabük University

---

## Article Info

### Article history:

Received Jun 1<sup>st</sup>, 2017

Revised Aug 20<sup>th</sup>, 2017

Accepted Oct 18<sup>th</sup>, 2017

---

### Keyword:

Energy absorption  
Finite element analysis  
HSLA steel  
Truncated tube  
Optimization

---

## ABSTRACT

Thin-walled structures is used commonly as energy absorbers at the front and back of the coaches. These parts should be designed to minimize the damage to the vehicle and prevent the passengers from fatality and/or injury by absorbing the collision energy in railway transportation. In this paper, deformation behaviors of tube like structures with truncated cone under the axial impact load were investigated by means of finite element analysis (FEA). The energy absorbers having tube like structures were modelled at the same weight and have three different wall thickness and taper angle. As a result of FEA, the performances of straight and truncated cone type energy absorbers were compared in terms of energy absorption capacities and an optimization study was done to determine the effects of thickness and taper angle on energy absorbing performances of the members. The analysis of variance in 95% confidence level was applied in order to determine the effects of design parameters on total efficiency (TE). Besides, optimum design parameters for TE were determined by using Taguchi optimization methodology. Thickness was found as the most significant parameter on total efficiency with 60.52% percentage contribution ratio according to ANOVA results.

---

## Corresponding Author:

First Author,  
Department of Mechatronics Engineering,  
Karabük University,  
Balıklarkayası Mevkii, 78050, Karabük, Turkey.  
Email: ramazanozmen@karabuk.edu.tr

---

## 1. Introduction

In railway transport, collision zones have been developed in front and rear of the car to damp the collision energy to prevent catastrophic events such as accidental death and injury. During the accident, the kinetic energy is consumed in a controlled manner by way of these collision zones to preserve the integrity of the passengers and the occupied areas [1][2].

In order to absorb impact energy, thin-walled tube-like components are generally used as energy absorbing members in vehicles such as cars, planes and trains etc. The static and dynamic axial impact behaviors of these members with different cross sections (circular, rectangular etc.) were examined by means of several experimental and theoretical studies and certain theoretical expressions were suggested according to the cross-sectional properties [3].

Energy absorption capabilities and axial impact behaviors of thin-walled tubes depend on many factors such as material properties [4], member geometry [5], impact velocity [6], applied boundary conditions [7], and forming history [8]. These studies have revealed that the hardening characteristics and strain rate sensitivity of the material are significant effects on the collision behavior of the energy absorber [4]. On the other hand, it

was stated that the stress-strain relationship of the material has a key place in the numerical simulation of the collision events in which the large deformations occurs [9].

In some studies, trigger structures like holes and groves have been utilized to provide a controlled deformation and to increase energy absorption. One of the most key features of this trigger mechanism is to reduce the initial peak force generated during the impact [10]. And, aluminum foams and honeycomb structures were placed inside the energy absorber to increase the energy absorption capability of the member [11].

The primary energy absorber is one of the crucial structure in the passenger wagon that is designed for the collapse of impact energy. The current primary energy absorber is comprised of two tube like structures in the form of square cross section. Holes are drilled on the member to improve energy absorption capability and the two members are joined to each other using welded intermediate diaphragm like members [12].

In this study, the deformation behaviors of tube like structures in the form of straight and truncated cone members were investigated by means of finite element analysis method. The investigated members have same weight and length and different wall thicknesses.

At the end of the study, the axial deformation performances of straight and truncated cone members were compared. An optimization study was done to determine the effects of thickness and taper angle on energy absorbing performances of the members.

## 2. Material and Method

### 2.1. Material model and design parameters

High-strength low alloy (HSLA) or micro alloyed steels present a yield strength of 340–420 MPa and ultimate tensile strength of 410–510 MPa, while their uniform elongation ranges between 10 and 25%. Consequently, HSLA steels generally require 25–30% more power to form due to of their higher strength and toughness, for example compared to carbon steels [13]. Thus, the steels are commonly used in trucks, construction equipment, off-highway vehicles, mining equipment, and heavy-duty vehicles for constructing chassis components, buckets and grader blades [14]. In the light of this knowledge, the HSLA 350 steel was chosen as material in the axial collision analysis of the energy absorbers or members used in the passenger coach. The design parameters for energy absorbers was selected as thickness (T) and taper angle (Ta), but the weights of circular section absorbers were kept as constant. The following design parameters were used for the finite element analyses; thickness of 4, 6 and 8 mm, taper angles of 0, 1.5 and 3 degrees. In order to achieve the same weight value, the cross section of the absorber is increased as the thickness is decreased, and the member cross section is decreased as the thickness is increased.

In the analysis, the mass and speed values of the impacting wall, which was modelled for the axial deformation of the structure in the form of the tube, were taken from the experiments applied to the existing energy absorber used in passenger coaches [15]. The method and material properties used during modelling are given below. In the axial collision analysis of the energy absorbers made of HSLA350 material, stress strain diagrams of the material were used depending on the strain rate. The stress-strain diagram of the HSLA350 high strength steel, depending on the deformation rate, is given in Figure 1.

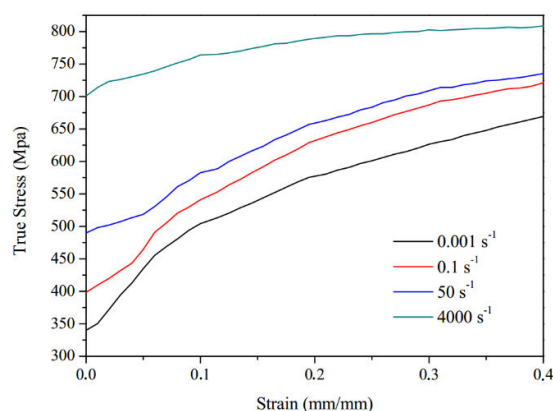


Figure 1. Stress-strain diagram of HSLA 350 steel [6]

In LS-DYNA, these stress-strain values were defined using the Type-24 material model. This material model is defined as a piecewise linear isotropic elastic-plastic material model. In Type-24 material model, the effect of strain rate is achieved by Cowper-Symonds equation. In this equation, the yield stress is multiplied by the factor given below [16]. In the equation (1),  $\sigma_d$ ,  $\sigma_s$ ,  $\dot{\epsilon}$ ,  $D$  and  $p$  are dynamic yield stress, yield stress, deformation rate and Cowper-Symonds material constants, respectively.

$$\sigma_d = \sigma_s [\dot{\epsilon}/D]^{1/p} \quad (1)$$

## 2.2. Finite Element Model

In this study, the deformation behaviors of thin-walled tubes under axial load were examined by the software of LS-DYNA. When describing the boundary conditions in the finite element model, existing installation conditions were considered. Under existing conditions, one end of one energy absorbing member free and the other is welded to the frame of the CEM (Crash Energy Management) system (Fig. 1). For this reason, all the degrees of freedom of the base nodes of the modelled member were restricted and no boundary conditions were applied to the ceiling nodes. The impacting body was modeled with a rigid plate with a mass of 2500 kg and a velocity of 21 m/s. The finite element model of the energy absorber used in the analyses is given in Fig. 2.

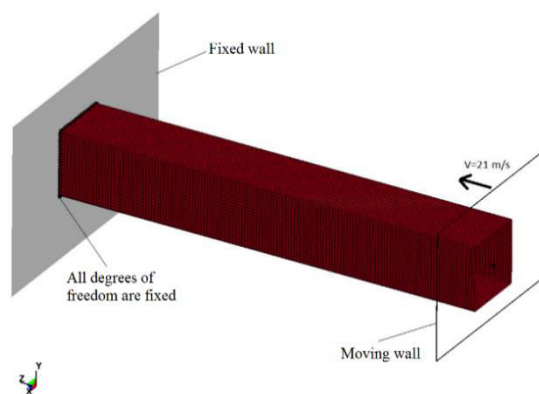


Figure 2. Finite element model of energy absorber

The automatic contact option was used to prevent the folding surfaces from penetrating into each other during deformation, and the friction coefficient was taken as 0.25 for dynamic and static conditions. In addition, the friction coefficient for the friction between the moving rigid plate and the tube was also taken as 0.25. Belytscho-Tsay shell elements with six degrees of freedom for each node and five integration points along the thickness was chosen for meshing the tube because of frequently used element type in the collision analysis for giving short solution times and approximate value assignments [9]. Consequently, the mesh size used in the analyses was chosen to be about twice the thickness value used for each energy absorber according to Ref.[10].

## 3. Results and Discussion

In this section, axial deformation behaviors of straight and truncated (with angles of 1,5° and 3°) tube-like structures under dynamic loading conditions were investigated. For truncated and straight circular cross-section members, rigid wall force-displacement graph is given in Figure 3, the mean force-displacement and absorbed energy displacement graphs are given in Figure 4. The deformation patterns of straight and truncated (with angle of 1,5°) members with wall thicknesses of 4 and 6 mm are given in Figure 5.

It is seen from Figure 7 that the local maximum and minimum force values are comprised during the formation of the folds in the axial deformation of the energy absorbing members. In the formation of the first fold the rigid wall force value reaches its maximum and then decreases suddenly. During the formation of the second and subsequent folds, the force fluctuates between the local maximum and minimum values.

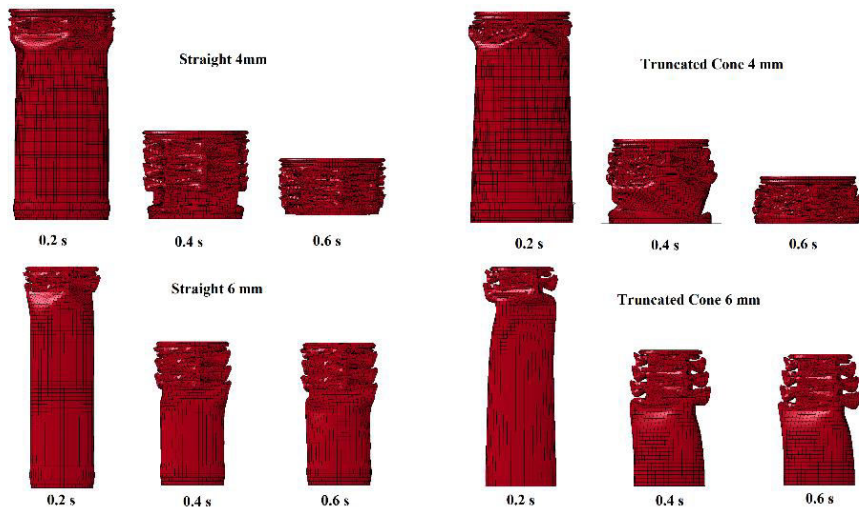


Figure 3. Deformation states of straight and truncated cone members versus time

Al Galib and Limam[17] emphasized this situation that, the initial force required to form the first fold of the member should be high because there is no deformation at the beginning of the tube. When the formation of the first fold, deformations occur in the member and that these deformations reduce the subsequent peak forces.

If the member has the capability to absorb the current impact energy, the force value reaches zero at the rigid wall force-displacement graph. Otherwise, the member loses its energy absorbing ability and starts to behave like a rigid body. When the rigid plate wall force-displacement graph is examined (Fig. 3), it is seen that the rigid wall force increases again towards the end of the analysis due to the loss of energy absorbing ability of members with 4 mm thickness.

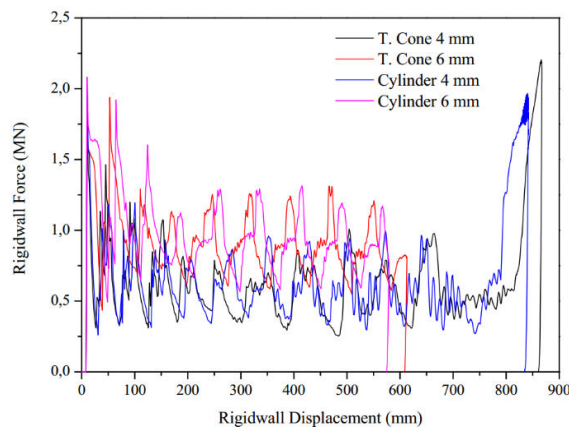


Figure 4. Rigid wall force-displacement for truncated and circular cross-section members

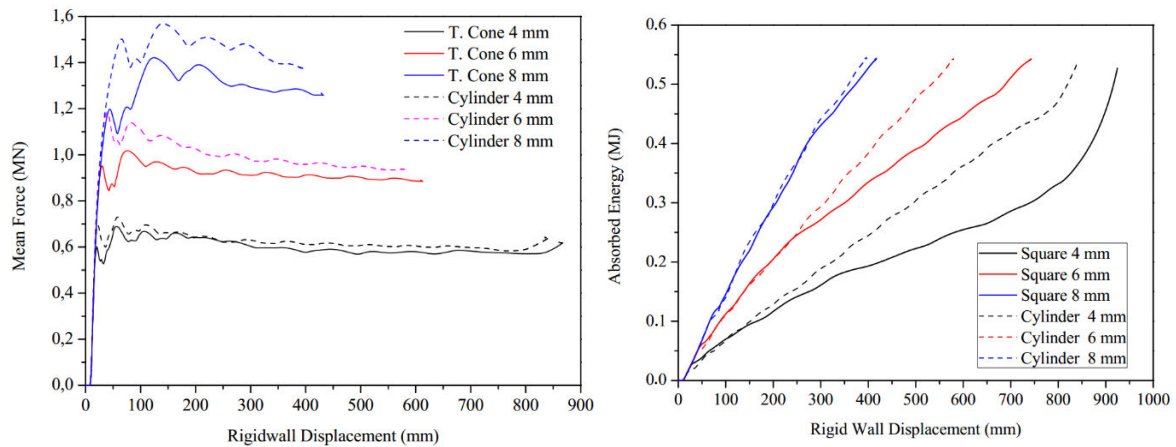


Figure 5. Mean force and absorbed energy versus displacement for 1.5° tapered and straight members

According to the average deformation force-rigid plate displacement graph (Fig. 4), it is seen that the average deformation force is increases as the thickness increases because a rigid structure is obtained at the same member weight. Though the weight is the same, the member becomes more rigid as the thickness increases. In this study, axial deformation behaviors of equally weighted members were examined, hence the cross-sectional dimensions change with increasing thickness. Even though the thickness and the cross-sectional properties of the members change, the amount of material required for plastic deformation remains the same. In this case, the increase of the average deformation force is due to the increase of the full plastic bending moment  $M_0 = \sigma_0 h^2 / 4$  required for buckling when the thickness increases. Figure 4 shows a comparison between straight and truncated members, it is seen that the average deformation force values of straight members are higher than those with truncated members with the same wall thicknesses. The amount of maximum deformation and the change in initial peak force with respect to thickness and taper angle for the members in the form of straight and truncated cone are given in Figure 6.

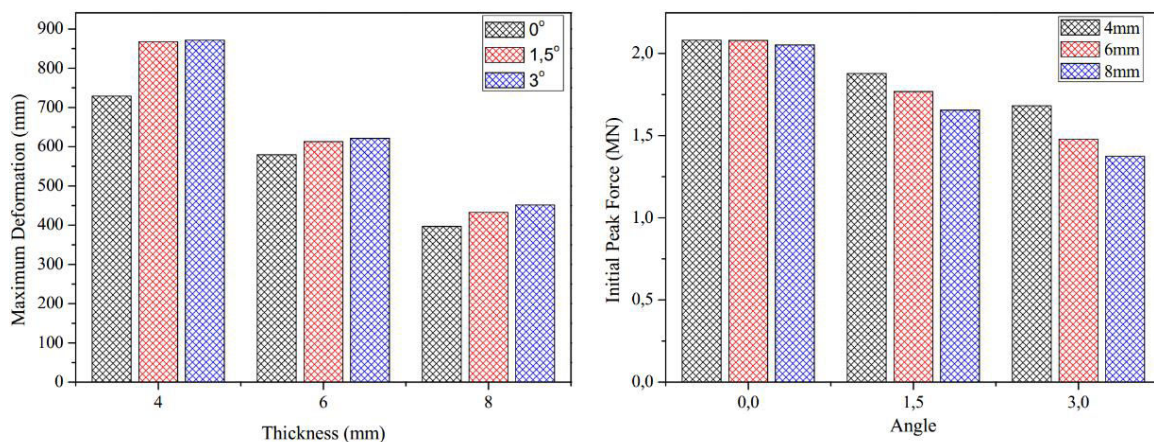


Figure 6. The effect of taper angle on maximum deformation of the member and initial peak force

As can be seen from the Figure 6, the amount of maximum deformation decreases as the thickness of the member increases. When the effect of the taper angle on the maximum deformation is examined for the same thickness elements, the amount of maximum deformation increases as the taper angle of the member increases.

The low initial peak force is desirable feature for energy absorbing members. Therefore, when the change of the first peak force with the taper angle is examined, it is seen that as the taper angle increases, the initial peak force decreases. The reduction in the initial peak force is very small for the straight elements, but this reduction is more pronounced for the truncated elements. The cross-sectional area of the member is decreased to provide the same weight as the thickness of the element increased. From the initial peak force vs angle graph, the initial peak force decreases even if the thickness of the member increases.

### 3.1. Optimization Procedure

The effect levels of design parameters on total efficiency (TE) were determined according to experimental results with %95 confidence level of analysis of variance (Table 1). Here, degree of freedom (DF), the sum of squares (SS), mean square (MS), F-ratio and the percent contribution ratio (PCR) is shown. The F-ratios and their PCR values have been considered to identify the significance levels of the design parameters. Table 1 shows that the most effective parameter is thickness of energy absorber with PCR of 60.52%. The taper angle is secondary important with PCR of 29.01% on the total efficiency according to ANOVA results.

Table 1. ANOVA for S/N ratios of total efficiency

Parameter	DF	SS	MS	F-ratio	%PCR
T	2	8.109	4.0546	11.56	60.52
Ta	2	3.887	1.9434	5.54	29.01
Error	4	1.403	0.3507		10.47
Total	8	13.399			100

### 3.2. Optimization of design parameters

Design parameters for energy absorbers were optimized based on Taguchi method. Therefore, the-larger-the-better approach was applied due to desire of maximum total efficiency (TE) which is determined as performance characteristic in finite element modelling. The design parameters giving optimum total efficiency value were determined in optimization study according to S/N ratio [18]. In the Eq. (2),  $n$  and  $y$  shows the number of simulations and performance characteristic, respectively.

$$S/N = -10 \log(1/n \sum_{i=1}^n 1/y_i^2) \tag{2}$$

The total efficiency which is calculated with the data obtained from finite element analysis and S/N ratios are given in Table 2. Statistical analyses and optimization studies were performed via Minitab software.

Table 2. FE simulation results and S/N ratios

Exp. No	T	Ta	TE	S/N
1	4	0	0.215605	-13.3268
2	4	1.5	0.233029	-12.6518
3	4	3	0.247227	-12.1381
4	6	0	0.267511	-11.4532
5	6	1.5	0.283052	-10.9627
6	6	3	0.366202	-8.72558
7	8	0	0.257682	-11.7783
8	8	1.5	0.257676	-11.7785
9	8	3	0.270111	-11.0534

S/N ratios of parameters are considered in Taguchi optimization method. The highest S/N ratio shows the optimum level of parameters according to “the-larger-the-better” approach. S/N ratios calculated by simulation results of total efficiency are shown in main effect plot (Fig. 7). Also, the variation of S/N ratios according to parameters is given in Table 3. It was shown that thickness is the most important thickness on TE when examining the main effect plots in Fig. 7 and the difference ( $\Delta$ ) between maximum and minimum values of S/N ratios in Table 2. The optimum levels for minimum TE according to S/N ratios were determined as T2, Ta3.

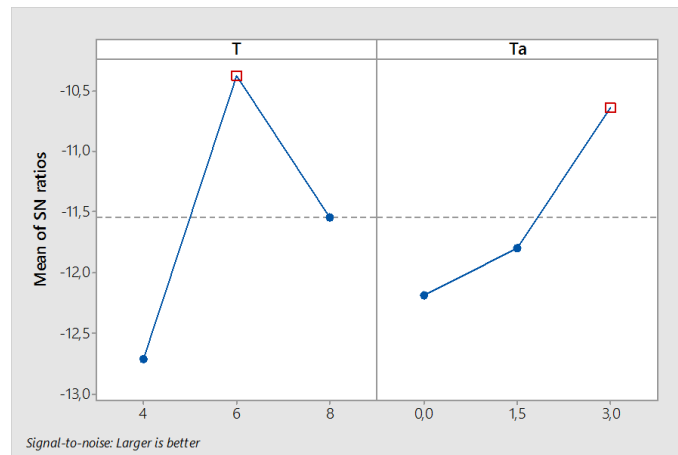


Figure 7. The main effect plot for SN ratio of total efficiency

Table 3. Response table of S/N ratios for total efficiency

Parameter	S/N ratios			$\Delta$
	Level 1	Level 2	Level 3	
Thickness	-12.71	-10.38*	-11.54	2.33
Taper angle	-12.19	-11.8	-10.64*	1.55

\*Optimum levels of parameters

Average of FE simulation results performed at optimal levels are evaluated by Eq. (3) to forecast the mean for the improvement conditions. Eq. (1) which is the expression of calculated total efficiency (TE) is derived from Eq. (4).

$$\eta_G = \bar{\eta}_G + (\bar{T}_0 - \bar{\eta}_G) + (Ta_0 - \bar{\eta}_G) \tag{3}$$

$$TE_{cal} = 10^{-\eta_G/20} \tag{4}$$

Where,  $\eta_G$  is the S/N ratio calculated at optimal level of factors (dB),  $\bar{\eta}_G$  is the mean S/N ratio of all parameters (dB),  $\bar{A}_0$  and  $\bar{B}_0$  are the mean S/N ratio once thickness and taper angle are at optimum levels, and  $TE_{cal}$  is the calculated value. Consequently,  $\eta_G$  and  $TE_{cal}$  for optimum design parameters were determined as -9.4785 dB and 0.3358, respectively. Lastly, confirmation experiments with FE modelling were done by using the optimum design parameters after the determination of these factors for TE and thus reliability of the optimization has been confirmed. The FE simulations conducted by considering the confidence interval (CI) calculated from Eqn. (5) and (6) [19].

$$CI = \sqrt{F_{\alpha,(1,ve)} V_e (1/\eta_{eff} + 1/r)} \tag{5}$$

$$\eta_{eff} = N / (1 + v_T) \tag{6}$$

Where;  $F_{\alpha,(1,ve)}$  is the F-ratio at the 95 % significance level,  $\alpha$  is the importance level,  $v_e$  is the degree of freedom of the error,  $V_e$  is the error variance,  $n_{eff}$  is the effective number of replications,  $r$  is the number of replications for the verification test. In Equation 6,  $N$  is the total number of experiments and  $v_T$  is the total main factor of the degree of freedom. Total efficiency obtained with FE simulation ( $TE_{exp}$ ), calculated total efficiency ( $TE_{cal}$ ), and S/N ratios ( $\eta_{exp}$ ,  $\eta_{cal}$ ) for TE are given by comparing between simulation results and calculated values (Table 4). Table 4 shows differences between confirmation experiment results and calculated values and their S/N ratios obtained by using Eqn. 2 and 3. As can be seen from the Table4, a difference of 0.7529 dB is under the confidence interval of 1.6893 dB for total efficiency. Thus, the optimum levels of design parameters for total efficiency were approved as confident.

Table 4. Comparison of simulation results and calculated values

Simulation results		Calculated value		Difference	
$TE_{exp}$ ( $\mu\text{m}$ )	$\eta_{exp}$ (dB)	$TE_{cal}$ ( $\mu\text{m}$ )	$\eta_{cal}$ (dB)	$TE_{exp} - TE_{cal}$	$\eta_{exp} - \eta_{cal}$
0.3662	-8.7256	0.3358	-9.4785	0.0304	0.7529

#### 4. Conclusions

In this study, the axial deformation behaviors of the energy absorbing members in the form of straight and truncated (with angles of  $1.5^\circ$  and  $3^\circ$ ) tubes were investigated under the impact force acting on the existing primary energy absorbing member.

Initially, deformation performances were compared with the condition that the weight and length of the energy absorbing members were the same. As a result of comparison, it was found that the average deformation force values of straight members are higher than those with truncated members with the same wall thicknesses. When the thickness of the member is increased, the average deformation force increased due to the increase of the full plastic bending moment required for buckling. Though the weight is the same, the member becomes more rigid as the thickness increases.

It was realized that the amount of maximum deformation decreases as the thickness of the member increases and increases as the taper angle of the member increases for the same thickness elements. The low initial peak force is desirable feature for energy absorbing members. Therefore, when the change of the first peak force with the taper angle is examined, it is seen that as the taper angle increases, the initial peak force decreases.

Consequently, design parameters for energy absorbers were optimized based on Taguchi method. Therefore, the-larger-the-better approach was applied due to desire of maximum total efficiency (TE) which is determined as performance characteristic of the member. The design parameters giving optimum total efficiency value were determined in optimization study according to S/N ratio. According to optimization study, the optimum energy absorbing member was determined as a truncated member with the 6mm thickness and taper angle of  $1.5^\circ$ . The effects of taper angle and thickness on total crush efficiency of the member calculated as 10.38 % and 10.64 % respectively.

#### 5. References

- [1] E. Martinez, David Tyrell, R. Rancatore, R. Stringfellow, and G. Amar, "A crush zone design for an existing passenger rail cab car," in *Proceedings of 2005 ASME International Mechanical Engineering Congress & Exposition*, 2004, pp. 85–94.
- [2] K. Jacobsen, D. Tyrell, and B. Perlman, "Impact Tests of Crash Energy Management Passenger Rail Cars: Analysis and Structural Measurements," in *ASME 2004 International Mechanical Engineering Congress and Exposition*, 2004, pp. 97–105.
- [3] W. Abramowicz and N. Jones, "Dynamic progressive buckling of circular and square tubes," *Int. J. Impact Eng.*, vol. 4, no. 4, pp. 243–270, 1986.
- [4] S. Simunovic, J. Shaw, and G. a Aramayo, "Material Modeling Effects on Impact Deformation of Ultralight Steel Auto Body," *SAE Tech. Pap.*, no. 724, 2000.
- [5] A. A. Nia and J. H. Hamedani, "Comparative analysis of energy absorption and deformations of thin walled tubes with various section geometries," *Thin-Walled Struct.*, vol. 48, no. 12, pp. 946–954, 2010.
- [6] M. Langseth, O. S. Hopperstad, and T. Berstad, "Crashworthiness of aluminium extrusions: validation of numerical simulation, effect of mass ratio and impact velocity," *Int. J. Impact Eng.*, vol. 22, no. 9–10, pp. 829–854, 1999.
- [7] A. Tasdemirci, "The effect of tube end constraining on the axial crushing behavior of an aluminum tube," *Mater. Des.*, vol. 29, no. 10, pp. 1992–2001, 2008.
- [8] R. Gümrük and S. Karadeniz, "The influences of the residual forming data on the quasi-static axial crash response of a top-hat section," *Int. J. Mech. Sci.*, vol. 51, no. 5, pp. 350–362, 2009.
- [9] R. Gümrük and S. Karadeniz, "A numerical study of the influence of bump type triggers on the axial crushing of top hat thin-walled sections," *Thin-Walled Struct.*, vol. 46, no. 10, pp. 1094–1106, 2008.
- [10] G. Chen, X. M. Chen, and M. F. Shi, "Experimental and Numerical Studies of Crash Trigger Sensitivity in Frontal Impact," *SAE Tech. Pap.*, no. 724, 2005.
- [11] A. G. Hanssen, M. Langseth, and O. S. Hopperstad, "Static and dynamic crushing of circular aluminium extrusions with aluminium foam filler," *Int. J. Impact Eng.*, vol. 24, no. 5, pp. 475–507, 2000.

- 
- [12] G. Mayville, R. A., Rancatore, R. J., Stringfellow, R. G., Amar, “Repair of Budd Pioneer Coach Car Crush Zones,” Cambridge, MA, 2007.
- [13] D. A. Skobir, “High-strength low-alloy (HSLA) steels,” *Mater. Technol.*, vol. 45, no. 4, pp. 295–301, 2011.
- [14] J. Patel, C. Klinkenberg, and K. Hulka, “Hot rolled HSLA strip steels for automotive and construction applications,” *Niobium Sci. Technol.*, no. Grade 100, pp. 647–674, 2001.
- [15] R. Mayville, A. D. Little, K. Johnson, and P. Engineering, “The Development of a Rail Passenger Coach Car Crush Zone,” in *Proceedings of the 2003 IEEE/ASME Joint Rail Conference*, 2003, pp. 1–8.
- [16] J. O. Hallquist, *LS-DYNA users manual*. Livermore, California: Livermore Software Technology Corporation, 1998.
- [17] D. Al Galib and A. Limam, “Experimental and numerical investigation of static and dynamic axial crushing of circular aluminum tubes,” *Thin-Walled Struct.*, vol. 42, no. 8, pp. 1103–1137, 2004.
- [18] G. Taguchi, S. Chowdhury, Y. Wu, *Taguchi's Quality Engineering Handbook*, John Wiley & Sons, Inc., New Jersey, USA, 2005.
- [19] M. Günay, M.E. Korkmaz, *Optimization of Honing Parameters for Renewal of Cylinder Liners*. *GU J Sci* 30(1), 111-119, 2017.

## Modeling and Simulation of the Resistance of Bacteria to Antibiotics

Cenab Batu Bora<sup>1</sup>, Sevcan Emek<sup>2</sup>, Vedat Evren<sup>3</sup>, Sebnem Bora<sup>2</sup>

<sup>1</sup>Uskudar American Academy, 34664, Uskudar/Istanbul, Turkey

<sup>2</sup>Department of Computer Engineering, Ege University, 35100, Bornova/Izmir, Turkey

<sup>3</sup>Department of Physiology, Faculty of Medicine, Ege University, 35100, Bornova/Izmir, Turkey

---

### Article Info

#### Article history:

Received Jun 1<sup>st</sup>, 2017

Revised Aug 20<sup>th</sup>, 2017

Accepted Oct 18<sup>th</sup>, 2017

---

#### Keyword:

Agent-Based Modeling

Antibiotic Resistance

Immune System

Simulation

---

### ABSTRACT

The unnecessary use of antibiotics has given rise to antibiotic resistance and for this reason is a cause of growing concern in contemporary health care contexts. Antibiotic resistance means that an antibiotic is losing or has lost the ability to kill a given bacteria and/or to prevent it from reproducing. The result: an increase in the number of patients suffering from and even dying of infections. Resistant bacteria continue to increase in number, as they survive the antibiotic designed and used to kill them. The disease induced by the bacteria lasts longer, therefore, than would have been the case were the bacteria not antibiotic resistant. Thus, prolonged treatment and/or even death results together with an increase in cost associated with these outcomes. The purpose of this study is to investigate the interactions among the bacteria, immune system cells, and antibiotics in a Repast Symphony 2.1 agent-based simulation environment modeled to observe the effects of the antibiotic resistance in the infection process. According to our results, increased antibiotic resistance constitutes a serious threat to the success of established methods used in the treatment of bacterial infections.

---

### Corresponding Author:

Sevcan Emek,

Department of Computer Engineering,

Ege University,

Bornova/Izmir, Turkey.

Email: sevcan.emek@ege.edu.tr

---

### 1. Introduction

In the domain of biology, the process of bacterial evolution and the biology of bacterial population are the main ways to describe antibiotic resistance—a phenomenon that poses a significant threat to human health. Antibiotic resistance refers to case in which an antibiotic has lost or is losing its ability to kill or prevent the reproduction of a bacteria it was designed to combat. This phenomenon leads to an increase in the number of patients suffering from and even dying of infections given the failure of treatment. In this study, we explore the interactions among the bacteria, immune system cells, and antibiotics by mimicking a real biological environment and thereby observe the effects of antibiotic resistance on the infection process. In order to explore the dynamics of antibiotic resistance, we developed an agent-based model that includes immune system cells, bacteria as agents, and nutrient and antibiotic layers as the simulated environment's objects.

Agent-based modeling is a rule-based computational modeling approach that focuses on rules and interactions among the individuals or components of a real system. The aim is to generate a large set of interacting agents and simulate their interactions and behaviors in a represented environment. Using agent-based modeling, we can develop an understanding of the mechanisms of antibiotic resistance and the dynamics of microbiological systems that take place in the process of bacterial evolution. Given that the properties of the process of bacterial evolution and the biology of bacterial population such as collective behavior can be accounted for by

simple rules of operation, lack of central control, adaptation, and sophisticated information processing, agent-based modeling is the most suitable technique for modeling bacterial populations and antibiotic resistance.

There are several approaches to modeling the effects of antibiotic resistance, and research on this topic has been widely published in journals. A mathematical model of bacterial transmission in a hospital is elaborated in [1] to show the effects of measures designed to control the nosocomial transmission of bacteria and to decrease antibiotic resistance in nosocomial pathogens. In order to explore the efficacy of cycling programs, a mathematical model of antimicrobial cycling in a hospital is developed and explained in [2]. In [3], a mathematical model is used to identify the conditions in which resistant bacteria continue to exist in a hospital and conversely to define the conditions in which prevalent resistant bacteria can be removed completely from a hospital environment. A model of the transmission dynamics of infection in the presence of dual resistance to antibiotics is developed by tracking several patients in hospital settings to observe their colonization status [4].

In this paper, we present our model for bacterial resistance to antibiotics in detail. The principal way in which our study is distinguished from other research in this area is that the system we propose is relatively simple: we identify simple rules for interactions between elements without complex mathematical calculations. Our goal in this regard is to offer a system that is as simple as possible through a bottom-up modeling approach.

The remaining sections of this paper are organized as follows. Section 2 provides background information detailing the biology of bacterial population. Section 3 presents a brief explanation of the fundamentals of Agent-Based Modeling and Simulation (ABMS). Section 4 introduces the agent-based model. Section 5 illustrates the experimental model developed for the study, presents the data, our analysis, and a discussion of the approach we used. Section 6 presents a summary of this research study.

## 2. Bacteria

Populations of bacteria known as bacteria flora live on human skin and in the mouth and digestive tract. Most bacteria flora is commensal or mutualist and are not harmful in the parts of the body where they ordinarily exist. However, they can be harmful if introduced to other parts of the body. If commensalistic and mutualistic bacteria do find their way to these other parts of the body, however, a bacterial infection can develop in the host as a consequence.

Pathogens, which do not usually live in healthy human bodies and are transmitted to healthy individuals from infected people, can also cause infections. Antibiotic treatment is often effective against both infections caused by flora bacteria and those caused by pathogenic bacteria. Before the discovery of penicillin, it was very difficult to treat some infections such as ear infections and bacterial pneumonia. However, antibiotics changed this, as they significantly improved a patient's chances of recovering from numerous kinds of bacterial infections. At present, there are almost 100 different antibiotics in clinical use. Yet, hospital patients continue to develop infections that cannot be cured by antibiotics because of bacterial evolution.

As it provides substance for natural selection, the emergence of mutations is an important phenomenon underlying evolution. Bacterial cells invade a host and then each bacterial cell divides, thereby forming two daughter cells. Not all the cells in a bacterial population are genetically identical, as cell division sometimes results in mutations, some of which reduce a cell's ability to survive and reproduce independently of the environment. However, the effects of many mutations are dependent on the environment.

A random mutation can change a bacterial protein required for the antibiotic to enter bacteria cells. In this case, the antibiotic will not be able to enter a mutant cell and, therefore, will not be able to undermine the protein synthesis. Thus, the mutant cell will reproduce even though an antibiotic has been introduced. In contrast, antibiotic-sensitive cells either fail to reproduce and/or die in this case [5].

## 3. Agent-Based Modeling and Simulation

Agent-Based Modeling and Simulation (ABMS) is a powerful technique used in order to understand the mechanisms of systems and/or the system dynamics of complex phenomena in many domains, including in the social sciences [6], ecology [7], economics [8], and biomedicine [9]. ABMS consists of three main components: agents, a simulated environment, and a simulation environment.

Agents are actors that operate in the real system and influence and are influenced by the simulated environment. The agents are involved in the simulation model as model components that perform actions individually and interact with other agents and the simulated environment, thereby representing behaviors in the real system.

Agent-based models consist of dynamically interacting autonomous agents that act according to their local knowledge (rules, behaviors, and information) by taking account of the environment and reacting to changes within it. Agent-based modeling provides a bottom-up approach in order to model a range of application domains. Adopting the bottom-up approach to model a complex system reduces the complexity of the system by distributing the complexity to a large set of interacting individuals with simple behaviors. As a result of individual behaviors and interactions, the system accounts for complex or adaptive behaviors at a higher level [10]. Thus, ABMS provides a sound opportunity to model complex systems that exhibit behaviors of this kind. A simulated environment consists of components that cannot be represented as agents in the real system but that represent important components in regard to representing the real system. Further, the simulated environment also represents the real environment in which agents live, operate, and interact with each other. The simulated environment is part of the simulation model. In a simulated environment, sources and state definitions are present and are often shared in the overall model by all the agents and contain information in some cases.

A simulation environment consists of agents and the simulated environment, enables the simulation model to operate, and represents the simulation infrastructure. Conceptually, the simulation environment is considered to be part of ABMS. The first reason for this is that if the simulation model is to represent the current system in real terms, the infrastructure required must be part of the real system. In ABMS, the concept of time is typically represented as time steps. In every time step, each agent in the model performs an operation, and/or interacts with other agents [11].

#### **4. Agent-Based Modeling and Simulation (ABMS) of the Resistance of Bacteria to Antibiotics**

The agent-based modeling and simulation (ABMS) of the resistance of bacteria to antibiotics has three main components: agents, a simulated environment, and a simulation environment. The immune system cells and bacteria are the agents of the model. They have attributes and behavior rules and react to changes in the environment. The virulence factor, which is an attribute of the bacteria, defines the extent of the pathogenicity of a given pathogen. Whereas bacteria engage in intraspecies and interspecies competition, immune system cells fight bacteria. These influence interactions among agents of the model and between agents of the model and the simulated environment.

The simulated environment in the model consists of a grid with  $100 \times 100$  grid cells to represent human tissue or a human organ. Each grid cell provides a suitable environmental layer with the nutritional resources needed for bacteria to live, grow, and reproduce. This layer is represented by tones of green color. Moreover, in order to observe the process whereby an antibiotic kills bacteria or whereby bacteria resist the introduction of an antibiotic, the model is designed so that each grid cell provides an antibiotic layer with a constant concentration level of antibiotics.

In this study, we used Repast Symphony 2.1 to create agents and system objects that cannot be implemented as agents [12]. In the Repast Symphony simulation environment, the agents and objects in the simulated environment are written using Java programming language. After defining the agents and system objects in the simulated environment, it is necessary to describe the behaviors of the agents.

##### **4.1. Bacterial Behavior**

At the initialization, the programmer defines the number of bacteria to create for the simulation. The bacterial cells are created and randomly assigned virulence factors of between 1 and 4. For example, a bacterial cell assigned a virulence factor of 1 reproduces in every time step of the simulation.

Each bacterial cell is randomly distributed on the simulation environment represented by a grid with  $100 \times 100$  grid cells. Each bacterial cell increases in cell size by consuming nutrients where it is located. Each grid cell provides a high level of nutrients to bacterial cells. The nutrients consumed by a bacterial cell are subtracted from the nutrient availability of its grid cell. At each time step, nutrient availability increases in accord with nutrient production. Under suitable conditions, each bacterial cell grows to a fixed size and then reproduces such that two identical daughter cells are produced.

##### **4.2. Immune System Cell Behavior**

At the initialization, the programmer defines the number of immune system cells to create for the simulation. Immune system cells are created and randomly distributed in the grid. An immune system cell kills one of the bacterial cells in the grid by looking at the neighboring 48 cells and locates in the dead bacterial cell's grid cell in every time step. If an immune system cell destroys 2 bacteria cells, this immune system cell signals an

immune system cell and then dies. If there are more than 40 bacterial cells in the neighborhood, an immune system cell also signals another immune system cell. If there are bacterial cells in the range of 2 to 15 in the neighborhood, then an immune system cell vanishes. If an immune system cell cannot kill a bacteria cell through 15 time steps after its creation, it then vanishes.

## 5. Experimental Study

We performed five experiments in order to observe the bacterial competition of the flora, interactions between the bacteria and the immune cells in the presence of an antibiotic, the resistance of bacteria to an antibiotic, the suppressed immune system in case the resistance of bacteria to an antibiotic exists, and the effect of the use of the second antibiotic in the treatment of the infection caused by the resistant bacteria.

### 5.1. Experiment: Bacterial Competition on Flora

In this experiment, we begin our consideration of competition in populations of bacteria with observations pertaining to bacterial populations and provide an introduction to how competition can affect interactions among the bacteria. Therefore, 4000 bacterial cells with virulence factors in the range of 2 to 4 were created in the Repast Symphony simulation environment. A nutrient layer was included in the simulation environment to enable the bacteria to live, grow, and reproduce.

At the initial time step, a settlement of 4000 bacterial cells accrued that ranged in terms of virulence factor from 2 to 4 in the Repast Symphony simulation environment, as shown in Fig. 1(a). Bacterial cells with a virulence factor of 2 are represented as yellow, those with a virulence factor of 3 are represented as red, and those with a virulence factor of 4 are represented as purple.

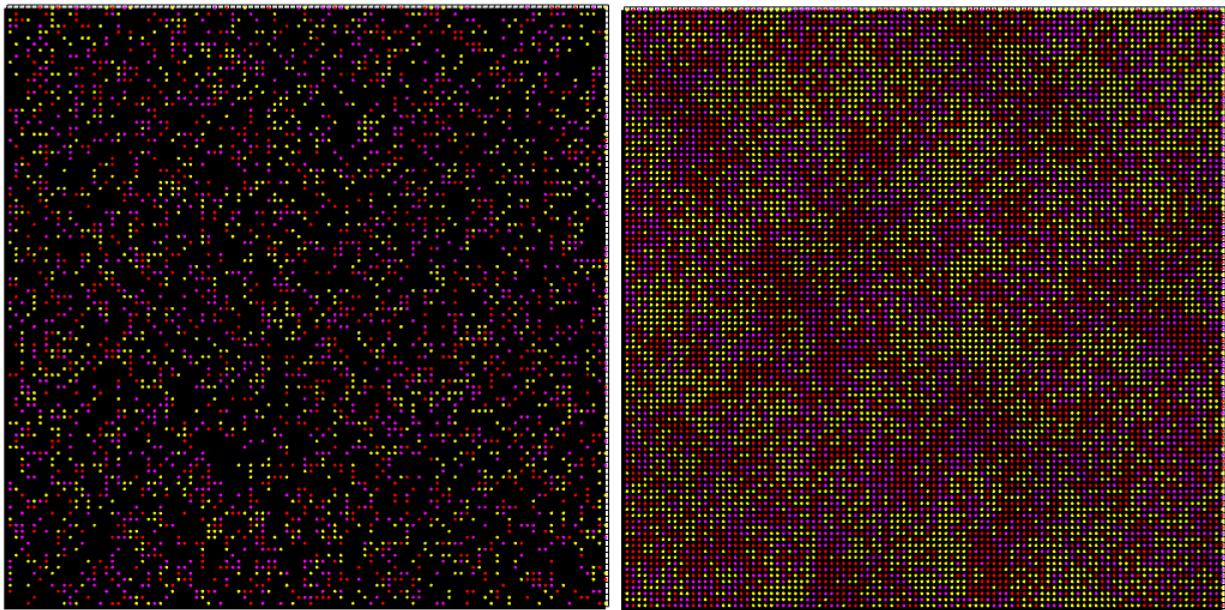


Figure 1. (a) Settlement of bacterial cells in the Repast Symphony simulation environment at the initial time step, (b) Bacterial cells in the Repast Symphony simulation environment at 1000<sup>th</sup> time step

After 1000 time steps, the bacterial cells are allocated to all the grid cells and there are no empty grid cells in the simulation environment, as shown in Fig. 1(b). The number of bacterial cells increases given that they grow and divide rapidly under appropriate conditions. The bacteria with a low virulence factor reproduce very rapidly; therefore, the number of bacteria shown in yellow is higher than the number of bacteria shown in either red or purple. Indeed, bacteria compete with their neighbors for space and nutritional resources. Bacteria with similar nutritional requirements, such as members of the same population or different bacterial species, compete for nutrients as these become depleted by the growing population of bacteria. In our simulated environment, competition can lead to selection for variants that have low virulence factors.

## 5.2. Experiment: Antibiotic Usage

In this experiment, 100 immune system cells and 4000 bacterial cells with virulence factors ranging from 2 to 4 were created in the Repast Symphony simulation environment. The nutrient layer was included in the simulation environment for the bacteria to live, grow, and reproduce. An antibiotic layer was also included in the simulation environment.

At the initial time step, a settlement of 100 immune system cells and 4000 bacterial cells with a range of virulence factors accrues in the Repast Symphony simulation environment, as shown in Fig. 2(a). The bacteria cells are represented by yellow, red, and purple circles, and the immune system cells are represented by blue circles.

As shown in Fig. 2(b), the simulation environment includes only 9 immune system cells and the bacterial cells are removed from the environment after 664 time steps. In our simulation, each grid cell provides a constant concentration level of antibiotics, which kill the bacteria. In Fig. 3, a graph shows the number of bacteria alive at each time step: the number of bacteria decreases when the simulation starts, as the immune system cells kill most of them before they can begin to reproduce. The bacteria must grow in cell size before they can reproduce. Then, the number of bacteria increases as they are in the simulation environment with a high level of nutrients as the simulation progresses. However, the increase in the population of bacterial cells cannot exceed the number given as the initial value (4000) because the antibiotic starts to kill some of the bacteria and helps the immune cells to handle the remaining bacterial cells. The bacterial population reaches its peak at the 155<sup>th</sup> and 305<sup>th</sup> time steps. Then, the simulation pauses at the 664<sup>th</sup> time step because there are no bacteria in the simulation environment. We expected this result as the antibiotic kills all the bacteria.

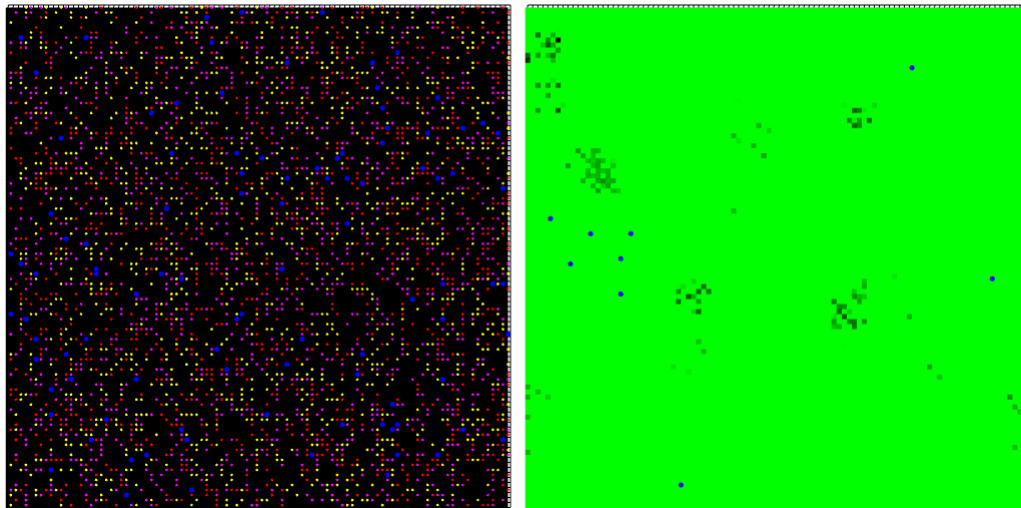


Figure 2. (a) Immune system cells and bacterial cells in the Repast Symphony simulation environment at the initial time step, (b) Immune system cells and bacterial cells in the Repast Symphony simulation environment at 664<sup>th</sup> time step

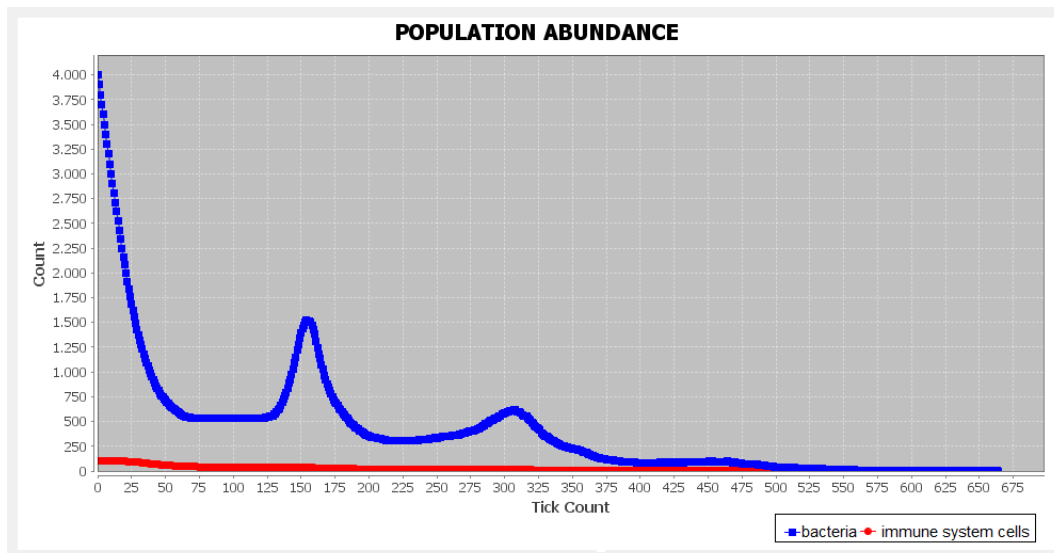


Figure 3. Populations at 664<sup>th</sup> time step

### 5.3. Experiment: Antibiotic Resistance

In this experiment, 100 immune system cells and 4000 bacterial cells with virulence factors ranging from 1 to 4 were created in the Repast Symphony simulation environment. Bacterial cells shown in white (virulencefactor=1) represent mutant cells, i.e., cells that have become resistant to antibiotics. The nutrient layer was included in the simulation environment for the bacteria to live, grow, and reproduce. An antibiotic layer was also included in the simulation environment for this experiment.

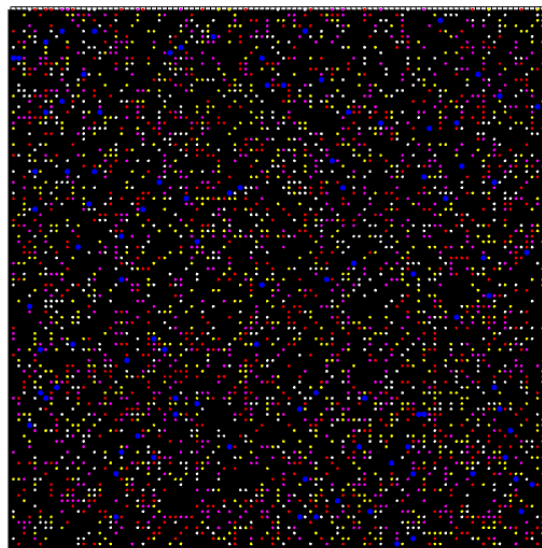


Figure 4. Settlement of 100 immune system cells and 4000 bacterial cells in the Repast Symphony simulation environment

At the initial time step, a settlement of 100 immune system cells and 4000 bacterial cells with a range of virulence factors accrues in the Repast Symphony simulation environment, as shown in Fig. 4: The bacterial cells are represented as white, yellow, red, and purple circles, and the immune cells are represented as blue circles. In this experiment, the bacteria shown in white are antibiotic-resistant such that the antibiotic cannot kill them.

We observed that the bacteria shown in yellow, red, and purple were removed from the simulation environment until time step 664, as described in Section 5.2. Some were killed by the antibiotic whereas the rest were killed by the immune system cells. As shown in Fig. 5, at the 454<sup>th</sup> time step, only immune system cells and antibiotic-resistant bacteria remain in the simulation environment. The number of immune system

cells is very high in this experiment, as the resistant bacterial cells divide rapidly (virulence factor=1) and the number of bacterial cells increases, which causes the immune cells to increase in the number as well.

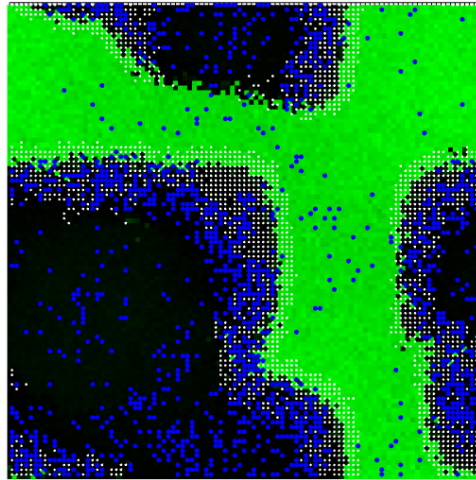


Figure 5. Immune system cells and bacterial cells in the Repast Simphony simulation environment at 454<sup>th</sup> time step

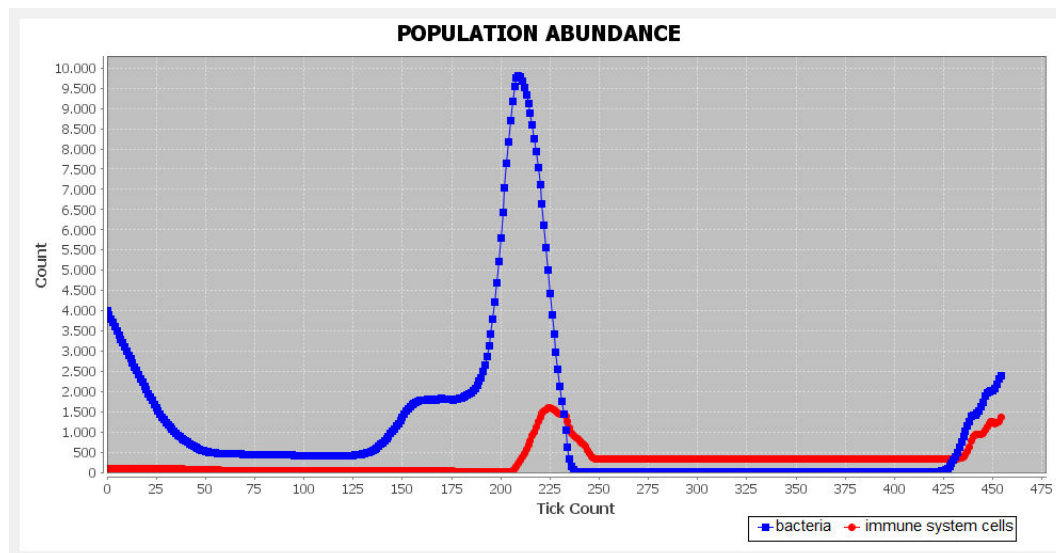


Figure 6. Populations graph of immune system cells and bacterial cells at 454<sup>th</sup> time step

Fig. 6 shows a graph of the number of bacteria alive at each time step: the number of bacteria decreases when the simulation starts because some are killed by the immune system cells and they cannot start reproducing immediately. The bacteria must grow in size before they can reproduce. The population of bacteria reaches its maximum value at the 200<sup>th</sup> time step whereas the immune cell population reaches its maximum value at the 225<sup>th</sup> time step to fight the bacterial cells. The bacterial population reaches almost 10,000 at the 200<sup>th</sup> time step. After the 200<sup>th</sup> time step, the antibiotic helps the immune system cells and both remove the bacteria shown in yellow, red, and purple. At the 454<sup>th</sup> time step, a new bacterial attack is initiated by the antibiotic-resistant bacteria.

The simulation is paused at the 1000<sup>th</sup> time step, at which point the simulation environment contains 28 antibiotic-resistant bacteria and 450 immune system cells, as shown in Fig.7. The body's immune system alleviates the bacterial attacks and works to maintain the body's tissues in balance. The bacterial attack is also shown in Fig.8 before the simulation is paused. After the 454<sup>th</sup> time step, the bacteria attack several times. The attacks will continue as long as these bacteria encounter an environment that supports their ability to live, grow, and reproduce.

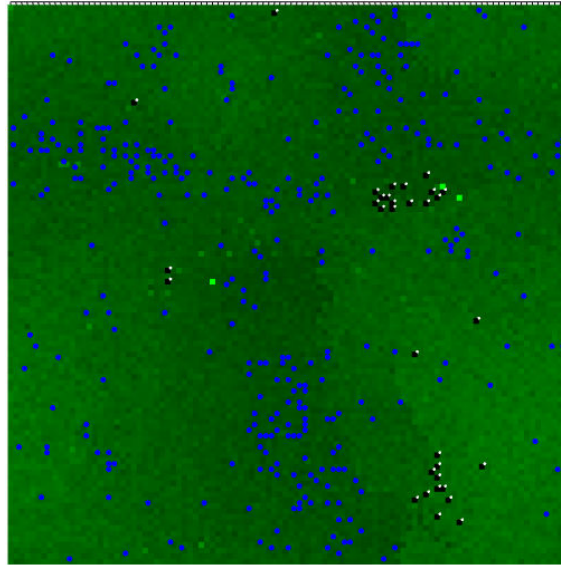


Figure 7. Immune system cells and bacterial cells in the Repast Symphony simulation environment at 1000<sup>th</sup> time step

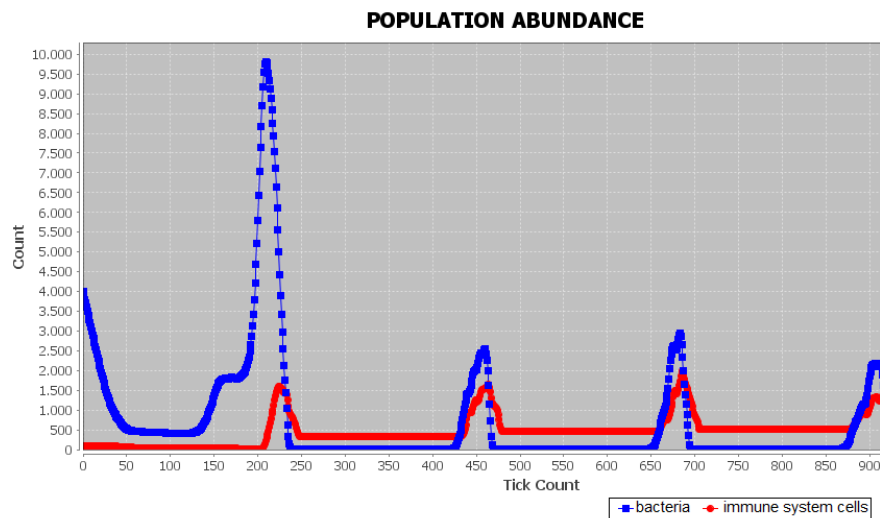


Figure 8. Populations graph of immune system cells and bacterial cells at 1000<sup>th</sup> time step

#### 5.4. Experiment: Antibiotic Resistance and the Suppressed Immune System

Cortisol is a hormone that is secreted from the adrenal cortex in response to stress. It has a strong effect in the body on blood sugar regulation, blood pressure regulation, immune system suppression, and in the reduction of inflammation. The use of hydrocortisone (a synthetic form of cortisol) during infections prevents an over-activation of the inflammatory response by weakening the activity of the immune system. In order to study the effect of cortisol on the immune system cells, a similar experimental setup as described in Section 5.3 was performed. For this simulation, 100 immune system cells and 4000 bacterial cells with arbitrary virulence factors ranging from 1 to 4 were created in the Repast Symphony simulation environment. A nutrient layer and an antibiotic layer were also included in the simulation environment for this experiment. The behavior of immune system cells in the simulation program was modified in order to fight the bacterial cells slowly since cortisol suppresses the immune system. Thus, an immune system cell kills one of the bacterial cells in the grid by looking at the neighboring 48 cells and moves into the dead bacteria's grid cell in every fourth time step. Immune system cell dies after killing 2 bacterial cells, and causes immune system to recruit another immune cell into the simulation environment.

At the initial time step, a settlement of 100 immune system cells and 4000 bacterial cells with a range of virulence factors accrues in the Repast Symphony simulation environment, are shown in Fig.9: The bacterial

cells are represented as white, yellow, red, and purple circles, and the immune system cells are represented as blue circles. In this experiment, the bacteria shown in white are antibiotic-resistant.

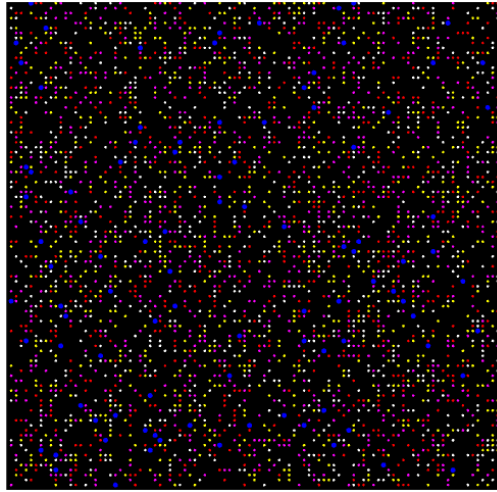


Figure 9. Settlement of 100 immune system cells and 4000 bacterial cells in the Repast Symphony simulation environment

Fig. 10 shows a graph of the number of bacteria alive at each time step: the number of bacteria decreases when the simulation starts because some are killed by the immune cells and they cannot start reproducing immediately. The bacteria must grow in size before they can reproduce. The population of bacteria reaches almost 7000 at the 225<sup>th</sup> time step whereas the immune system cell population reaches its maximum value at the 225<sup>th</sup> time step to fight the bacterial cells. We observed that the antibiotic helped the immune system cells and both removed the bacteria shown in yellow, red, and purple until the 400<sup>th</sup> time step. As shown in Fig. 11, at the 400<sup>th</sup> time step, only immune system cells and antibiotic-resistant bacteria remain in the simulation environment.

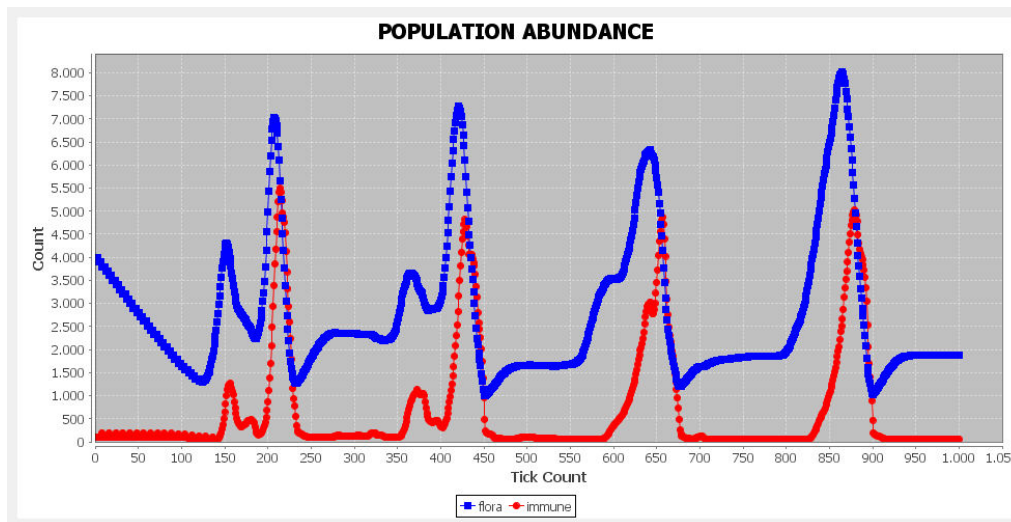


Figure 10. Populations graph of immune system cells and bacterial cells at 1000<sup>th</sup> time step

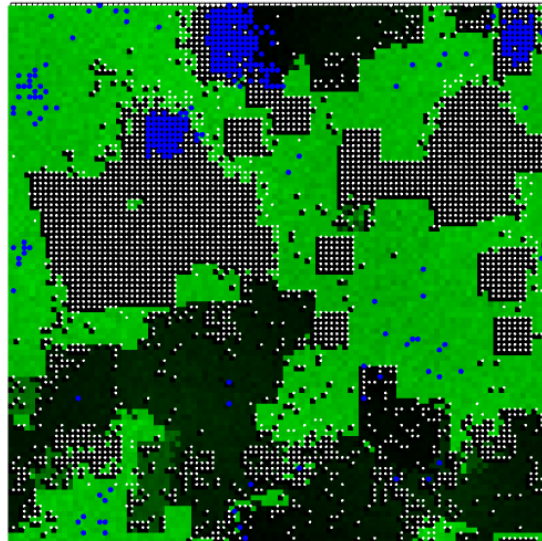


Figure 11. Immune system cells and bacterial cells in the Repast Symphony simulation environment at 400<sup>th</sup> time step

The number of the bacterial cells is very high during this experiment. As the number of bacterial cells increases, it causes the immune system cells to increase in the number as well. As shown in Fig. 10, after 400 time steps, several bacterial attacks are initiated by the resistant bacteria. However, the immune system cells cannot totally remove the antibiotic resistant bacterial cells or decrease the number of bacterial cells to a small number such that the immune system can alleviate the infection; because, the immune system cells are too slow to defend the body against the bacterial attacks. The simulation is paused at the 1000<sup>th</sup> time step, at which point the simulation environment contains almost 1800 antibiotic-resistant bacteria and 40 immune system cells, as shown in Fig. 12. Cortisol suppresses the immune system and the body is at increased risk of infection.

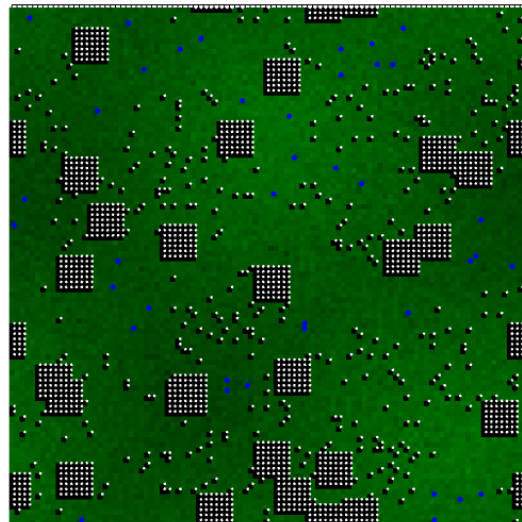


Figure 12. Immune system cells and bacterial cells in the Repast Symphony simulation environment at 1000<sup>th</sup> time step

### 5.5. Experiment: Usage of a Second Antibiotic

A second antibiotic course can be justified only if infection with the resistant bacteria is suspected. In order to study the effect of the use of a second antibiotic on the resistant bacteria, a similar experimental setup as described in Section 5.4 was performed. Thus 100 immune system cells and 4000 bacterial cells with virulence factors ranging from 1 to 4 were created in the Repast Symphony simulation environment. The nutrient layer, antibiotic layer and antibiotic2 layer were also included in the simulation environment for this experiment. Antibiotic2 layer represented the use of second antibiotic for the treatment of the infection caused by the

antibiotic resistant bacteria and it was activated at 400<sup>th</sup> time step. The behavior of immune system cells in the simulation program was modified in order to fight the bacterial cells slowly since cortisol suppresses the immune system. Thus, an immune system cell kills one of the bacterial cells in the grid by looking at the neighboring 48 cells and moves into the dead bacteria's grid cell in every fourth time step. Immune system cell dies after killing 2 bacterial cells, and causes immune system to recruit another immune cell into the simulation environment.

At the initial time step, a settlement of 100 immune system cells and 4000 bacterial cells with a range of virulence factors accrues in the Repast Symphony simulation environment are shown in Fig.13: The bacteria cells are represented as white, yellow, red, and purple circles and the immune cells are represented as blue circles. In this experiment, the bacteria shown in white are antibiotic-resistant.

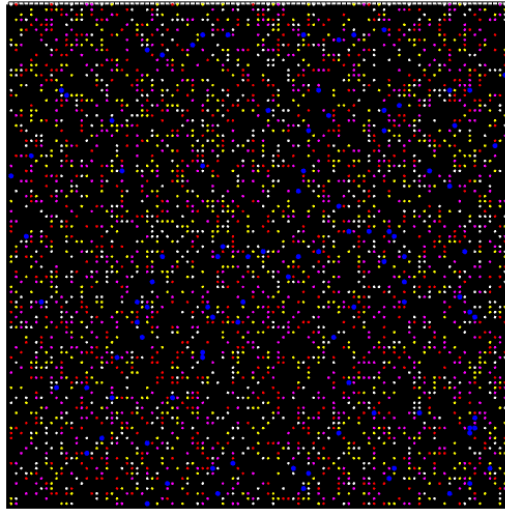


Figure 13. Settlement of 100 immune system cells and 4000 bacterial cells in the Repast Symphony simulation environment

At the 350<sup>th</sup> time step, we observed that the bacteria shown in yellow, red, and purple still existed in the simulation environment, as shown in Fig. 14(a) and they were removed from the simulation environment until the 400<sup>th</sup> time step. Some were killed by the antibiotic whereas the rest were killed by the immune system cells. As shown in Fig. 14(b), at the 400<sup>th</sup> time step, only immune system cells and antibiotic-resistant bacteria remain in the simulation environment. The numbers of immune system cells and antibiotic resistant bacterial cells are very high in this experiment, as the resistant bacterial cells divide rapidly (virulence factor=1) and the number of bacterial cells increases, which causes the immune cells to increase in the number as well. In order to remove the resistant bacteria from the simulation environment, Antibiotic2 layer was activated at the 400<sup>th</sup> time step. Thus, “antibiotic2” was able to alleviate the chronic infection caused by the resistant bacteria since the resistant bacteria shown in white were sensitive to “antibiotic2”.

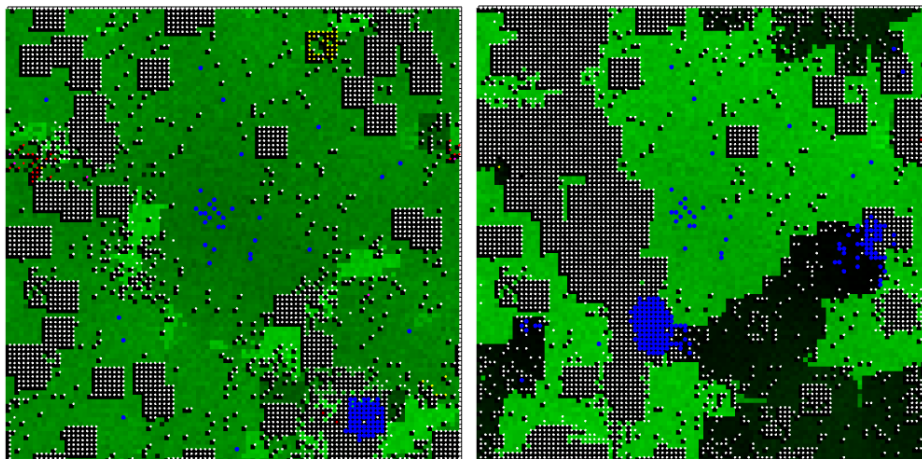


Figure 14. (a) Immune system cells and bacterial cells in the Repast Symphony simulation environment at the 350<sup>th</sup> time step, (b) Immune system cells and bacterial cells in the Repast Symphony simulation environment at the 400<sup>th</sup> time step

The simulation pauses at the 753<sup>rd</sup> time step because there are no bacteria in the simulation environment. As shown in Fig. 15, the simulation environment includes only 72 immune system cells and the resistant bacterial cells shown in white are removed from the environment since each grid cell provides a constant concentration level of “antibiotics2”, which kill the resistant bacteria after 400 time steps. Fig. 16 shows a graph of the number of bacteria alive at each time step: At the 425<sup>th</sup> time step, the number of bacteria increases and the population of the resistant bacteria reaches almost 7000 whereas the immune system cell population reaches its peak to fight the resistant bacterial cells. After 550 time steps, the resistant bacteria attempt to attack one more time; however, the “antibiotic2” helps the immune system cells and both remove the resistant bacteria until 753<sup>rd</sup> time step.

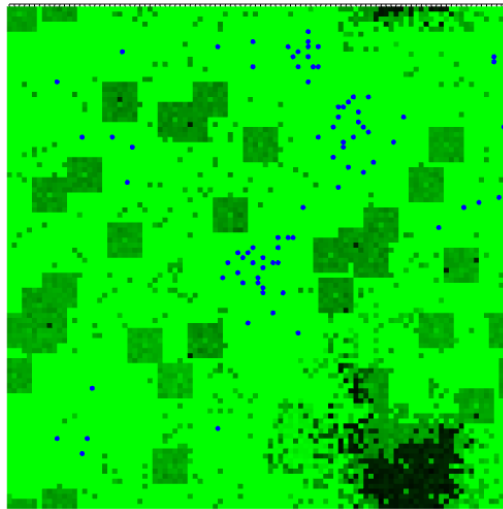


Figure 15. Immune system cells in the Repast Symphony simulation environment at the 753<sup>rd</sup> time step

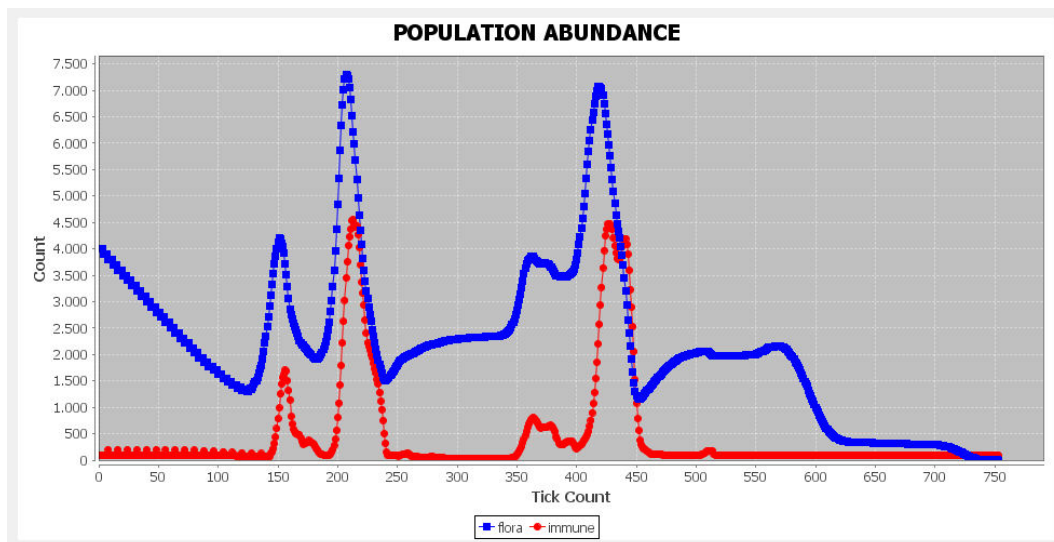


Figure 16. Populations graph of immune system cells and bacterial cells

## 6. Conclusions

In this study, we used ABMS technique to observe the competition between bacteria traits and the interaction between the bacteria and immune system cells. We observed the effects of variability of antibiotic resistance on the infection process. In our experiments, we show that resistance to antibiotics increases with the survival of bacterial cells that are immune to the effects of the antibiotic. Their daughter cells inherit this resistance, thereby creating a population of resistant bacteria. Besides, we show that the effect of the suppressed immune

system on the infection process and the necessity of the use of second antibiotic for the treatment of the infection caused by the antibiotic-resistant bacteria.

## References

- [1] M. Lipsitch, C.T. Bergstrom, and B. R. Levin. "The Epidemiology of Antibiotic Resistance in Hospitals: Paradoxes and Prescriptions," *Proceedings of the National Academy of Sciences* 97.4, 2000, pp. 1938-1943.
- [2] C.T. Bergstrom, L. Monique, and M. Lipsitch. "Ecological Theory Suggests that Antimicrobial Cycling Will not Reduce Antimicrobial Resistance in Hospitals," *Proceedings of the National Academy of Sciences of the United States of America* 101.36, 2004, pp. 13285-13290.
- [3] M. Lipsitch and C. T. Bergstrom, Modeling of antibiotic resistance in the ICU-US slant. Kluwer, 2002.
- [4] K. Chow , X. Wang , R. Curtiss III & Carlos Castillo-Chavez, "Evaluating the Efficacy of Antimicrobial Cycling Programmes and Patient Isolation on Dual Resistance in Hospitals", *Journal of Biological Dynamics*, 5:1, pp. 27-43, DOI: 10.1080/17513758.2010.488300, 2011.
- [5] DP Genereux and CT Bergstrom, "Evolution in Action: Understanding Antibiotic Resistance", *Evolutionary Science and Society: Educating a New Generation*, AIBS/BCSC, Washington, DC. 2005.
- [6] J. Epstein and R. Axtell, *Growing Artificial Societies: Social Science from the Bottom up*. Brookings Institution Press, 1996.
- [7] V. Grimm, E. Revilla, U. Berger, F. Jeltsch, W.M. Mooij, S.F. Railsback, H.-H. Thulke, J. Weiner, T. Wiegand, and D. L. DeAngelis, "Pattern-oriented Modeling of Agent-based Complex Systems: Lessons from Ecology," *Science* 310(5750), pp. 987–991, 2005.
- [8] D. Phan and F. Varenne, "Agent-Based Models and Simulations in Economics and Social Sciences: From Conceptual Exploration to Distinct Ways of Experimenting," *Journal of Artificial Societies and Social Simulation* 13 (1) 5 <http://jasss.soc.surrey.ac.uk/13/1/5.html>, 2010.
- [9] Z. Shi, C. Wu, and D. Ben-Arieh, "Agent-Based Model: A Surging Tool to Simulate Infectious Diseases in the Immune System," *Open Journal of Modelling and Simulation*, 2, pp. 12-22, doi: 10.4236/ojmsi.2014.21004, 2014.
- [10] V. Crespi, A. Galstyan, and K. Lerman, "Top-down vs bottom-up methodologies in multi-agent system design," *Autonomous Robots*, 24(3), pp. 303-313, doi: 10.1007/s10514-007-9080-5, 2008.
- [11] I. Cakirlar, Development of Test Driven Development Methodology for Agent-Based Simulations, Phd Thesis in Computer Engineering, Ege University, Izmir, 2015.
- [12] (2016) Repast Symphony website. [Online]. Available: [http://repast.sourceforge.net/repast\\_symphony.php](http://repast.sourceforge.net/repast_symphony.php)

## Application of Monte Carlo simulation and PERT/CPM techniques in planning of construction projects: A Case Study

Mertcan Karabulut

Industrial Engineering, International University of Sarajevo

---

### Article Info

#### Article history:

Received Oct 3<sup>th</sup>, 2017

Revised Dec 10<sup>th</sup>, 2017

Accepted Dec 15<sup>th</sup>, 2017

#### Keyword:

Critical Path Method  
Monte Carlo Simulation  
Gantt Chart  
Risk Analysis  
Luxury Villa

---

### ABSTRACT

Construction project scheduling and monitoring is challenging in today's very dynamic business environment. In this study, a project execution tracking system in a medium-sized construction company was studied. Two different methods were proposed as problem solution for project scheduling and monitoring. Traditional CPM and PERT methods, and Monte Carlo simulation as risk analysis tool were used in this case study. The results show that 186 working days (which is optimistic estimate) is required to finish a luxury villa is determined by CPM method, while Monte Carlo simulation implies that there is 50% of chance that the luxury villa will be done in 205 days, but still there is a risk of 50% that the villa construction may be delayed.

---

#### Corresponding Author: Mertcan KARABULUT

International University of Sarajevo

Email: sansimya@hotmail.com

---

### 1. Introduction

Completing any project on time with the determined project cost is not always easy job for any project manager. Although, project management techniques and tools are very efficient and motivating for the establishment of many project, still there are still common mistakes which leads a complication in a project. There are many factors which causes complexity such as, lack of analyzing risk factors, manager mistakes, internal and external factors, usage of the only one technique without comparison with other tools and techniques and labor-force factors.

These factors play a significant role in the establishment of a project. Therefore, in long term these kind of complications causes problems for completion time, budget-cost arrangements, correct usage of labor-force and resources. Therefore, the proper usage of fine constructed project management tools and techniques are key factors for the establishment of proper project within a proportional budget and resource to be completed in a planned time interval. In this article, the work system of the construction company will be explored and investigated due to problem of monitoring the work system. The Mehmet's construction company was established in 2001 in Ankara.

The company is very comprehensive and based on construction along with project control. The company is carrying on a business in several cities in Turkey as well as at abroad [1]. The company is serving at abroad as well in such countries, Libya, Iraq, Syria and Afghanistan. The company is constructing a various type of housing such as dormitories for the students, hospitals private or the public, luxury residential or intermediate houses, hotels for touristic purposes as well as small apartments for the use of local people, educational buildings, and workshops. The most important objective of the company is awareness by whole market and perceived. The problem of the company is an inability of having a system in which current business can be properly monitored and controlled.

The current work system of the company is based on old-fashioned methods which prevents the development of the company below the expectations. Nowadays it is not easy for a construction company to do all the work by order because the possibilities of many types of error which are undesirable.

For Mr. Mehmet's company, there is a significant problem for keeping track of the business which puts the company in hard circumstances. There are no project management techniques which should be used to lower the hardness of the works in the company, hence the company is struggling each time due to lack of project management tools. There are always causes and effects in every problem and the existence of the problem is the reflection of the primary causes. Those causes are time management, change management, cost management and project status.

The inability of managing the time, the lack of cost management method, the technical incompetence of the company for sudden alterations and the inevitable hardship of representing processes by diagrams, charts, or any other proper tool puts the company in a hard time for monitoring the status of the project. Energy efficiency plays one of the major roles in the construction by using proper energy efficient building components [2] [3] in various construction phases, such as first and second floor works along with roof works [4]. It is very long process, most importantly after the construction is done, construction work delivery must be in a good quality and produced components built in the house should be produced as it was reported in [5], to have better interior and exterior finish. Critical Path Method and Project Evaluation and Review Technique are very effective and mostly used methods in the history of the project management. By the establishment of these two methods, it does provide many benefit to its project managers such as deterministic times for three different time values.

In addition, for all the activities times can be found using these two algorithm such as the earliest and latest time where can a task begin or the latest or earliest time where can an activity completed along with slack time, which is the differences between start and finish times. These two methods are very effective way of illustrating the critical path and complete project duration. Thanks to these two approaches, any project can be managed and monitored easily on determined completion time of a project [6]. Another method used is Monte Carlo simulation to identify the project completion date by every possible combination of uncertain activities. While CPM and PERT methods gives the deterministic completion date for the project, Monte Carlo simulation gives the completion date based on probabilistic approach for the whole combined uncertain events. Critical Path Method does not consider the possible risk which might occur in the process of construction while Monte Carlo Simulation is taking account of every possible risks which may occur in the phases of construction which will directly affect the completion date of construction. In order to better understand and making comparison between these two methods, identification of possible risks and visual representation of those risks have a cruel role in the final result.

The quality of the deliverables and the whole system of project monitoring and executing is important aspect of customer satisfaction for innovation areas such as product, process, and administration. To achieve this soft and hard tools are used such as strategic planning, customer focus, employee involvement and trainings; and continuous improvement standardization and measurement [7]. The overall goal of the company is to continuously improve monitoring of the project completion and improve deliverables by applying one of the quality initiatives [8][9].

The following section called as methods and techniques will be explored and investigated for the comparison of completion date for the Critical Path and Monte Carlo Simulation methods.

## 2. Methods, Techniques and Tools

Project planning and scheduling methods proposed for Mehmet's company are based on these three project objectives: scope, schedule and budget. Before the establishment of any method for any project, the project triple constraints must be understood carefully for a better understanding of forthcoming methods. There are certain constraints which are fulfilled in every project as following, cost, schedule and time which represents the triangle shown below to satisfy the quality of the deliverable outcome. One constraint cannot be whole before another satisfies. The following Figure 1 represents the triple constraints of project management.

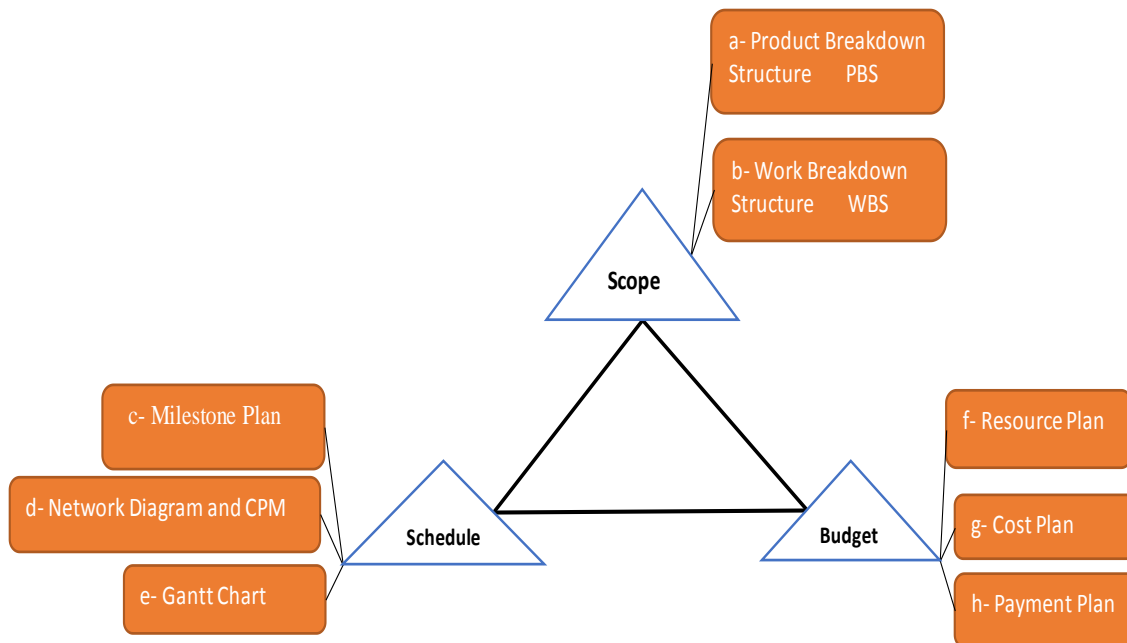


Figure 1: Project Objectives

After the explanation of Project Triple Constraints, in the following headings, the methods and tools which will be conducted in the establishment of Critical Path Algorithm and Monte Carlo simulation will be mentioned along with necessary formulas.

### 1) Scope

#### *PBS (Product Breakdown Structure)*

For better representation of activities of any particular project, the Product Work Breakdown structure is used to illustrate the activities in hierarchical order which generate the whole project with easier representation for the users. There are many ways to use PBS structure for the purposes of examining and authenticating [10].

#### *WBS (Work Breakdown Structure)*

Work Breakdown Structure (WBS) is the exact opposite way of creating a hierarchical structure of Product Work Breakdown Structure. In this method, project is divided into primary elements in order to show the project which is defining the scope of the project. It is very good representation for the users in which easy way of understanding the scope for, what is exactly needs to be done. Work Breakdown Structure is very effective tool in Project Management [11].

### 2) Schedule

#### *Milestone Plan*

Milestones in project management are activities which are representing the key events of a project and they are most important activities to achieve to finish the project. The project milestone has no duration which indicates the importance of activity.

*Network Diagram and CPM (Critical Path Method)*

There are many areas of the usage for network diagrams which was created in the intention of making the project more manageable form for the users. Network diagram is mostly used for projects to be scheduled. Network diagram is representing the associations among the activities of any project for easier understanding [12]. Model of network diagram is shown in Figure 2.

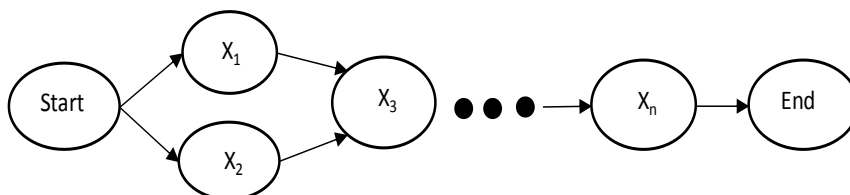


Figure 2: Network diagram model

On the network diagram, durations of some activities are given also their start and end time can be found using the network diagram. There is a special order in the sequence of network diagram, activities are arranged according to their predecessors. There is a formula to estimate the duration of the project by the expected time (*TE*) of the activities according to each activity optimistic and pessimistic times based on Beta distribution.

$$TE = \frac{a + 4m + b}{6}$$

where, *a* represents the optimistic estimate, *m* represents the most likely estimate and where *b* represents the pessimistic estimate.

The visual representation of the Earliest Finish, Earliest Start, Latest Start, Latest Finish, Slack Time with corresponding form of usage in a network diagram with basic formulas is shown in the Figure 3 below.

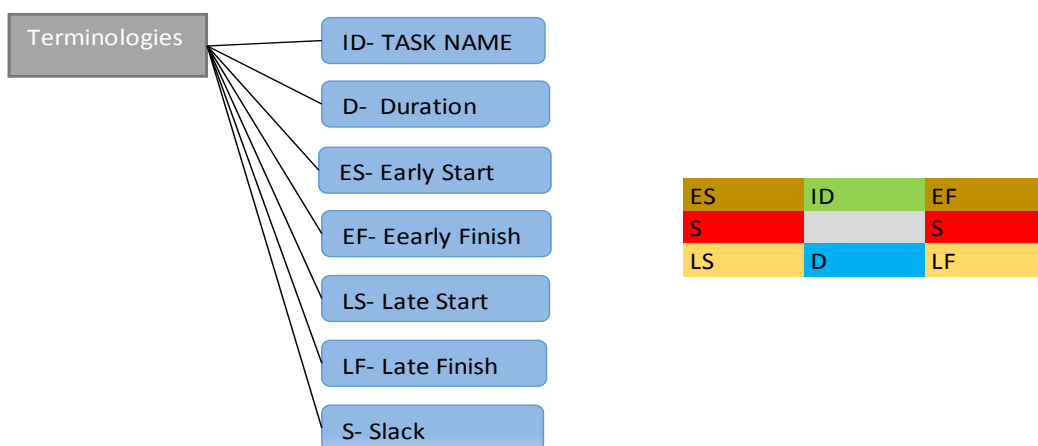


Figure 3: Terminologies for Network Diagram with corresponding form

Earliestfinish time (*EF*) for *j*- *th* activity was determined as:

$$EF_j = ES_j + TE_j$$

where, *ES<sub>j</sub>* is earliest start time, while *TE<sub>j</sub>* is estimated time for *j*- *th* activity.

Earliest start time (ES) for  $j$ -th activity was determined as:

$$ES_j = \max (EF_j)$$

where,  $EF_j$  is maximum earliest finish time from the predecessor for  $j$ -th activity.

Completion time for the last activity represent project completion time ( $\mu$ ) and it was determined as:

$$\mu = EF$$

To find critical activity and determine critical path, backward path was calculated. Therefore, earliest finish time for the last activity becomes latest finish.

$$LF = EF$$

Latest start time (LS) for  $j$ -th activity was determined as:

$$LS_j = LF_j - TE_j$$

where,  $LF_j$  is latest finish time for  $j$ -th activity.

Latest finish time (LF) for  $j$ -th activity was determined as:

$$LF_j = \min (LS_j)$$

where,  $LS_j$  is minimum latest start time of successor activity.

Slack time calculation helps to determine critical path activities

$$\text{Slack of activity } j = LS_j - ES_j$$

where,  $LS_j$  latest finish time for  $j$ -th activity

Activities with zero slack time represent critical path activities.

After calculation, the critical path by the given formula above, the next step is to find standard activity variances to be able to calculate uncertainty of a project completion [12].

$$\sigma^2 = \frac{(a - b)^2}{6}$$

where,  $a$  represents the optimistic duration and  $b$  represents the pessimistic duration of an activity. While project variance is determined as sum of variances on the critical path activities:

$$\sigma_p^2 = \sum (\text{variances of activities on critical path})$$

Square root of the project variance gives the standard deviation of the project duration.

$$\sigma_p = \sqrt{\sigma_p^2}$$

PERT uses the following assumptions to determine probability of project completion time: project duration follows a normal probability distribution, while activity times are statistically independent. Therefore, with these assumptions it is possible to determine probability of the project completion earlier or later  $\mu$ , and standard normal equation can be applied.

$$Z = \frac{X - \mu}{\sigma_p}$$

In order to finish any project at the desired time, the formula above was used, where  $\mu$  is estimated project duration time,  $X$  is given time and  $\sigma_p$  is project variance.

### Gantt Chart

The Gantt chart shows planned and actual progress for many tasks displayed as bars against a horizontal time scale. It is a particularly effective and easy-to-read method of indicating the actual status for each of a set of tasks compared to the planned progress for each item of the set [13]. Sample of Gantt chart is shown in Figure 5.

#### *CPM (Critical Path Method)*

In order to identify the activities in the network diagram, to know which one is critical and which one is not, Critical Path Method were used for analyzing. Critical path method is a common project management technique which has been using for a long time. Especially for the projects which consist of dozens of activities. Therefore, Critical Path Method is a very effective project management technique which is used to identify important activities **Invalid source specified..**

#### 3) Budget

The budget was estimated according to historical data and using three-point estimate as well as using quotation system.

#### *Swott Analysis*

In order to make a proper analyze for any project, the Swott analysis is very effective and required tool to be conducted. Because, thanks to the properties of the Swott analysis, it gives an overall analysis for the strengths, weaknesses, opportunities and threats of any organizations. For clear understanding, there are internal and external factors in the Swott analysis, internal factors are the strengths and weaknesses of the organization and external factors are opportunities and threats of the organization.

These factors were identified and analyzed for the determination of what is preventing a workstation from its objectives and what is contributing to achieve the desired goal of the company. Therefore, Swott analysis is assisting for the workstation to operate more efficiently [14].

#### *Monte Carlo Simulation*

Monte Carlo Simulation has very long usage area in very Project management aspects like industrial purpose, scientific purpose, and logistical purpose. Monte Carlo Simulation was used in order to estimate the completion date of the project and the overall cost of the project with every doable integration of undetermined activity run. Monte Carlo simulation takes the deterministic times obtained and put them in long repeatable trials by iterating over long repeat of durations.

These coincidental values for each probabilistic distribution were used to estimate the completion time for a project with different durations between some frequencies. All possible risks which may delay the project completion date is considered in these combinations of trials [15].

To perform Monte Carlo simulation for luxury villa case the following steps were taken and the process is shown in Figure 4:

- 1) Quantitative model definition for project duration as  $y = f(x_1, x_2, \dots, x_j, \dots, x_n)$ , where  $x_j$  is  $j$ -th activity duration, and  $n$  is number of activities.
- 2) Random variables generation for  $i$ -th run and  $j$ -th activity (where  $i = 1$  to  $k$ , while  $k$  is number of iterations).
- 3) Estimate of  $xi_1, xi_2, \dots, xi_n$  activity duration as well as project duration  $y_i$  for  $i$ -th run.
- 4) Storage of the model and output in  $y_i$ .
- 5) Steps (2) and (3) were repeated for  $k$  times.
- 6) The results were analyzed and graphically represented using probability density function and cumulative density function.

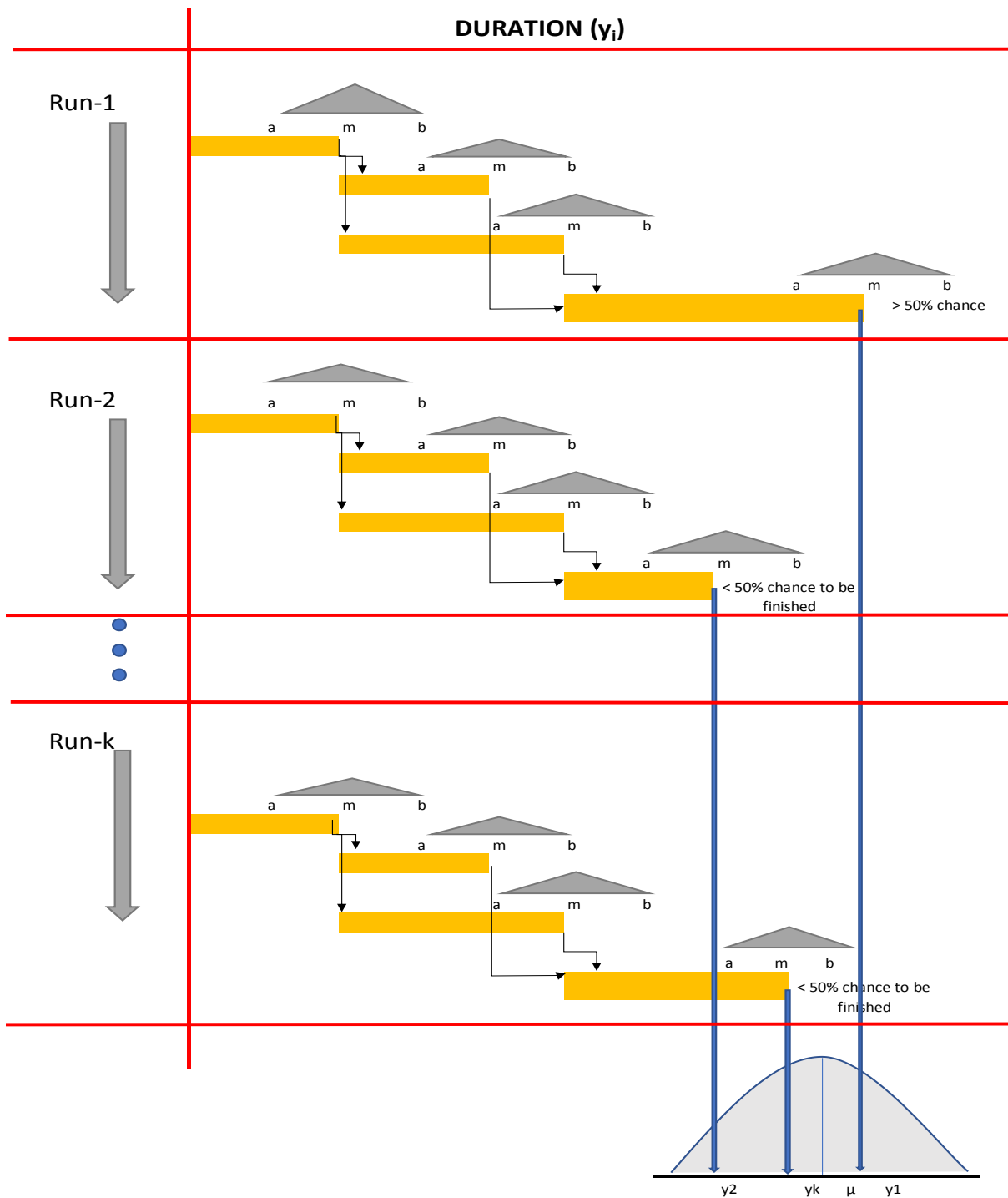


Figure 4: Example of Monte Carlo Simulation

Monte Carlo Simulation computes the obtained deterministic times for  $k = 9000$  iterations and over again according to end date for all possible uncertain activities to have more realistic final outcomes. Monte Carlo Simulation is taking the risk factor into an account that is why it is randomly generating the deterministic completion times for each activity for each trial. This step is repeated 9000 times as in Figure 4. In order to simulate all the possible outcomes, Monte Carlo Simulation giving for each trial different but very close final outcomes.

After the explanation of the Monte Carlo Simulation method, the following section will be about results and discussions for the establishment of Critical Path Method and Monte Carlo Simulation.

### 3. Results and Discussions

In this section, after the establishment of Critical Path Method and Monte Carlo Simulation, the obtained values and conclusions will be mentioned. The table below shows the all activities with their predecessors and 3 different time measurement which will help to conduct Critical Path Method and Monte Carlo Simulation for Luxury Villa in result section of the article.

Table 1: Activities with durations of the Luxury Villa

Activities	Activity Names	Predecessor	a	m	b	TE	ES	EF	LS	LF	SL	$\sigma^2$	$\sigma$
1.1	Building Design	-	4	7	10	7	0	7	0	7	0	1	1
1.2	Electrical Design	1.1	2	3	4	3	7	10	8	11	1	0.33	0.11
1.3	Plumbing Design	1.1	2	4	6	4	7	11	7	11	0	0.67	0.44
1.4	Fire System Design	1.1	1	2	3	2	7	9	9	11	2	0.33	0.11
2.1	Signing Project Contract	1,2-1,3-1,4	1	2	3	2	11	13	11	13	0	0.33	0.11
2.2	Project Permit	2.1	2	3	4	3	13	16	14	17	1	0.33	0.11
2.3	Electrical Permit	2.1	3	4	5	4	13	17	13	17	0	0.33	0.11
2.4	Plumbing Permit	2.1	2	3	4	3	13	16	14	17	1	0.33	0.11
3.1	Installation of Mobilization Building	2,2-2,3-2,4	3	5	7	5	17	22	17	22	0	0.67	0.44
3.2	Road Work	3.1	2	3	4	3	22	25	22	25	0	0.33	0.11
3.3	Fence Work	3.1	1	2	3	2	22	24	23	25	1	0.33	0.11
4.1	Cleaning and Grubbing	3,2-3,3	1	3	5	3	25	28	25	28	0	0.67	0.44
4.2	Excavation	4.1	4	7	10	7	28	35	28	35	0	1	1
4.3	Filling	4.2	7	10	13	10	35	45	35	45	0	1	1
5.1	Pile	4.3	6	11	16	11	45	56	45	56	0	1.67	2.78
5.2	Concrete	5.1	7	9	11	9	56	65	60	69	4	0.67	0.44
5.3	Raft Foundation	5.1	10	13	16	13	56	69	56	69	0	1	1
6.1	Column and Curtain Wall	5,2-2,3	7	5	9	6	69	75	69	75	0	0.33	0.11
6.2	Slab	6.1	2	4	6	4	75	79	76	80	1	0.67	0.44
6.3	Slab Insulation	6.1	4	5	6	5	75	80	75	80	0	0.33	0.11
6.4	Masonry	6.1	2	3	4	3	75	78	77	80	2	0.33	0.11
6.5	Upper Slab	6.1	1	2	3	2	73	75	78	80	5	0.33	0.11
7.1	Column and Curtain Wall	6,2-6,3-6,4-6,5	3	5	7	5	80	85	80	85	0	0.67	0.44
7.2	Slab	7.1	3	4	5	4	85	89	86	90	1	0.33	0.11
7.3	Slab Insulation	7.1	2	5	8	5	85	90	85	90	0	1	1
7.4	Masonry	7.1	1	3	5	3	85	88	87	90	2	0.67	0.44
7.5	Upper Slab	7.1	1	2	3	2	85	87	85	90	3	0.33	0.11
8.1	Roof Beam Installation	7,2-7,3-7,4-7,5	3	4	5	4	90	94	90	94	0	0.33	0.11
8.2	Roof Installation	8.1	3	5	7	5	94	99	99	105	6	0.67	0.44
8.3	Roof Isolation	8.1	1	3	5	3	94	97	96	99	2	0.67	0.44
9.1	Installation of Electric	8,2-8,3	4	6	8	6	99	105	99	105	0	0.67	0.44
9.2	Installation of Plumbing	8,2-8,3	3	5	7	5	99	104	100	105	1	0.67	0.44
9.3	Installation of Fire System	8,2-8,3	1	3	5	3	99	102	102	105	3	0.67	0.44
10.1	Drywall	10,2-10,3	6	10	14	10	117	127	117	127	0	1.33	1.78
10.2	Interior Brick Wall	9,1-9,2-9,3	11	12	13	12	105	117	105	117	0	0.33	0.11
10.3	Exterior Brick Wall	9,1-9,2-9,3	9	12	15	12	105	117	105	117	0	1	1
11.1	Plaster(ext-int)	10.1	6	10	14	10	127	137	127	137	0	1.33	1.78
12.1	Travertine Coating	11.1	9	11	13	11	137	148	137	148	0	0.67	0.44
12.2	Marble Coating	11.1	5	7	9	7	137	144	141	148	4	0.67	0.44
12.3	Tile Mosaic Coating	11.1	3	4	5	4	137	141	144	148	7	0.33	0.11
12.4	Ceramic Coating	11.1	1	2	3	2	137	139	146	148	9	0.33	0.11
12.5	Epoxy	11.1	1	2	3	2	137	139	146	148	9	0.33	0.11
12.6	Suspended Ceiling Cover	11.1	5	8	11	8	137	145	140	148	3	1	1
12.7	Outer Wall Covering	11.1	8	10	12	10	137	147	138	148	1	0.67	0.44
13.1	Fenestration Installation	12,1-12,2-12,3 12,4-12,5 12,6	2	4	6	4	148	152	148	152	0	0.67	0.44
13.2	Wood Work	13.1	4	5	6	5	152	157	153	158	1	0.33	0.11
13.3	Aluminum Joinery	13.1	3	6	9	6	152	158	152	158	0	1	1
13.4	Metal Joinery	13.1	2	3	4	3	152	155	155	158	3	0.33	0.11
14.1	Interior Paint	13,2-13,3-13,4	3	4	5	4	158	162	158	162	0	0.33	0.11
14.2	Exterior Paint	14.1	6	8	10	8	162	170	162	170	0	0.67	0.44
15.1	Ventilation System	14.2	1	3	5	3	170	173	172	175	2	0.67	0.44
15.2	Clean-Waste Water	14.2	4	5	6	5	170	175	170	175	0	0.33	0.11
15.3	Rain Water	14.2	1	2	3	2	170	172	173	175	3	0.33	0.11
15.4	Mechanical Automation	15,1-15,2-15,3	1	3	5	3	175	178	175	178	0	0.67	0.44
15.5	Mechanical Electric Work	15,1-15,2-15,3	1	2	3	2	175	177	176	178	1	0.33	0.11
16.1	Fire Protection System	15,4-15,5	1	2	3	2	178	180	179	181	1	0.33	0.11
16.2	Fire Detection System	15,4-15,5	2	3	4	3	178	181	178	181	0	0.33	0.11
16.3	Security Lighting	15,4-15,5	1	2	3	2	178	180	179	181	1	0.33	0.11
17.1	Cleaning	16,1-16,2-16,3	1	2	3	2	181	183	181	183	0	0.33	0.11
17.2	Final Control	17.1	1	2	3	2	183	185	183	185	0	0.33	0.11
17.3	Delivery	17.2	1	1	1	1	185	186	185	186	0	0	0

? TE<sub>(cp-0)</sub> = 186 days

Table above shows the times of each activities with their predecessors and ES, EF, LS, LF Slack time along with standard deviations and variances. Using this method, it is estimated project duration of 186 day for luxury villa construction.

The duration is obtained by summing all zero critical path activities.

Based on the Table 1, the Gantt Chart is constructed below and Figure 5 shows the total duration of the Luxury Villa as 186 days without analyzing risks which can alter the deterministic times obtained by CPM and PERT method.

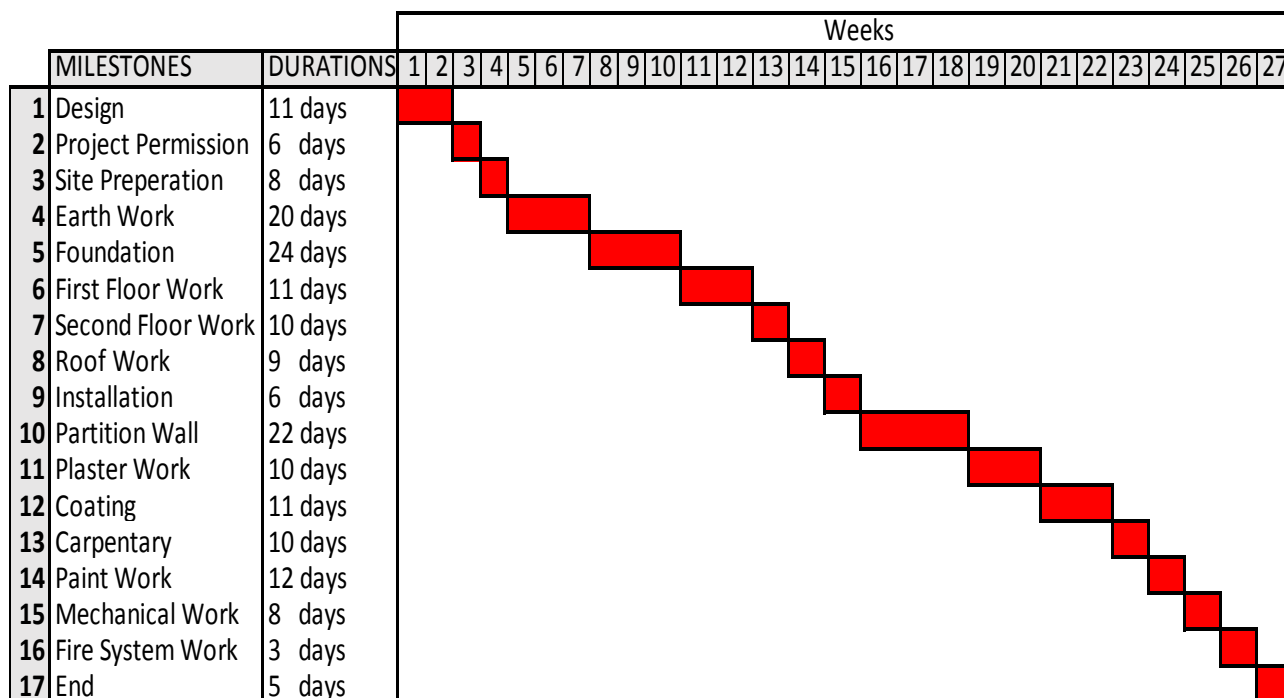


Figure 5: The Gantt chart of Luxury Villa

The Figure 5 above shows the Gantt Chart of the Luxury Villa. It was conducted by using of 17 milestones of the construction. Milestones of the Luxury Villa is as follows, Design, Project Permissions, Site Preparation, Earth Work, Foundation, First Floor Work, Second Floor Work, Roof Work, Installations, Partition Wall, Plaster Work, Coating, Carpentry, Paint Work, Mechanical Work, Fire System Work and the End of the construction with total duration of 186 days which is equivalent to approximately 27 weeks.

In the process of establishment of the Critical Path method, all the times were taken and calculated were deterministic without risk considerations. 186 days was obtained, as if there will not be any obstacles which will change the time of the completion day of the Luxury Villa. Therefore, when all possible risks were taken account and identified carefully, there will be another probabilistic completion time for the construction of Luxury Villa. Those risks can vary, as internal risks, external risks, political risks, technological risks, natural risks and unexpectable risks.

There is a possible percentage for every risk which should be taken account. Because, these risks can be very significant in case of occurrence. But, it may also not occur. Figure 6 shows impact-probability risk analysis matrix.

<b>LIKELIHOOD</b>	Expected to occur regularly under normal circumstances	ALMOST CERTAIN	MANAGE AND CONTROL RISK	MANAGE AND CONTROL RISK	MUST TAKE PRECAUTION	MUST MANAGE AND MONITOR RISK	MAKE INSURANCE
	Expected to occur some time	LIKELY	ACCEPT BUT MONITOR RISK	MANAGE AND CONTROL RISK	MUST TAKE PRECAUTION	MUST MANAGE AND MONITOR RISK	MAKE INSURANCE
	May Occur at some time	POSSIBLE	MONITOR RISK	ACCEPT BUT MONITOR RISK	MONITOR RISK	MUST MANAGE AND MONITOR RISK	MAKE INSURANCE
	Not likely to Occur in normal circumstances	UNLIKELY	ACCEPT RISK	ACCEPT BUT MONITOR RISK	MONITOR RISK	CONSIDERABLE MANAGEMENT REQUIRED	EXTENSIVE MANAGEMENT REQUIRED
	Could happen but Probably will never	RARE	ACCEPT RISK	ACCEPT BUT MONITOR RISK	MUST MANAGE AND MONITOR RISK	CONSIDERABLE MANAGEMENT REQUIRED	MUST MANAGE AND MONITOR RISK
			NOT SIGNIFICANT	MINOR	MODERATE	MAJOR	SEVERE
			1)Wheather Conditions 2)Labor Productivity 3)Changes in Project	1)Construction Type 2)Technology used 3) Equipment Faults	1) Government Pressure 2)Ground conditions 3) Additional Changes	1)Disease 2) Political Issues 3) Erros of Construction	1)Occupational-Work Accident 2) Naturel Disaster 3)Financial Crisis
<b>POTENTIAL CONSEQUENCES</b>							

Figure 6: Risk Analysis for Luxury Villa

The table above represents the potential risks with their consequences and probability which directly affect the completion date of the project. After formation of the risk analysis table, now it will help to re-define completion date of the project with given risks.

Referring to Figure 6, the Occupational wok accidents, natural disasters and financial crisis were identified as the highest impact risks to the project. But the likelihood being happened is with catastrophic consequences is very rare, thus they are managed and monitored.

Disease, political issues and errors of construction were identified as major risk to the project. But the likelihood being happened is with fatal consequences is unlikely, thus they are managed and monitored. Government pressure, ground conditions and additional changes were identified as moderate risk to the project. However, the likelihood being happened is with hazard is possible, thus precautions are taken into consideration.

Construction type, technology used and equipment faults were identified as minor risks to the project. But the likelihood being happened is with significant consequence is very likely thus, risks must be accepted and monitored.

Weather conditions, labor productivity and changes in project were identified as not significant risks. However, the likelihood being happened is with insignificant consequences are very low thus, the risks must be accepted.

By Monte Carlo Simulation, it will be easy to identify the risks of completion project on time, and comparing the result to PERT/CPM. The table below is called Risk Analysis for the construction of the Luxury Villa with a precaution. The result of Monte Carlo simulation is represented using probability density function and cumulative density function and shown in Figure 7.

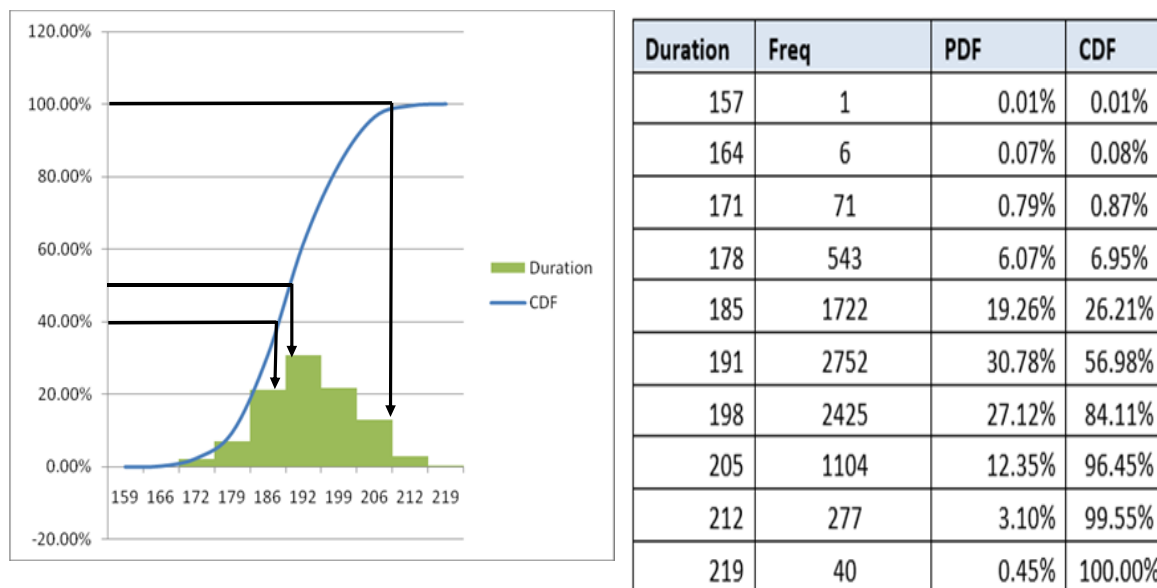


Figure 7: Results of Monte Carlo Simulation

The probability of finishing the construction in 186 days as it determined by CPM is about 38%, in 190 days is about 50% and in 205 days is approximately 100% according to Monte Carlo Simulation. These results show more realistic values since CPM and PERT did not consider the possible risks which may happen during the construction phases.

#### 4. Conclusion

Two different method were used in order to make comparison between Monte Carlo simulation and Critical Path Method. As it can be understandable, Monte Carlo simulation is giving more realistic outcomes. When Critical Method is compared with Monte Carlo simulation, it is seen that, by the establishment of risk analysis, it is giving better control over monitoring and identifying the risks. Another conclusion is obtained is, according to Critical Path method, the completion date of the Luxury Villa was 186 days (which is optimistic estimate). After the establishment of Monte Carlo simulation, by taking an account of risks, it gave about 38% for 186 days, about 50% for 190 days and approximately 100% for 205 days for completion date of the Luxury Villa along with uncertainty about 50% of chance which implies that Luxury Villa may be delayed.

#### 6. References

- [1] Ramo Palalic, Benjamin Durakovic, Azra Brankovic and Ognjen Ridic, "Students' entrepreneurial orientation intention, business environment and networking: insights from Bosnia and Herzegovina," *International Journal of Foresight and Innovation Policy*, vol. 11, no. 4, pp. 240-255, 2016.
- [2] Benjamin Durakovic and Muris Torlak, "Experimental and numerical study of a PCM window model as a thermal energy storage unit," *International Journal of Low-Carbon Technologies*, vol. 12, pp. 272-280, 2016.
- [3] M. Torlak, B. Durakovic, H. Gabranovic and N. Delalic, "CFD-Based Assessment of Thermal Energy Storage in Phase-Change Materials (PCM)," *ENTECH\_2014*, no. 1, pp. 263-275, 2014.
- [4] Benjamin Durakovic and Muris Torlak, "Simulation and experimental validation of phase change material and water used as heat storage medium in window applications," *Journal of Materials and Environmental Sciences ISSN : 2028-2508*, vol. 8, no. 5, pp. 1837-1846, 2017.
- [5] H. Basic, B. Durakovic and A. Softic, "Six Sigma Model Testing in Optimizing Medium-Sized Company Production Process," *Journal of Trends in the Development of Machinery and Associated Technology*, vol. 16, no. 1, pp. 103-106, 2012.

- 
- [6] W. Agyei, "Project Planning And Scheduling Using PERT and CPM Techniques With Linear Programming," vol. 4, pp. 222-223, 2015.
- [7] B. Durakovic, H. Basic and H. Muhic, "The Interrelationships Between Quality Management Practices and Their Effects on Innovation Performance," *Trends in the Development of Machinery and Associated Technology TMT 2014*, pp. 181-184, 2014.
- [8] B. Durakovic and H. Basic, "Continuous Quality Improvement in Textile Processing by Statistical Process Control Tools: A Case Study of Medium-Sized Company," *Periodicals of Engineering and Natural Sciences*, vol. 1, no. 1, pp. 39-46, 2013.
- [9] B. Durakovic and H. Basic, "Textile Cutting Process Optimization Model Based on Six Sigma Methodology in A Medium-Sized Company," *Journal of Trends in the Development of Machinery and Associated Technology*, vol. 16, no. 1, pp. 107-110, 2012.
- [10] Duncan Haughey, *Project Management Tools*, 2015.
- [11] G. Hagan, *Glossary of Defense Acquisition Acronyms and Terms: Contract Work Breakdown Structure (CWBS)*, vol. 13, Fort Belvoir, Virginia: Defense Acquisition University Press", 2017.
- [12] M. W. NEWELL and M. N. Grashina, "The project Management Question and Answer," p. 68.
- [13] S. J. Mantel and J. R. Meredith, "Network Techniques: PERT (ADM) and CPM (PDM)," in *Project Management, A Managerial Approach Seventh Edition*, United States of America, John Wiley & Sons, 2009, pp. 343-344.
- [14] "[www.investopedia.com/terms/s/swot.asp](http://www.investopedia.com/terms/s/swot.asp)," [Online].
- [15] K. Zhaoni , Z. Jianping , L. Chao , Z. Xiaoying and Q. , "Risk Assessment of Plan Schedule by Monte Carlo Simulation," pp. 509-510, 2015.

# Design of Experiments Application, Concepts, Examples: State of the Art

**Benjamin Durakovic**

Industrial Engineering, International University of Sarajevo

---

## Article Info

### Article history:

Received Aug 3<sup>th</sup>, 2018

Revised Oct 20<sup>th</sup>, 2018

Accepted Dec 1<sup>th</sup>, 2018

---

### Keyword:

Design of Experiments,  
full factorial design;  
fractional factorial design;  
product design;  
quality improvement;

---

## ABSTRACT

Design of Experiments (DOE) is statistical tool deployed in various types of system, process and product design, development and optimization. It is multipurpose tool that can be used in various situations such as design for comparisons, variable screening, transfer function identification, optimization and robust design. This paper explores historical aspects of DOE and provides state of the art of its application, guides researchers how to conceptualize, plan and conduct experiments, and how to analyze and interpret data including examples. In addition, this paper reveals that in past 20 years application of DOE have been growing rapidly in manufacturing as well as non-manufacturing industries. It was most popular tool in scientific areas of medicine, engineering, biochemistry, physics, computer science and counts about 50% of its applications compared to all other scientific areas.

---

### Corresponding Author:

**Benjamin Durakovic**

International University of Sarajevo,

Hrasnickacesta 15,

7100 Sarajevo, Bosnia.

Email: [bdurakovic@ius.edu.ba](mailto:bdurakovic@ius.edu.ba)

---

## 1. Introduction

Design of Experiments (DOE) mathematical methodology used for planning and conducting experiments as well as analyzing and interpreting data obtained from the experiments. It is a branch of applied statistics that is used for conducting scientific studies of a system, process or product in which input variables (Xs) were manipulated to investigate its effects on measured response variable (Y).

Over past two decades, DOE was a very useful tool traditionally used for improvement of product quality and reliability [1]. The usage of DOE has been expanded across many industries as part of decision making process either along a new product development, manufacturing process and improvement. It is not used only in engineering areas it has been used in administration, marketing, hospitals, pharmaceutical [2], food industry [3], energy and architecture [4][5], and chromatography [6]. DOE is applicable to physical processes as well as computer simulation models [7].

### 1.1. Historical perspective

One Factor At a Time (OFAT) was very popular scientific method dominated until early nineteen century. In this method one variable/factor is tested at a time while the other variables are constrained except the investigated one. Testing multiple variables at a time is better especially in cases where data must be analyzed

carefully. In the 1920s and 1930s **Ronald A. Fisher** conducted a research in agriculture with the aim of increasing yield of crop in the UK. Getting data and was challenging e.g. if he relayed on his traditional method ANOVA (*F*-test, means *Fisher* - test) he may plant a crop in spring and get results in fall which is too long for getting data. Finally, he came up with design of experiment and officially he was the first one who started using DOE. In 1935, he wrote a book on DOE, in which he explained how valid conclusion could be drawn from the experiment in presence of nuisance factors. He analyzed presence of nuisance factors with fluctuation of weather conditions (temperature, rainfall, soil condition). Credit for Response Surface Method (RSM) belongs to **George Box** who is also from the UK. He was concerned with experimental design procedures for process optimization. In 1950s, **W. Edwards Deming** was concerned with design of experiment as well as statistical methods. **Genichi Taguchi** was Japanese statistician concerned with quality improvement methods. He contributed to statistic by introducing Loss function and experiments extending with an "outer array" in DOE as an advanced method in the Six Sigma initiatives [8].

## 1.2. The main uses of DOE

Design of experiment is multipurpose tool that can be used in various situations for identification of important input factors (input variable) and how they are related to the outputs (response variable). Therefore, DOE mainly uses "hard tools" as it was reported in [9]. In addition, DOE is basically regression analysis that can be used in various situations. Commonly used design types are the following[10]:

1. **Comparison** – this is one factor among multiple comparisons to select the best option that uses *t*-test, *Z*-test, or *F*-test.
2. **Variable screening** – these are usually two level factorial designs intended to select important factors (variables) among many that affect performances of a system, process, or product.
3. **Transfer function identification** – if important input variables are identified, the relationship between the input variables and output variable can be used for further performance exploration of the system, process or product via transfer function.
4. **System Optimization** – the transfer function can be used for optimization by moving the experiment to optimum setting of the variables. On this way performances of the system, process or product can be improved.
5. **Robust design** – deals with reduction of variation in the system, process or product without elimination of its causes. Robust design was pioneered by Dr. Genichi Taguchi who made system robust against noise (environmental and uncontrollable factors are considered as noise). Generally, factors that cause product variation can be categorized in three main groups:
  - external/environmental (such as temperature, humidity and dust);
  - internal (wear of a machine and aging of materials);
  - Unit to unit variation (variations in material, processes and equipment).

## 1.3. DOE application in research and procedure

Even though DOE tool are not new techniques but its application has expended rapidly over the scientific areas including product/process quality improvement [11], product optimization [12] and services in the past two decades. Trainings and recent user-friendly commercial and non-commercial statistical software packages contributed significantly to DOE expansion in the research in this period. DOE application over the globe and across various scientific areas in the period from 1920 to 2018 is shown in Figure 1.

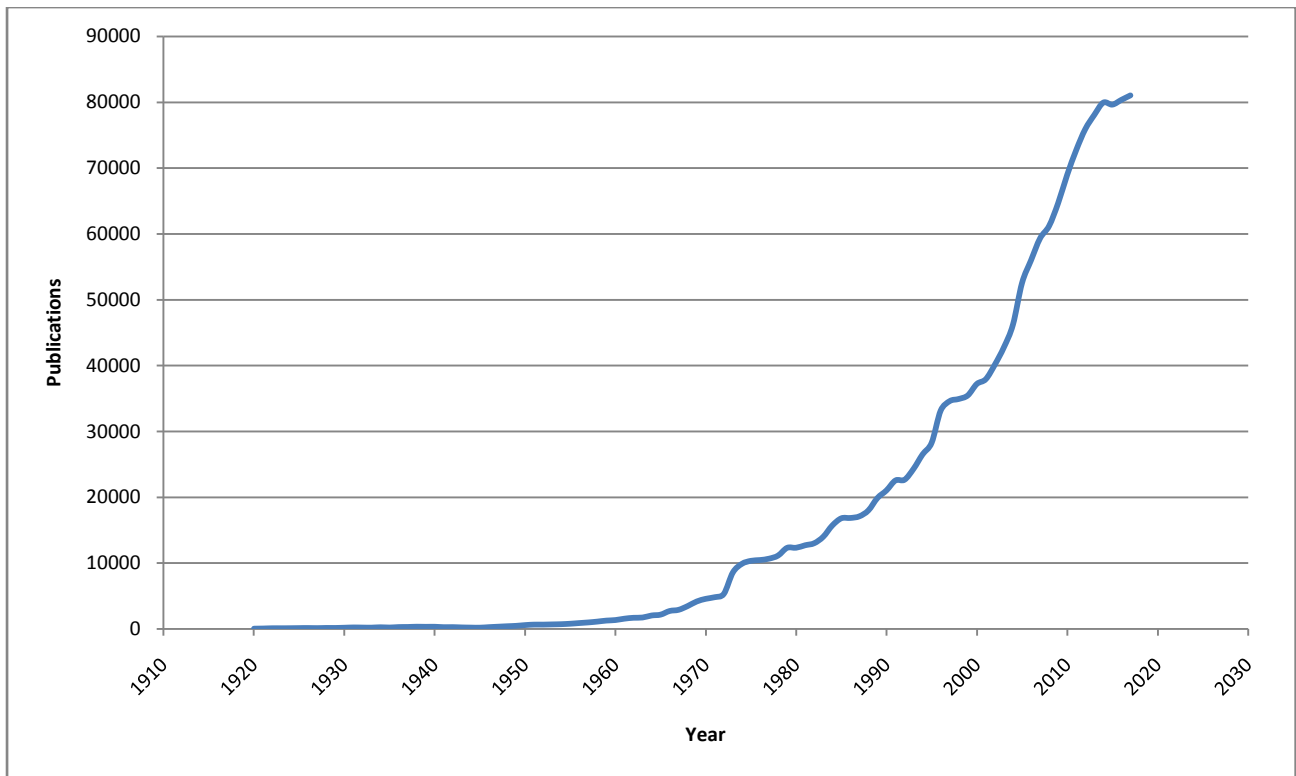


Figure 1. DOE application in scientific research[13]<sup>1</sup>

Application of DOE in research started in 1920s with Fisher's research in agriculture. Over four upcoming decades later its application in the research was negligible. Significant use of DOE in the research project was noticed in the late 1960s and 1970s. Thus, it took about 50 years for the DOE to achieve significant application in the research. Since in this period there were no software packages that would foster its application DOE had not signified a strong expansion. Thanks to education and software development in 1990s and later, the use of DOE in research over various scientific areas has risen sharply. A linear model that represents a rapid increase in the use of DOE in the research projects is shown in Figure 2 and represented by a mathematical linear model.

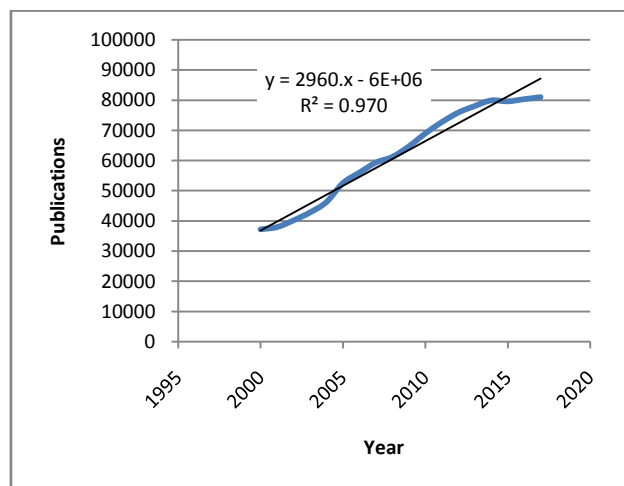


Figure 2. Progressive use of DOE as scientific method over past two decades[13]<sup>2</sup>

<sup>1</sup> Data obtained from Scopus for search “design of experiments” OR “experimental design” OR “DOE” in Title – abstract – Key words

<sup>2</sup> Data obtained from Scopus for search “design of experiments” OR “experimental design” OR “DOE” in Title – abstract – Key words

DOE application in the future can be predicted with linear regression model, which is based on past data over 18 years. Therefore, it can be expected that DOE usage expansion will continue in the future including its application in the existing and new scientific areas. The state of the art of DOE application in certain scientific areas is shown in Figure 3.

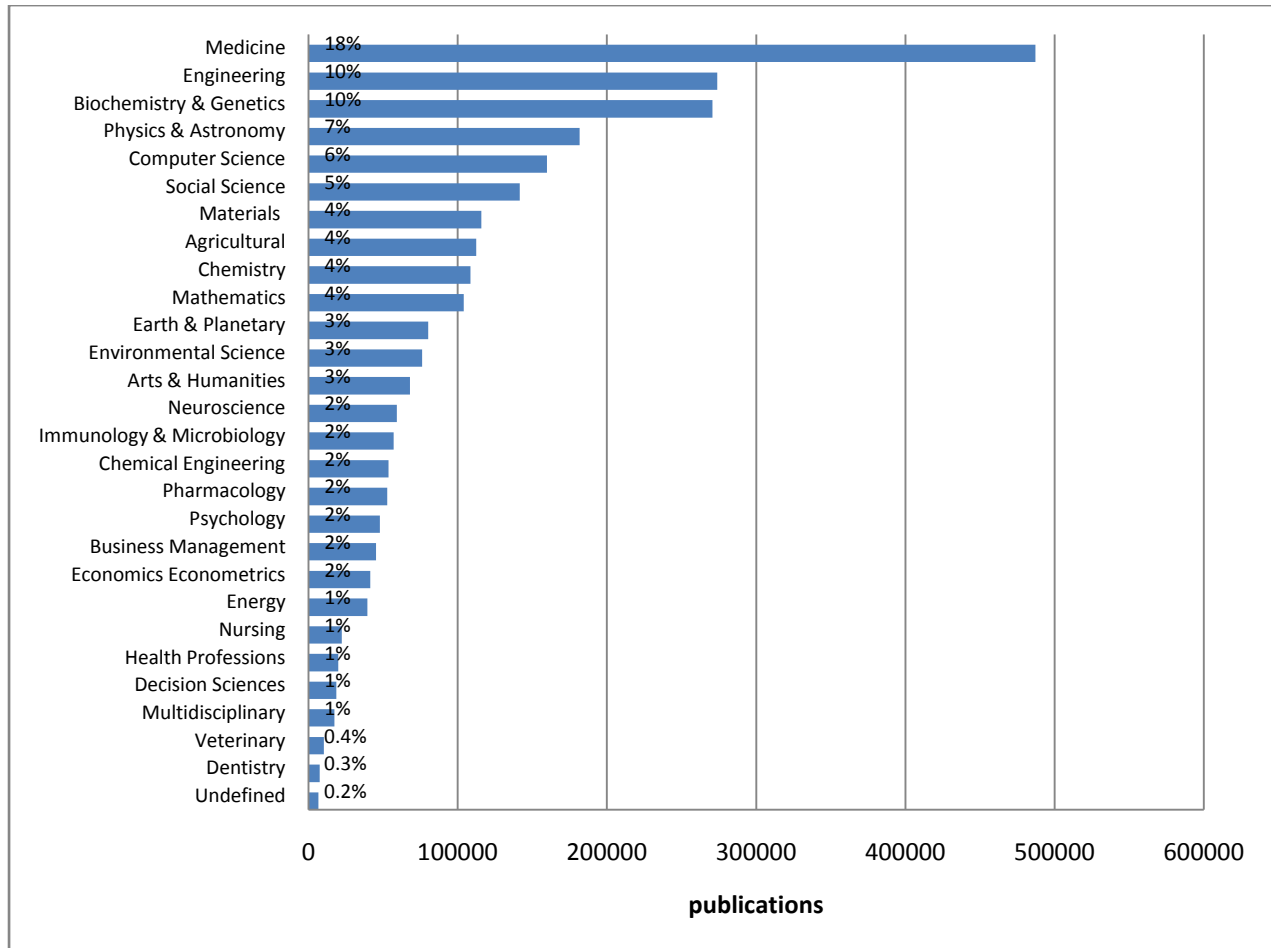


Figure 3. DOE application per scientific area[13]<sup>3</sup>

DOE as scientific method was most popular in scientific areas of medicine, engineering, biochemistry, physics and computer science. Its application in these areas counts about 50% compared to all other scientific areas. Only medicine participates about 18%, while engineering and biochemistry together participate with 20%; and physics and computer together science participate with 13%.

General practical steps and guidelines for planning and conducting DOE are listed below:

1. **State the objectives** – it is a list of problems that are going to be investigated.
2. **Response variable definition**– this is measurable outcome of the experiment that is based on defined objectives.
3. **Determine factors and levels** – selection of independent variable (factors) that case change in the response variable. To identify factors that may affect the response variable fishbone diagram might be used.

<sup>3</sup> Data obtained from Scopus for search "design of experiments" OR "experimental design" OR "DOE" in Title – abstract – Key words

4. **Determine Experimental design type**– e. g. a screening design is needed for significant factors identification; or for optimization factor-response function is going to be planned, number of test samples determination.
5. **Perform experiment** using design matrix.
6. **Data analysis** using statistical methods such as regression and ANOVA.
7. **Practical conclusions and recommendations**– including graphical representation of the results and validation of the results.

Most difficult part of DOE is to plan experiment in term of selecting appropriate factors for testing ( $x$ -variables), what ranges of  $x$ 's to select, how many replicates is supposed to be used, and is center point required?

#### 1.4. DOE Software

DOE can be quickly designed and analyzed with the help of suitable statistical software. For this purpose, there are some commercial and freeware statistical packages. The well-known commercial packages include: Minitab, Statistica, SPSS, SAS, Design-Expert, Statgraphics, Prisma, etc. The well-known freeware packages are: R and Action for Microsoft Excel [14].

The most popular commercial packages Minitab and Statistica are equipped with user friendly interface and very good graphics output. Freeware package Action has suitable graphics output and utilizes R platform together with Excel

Also, DOE design and analysis can be done easily in Microsoft Excel, using the procedure and formulas described in the following paragraphs. To perform any DOE as it was described earlier, understanding of analysis of variance (ANOVA) and linear regression as statistical methods is required. Therefore, more details about these two statistical methods are provided below.

## 2. Statistical Background

### 2.1. Analysis of variance (ANOVA)

In cases that there are more than two test samples ANOVA is used to determine whether there are statistically significant differences between the means the samples (treatments). In cases, that experiment contains two samples only, and then  $t$ -test is good enough to check whether there are statistically significant differences between the means of treatments. In this case it is tested hypothesis assuming that a least one mean treatment value ( $\mu$ ) differs from the others. Therefore, null and alternative hypotheses can be express as [15]:

$$\begin{aligned} H_0: \mu_1 = \mu_2 = \dots = \mu_k = 0 \\ H_1: \mu_j \neq 0 \text{ for at least one } j \text{ different than zero.} \end{aligned} \quad (1)$$

The procedure of test involves an *analysis of variance (ANOVA)* and performing  $F$ -test. Observed value is calculated as the ratio between treatment mean squares ( $MS_{Tr}$ ) and error mean squares  $MS_E$  (error variance):

$$F_o = \frac{MS_{Tr}}{MS_E} = \frac{\frac{SS_{Tr}}{a-1}}{\frac{SS_E}{a(n-1)}} \quad (2)$$

where,  $SS_{Tr}$  is sum of squares of treatment,  $SS_E$  is sum of squares of error,  $(a - 1)$  represents treatments degrees of freedom,  $a(n - 1)$  represents error degrees of freedom,  $a$  is number of treatments (number of

samples),  $n$  is number of observation for particular treatment. Total sum of squares ( $SS_T$ ) is addition of sum of squares of treatment and sum of squares of error and it is calculated as:

$$SS_T = SS_{Tr} + SS_E = \sum_{i=1}^n (\hat{y}_i - \bar{y})^2 + \sum_{i=1}^n (y_i - \hat{y}_i)^2 \tag{3}$$

whre,  $\hat{y}_i$  is the predicted value for the  $i_{th}$  test,  $\bar{y}$  is the mean of response variable observations,  $y_i$  is the  $i_{th}$  observed value of the response variable.

Having calculated  $F_o$ ,  $H_0$  can be accepted or rejected in the following cases:

$$H_0 \text{ is } \begin{cases} \text{Rejected if } F_o > F_{\alpha,(a-1),a(n-1)} \\ \text{Accepted if } F_o < F_{\alpha,(a-1),a(n-1)} \end{cases} \tag{4}$$

$H_0$  is going to be rejected if observed value of  $F_o$  is grater than its critical value  $F_{\alpha,(a-1),a(n-1)}$ . The critical value is taken from corresponding statistical table for significance level  $\alpha$ , the degrees of freedom for the numerator  $(a - 1)$ , and degrees of freedom for the denominator  $a(n - 1)$ . Also,  $H_0$  is going to be accepted if observed value is lower than its critical value ( $F_o < F_{\alpha,(a-1),a(n-1)}$ ). If  $p$ -value approach for the statistics  $F_o$  is used than  $H_0$  is going to be rejected if  $p < \alpha$ , and will be accepted if  $p > \alpha$ .

### 2.2. Linear regression

A general multiple linear regression model with  $k$  repressor variables is express as:

$$y = \beta_0 + \beta_1 x_1 + \beta_2 x_2 + \dots + \beta_k x_k + \varepsilon \tag{5}$$

where,  $y$  is response variable also called dependant variable,  $\beta_j, \beta_j, j = 0, 1, 2, \dots, k$ , are regression coefficients or parameters and represent expected change in response variable per unit change in input variable,  $x_j$ , is regressesor variable or input variable or independent variable,  $\varepsilon$  is random error, which supposed to be normally distributed with  $N(0, \sigma^2)$  for given values of  $x$  and  $y$ .

Parameter estimate in multiple linear regression models is done using least squares method. In case that there are multiple observations ( $n$ ) on the response variable  $y_1, y_2, \dots, y_n$ , and that there are observation at each input variable  $x_{ij}, (i = 1, 2, \dots, n)$  than it can be represented as matrix in Table 1 an written as[16]:

$$y_i = \beta_0 + \beta_1 x_{i1} + \beta_2 x_{i2} + \dots + \beta_k x_{ik} + \varepsilon_i \tag{6}$$

$$y_i = \beta_0 + \sum_{j=1}^k \beta_j x_{ij} + \varepsilon_i; i = 1, 2, \dots, n \tag{7}$$

Table 1. Multiple linear regression model data

$y$	$x_1$	$x_2$	...	$x_k$
$y_1$	$x_{11}$	$x_{12}$	...	$x_{1k}$
$y_2$	$x_{21}$	$x_{22}$	...	$x_{2k}$
...	...	...	...	...
$y_n$	$x_{n1}$	$x_{n2}$	...	$x_{nk}$

Referring to Table 1, it can be formulated using the general multivariate linear regression model in matrix form as follows:

$$Y_{n \times 1} = X_{n \times (k+1)} \beta_{(k+1) \times 1} + \varepsilon_{n \times 1} \tag{8}$$

where,  $Y$  denotes a  $(n \times 1)$  vector of dependent variable observation,  $X$  is a  $n \times (k+1)$  matrix of independent variables,  $\beta$  is a  $((k+1) \times 1)$  vector of unobserved parameters of interest, and  $\varepsilon$  is an  $(n \times 1)$  random errors vector. Subscript  $n$  is a number of observations, subscript  $k$  is a number of independent variables. The general matrix form of the model becomes as follows:

$$\begin{bmatrix} y_1 \\ y_2 \\ \vdots \\ y_n \end{bmatrix} = \begin{bmatrix} 1 & x_{11} & x_{12} \dots & x_{1k} \\ 1 & x_{21} & x_{22} \dots & x_{2k} \\ \vdots & \vdots & \vdots \ddots & \vdots \\ 1 & x_{n1} & x_{n2} \dots & x_{nk} \end{bmatrix} \begin{bmatrix} \beta_0 \\ \beta_1 \\ \vdots \\ \beta_k \end{bmatrix} + \begin{bmatrix} \varepsilon_1 \\ \varepsilon_2 \\ \vdots \\ \varepsilon_n \end{bmatrix} \tag{9}$$

After solving the function that minimizes sum of squared errors  $\varepsilon^2$ , the least squared estimator of  $\beta$  can be calculated from the following:

$$\hat{\beta} = (X'X)^{-1} X'Y \tag{10}$$

Significance test of regression model is to determine existence of the significant relationship between input variable and output variable. In this case it is tested hypothesis assuming that a least one  $\beta$  parameter differs from the others.

$$\begin{aligned} H_0: & \beta_1 = \beta_2 = \dots \beta_k = 0 \\ H_1: & \beta_j \neq 0 \text{ for at least one } j \text{ different than zero.} \end{aligned} \tag{11}$$

The procedure of test involves an *analysis of variance (ANOVA)* and performing  $F$ -test. Observed value is calculated as the ratio between regression mean squares ( $MS_R$ ) and error mean squares  $MS_E$  (error variance):

$$F_o = \frac{MS_R}{MS_E} = \frac{\frac{SS_R}{k}}{\frac{SS_E}{n-k-1}} \tag{12}$$

where,  $SS_R$  regression sum of squares,  $SS_E$  is error sum of squares,  $k$  is degree of freedom for the numerator,  $(n - k - 1)$  is degree of freedom for the denominator. Total sum of squares is addition of regression sum of squares and error sum of squares and it is calculated as:

$$SS_T = SS_R + SS_E = \sum_{i=1}^n (\hat{y}_i - \bar{y})^2 + \sum_{i=1}^n (y_i - \hat{y}_i)^2 \tag{13}$$

where,  $\hat{y}_i$  is the predicted value for the  $i_{th}$  test,  $\bar{y}$  is the mean of all response variable observations,  $y_i$  is the  $i_{th}$  observed value of the response variable.

$$H_0 \text{ is } \begin{cases} \text{Rejected if } F_o > F_{\alpha, k, n-k-1} \\ \text{Accepted if } F_o < F_{\alpha, k, n-k-1} \end{cases} \tag{14}$$

$H_0$  is going to be rejected if observed value of  $F_o$  is greater than its critical value  $F_{\alpha,k,n-k-1}$ . The critical value is taken from corresponding statistical table for significance level  $\alpha$ , the degrees of freedom for the numerator  $k$ , and degrees of freedom for the denominator  $(n - k - 1)$ . Also,  $H_0$  is going to be accepted if observed value is lower than its critical value ( $F_o < F_{\alpha,k,n-k-1}$ ). If  $p$ -value approach for the statistics  $F_o$  is used then  $H_0$  is going to be rejected if  $p < \alpha$ , and will be accepted if  $p > \alpha$ .

Goodness of fit of a model is measured by coefficient of determination  $R^2$ , which is a measure of how well real data points are approximated with regression model. It measures how amount of reductions of variability in response variable caused using input variables in regression model.

$$R^2 = \frac{SS_R}{SS_T} \quad (15)$$

Higher value of  $R^2$  means better fit. If  $R^2 = 1$  it means that there is perfect fit. However, having a higher value does not mean that there is a good fit and that regression model is good one because adding a new variable to the model (either the variable is significant or not) will increase  $R^2$  value, which will lead to poor prediction. To solve this, an adjusted  $R^2$  is introduced, which will not always increase with adding a new variable.

$$R_{adj}^2 = \frac{SS_R}{SS_T} \quad (16)$$

If non-significant variable is added to the model  $R_{adj}^2$  will decrease and vice versa.

### 3. Factorial Design

Factorial experiments can be design with one, two, three and more factors. Experiments with only one factor are often called simple comparative experiments. In these cases,  $t$ -test or ANOVA were used for analysis.

Factorial experiments with two factors ( $A$  and  $B$ ) usually include two level factorial designs for identification of factor effects on the response variable by investigating all possible combinations of the factor levels. The factor effect is defined as change in the response variable by changing the level of the factor.

Factorial experiments with multiple factors ( $A, B, \dots, K$ ), with two levels ("low" and "high") the complexity of experimentation might be a problem. The number of possible combinations goes up with the number of factors, for instance a 2-level design with 8 factor has 256 combination which very set such type of experiments and analyze data. Multiple factor experiment requires a lot of resources, materials and it is time consuming and expensive. Additional problem with multiple factorial design is to maintain experimental conditions unchanged during a huge number of experiments.

Trying to overcome the problems with multiple factor factorial designs and depending from a case to case, it is possible to be designed as Full Factorial Design  $2^k$  or Fractional Factorial Design  $2^{k-p}$ . In this case number 2 represents number of levels, while  $k$  is number of factors and  $p$  is the fraction size of the full factorial used. More details about full factorial and fractional factorial design with examples is provided below[17].

#### 3.1. Full Factorial Design

A full factorial design is convenient for a low number of factors if the resources are available. Conceptual approach for DOE is explained for two  $2^2$  and three  $2^3$  factors as well as general  $2^k$  factorial design, in which  $k$  represents number of factors while number 2 represents number of levels. Uppercase letters  $A, B, C, \dots$  are usually used for *factor* designation while lowercase letters are used treatments. Each factor has two levels *low* (–) and *high* (+). Number of combinations for  $2^2$  is four, for  $2^3$  is eight and so on. Each combination is called *treatment* which is represented with a lowercase letter. The number of test units for each treatment is called

the number of *replicates*. For example, if three units / samples were tested at each treatment, the number of replicates is three.

Design matrix for a  $2^2$  factorial design is given in Table 2:

Table 2. design matrix and signs for effects in  $2^2$  factorial design

	A	B	AB
$-I$	-1	-1	+1
$a$	+1	-1	-1
$b$	-1	+1	-1
$ab$	+1	+1	+1

where, A and B represent factors while AB represents interaction between A and B factor.

This design is an orthogonal. The following linear regression model is used for the analysis the analysis:

$$y = \beta_0 + \beta_1 x_1 + \beta_2 x_2 + \beta_{12} x_1 x_2 + \varepsilon \quad (17)$$

Where,  $x_1$  and  $x_2$  represent coded variables of factors A and B respectively, while  $x_1 x_2$  cross-product and represents AB interaction,  $x_j = -1$  and  $x_j = +1$  represent *low* and *high* levels of factors.

$$ss = \frac{1}{n2^2} (\text{contrast})^2 \quad (18)$$

Where, *contrast* is obtained from Table 2 as sum of products of signs in corresponding column and the runs listed in corresponding rows.

### 3.2. General $2^k$ Factorial Design

Experimental data analysis was done using Design of Experiment (DOE) – full factor factorial design. Generalized case of a  $2^k$  factorial design is introduced and applied in this study, where  $k$  is number of factors at two levels. Statistical model includes  $k$  main effects,  $\binom{k}{2}$  two-factor interaction,  $\binom{k}{3}$  three-factor interactions, ...,  $\binom{k}{k}$  one  $k$ -factor interaction. The procedure for a  $2^k$  factorial design was the following:

1. estimated factor effect – effects are estimated and their magnitudes were examined with the aim of important factors identification;
2. initial model formulation – full model is included that takes in account all main effects and interactions;
3. statistical testing – ANOVA is used to test significance of main effects and interactions;
4. model refinement – non-significant factors from initial model are removed;
5. residual analysis – to check adequacy of the model and assumptions;
6. result interpretation – graphical analysis of the results such as main effects, interactions etc.

General form of ANOVA mentioned in step 3 is shown in the following table [17]:

Table 3. ANOVA for a general  $2^k$  design

Source of variation	Sum of squares	Degrees of freedom	Mean Square	Fo
<b><math>k</math> main effects</b>				
<i>A</i>	$SS_A$	1	$MS_A = \frac{SS_A}{a-1}$	$F_o = \frac{MS_A}{MS_E}$
<i>B</i>	$SS_B$	1		
...	...	...		
<i>K</i>	$SS_K$	1		
<b><math>\binom{k}{2}</math> two-factor interaction</b>				
<i>AB</i>	$SS_{AB}$	1	$MS_{AB} = \frac{SS_{AB}}{(a-1)(b-1)}$	$F_o = \frac{MS_{AB}}{MS_E}$
<i>AC</i>	$SS_{AC}$	1		
...	...	...		
<i>JK</i>	$SS_{JK}$	1		
<b><math>\binom{k}{3}</math> three-factor interactions</b>				
<i>ABC</i>	$SS_{ABC}$	1	...	...
<i>ABD</i>	$SS_{ABD}$	1		
...	...	...		
<i>IJK</i>	$SS_{IJK}$	1		
...	...	...		
<b><math>\binom{k}{k}</math> <math>k</math>-factor interaction</b>				
<i>ABC...K</i>	$SS_{ABC...K}$	1	...	...
<b>Error</b>	$SS_E$	$2^k(n-1)$		
<b>Total</b>	$SS_T$	$n2^k-1$		

To estimate sum of squares and effects, contrasts associated with the effect were determined first.

$$Contrast_{AB...K} = (a \pm 1)(b \pm 1) \dots (k \pm 1) \tag{19}$$

where,  $a, b, \dots, k$  are experiment treatment combinations.

After computation of the contrast, the **effects** and the **sum of squares** can be estimated as follows:

$$A, B \dots K = \frac{2}{n2^k} (Contrast_{AB...K}) \tag{20}$$

$$SS_{A,B...K} = \frac{1}{n2^k} (Contrast_{AB...K})^2 \tag{21}$$

where,  $n$  represents number of replicates.

Total sum of squares is calculated using the following equation:

$$SS_T = \sum_{i=1}^a \sum_{j=1}^b \sum_{k=1}^n (y_{ijk} - \bar{y}_{...})^2 = SS_A + SS_B + \dots + SS_E \tag{22}$$

where,  $y_{ijk}$  is an observation for factor A at  $i$ -th level ( $i = 1, 2, \dots a$ ) and for B factor at  $j$ -th level ( $j = 1, 2, \dots b$ ) and for  $k$ -th replicate ( $k = 1, 2, \dots n$ ).

Sum of squares of error can be obtained from using the following equation:

$$SS_E = SS_T - SS_M \tag{23}$$

where,  $SS_M$  is model sum of squares and it is equal:  $SS_M = SS_A + SS_B + \dots + SS_K$ .

### 3.3. Fractional Factorial Design

If the number of factors is increased, then the number of test units and treatment combinations (runs) is going to be increased. For instance, for 5 factors, 32 units and treatments are needed ( $2^5=32$ ). Since a low number of main effects and lower order interactions are significant to the response variable, and usually higher order interactions are not significant to the response variable, than fractional factorial designs are introduced. Therefore, fractional factorial designs take in account only a low number of main effects and lower order interactions. The higher order interactions are neglected due to its negligible effects on the response variable. For instance,  $2^3 = 8$ , and has 8 treatment combination and 8 test units is required. For some reason he cannot afford all 8 combinations he decided to run one half factorial design  $2^{3-1} = 4$ . Therefore, instead of 8 test units he will test only 4. Now he needs to determine which four treatment combinations to test. As the first step, he complete  $2^3$  full factorial design matrix shown in Table 4 and selected those with positive values in ABC column as it shown in

Table 5.

Table 4. Full  $2^3$  factorial design matrix

	<i>I</i>	<i>A</i>	<i>B</i>	<i>AB</i>	<i>C</i>	<i>AC</i>	<i>BC</i>	<i>ABC</i>
<i>(I)</i>	1	-1	-1	1	-1	1	1	-1
<i>a</i>	1	1	-1	-1	-1	-1	1	1
<i>b</i>	1	-1	1	-1	-1	1	-1	1
<i>ab</i>	1	1	1	1	-1	-1	-1	-1
<i>c</i>	1	-1	-1	1	1	-1	-1	1
<i>ac</i>	1	1	-1	-1	1	1	-1	-1
<i>bc</i>	1	-1	1	-1	1	-1	1	-1
<i>abc</i>	1	1	1	1	1	1	1	1

Table 5. The  $2^{3-1}$  factorial design factorial design matrix with the defining relations  $I = ABC$  and  $I = -ABC$

	<i>I</i>	<i>A</i>	<i>B</i>	<i>AB</i>	<i>C</i>	<i>AC</i>	<i>BC</i>	<i>ABC</i>
<i>a</i>	1	1	-1	-1	-1	-1	1	1
<i>b</i>	1	-1	1	-1	-1	1	-1	1
<i>c</i>	1	-1	-1	1	1	-1	-1	1
<i>abc</i>	1	1	1	1	1	1	1	1
(1)	1	-1	-1	1	-1	1	1	-1
<i>ab</i>	1	1	1	1	-1	-1	-1	-1
<i>ac</i>	1	1	-1	-1	1	1	-1	-1
<i>bc</i>	1	-1	1	-1	1	-1	1	-1

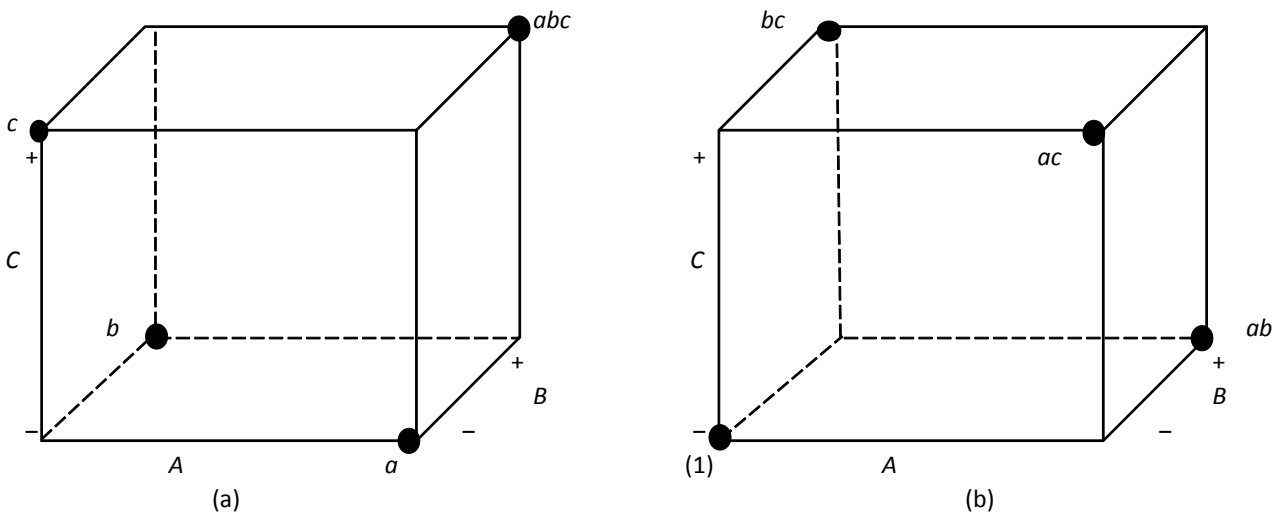


Figure 4. The  $2^{3-1}$  factorial design factorial design orthogonal representation with defining relations: (a) principal fraction  $I = ABC$ ; (c) alternative fraction  $I = -ABC$

In this example  $ABC$  is called the generator. It noticed that some columns in

Table 5 have the same values (they are the same) and they are colored in the same color ( $I = ABC$ ,  $A = BC$ ,  $B = AC$ ,  $C = AB$ ), where  $I$  is called *defining relation*, which may be aliased with several effects. The alias can be determined by using the defining relation  $I = ABC$  by multiplying any column by the defining relation yields the aliases such as:  $A \cdot I = A \cdot ABC = A^2BC$ . Since square of any column is equal to identity  $I$ , then it can be written as:  $A = BC$ . The other aliases may be obtained,  $B \cdot I = B \cdot ABC = AB^2C$  and  $C \cdot I = C \cdot ABC = ABC^2$ , and replacing squared member by  $I$  it is obtained  $B = AC$ ,  $C = AB$ . Therefore, when  $A$ ,  $B$  and  $C$  is estimated it is actuality estimated  $A + BC$ ,  $B + AC$ ,  $C + AB$ .

Resolution a two-level fractional factorial design  $2^{3-1}$  is called a **resolution III design** and it is equal to the number of letters in the shortest word in the defining relation in which Roman numbers in subscript are used to define resolution (e.g.  $2_{III}^{3-1}$  design for  $I = ABC$  and  $I = -ABC$ ;  $2_{IV}^{4-1}$  design for  $I = ABCD$  and  $I = -ABCD$  etc.).

Designs with a resolution less than III are never used. Fractional factorial designs with the highest available resolution with their defining relations is shown in Table 6.

Table 6. The  $2^{3-l}$  factorial design factorial design matrix with the defining relations  $I = ABC$  and  $I = -ABC$

Number of factors	Fraction	Resolution	Runs (treatments)	Defining relation
3	$2^{3-1}$	III	4	$I = ABC$
4	$2^{4-1}$	IV	8	$I = ABCD$
5	$2^{5-1}$	V	16	$I = ABCDE$
6	$2^{6-1}$	VI	32	$I = ABCDEF$
7	$2^{7-1}$	VII	64	$I = ABCDEFG$

#### 4. Application

##### 4.1. The $2^4$ Full Factorial Design

DOE a very suitable tool used for process performance and product quality improvement [18], for solar technologies [19] etc. In this example DOE is applied on injection-molding process with the aim of improving product quality such as excessive flash. Factors considered as affecting for flash formation are: pack pressure (A), pack time (B), injection speed (C), and screw RPM (D), while clamping pressure, injection pressure and melting temperature were under control. Each factor affecting flash formation is considered at low and high levels and shown in Table 7.

Table 7. Factors contributing to flash formation

FACTORS	low (-1)	High +1
Pack pressure (A) in bar	10	30
Pack time (B), in sec	1	5
Injection speed (C) in mm/sec	12	50
Screw RPM (D) in rpm	100	200

The design matrix for  $2^4$  factorial design and single replicate response data for flash size in millimeters is shown in Table 8.

Table 8. Design matrix for flash formation

Run	Run label	A	B	C	D	AB	AC	AD	BC	BD	CD	ABC	BC D	AC D	AB D	ABCD	Flash (mm)
1	(1)	-1	-1	-1	-1	1	1	1	1	1	1	-1	-1	-1	-1	1	0.22
2	a	1	-1	-1	-1	-1	-1	-1	1	1	1	1	-1	1	1	-1	6.18
3	b	-1	1	-1	-1	-1	1	1	-1	-1	1	1	1	-1	1	-1	0
4	ab	1	1	-1	-1	1	-1	-1	-1	-1	1	-1	1	1	-1	1	5.91
5	c	-1	-1	1	-1	1	-1	1	-1	1	-1	1	1	1	-1	-1	6.6
6	ac	1	-1	1	-1	-1	1	-1	-1	1	-1	-1	1	-1	1	1	6.05
7	bc	-1	1	1	-1	-1	-1	1	1	-1	-1	-1	-1	1	1	1	6.76
8	abc	1	1	1	-1	1	1	-1	1	-1	-1	1	-1	-1	-1	-1	8.65
9	d	-1	-1	-1	1	1	1	-1	1	-1	-1	-1	1	1	1	-1	0.46
10	ad	1	-1	-1	1	-1	-1	1	1	-1	-1	1	1	-1	-1	1	5.06
11	bd	-1	1	-1	1	-1	1	-1	-1	1	-1	1	-1	1	-1	1	0.55
12	abd	1	1	-1	1	1	-1	1	-1	1	-1	-1	-1	-1	1	-1	4.84
13	cd	-1	-1	1	1	1	-1	-1	-1	-1	1	1	-1	-1	1	1	11.55
14	acd	1	-1	1	1	-1	1	1	-1	-1	1	-1	-1	1	-1	-1	9.9
15	bcd	-1	1	1	1	-1	-1	-1	1	1	1	-1	1	-1	-1	-1	9.9
16	abcd	1	1	1	1	1	1	1	1	1	1	1	1	1	1	1	9.9

Applying Equations (19) and Equation (20) in the design matrix (Table 8) main effects are calculated and shown in Table 9.

Table 9. Factor effect estimate and sum of squares

Model term	Effects	Coefficients = (effect / 2)	SS	Percent contribution
A	2.5575	1.27	26.16323	0.12126637
B	0.061875	0.03	0.015314	7.0981E-05
C	5.76125	2.88	132.768	0.6153788
D	1.47125	0.73	8.658306	0.04013119
AB	0.466125	0.23	0.86909	0.00402823
AC	-2.6345	-1.31	27.76236	0.12867835
AD	-0.748	-0.374	2.238016	0.01037319
BC	0.218625	0.10	0.191188	0.00088615
BD	-0.507375	-0.25	1.029718	0.00477273
CD	1.82325	0.91	13.29696	0.06163133
ABC	0.556875	0.27	1.240439	0.00574943
BCD	-0.598125	-0.29	1.431014	0.00663274
ACD	2.22045E-16	1.11E-16	1.97E-31	9.1409E-34
ABD	-0.130625	-0.06	0.068252	0.00031635
ABCD	-0.067375	-0.03	0.018158	8.416E-05
Mean <sup>4</sup>		5.78		

In this example there is a problem to apply *F*-test. Since there is only one replicate of the response variable *F*-test is not possible to be done because error degrees of freedom is zero ( $MS_E = SS_E/0$ ; – division by zero is undefined). Potential solution can be a graphical solution such as Normal probability diagram of effects<sup>5</sup>, or dropping entire factors from the model. Therefore based on Table 9, a graphical solution is used to represent main effects and identification of those significant, which is shown in Figure 5.

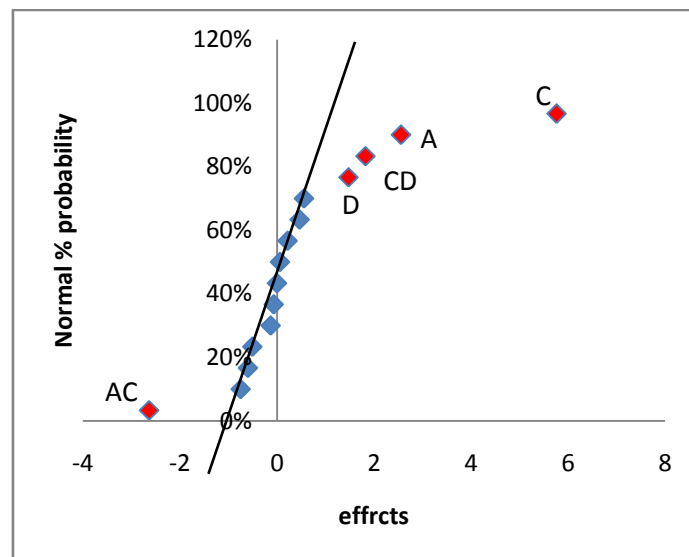


Figure 5. Normal probability plot of the effects

<sup>4</sup>Mean response, calculated as average flash value.

From normal probability diagram of effects, it is observed that *A*, *C*, *D*, are significant factors and *AC*, and *CD* are significant interactions. Plots of the main effects of factor *A*, *C*, *D* as well as *AC* and *CD* interactions are shown in Figure 6.

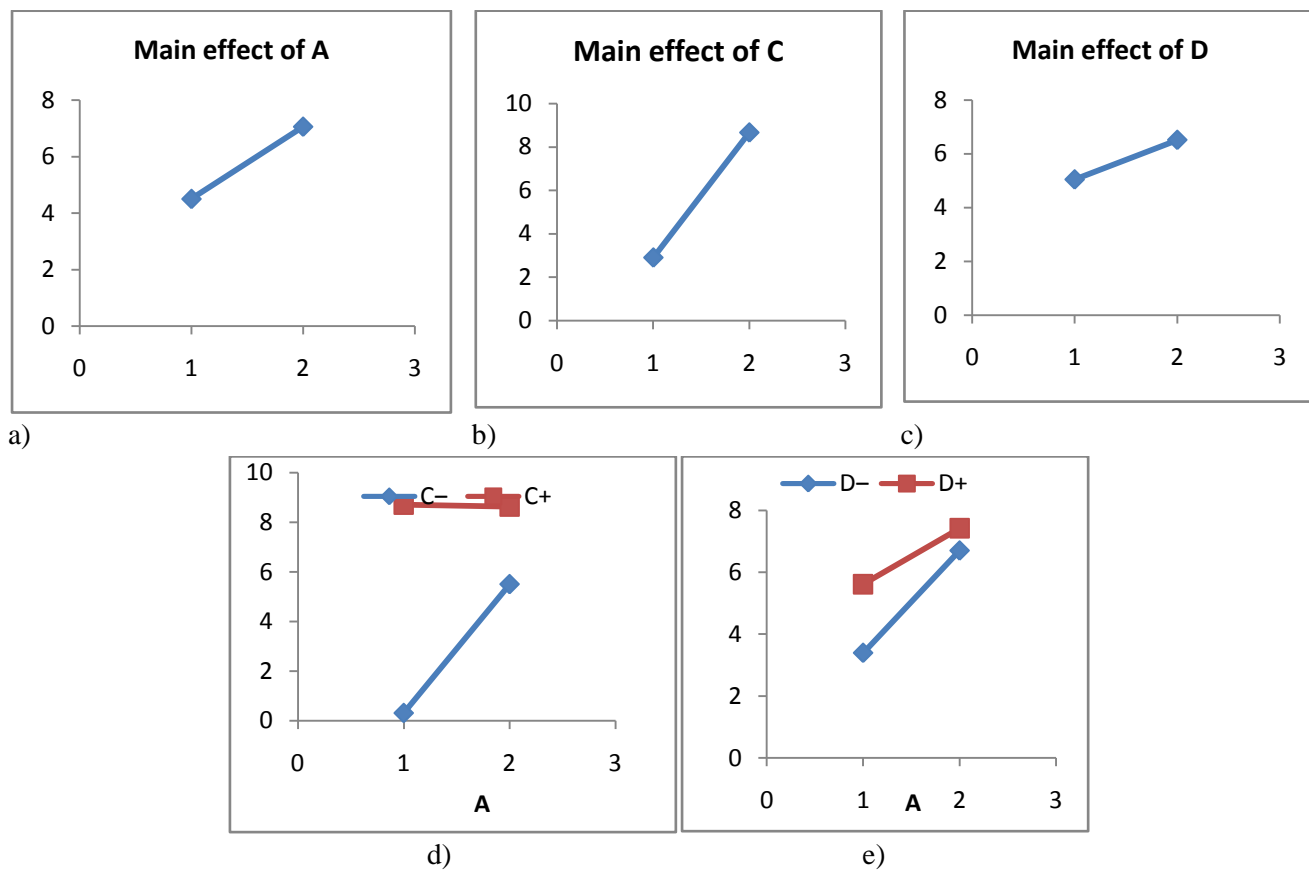


Figure 6. Main effects and interactions

Referring to Figure 6 it is observed that all three main effects are positive indicating that the molding process supposed to be performed on low level to minimize flash size. Alongside main effects there are significant interactions. Since main effect are involved with significant interactions than they have no much meaning. Screw RPM and injection speed have little meaning at high pack pressure but has better performances in reducing flash size at low level. Therefore, the best setup for getting better product quality (reducing flash size), is obtained when all factors *A*, *C*, *D* are at the low level.

Since factor *B* is not significant it is dropped from the model. All associated interactions with *B* factor are dropped from as well. Therefore, the design becomes a  $2^3$  factorial design with two replicates so called *hidden replication* (still has 16 responses). In this the mean case sum of squares of error ( $MS_E$ ) can be calculated because degrees of freedom are different than zero ( $2^k(n-1) = 2^3(2-1) = 8$ ). ANOVA result for  $2^3$  factorial design with two replicates is shown in Table 10.

Table 10. Factor effect estimate and sum of squares

	SS	DF	MSS	Percent contribution	$F_0$	$F_{cr} = F_{0 > F_{\alpha=5\%, v1, v2}}$	
<b>A*</b>	26.16	1	26.16	0.1212	29.47	5.32	Sign.
<b>C*</b>	132.76	1	132.76	0.6153	149.57	5.32	Sign.
<b>D*</b>	8.65	1	8.65	0.0401	9.75	5.32	Sign.
<b>AC*</b>	27.76	1	27.76	0.1286	31.27	5.32	Sign.
<b>CD*</b>	13.29	1	13.29	0.0616	14.97	5.32	Sign.
<b>Model (SS<sub>M</sub>)</b>	208.64						
<b>Error (SS<sub>E</sub>)</b>	7.10	8	0.88				
<b>Total (SS<sub>T</sub>)</b>	215.75	15	14.38				

Where, total sum of squares (SS<sub>T</sub>) is obtained using Equation (22), model sum of squares is obtained as SS<sub>M</sub> =  $\Sigma SS_{A,B,C...K} = SS_A + SS_C + SS_D + SS_{AD} + SS_{CD}$ , while error sum of squares is obtained as SS<sub>E</sub> = SS<sub>T</sub> - SS<sub>M</sub>.

Regression model that represent **predicted/fitted** value for flash formation is given below, and includes only significant factor and interactions.

$$\hat{y} = 5.78 + 1.3x_1 + 2.9x_3 + 0.7x_4 - 1.3x_1x_3 + 0.9x_3x_4 \quad (24)$$

Based on Equation (24), it is possible to perform diagnostic check if it is applied to the residuals.

Table 11. Factor effect estimate and sum of squares

Run label	y	$\hat{y}$	$e = y - \hat{y}$
(1)	0.22	-0.427625	0.647625
<b>a</b>	6.1875	4.764375	1.423125
<b>b</b>	0	-0.427625	0.427625
<b>ab</b>	5.9125	4.764375	1.148125
<b>c</b>	6.6	7.968125	-1.368125
<b>ac</b>	6.05	7.891125	-1.841125
<b>bc</b>	6.765	7.968125	-1.203125
<b>abc</b>	8.657	7.891125	0.765875
<b>d</b>	0.462	1.043625	-0.581625
<b>ad</b>	5.06	6.235625	-1.175625
<b>bd</b>	0.55	1.043625	-0.493625
<b>abd</b>	4.84	6.235625	-1.395625
<b>cd</b>	11.55	9.439375	2.110625
<b>acd</b>	9.9	9.362375	0.537625
<b>bcd</b>	9.9	9.439375	0.460625
<b>abcd</b>	9.9	9.362375	0.537625

Normal probability plot of residuals and residuals versus predicted value of flash size is shown in Figure 7.

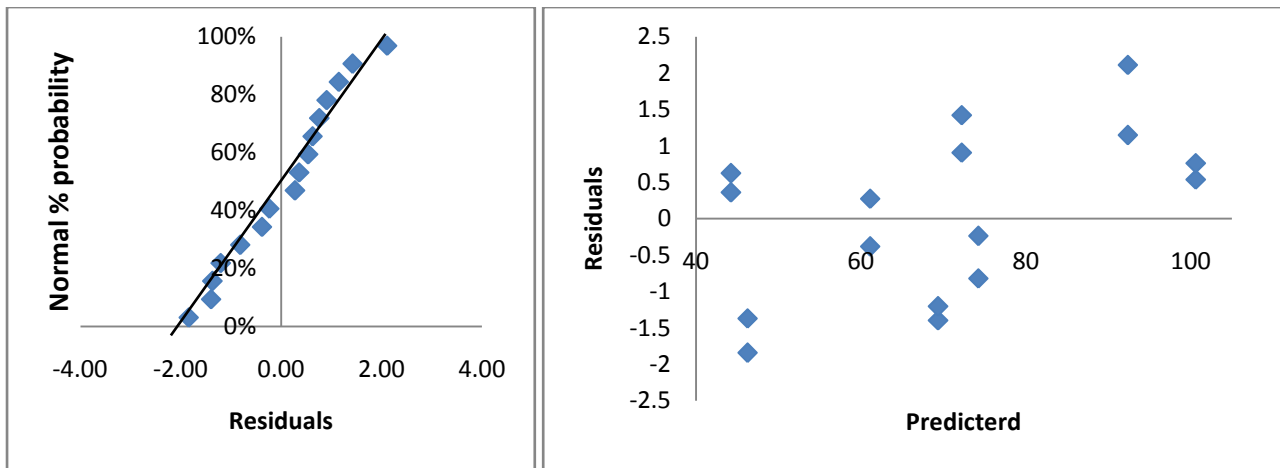


Figure 7. Model adequacy checking

Residuals versus predicted value plot shows randomly dispersed data around the horizontal axis (predicted values), therefore the variance has no tendency to change along predicted value axis indicating that linear regression model is appropriate for the data.

**4.2. The  $2^{4-1}$  Fractional Factorial Design**

Applying the  $2^{4-1}$  fractional factorial design on the previous example with the highest possible resolution (IV) and using defining relation  $I=ABCD$  it is obtained the  $2^3$  design, which is shown in Table 12.

Table 12. The  $2^{4-1}_{IV}$  factorial design with the defining relation  $I=ABCD$

		Basic Design				Flash				Residuals		
RUN	Run label	A	B	C	D=ABC	AB	AC	AD	y	$\hat{y}$	$\Sigma(y_i - \bar{y})^2$	e = y - $\hat{y}$
	alias	BCD	ACD	ABD	ABC	BC	BD	CD				
1	(1)	-1	-1	-1	-1	1	1	1	0.22	-0.8975	30.4704	1.1175
2	ab	1	1	-1	-1	1	-1	-1	5.9	4.7375	0.0256	1.1625
3	ac	1	-1	1	-1	-1	1	-1	6.05	7.2125	0.0961	-1.1625
4	bc	-1	1	1	-1	-1	-1	1	6.7	7.8175	0.9216	-1.1175
5	ad	1	-1	-1	1	-1	-1	1	5.1	6.2625	0.4096	-1.1625
6	bd	-1	1	-1	1	-1	1	-1	0.55	1.6675	26.9361	-1.1175
7	cd	-1	-1	1	1	1	-1	-1	11.5	10.3825	33.1776	1.1175
8	abcd	1	1	1	1	1	1	1	9.9	8.7375	17.3056	1.1625
mean									5.74			

Referring to Table 12 factors A, B and C, represent basic design factors that are aliased with three factor interactions BCD, ACD and ABD respectively, while factor D is aliased with ABC three factor interaction. The two factor interactions AB, AC and AD are re aliased with the other two factor interactions BC, BD and CD respectively. Therefore, the relationships are: A = BCD, B = ACD, C = ABD, D = ABC, AB = BC, AC = BD and AD = CD. Using Equation (20) and multiplying corresponding column with measured values (flash) and summing up, a **contrast** is obtained for the certain column. Using Eq. (21), contrast is divided by  $n2^k$  and main effects are obtained for number of replicates  $n = 1$ , and number of factors  $k = 3$  and shown in Table 13.

Table 13. Estimate of effects and aliases

Effect estimate	Aliased structure
[A] = 1.995	[A] → A + BCD
[B] = 0.045	[B] → B + ACD
[C] = 5.595	[C] → C + ABD
[D] = 2.045	[D] → D + ABC
[AB] = 2.28	[AB] → AB + BC
[AC] = -3.12	[AC] → AC + BD
[AD] = -0.52	[AD] → AD + CD

Plot of main effects is shown in Figure 8.

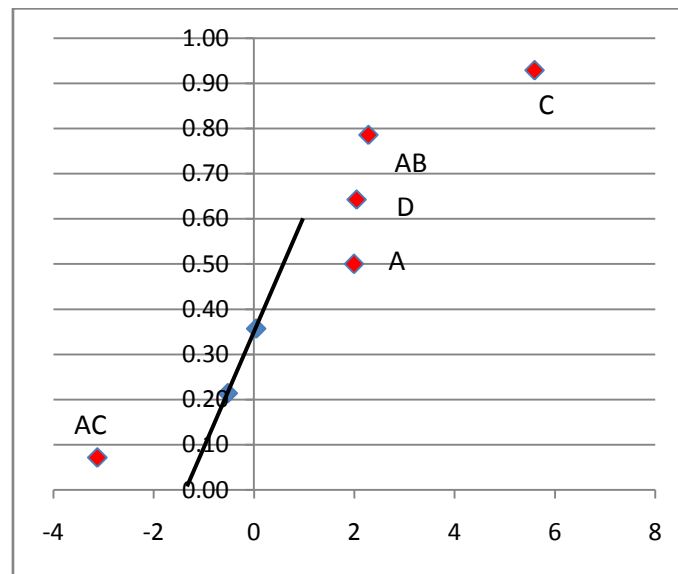


Figure 8. Normal Probability plot of effects

From normal probability diagram of effects it is observed that A, C, and D, are significant factors and AC, and AB are significant interactions. Based on the above analysis it is possible to predict flash size using the following regression model:

$$\hat{y} = 5.74 + 1.99x_1 + 5.59x_3 + 2.04x_4 + 2.28x_1x_2 - 3.12x_1x_3 \tag{25}$$

### 5. Conclusion

Thanks to software development, the use of DOE as scientific tool has increased rapidly in past 20 years in manufacturing and non-manufacturing industries over the world. It was most popular tool used by scientist in medicine (with 18%), engineering and biochemistry (with 20%), physics and computer science (with 13%), providing about 50% participation of these scientific areas compared to the all other scientific areas. The trend of use of DOE is rapidly growing and it is expected to slow down in the near future for current scientific areas, but also will expanded over new scientific areas and have rapid grow there.

Implementing valid and efficient factorial experiments provide quantitative data that can be used as support for decision making during system, process and product design or improvement. Full factorial design and fractional factorial design with examples of application of DOE in product quality improvement is presented with sep-by-step procedures and result interpretation. This can be a very useful guide to experimenter how to design and conduct experiments, and how to analyze and interpret data.

**References**

- [1] B. Duraković and H. Bašić, "Continuous Quality Improvement in Textile Processing by Statistical Process Control Tools: A Case Study of Medium-Sized Company," *Periodicals of Engineering and Natural Sciences*, vol. 1, no. 1, pp. 36-46, 2013.
- [2] F. Paulo and L. Santos, "Design of experiments for microencapsulation applications: A review," *Materials Science and Engineering: C*, vol. 77, no. August, pp. 1327-1340, 2017.
- [3] P. Yu, M. Y. Low and W. Zhou, "Design of experiments and regression modelling in food flavour and sensory analysis: A review," *Trends in Food Science & Technology*, vol. 71, no. January, pp. 202-215, 2018.
- [4] A. Schlueter and P. Geyer, "Linking BIM and Design of Experiments to balance architectural and technical design factors for energy performance," *Automation in Construction*, vol. 86, no. February, pp. 33-43, 2018.
- [5] B. Durakovic and M. Torlak, "Simulation and experimental validation of phase change material and water used as heat storage medium in window applications," *J. of Mater. and Environ. Sci.*, vol. 8, no. 5, pp. 1837-1746, 2017.
- [6] D. B. Hibbert, "Experimental design in chromatography: A tutorial review," *Journal of Chromatography B*, vol. 910, no. Dec, pp. 2-13, 2012.
- [7] S. S. Garud, I. A. Karimi and M. Kraft, "Design of computer experiments: A review," *Computers & Chemical Engineering*, vol. 106, no. November, pp. 71-95, 2017.
- [8] J. K. Telford, "A Brief Introduction to Design of Experiments," *Johns Hopkins APL Technical Digest*, vol. 27, no. 3, pp. 224-232, 2007.
- [9] B. Durakovic, H. Bašić and H. Muhič, "The Interrelationships between quality management practices and their effects on innovation," in *Trends in the Development of Machinery and Associated Technology*, Budapest, 2014.
- [10] H. Guo and A. Mettas, "Design of Experiments and Data Analysis," in *2012 Annual Reliability and Maintainability Symposium*.
- [11] B. Duraković and H. Bašić, "Textile Cutting Process Optimization Model Based On Six Sigma Methodology In A Medium-Sized Company," *Journal of Trends in the Development of Machinery and Associated Technology*, vol. 16, no. 1, pp. 107-110, 2012.
- [12] B. Durakovic and M. Torlak, "Experimental and numerical study of a PCM window model as a thermal energy storage unit," *International Journal of Low-Carbon Technologies*, vol. 12, no. 3, p. 272–280, 2017.
- [13] "Scopus," 2017. [Online]. Available: [www.scopus.com](http://www.scopus.com). [Accessed September 2017].
- [14] D. Granato, V. M. d. A. Calado and B. Jarvis, "Observations on the use of statistical methods in Food Science and Technology," *Food Research International*, vol. 55, p. 137–149, 2014.
- [15] D. C. Montgomery, *Statistical Quality Control*, John Wiley, 2009.
- [16] D. C. Montgomery and G. C. Runger, *Applied Statistics and Probability for Engineers*, Willey, 2005.
- [17] D. C. Montgomery, *Design and Analysis of Experiments*, 5th edition, John Wiley and Sons, Inc. New York, 2001., 8 ed., John Wiley & Sons, Inc, 2013.
- [18] H. Bašić, B. Duraković and A. Softić, "Six Sigma Model Testing In Optimizing Medium-Sized Company Production Process," *Journal of Trends in the Development of Machinery and Associated Technology*, vol. 16, no. 1, pp. 103-106, 2012.
- [19] V. Okatia, A. Behzadmehra and S. Farsad, "Analysis of a solar desalinator (humidification–dehumidification cycle) including a compound system consisting of a solar humidifier and subsurface condenser using DoE," *Desalination*, vol. 397, no. November, pp. 9-21, 2016.